Interfacial Mass Transfer in Microfluidic Systems: Existence and Persistence of the Modified Grætz Behavior

by Joseph David Kirtland

INTERFACIAL MASS TRANSFER IN MICROFLUIDIC SYSTEMS: EXISTENCE AND PERSISTENCE OF THE MODIFIED GRÆTZ BEHAVIOR

A Dissertation

Presented to the Faculty of the Graduate School

of Cornell University

In Partial Fulfillment of the Requirements for the Degree of

Doctor of Philosophy

by

Joseph David Kirtland

August 2010

INTERFACIAL MASS TRANSFER IN MICROFLUIDIC SYSTEMS: EXISTENCE AND PERSISTENCE OF THE MODIFIED GRÆTZ BEHAVIOR

Joseph David Kirtland, Ph. D.

Cornell University 2010

In the works contained in this dissertation, we study interfacial mass transfer to stationary, moving, and diffusive interfaces in steady, laminar flows in microfluidic systems. These processes operate in the low Reynolds number, high Péclet number regime, where, for uniaxial flows, the absence of turbulence leads to poorly mixed bulk flows and a thick region depleted of solute (called the concentration boundary layer) near the reactive interface. The classic solutions for mass transfer to the walls of a pipe in uniaxial flow, due to Grætz and Lévêque, present an entrance region where the reactive flux drops quickly as the boundary layer thickness increases and an asymptotic region where the boundary layer has grown to the full thickness of the pipe and the shape of the concentration profile becomes self-similar. We present a generalization of the classic solutions to the case of three-dimensional flow, called the modified Grætz behavior: the transverse flow sweeps depleted fluid away from the reactive interface, keeping the boundary layer thin and maintaining high gradients of concentration and therefore high rates of mass transfer. Casting the problem in terms of the Sherwood number (a non-dimensionalized mass transfer coefficient), we distill the full convection-diffusion problem in a mathematically tractable form that leads to predicted correlations in uniaxial and three-dimensional flows. The local Sherwood number and the shape of the concentration profile in the cross section allow for the investigation of the role of Lagrangian chaos in maintaining this modified Grætz

behavior at arbitrarily large axial distance and Péclet number: chaos ensures that fluid swept away from the reactive surface is homogenized with the bulk before it returns to the reactive surface. We approach the problem by three methods: numerically – building the flux profile, concentration field, and local Sherwood number from particle trajectories; theoretically – generalizing the classic Grætz result to three-dimensional flow and moving interfaces; and experimentally, with studies of an electrochemical potential cell to extract the average Sherwood number from measurements of the total current. Our numerical and experimental results support the theoretical predictions and inform the design of efficient microfluidic reactors.

BIOGRAPHICAL SKETCH

Joseph was born to James and Mary Lou Kirtland in October of 1978 and grew up with two brothers and two sisters (Ruth, James, Jonathan, and Rebecca) in Berkeley Heights, NJ. The siblings were all old enough that it was a bit like growing up with six parents. That may sound terrifying, but it was in fact a major contributing factor in his ending up in academia, as it always kept him a bit ahead of the curve. He attended the Albert Nerken School of Engineering at the Cooper Union for the Advancement of Science and Art, in the East Village of New York City, where he received a Bachelors of Chemical Engineering (BChE) in 2001. Feeling a pull toward more fundamental studies and unspeakable dread at the thought of checking pressure gauges all day, he started his graduate work in the physics department at Cornell University in August of 2002. After two years of work as a teaching assistant, he happened upon a colloquium about fake plastic trees where he heard something about un-mixing the cream out of your coffee. That sounded just ridiculous enough to warrant a visit to the man would become his advisor, Abraham D. Stroock. Funny that he should end up working under a chemical engineering professor after all that talk about fundamental studies and pressure gauges, but you never do know where you'll end up next, do you? After another three years at Cornell, he passed the admission to candidacy exam and earned a Masters of Science in Physics from Cornell University in 2007. As of Fall 2010, he is working as an assistant professor of physics at Dordt College in exciting northwest Iowa.

Soli Deo Gloria

Many thanks for the grace and peace…

ACKNOWLEDGMENTS

First and foremost, I would like to thank God for the wonderful creation that He has given me to explore and contemplate, and for His direction and strength along the path that He has set before me. I thank my parents for all of their support and advice through the years, and the rest of my family for putting up with the odd-ball academic that I've become. I thank the members of the Graduate Christian Fellowship and Ithaca Baptist Church for support in my work and for challenging me to grow in my faith. I owe a huge debt of gratitude to Abe Stroock, who has been a remarkable advisor and a great friend throughout my studies. I would like to thank all the members of the Stroock group through the years, but especially Tobias Wheeler and Pavithra Sundararajan for their scientific and moral support. I would like to thank our collaborators, especially Hector Abruña and his students Jamie Cohen and David Finkelstein, as well as Donald Koch, for many helpful conversations. I would also like to thank all of the staff at Cornell, but especially the staff of the Cornell NanoScale Science and Technology Facility for all of their help with the fabrication processes that made my research possible. I greatly appreciate the willingness of Eric Siggia and Carl Franck to sit on my committee and for their direction in the doctoral process. Finally, I thank the Department of Physics and the Department of Chemical and Biomolecular Engineering at Cornell University. This work was funded by a Start-Up Grant from the North American Mixing Forum, the National Science Foundation (CTS-0529042), and the Department of Energy (DE-FG02-05ER46250). This research was conducted using the resources of the Cornell University Center for Advanced Computing, which receives funding from Cornell University, New York State, the National Science Foundation, and other leading public agencies, foundations and corporations.

TABLE OF CONTENTS

LIST OF FIGURES

LIST OF TABLES

CHAPTER 1

INTRODUCTION

The works contained in this dissertation are concerned with scalar transport in fluid flows that are laminar, three-dimensional, and chaotic. A phenomenon that we call the modified Grætz behavior (described below and investigated throughout the following chapters) has become evident through our consideration of the following questions:

(1) What effect do steady laminar three-dimensional flows have on mass transfer to interfaces within and bounding such flows?

(2) What information about a flow do we need in order to predict its effect on the rate of transfer?

And since most people would most likely never raise these questions,

(3) Why should we even ask them in the first place?

The laminar mixing community agrees on the answer to (1): rates of interfacial mass transfer increase in the presence of three-dimensional (3D) flow relative to corresponding uniaxial flows. As for question (2), the story that is laid out in the chapters of this dissertation will demonstrate that we can indeed predict the effects of a flow given only a few pieces of information about the flow, mainly geometric parameters, operating conditions, and shear rates at the interface in question. But perhaps most important at this point is an answer to (3). The mechanism by which efficient mixing increases rates of interfacial transfer has not been entirely well-understood (Chang and Sen 1994, Ganesan *et al* 1997), but efficient mass transfer is crucial in a variety of contexts, from analytical to industrial. Applications that involve mass transfer to interfaces in the laminar flow regime include microfluidic fuel cells for analysis and energy generation (Ferrigno *et al* 2002, Cohen *et al* 2005, Shrivastava

et al 2008), separation systems with and without membranes (Aref and Jones 1989, Brody and Yager 1997, Shrivastava *et al* 2008), and sensors utilizing surface-based reactions (Kamholz *et al* 1999, Ismagilov *et al* 2000, Vijayendran *et al* 2003, Golden *et al* 2007, Foley *et al* 2008, Squires *et al* 2008, Teles and Fonseca 2008). Microfluidic systems are especially sensitive to the introduction of 3D flow as their small size generally rules out the turbulent fluctuations that stir the fluid in larger systems. Increases in rates of interfacial transfer in these systems means greater power output from fuel cells, more efficient separations, and faster and more accurate detection of disease. The microfluidic platform makes devices portable and convenient, and enables scaling up for high throughput separations and screening, making deployment to remote and undeveloped communities feasible.

But there is another answer to question (3) that goes beyond the technological relevance of interfacial transfer in laminar flows. Working toward answers to question (1) by way of (2) allows us to explore the mechanism of interfacial transfer itself, and to develop a deeper understanding of the connection between mixing and mass transfer. It also requires us to refine and expand our first set of questions:

- How do the characteristics of a flow (flow rate, shear rate, shape of the velocity field) impact interfacial mass transfer, and what characteristics are most important? How do we connect Lagrangian properties (*e.g.* trajectories in the flow) and Eulerian properties (*e.g.* velocity and concentration fields) of the flow to the local and global characteristics of the transfer process (*e.g.* local flux and total integrated flux)?
- What role does Lagrangian chaos (which is essential for efficient laminar mixing in the bulk flow) play in interfacial mass transfer processes?

- In what mathematical framework can we cast the problem in order to glean more understanding? What measurable quantities best describe the transfer process, and how do we relate them to the characteristics of the flow? What insight do the resulting correlations give us about transfer processes in general?

In order to go about answering these questions, we define our system as a stream of fluid flowing in a rectangular duct with or without grooves along one or more of the duct walls (see Figure 1.1). In the scalar transport processes that we consider, the scalar is taken to be the concentration of a reactive solute dissolved in the fluid. This choice of system is convenient, but our conclusions are generalizable to other geometries and also applicable to heat transfer in some cases. In order to study the effects of the characteristics of a particular flow, we must consider the equation of motion for fluid flow, the Navier-Stokes equation:

$$\rho\left(\frac{\partial \mathbf{u}}{\partial t}+\mathbf{u}\cdot\nabla\mathbf{u}\right)=-\nabla p+\nabla\cdot\mathbf{T}+\mathbf{f}, \tag{1.1}$$

where ρ is the fluid density, $\mathbf{u}$ is the velocity field in the fluid, p is the pressure in the fluid, $\mathbf{T}$ is the stress tensor, and $\mathbf{f}$ represents any body forces felt by the fluid, such as gravity. The Navier-Stokes equation represents the force or momentum balance on an element of fluid. The velocity field is to be found given the other parameters in (1.1) and the continuity equation (the mass balance of fluid in the element):

$$\frac{\partial \rho}{\partial t}+\mathbf{u}\cdot\nabla\rho=0, \tag{1.2}$$

and then used as input for the mass transfer problem described below. Although in the general case the velocity field will depend on the local concentration of dissolved

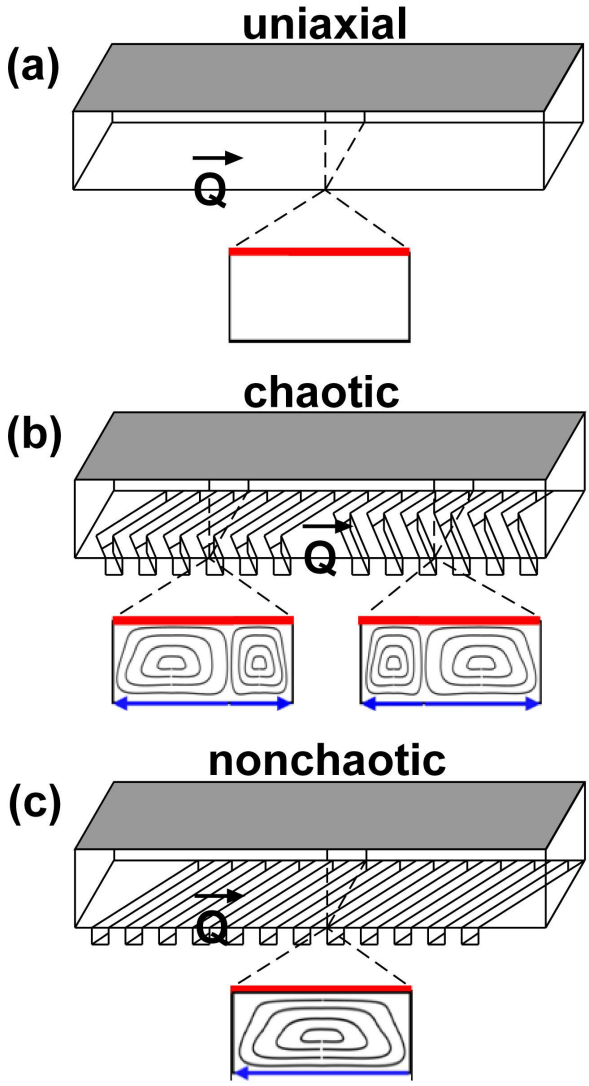

Figure 1.1. Flow geometries. (a) Uniaxial flow. (b) Chaotic three-dimensional flow generated by staggered herringbone grooves. (c) Non-chaotic three-dimensional flow generated by diagonal grooves.

solutes (or the local temperature in the case of heat transfer) we consider only dilute solutions where this dependence is negligible. The flows considered are steady, incompressible, viscous and Newtonian, and have negligible dependence on gravity or other body forces; the resulting simplification in the Navier-Stokes equation is:

$$\rho \mathbf{u} \cdot \nabla \mathbf{u} = -\nabla p + \mu \nabla^2 \mathbf{u}, \tag{1.3}$$

where μ is the dynamic viscosity of the fluid. Furthermore, we are interested in laminar flow in particular, and so we consider flows at very low Reynolds number, $Re = \rho UH / \mu = UH / \nu$, where U is the average fluid velocity, H is the characteristic length scale in the cross section, and $\nu = \mu / \rho$ is the kinematic viscosity of the fluid. At low *Re*, viscous effects outweigh inertial effects, and turbulent instabilities are entirely absent from the flow. In the limit $\mathrm{Re} = 0$, the nonlinear Navier-Stokes equation further simplifies to the linear Stokes equation for creeping flow:

$$\nabla p = \mu \nabla^2 \mathbf{u}. \tag{1.4}$$

Solutions of the Stokes equation depend on the appropriate boundary conditions at the surfaces bounding the flow:

$$\begin{aligned} &\text{stationary surface: } \mathbf{u} = 0 \\ &\quad \text{moving surface: } \mathbf{u} = \mathbf{u}_{\text{surface}}. \end{aligned} \tag{1.5}$$

These boundary conditions are responsible for the characteristics of the velocity field. In the case of a rectangular duct with no grooves and only stationary surfaces, the velocity is uniaxial and its magnitude depends on the position in the cross section. With the introduction of moving boundaries as in a lid-driven cavity (LDC) or the grooved geometries of the staggered herringbone mixer (SHM) (Stroock and McGraw

2004), secondary flows can develop in the cross section which give rise to stirring (see approximation to cross sectional flows below the actual geometries in Figure 1.1). The SHM flow and similar flows depend both on position in the cross section and position along the axial dimension and are difficult to represent analytically. Therefore these flows are often most accessible through experiments, while the study of uniaxial and LDC flows can provide intuition for a theoretical understanding of the salient characteristics of these complicated flows.

If the boundary conditions are modulated along the axial dimension of the flow (see Figure 1.1(b)), the fluid elements can experience chaotic trajectories, resulting in exponential stretching of fluid elements and efficient mixing if fluid elements sample large regions of the cross section (Aref 1984). The grooves create counterrotating vortices in the flow that periodically exchange fluid as the flow is modulated. Vortices produced by unmodulated grooves (see Figure 1.1(c)) will induce three-dimensional flows and stir the cross section, but will not create chaotic trajectories. The chaotic or non-chaotic character of these flows is difficult to infer from a solution to the Navier-Stokes or Stokes equation because the velocity field **u** is an Eulerian property of the flow, which is to say that it gives us the velocity at any point in the flow, but tells us nothing directly about the path that fluid elements actually take. The trajectories followed by individual fluid elements are a Lagrangian property of the flow and can be found by integration of the velocity field:

$$\frac{d\mathbf{x}}{dt} = \mathbf{u}(\mathbf{x}) \rightarrow \mathbf{x}(t) = \mathbf{x}_0 + \int_0^t \mathbf{u}(\mathbf{x})dt \tag{1.6}$$

where $\mathbf{x}$ is the position of the element along its trajectory and $\mathbf{x}_0$ is the initial position of the element. By integration of the velocity field for the LDC geometries that correspond to the flows in Figure 1.1, the positions of particles at periodic intervals

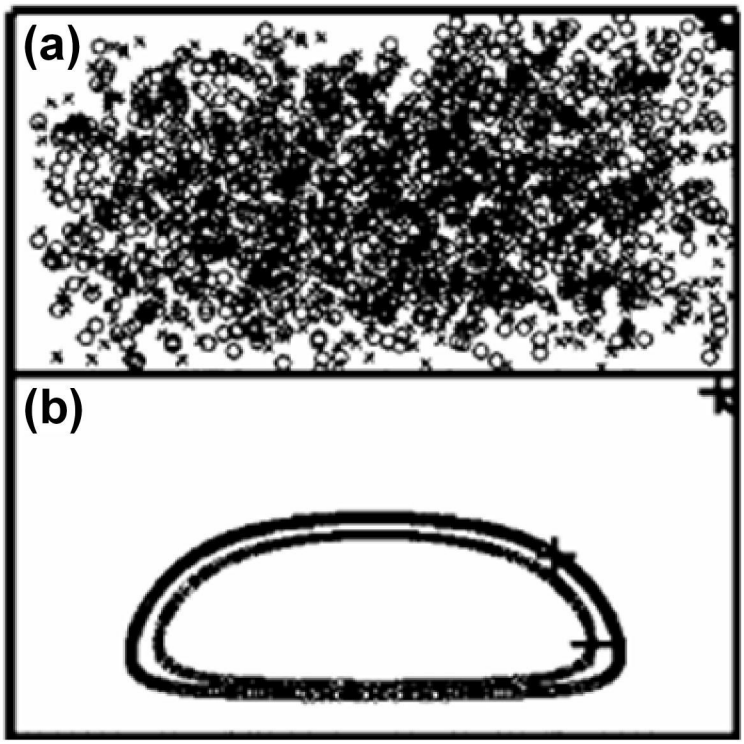

Figure 1.2. Poincaré sections. Frame (a) corresponds to the chaotic flow in Figure 1.1(b). Frame (b) corresponds to the non-chaotic flow in Figure 1.1(c).

can be mapped onto the cross-section of the channel, producing what is called a Poincaré section of the flow (see Figure 1.2). This tool used in nonlinear dynamics demonstrates that the LDC flow corresponding to Figure 1.1(b) causes most trajectories to sample almost the entire cross section, while the LDC flow corresponding to Figure 1.1(c) produces trajectories that each lie on a single streamline in the flow. We say that Figure 1.2(a) exhibits a large chaotic set that fills most of the cross section with small non-chaotic islands in the upper corners, while Figure 1.2(b) does not exhibit chaos at all. The large chaotic set associated with the modulated LDC or SHM flow (Figure 1.1(b)) is the reason that these flows mix fluid more efficiently than similar but unmodulated flows (Figure 1.1(c)). The Eulerian viewpoint can be thought of as a look at the whole system from the outside, while the Lagrangian viewpoint is like exploring the flow from the inside. They give complementary perspectives and are both important to a full picture of the flow.

With an understanding of the flow, we can begin to ask how it affects transfer processes taking place at interfaces within or adjacent to the flow. The phenomena of interest arise as consequences of the convection-diffusion equation:

$$\frac{\partial C}{\partial t} + \mathbf{u}\cdot\nabla C = D\nabla^2 C, \tag{1.7}$$

where C is the concentration of the solute in the flow and D is the diffusivity of that solute in the fluid. Assuming steady-state transfer, we have the time-independent convection-diffusion equation:

$$\mathbf{u}\cdot\nabla C = D\nabla^2 C. \tag{1.8}$$

Whereas the Navier-Stokes equation is a force balance on an element of fluid, the convection-diffusion equation is a statement of conservation of mass of solute in a

fluidic element, much like the incompressible continuity equation (1.2) is a statement of conservation of mass of fluid in a fluidic element. Just as the velocity field is dependent on the boundary conditions of velocity at the bounding surfaces of the flow, the concentration field (and therefore the flux of solute between regions within the system and into or out of the system) is dependent on the concentration boundary conditions at reactive or diffusive interfaces in the flow. We generally take the inlet stream to be at some uniform concentration C_0, and solute may leave the system through reactive interfaces but not through insulated interfaces (see Figure 1.3(a)):

$$\begin{aligned} \text{inlet condition: } & C = C_0 \\ \text{reactive interface: } & C = 0 \\ \text{insulated interface: } & \frac{\partial C}{\partial \mathbf{n}} = 0. \end{aligned} \tag{1.9}$$

The zero concentration condition at reactive interfaces is a consequence of our choice to only consider reactions with very fast kinetics, such that the surface concentration approaches zero. We consider transfer processes occurring at high Péclet number, $Pe = UH / D = Q / WD$, where D is the molecular diffusivity of the solute, Q is the volumetric flow rate, and W is the width of the channel. This regime corresponds to most processes operating at intermediate to high flow rate in aqueous solution in a microfluidic platform. Operating at high Pe implies that the characteristic time scale for diffusion is long compared to the time scale for convection, and therefore that inhomogeneities of concentration tend to persist for relatively long axial distances unless convection can be used to homogenize the fluid. The turbulent instabilities that generally serve to mix large scale flows are absent in our system, because Re is low; therefore the chaotic character of the flow, programmed into the system through the velocity boundary conditions but evident in the trajectories of solute particles, is crucial to the mixing of the fluid. We are interested in how characteristics of solutions

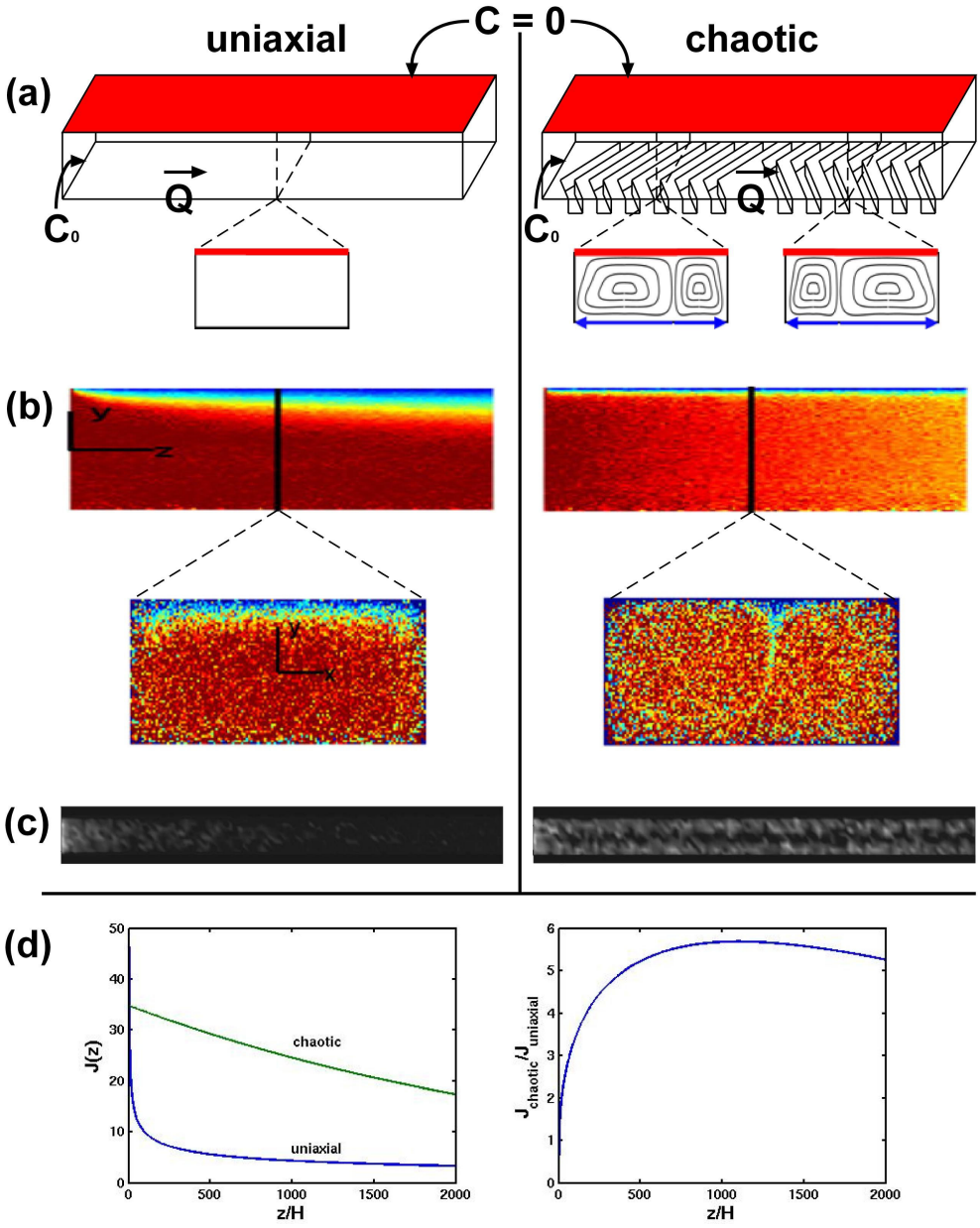

Figure 1.3. Effects of three-dimensional flow on interfacial mass transfer. (a) Geometry for uniaxial and chaotically stirred cases; red surface is reactive; approximate cross sectional flow shown below channels. (b) Side view of concentration profiles showing thickening of boundary layer; snapshot of cross sectional concentration profile shown below side view; red (blue) implies high (low) concentration. (c) Local flux along reactive surface; White (black) implies high (low) flux. (d) Average flux at reactive surface as function of axial distance for uniaxial and chaotically stirred flow on left; ratio of fluxes for the two cases on right. $Pe = 10^5$ in all cases.

to the Navier-Stokes equation – in particular, properties of the resulting flow such as shear rates and the presence or absence of secondary flows and chaotic sets – affect the characteristics of solutions to the convection-diffusion equation – in particular the magnitude and distribution of flux out of the system and the shape of the concentration profile in the cross section.

The concentration field resulting from solutions to the convection-diffusion equation can be thought of as the Eulerian aspect of the mass transfer process, while the individual trajectories of solute particles and, more importantly, the positions where they interact with a reactive interface are the Lagrangian aspect of the process. The effects of Lagrangian chaos will be evident in the profile of flux to reactive interfaces because the flux is composed of reaction events along the trajectories of solute particles. The convection-diffusion equation, though linear and relatively simple, is difficult to solve directly in systems such as the SHM due to the complexity of the system geometry, and LDC flows tend to exhibit sharp discontinuities and large gradients of velocity that also make direct solution difficult. We have therefore chosen to pursue answers to the questions above through experimental studies, which necessarily involve the simultaneous study of very large numbers of solute particle trajectories, and a simulation technique based on numerical integration of the velocity field in order to follow large numbers of solute particles in a simulated flow. We simulate diffusion as a 3D random walk $\boldsymbol{\beta}(\Delta t)$ chosen from a Gaussian distribution with mean zero and standard deviation $\sqrt{2Dt}$ in x, y, and z:

$$\Delta\mathbf{x}(t) = \Delta\mathbf{x}_{\mathrm{c}}(t) + \Delta\mathbf{x}_{\mathrm{d}}(t) = \int_{t}^{t+\Delta t} \mathbf{u}(\mathbf{x})dt + \boldsymbol{\beta}(\Delta t) \tag{1.10}$$

where $\Delta\mathbf{x}$ is the displacement of the particle for a given time step Δt, and $\Delta\mathbf{x}_{\mathrm{c}}$ and $\Delta\mathbf{x}_{\mathrm{d}}$ are the convective and diffusive components of the displacement, respectively

(McQuarrie 1976). Simulation data in the form of particle trajectories makes it possible to gather information about flux to reactive interfaces and cross-sectional profiles of the concentration field, allowing us to bridge the gap between the mass transfer process and the shape of the concentration profile. This simulation work provided the initial data that informed our theoretical understanding of the mechanisms by which chaotic mixing increases rates of interfacial mass transfer.

The classic solutions for transfer to stationary pipe walls in laminar pipe flow are instructive for choosing a framework for our analysis, because they highlight phenomena that appear, in somewhat different form, in our results for three-dimensional flows. Significant contributions in heat transfer at high *Pe* were made by Grætz and Lévêque, and due to the identical forms for the convection-diffusion equation for heat and mass transfer, their results are useful for the present case as well. Grætz (1885) considered transfer to the wall of a pipe in steady, fully developed, laminar, uniaxial flow, with a parabolic flow profile and zero velocity at the stationary pipe surface. The symmetry of the velocity field simplifies the convection-diffusion equation, and Grætz was able to write the solution for the concentration field analytically to reveal two regions in the development of the profile:

- an entrance region where the concentration boundary layer (the region across which the concentration changes from the bulk value to the surface value) is near the surface, and the bulk concentration remains at the inlet concentration; the flux is high near the inlet, but decreases quickly as the thickness of the concentration boundary layer grows;
- an asymptotic region where the concentration boundary layer has grown to the size of the pipe; the concentration boundary layer becomes self-similar in shape but continues to decay in magnitude; the flux continues to decrease although not as quickly as in the entrance region.

Lévêque (1928) considered transfer to a stationary wall in a simple shear flow. This case maps directly onto the entrance region of the Grætz case. The velocity profile near the wall of a pipe can be approximated as a shear flow with shear rate $\dot{\gamma} = 6U / H$ and axial velocity $u_z = \dot{\gamma} y$, where y is the distance from the wall. In the entrance region of the Grætz case, the concentration boundary layer is thin and confined to the region near the wall, and therefore all of the variation in concentration occurs in what is approximately a simple shear. The convection-diffusion equation in this case permits a similarity solution for the concentration. This analysis allows for the calculation of the flux of solute to the wall and also demonstrates the relationship between the axial distance from the inlet, z, and the thickness of the concentration boundary layer, $\delta(z) \sim (z / PeH)^{1/3}$. Lévêque's result simplifies the mathematics involved in developing an understanding of the growth of $\delta(z)$ and its scaling with Pe (*i.e.* flow rate). This result allows for an approximate understanding of the behavior in the asymptotic region, as the transfer process in this region occurs across a concentration boundary layer with a thickness of approximately the radius of the pipe.

The classic results of Grætz and Lévêque create a framework for thinking about transfer to interfaces in laminar flows, but what is it that we hope to add to the discussion? By studying interfacial transfer in several three-dimensional laminar flows, we ask and subsequently posit answers to the following questions:

- **Do important transfer quantities (such as local flux of solute to the surface, total integrated flux to the surface, and local and overall mass transfer coefficients) benefit from the introduction of transverse flows, over and above the uniaxial case?** At a given value of Pe, local and total integrated flux can be many times larger in a system with strong secondary flows (see Figure 1.3(c, d)), and mass transfer coefficients can be increased by several orders of magnitude at high Pe.

- **In the case of three-dimensional flows, is there an asymptotic state that is distinct from the uniaxial case, and what does this asymptotic state look like?** In certain three-dimensional flows, in particular those that exhibit chaotic fluid trajectories, there is an asymptotic state with a self-similar shape determined by the shape of the transverse flow and with a characteristic concentration boundary layer thickness that depends on the strength of the transverse flow near the reactive surface. The asymptotic state tends to have a periodicity that is identical to that of the velocity field, and a continued decay of concentration in the asymptotic region that is reminiscent of that in the Grætz case. We therefore call this result the *modified Grætz behavior*.
- **What is the role of chaos in maintaining this asymptotic state, *i.e.* in keeping the system from collapsing to the uniaxial result of a boundary layer filling the entire bulk of the channel?** Chaos is crucial in maintaining the shape and self-similarity of the asymptotic state. This behavior is accomplished through the removal of the depleted fluid from the reactive surface by the transverse flow, and the homogenization of that fluid before it returns to the surface again. Chaos ensures that if the axial length required to homogenize fluid is shorter than the axial length traveled by the fluid before it returns to the surface at a particular axial distance z and value of Pe, this modified Grætz behavior will continue to hold for arbitrarily large z and Pe.

Our approach for developing a platform to compare results from various flows and at various axial distances and values of Pe involves the casting of flux and concentration information in the form of a mass transfer coefficient. This analysis allows us to distill the microscopic information contained in the three-dimensional concentration distribution into a one-dimensional representation of the ability of the flow to bring available solute from the bulk to the surface to react. The local mass

transfer coefficient $k(z)$ is defined as the ratio of the reactive flux at the surface, $J(z)$, to the difference between the average concentration in the bulk, $C_b(z)$, and the concentration at the surface, $C_s(z)$:

$$k(z) = -\frac{J(z)}{C_b(z) - C_s(z)} \rightarrow \frac{D}{\delta(z)}, \tag{1.11}$$

where the ratio of solute diffusivity D to concentration boundary layer thickness $\delta(z)$ provides an order of magnitude estimate of $k(z)$ by dimensional analysis. We further nondimensionalize this mass transfer coefficient by defining the local Sherwood number $Sh(z)$:

$$Sh(z) = \frac{k(z)H}{D} \rightarrow \frac{H}{\delta(z)}, \tag{1.12}$$

where the ratio of the characteristic cross sectional length scale H to the thickness of the boundary layer gives an estimate of the Sherwood number. This analysis defines an emergent length scale relative to the channel dimension, $\delta(z)/H \sim 1/Sh(z)$, that captures the important features of the transfer process and will give us a useful means of comparing various flows and systems of different size scale and solute diffusivity.

From the Grætz and Lévêque results, we can predict forms for the Sherwood number in the entrance region and the asymptotic region of various flows. Lévêque tells us what to expect for the dependence of the boundary layer thickness on z and Pe in the entrance region, which gives a Sherwood number $Sh(z) \sim H / \delta(z) \sim (z / PeH)^{-1/3}$ for transfer to a stationary interface and $Sh(z) \sim (z / PeH)^{-1/2}$ for transfer to a moving interface by extension of the Lévêque result to a uniform velocity profile or plug flow. The relative strength of the axial and transverse flows determines how long the boundary layer will grow before it is swept off the surface and into the bulk. If the

boundary layer structure is indeed asymptotic, the asymptotic shape determines its average asymptotic thickness, and therefore the average asymptotic Sherwood number. We therefore find that the asymptotic Sherwood number for transfer to a stationary interface in the modified Grætz case scales with $\left(Pe\frac{u_{\text{trans}}}{U} \right)^{1/3}$, where u_{trans} is the magnitude of the transverse velocity. This result is particularly interesting because the asymptotic Sherwood number in the uniaxial case has no *Pe* dependence; as we increase *Pe*, the improvement over the uniaxial case also increases.

The ability to represent the solution of a complex convection-diffusion problem in the form of a power law correlation that applies across a variety of systems and over many decades in *Pe* is often lost on the student of fluid mechanics and mass transfer. Indeed, it was very much lost on me as an undergraduate engineer. The use of correlations often gives the idea that the underlying science is being masked or hidden, that it is just too complicated, and that it is not worth the time to understand. But having worked through the development of a correlation for the modified Grætz behavior through exploration of the mechanism by which the behavior arises, it is clear that the correlation is actually a testament to the deep science that is distilled into such a compact package. Correlations are not just the best that we can do in closed form or a convenient avenue to a numerical result, but rather they tell of the universality of the result, that it really does apply beyond the scope of the research at hand. And as a physicist, I find joy in the simplicity and generality of results like the correlations presented here because they imply that there is deep meaning lying behind the simple relationships.

The dependence of the Sherwood number on *z* and *Pe* highlights the interplay between two of the intrinsic length scales in our system: the convective length scale L_C and the diffusive length scale L_D (see Figure 1.4(a)). The convective length scale is effectively the axial distance at which we consider the concentration profile. The

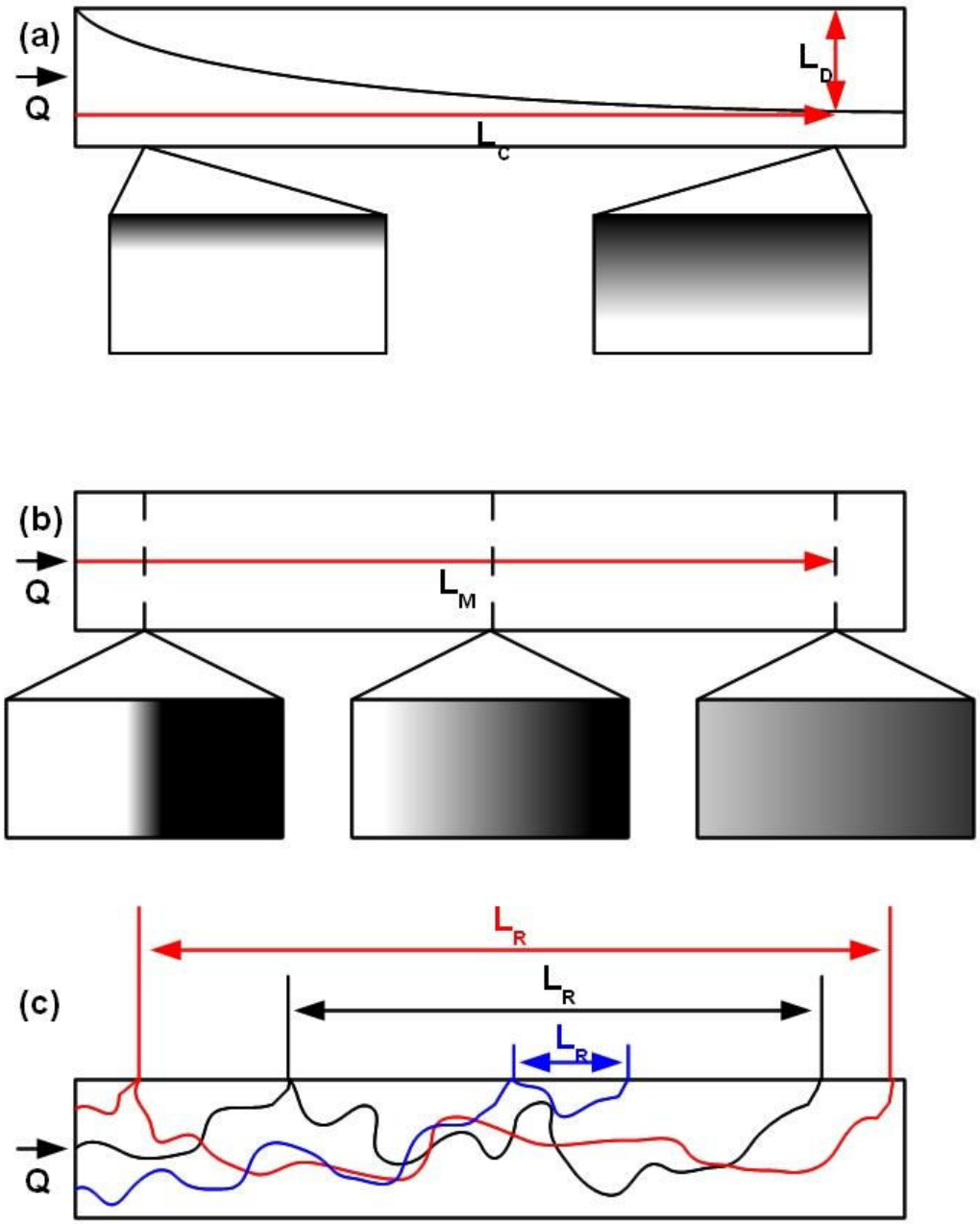

Figure 1.4. Relevant length scales inherent to the mass transfer process. (a) Length scale of axial convective flow (L_C) and length scale across which solute must diffuse to react at surface (L_D). (b) Mixing length (L_M): length scale for homogenization of initially inhomogeneous concentration profile. (c) Return length (L_R): length scale for return to reactive surface after leaving surface.

diffusive length scale is the distance across which solute must diffuse in order to arrive at the reactive surface, *i.e.* the thickness of the boundary layer. We have seen already that these lengths are related in the entrance region, where $\delta(z)$ grows with axial distance (as the cube root of the axial distance for a stationary reactive surface). Once an asymptotic state has been set up, the diffusive length no longer changes as the convective length is further increased.

There are also two other length scales intrinsic to the transfer process: the return length L_R and the mixing length L_M (see Figure 1.4(b,c)). The return length is the axial distance traveled by a fluid element after it has been swept off of the reactive surface (depleted of solute) but before it returns to the reactive surface (to participate in the interfacial transfer process again). This length depends strongly on the transfer process itself, and therefore on the asymptotic thickness of the boundary layer: for stationary reactive surfaces, the return length scales with $Pe^{2/3}$. The mixing length is the axial distance required for a fluid element at some concentration other than the bulk average (*i.e.* depleted of solute by the transfer process) to be homogenized with the bulk fluid, such that it has the average bulk concentration when it next comes near the reactive surface. This length depends strongly on the behavior of the bulk fluid, and in particular on the chaotic character of the flow: our standard chaotic transverse flow has a mixing length that scales with $Pe^{1/6}$ while a nonchaotic flow with similar shear rate has a mixing length that scales linearly with Pe.

In order for the asymptotic state to emerge and persist at a particular value of Pe in a given transverse flow, fluid that leaves the surface depleted by the transfer process must be mixed with the bulk fluid before it returns to the surface, *i.e.* the mixing length must be shorter than the return length at that value of Pe. And in order for the asymptotic state to be present at larger values of Pe, the return length must depend at least as strongly on Pe as does the mixing length. Thus the role of chaos in

the development of the asymptotic state and therefore in creating and maintaining higher rates of mass transfer lies in its ability to mix the fluid efficiently and to present fluid at the bulk average concentration to the reactive interface at all times.

The work leading to these conclusions has been conducted primarily on three fronts: numerical, theoretical and experimental. In order to run the initial simulations that led to the discovery of the modified Grætz behavior, a particle tracking code was implemented to integrate particle velocities and build trajectories through the length of a simulated microreactor (see Appendix). Collisions of these particles with the walls of the channel yielded flux data for a given channel surface and therefore allowed for the calculation of $Sh(z)$. The positions of the unreacted particles in the cross section also gave information about the local distribution of concentration, which allowed for independent investigation of the thickness of the boundary layer and the shape of the asymptotic state of the concentration profile. Theoretical work in generalizing the Grætz and Lévêque results to a three-dimensional flow yielded an independent prediction for the form of $Sh(z)$ in the entrance and asymptotic region of various simulated flows as well as arguments for what we would expect from an actual staggered herringbone geometry, with grooves composed of a large number of stationary surfaces. This prediction provides the link between the numerical work on lid-driven cavity flows and the experimental study of SHM structures. This experimental work was conducted in collaboration with the Abruña group in the Department of Chemistry, Cornell University, in order to increase efficiency and power output of a laminar flow fuel cell that had already been demonstrated by their group in a uniaxial geometry. Electrochemical methods enabled analytical work on a chaotically stirred potential cell, yielding experimental measurements of total integrated flux to the reactive surface that are compatible with our theoretical and numerical understanding. Our collaborators demonstrated an increase in power density

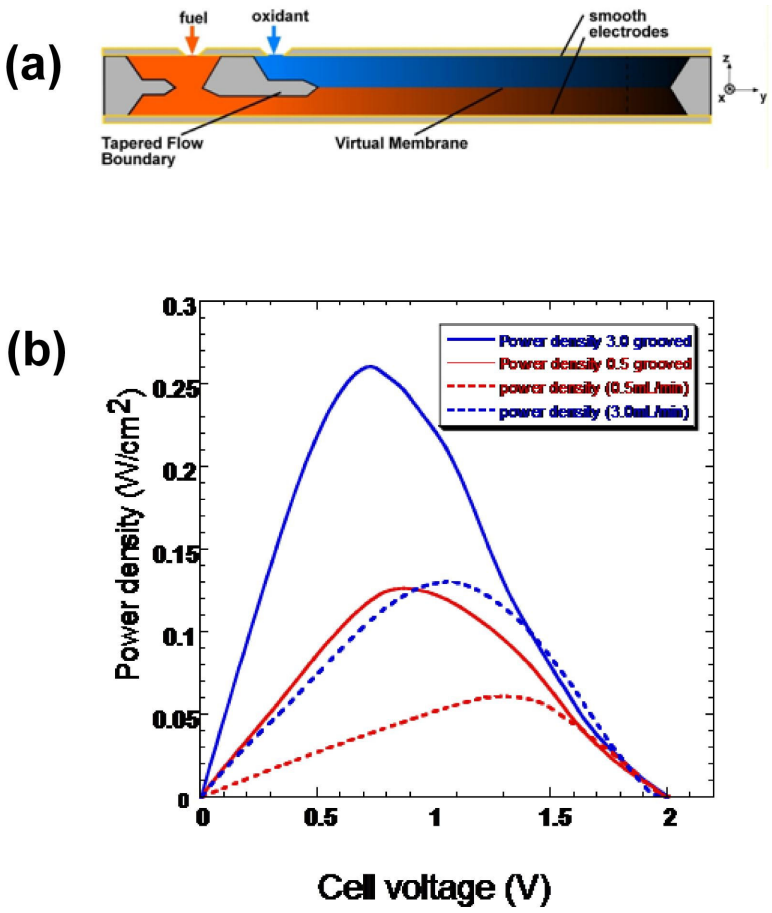

Figure 1.5. Effect of three-dimensional flow on laminar flow based fuel cell. (a) Fuel cell geometry. (b) Preliminary results of increased fuel cell performance due to incorporation of 3D chaotic flow. Flow rates: blue → 3.0 mL/min; red → 0.5 mL/min. Electrode surface geometry: dashed line → flat electrodes with uniaxial flow; solid line → grooved electrodes with chaotic three-dimensional flow.

by over a factor of two in the laminar flow based fuel cell due to introduction of a three-dimensional SHM flow (see Figure 1.5).

The structure of this dissertation is as follows: Chapter 1 is the introduction that you are currently reading, summarizing the story that is presented in greater detail in the remaining chapters; Chapter 2 covers the initial computational studies of transfer to stationary solid surfaces in uniaxial duct flow and three-dimensional laminar flows based on the lid-driven cavity model – this is where the modified Grætz behavior was first identified and discussed, and was published in Physics of Fluids in 2006; Chapter 3 involves the generalization of the methods and analysis in Chapter 2 to include transfer to moving solid interfaces and fluid-fluid diffusive interfaces – this includes further investigation of the origin and properties of the modified Grætz behavior and arguments as to the role of chaos in terms of the characteristic mixing and return length scales, and was published in the New Journal of Physics in 2009; Chapter 4 contains experimental studies of the modified Grætz behavior in uniaxial and three-dimensional laminar flows in microchannels through electrochemical measurements – this work includes the substantiation of the theoretical basis developed in the earlier studies by calculation of the length-averaged Sherwood number in several cases, and will be published in 2010.

REFERENCES

Aref H 1984 Stirring by chaotic advection *J. Fluid Mech.* **143** 1–21

Aref H and Jones S W 1989 Enhanced separation of diffusing particles by chaotic advection *Phys. Fluids* A **1** 470–4

Brody J P and Yager P 1997 Diffusion-based extraction in a microfabricated device *Sensors Actuators* A **58** 13–8

Chang H C and Sen M 1994 Application of chaotic advection to heat transfer *Chaos Solitons Fractals* **4** 955–75

Cohen J L, Westly D A, Pechenik A and Abruna H D 2005 Fabrication and preliminary testing of a planar membraneless microchannel fuel cell *J. Power Sources* **139** 96–105

Ferrigno R, Stroock A D, Clark T D, Mayer M and Whitesides G M 2002 Membraneless vanadium redox fuel cell using laminar flow *J. Am. Chem. Soc.* **124** 12930–1

Foley J O, Mashadi-Hossein A, Fu E, Finlayson B A and Yager P 2008 Experimental and model investigation of the time-dependent 2-dimensional distribution of binding in a herringbone microchannel *Lab Chip* **8** 557–64

Ganesan V, Bryden M D and Brenner H 1997 Chaotic heat transfer enhancement in rotating eccentric annular-flow systems *Phys. Fluids* **5** 1296–306

Golden J P, Floyd-Smith T M, Mott D R and Ligler F S 2007 Target delivery in a microfluidic immunosensor *Biosens. Bioelectron.* **22** 2763–7

Grætz L 1885 *Ann. Phys. Chem.* **25** 337–57 Q1

Ismagilov R F, Stroock A D, Kenis P J A, Whitesides G and Stone H A 2000 Experimental and theoretical scaling laws for transverse diffusive broadening in two-phase laminar flows in microchannels *Appl. Phys. Lett.* **76** 2376–8

Kamholz A E, Weigl B H, Finlayson B A and Yager P 1999 Quantitative analysis of molecular interaction in a microfluidic channel: the T-sensor *Anal. Chem.* **71** 5340–7

Lévêque A M 1928 Les lois de la transmission de chaleur par convection *Annal. Mines* **13** 283–99

McQuarrie D A 1976 *Statistical Mechanics* (New York: Harper)

Shrivastava A, Kumar S and Cussler E L 2008 Predicting the effect of membrane spacers on mass transfer *J. Memb. Sci.* **323** 247–56

Squires T M, Messinger R J and Manalis S R 2008 Making it stick: convection, reaction and diffusion in surfacebased biosensors *Nat. Biotechnol.* **26** 417–26

Stroock A D and McGraw G J 2004 Investigation of the staggered herringbone mixer with a simple analytical model *Philos. Trans. R. Soc.* A **362** 971–86

Teles F R R and Fonseca L P 2008 Trends in DNA biosensors *Talanta* **77** 606–23

Vijayendran R A, Motsegood K M, Beebe D J and Leckband D E 2003 Evaluation of a three-dimensional micromixer in a surface-based biosensor *Langmuir* **19** 1824–8

CHAPTER 2

MASS TRANSFER TO REACTIVE BOUNDARIES FROM STEADY THREE-DIMENSIONAL FLOWS IN MICROCHANNELS[1]

I. Introduction

Mass transfer to reactive boundaries is of great technological relevance in fields ranging from industrial chemical engineering to analytical biochemistry. Surface catalyzed reactions (Khinast *et al* 2003) electrochemical reactions as in fuel cells (Ferrigno *et al* 2002, Choban *et al* 2004, Cohen *et al* 2005) and surface interactions as in biological sensors (Yarmush *et al* 1996, Myszka *et al* 1997, Sikavitsas *et al* 2002) all rely on the delivery of solute to solid boundaries. The more efficient this delivery is, the higher the yield (*e.g.*, in surface catalyzed reactions), fuel efficiency and current density (*e.g.*, in fuel cells), or speed of analysis (*e.g.*, in sensors) will be. Significant efforts are being made to translate these processes to microfluidic platforms in order to allow for portability, to decrease sample volumes, and to increase rates of operation. In standard microchannels, rectangular ducts with constant cross-sectional dimensions of $10–10^3$ μm and an axial dimension of $10^{-1}–10^2$ cm, achieving efficient mass transfer can pose a particular challenge. In a rectangular microchannel, pressure-driven flows are uniaxial with low Reynolds number, $Re = UH/\nu < 100$, and high Péclet number, $Pe = UH/D > 100$, where U (m/s) is the average axial velocity, H (m) is the characteristic dimension of the channel, ν (m^2/s) is the kinematic viscosity of the fluid, and D (m^2/s) is the diffusivity of the solute in the fluid; mass transfer toward reactive boundaries is purely diffusive and slow relative to convection. In this low *Re*, high *Pe* regime, there is an inevitable compromise between high flux (*e.g.*, with fast flows) and efficient use of reagents (*e.g.*, with slow flows that allow reagents to

[1] *Physics of Fluids* **18** (2006) 073602, © 2006 *American Institutes of Physics*

diffuse to the surface). Many researchers have shown that three-dimensional (3D) flows created with laminar mixers can moderate this compromise by increasing rates of transfer relative to uniaxial laminar flow. (Chang and Sen 1994, Jana and Ottino 1992) Nonetheless, we are unaware of a predictive model of this effect that is appropriate for the design of microreactors or laminar reactors more generally.

In this article, we present numerical and theoretical studies that elucidate the effect of steady, three-dimensional flows on rates of mass transfer to boundaries in microchannels. We develop and validate predictive correlations for rates of transfer, address the outstanding question of the mechanism by which Lagrangian chaos influences transfer to boundaries, and translate our findings into specific design rules for microfluidic reactors. We employ an approximate model of the 3D flows that can be achieved with the incorporation of obliquely oriented grooves in one wall of a microchannel, as in the Staggered Herringbone Mixer (SHM). (Stroock *et al* 2002a) Figure 2.1 presents a schematic diagram of the SHM and the geometry used here to approximate the flow in the SHM. Figure 2.1(a) shows one cycle of a typical SHM device. These structures can be fabricated by standard lithographic techniques. Our model flow mimics the effect of the grooves by replacing the grooved surface with a flat boundary with transverse slip velocities, as indicated in Figure 2.1(b). (Stroock *et al* 2002b, Stroock and McGraw 2004) The streamlines of the transverse flow field generated by these slip velocities are presented in Figure 2.1(c).

We simulate convection-diffusion-reaction in this model flow to calculate the rate of mass transfer to a single reactive boundary on the wall opposite the grooved surface that induces the transverse flow. We focus on transfer to this unstructured boundary for several reasons: it is representative of a generic no-slip boundary in a three-dimensional duct flow; our model, while accurate in the bulk and near the far wall, does not capture the true geometrical detail near the patterned surface; and this

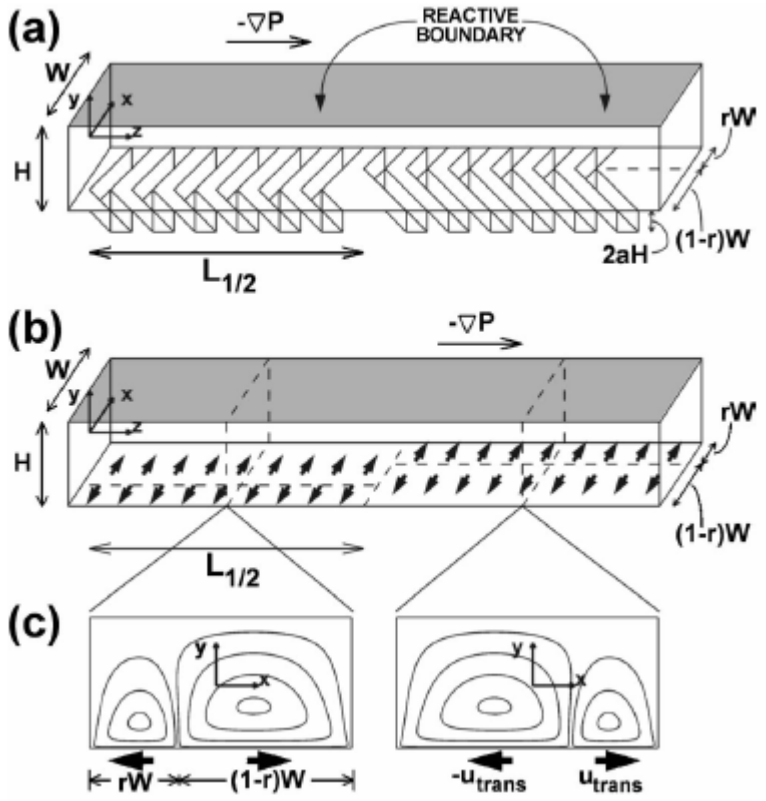

Figure 2.1. Schematic diagram of the staggered herringbone mixer (SHM) and of the lid-driven cavity model of the flow in such a structure. (a) One cycle of the SHM. Grooves along the floor induce transverse secondary flows when a steady pressure gradient is applied along the channel. (b) Lid-driven cavity approximation of the SHM. Transversely (along x) slipping regions on a smooth boundary generate transverse flows that mimic those induced by grooves. (c) Streamlines of cross-sectional flow produced by lid-driven cavity approximation of the SHM. The degree of asymmetry r and the half-cycle length $L_{1/2}$ can be tailored to produce regular or chaotic flow (Stroock and McGraw 2004).

reactor geometry involving a flat reactive wall opposite a topographically patterned wall is experimentally convenient because a microchannel with mixing grooves can simply be sealed against a flat reactive surface. Our model assumes a Stokes flow ($\mathrm{Re} = 0$); we take this limit to simulate flows with low to moderate *Re* ($Re < 10$). We consider Péclet numbers in the range, $10^2 \le Pe \le 10^5$. Our model assumes instantaneous kinetics at the reactive boundary. For systems with finite chemical rate constants at the boundaries, the conclusions presented here are still instructive; in those cases, mass transfer resistances predicted here would need to be added in series with those due to the finite surface rate constant to find the overall resistance to transfer. (Bird *et al* 2002)

Transfer to solid boundaries from 3D laminar flows has been studied in a variety of systems. (Khinast *et al* 2003, Nishimura and Kunitsugu 1997, Ganesan *et al* 1997, Ghosh *et al* 1992, Saatdjian *et al* 1996, Leprevost *et al* 1997, Saatdjian and Leprevost 1998, Janssen and Hoogendoorn 1978, Mokrani *et al* 1997, Acharya *et al* 2001, Lemenand and Peerhossaini 2002) Heat transfer has been studied in more detail than mass transfer in these systems; this work tends to consider a low *Pe* regime due to the high diffusivity of heat, but it is otherwise analogous to questions of mass transfer. Chang and Sen have identified two distinct classes of transfer (1994): transfer of solute from one boundary to another across the flow (Nishimura and Kunitsugu 1997, Ghosh *et al* 1992, Saatdjian *et al* 1996, Leprevost *et al* 1997, Saatdjian and Leprevost 1998) and transfer of solute between the bulk and the wall (*i.e.*, to fill or empty the solute from the bulk); (Khinast *et al* 2003, Ganesan *et al* 1997, Janssen and Hoogendoorn 1978, Mokrani *et al* 1997, Acharya *et al* 2001, Lemenand and Peerhossaini 2002) our study falls into the category of bulk-to-wall transfer. Studies have also considered transfer to slip (Nishimura and Kunitsugu 1997, Ganesan *et al* 1997, Ghosh *et al* 1992, Saatdjian *et al* 1996, Leprevost *et al* 1997, Saatdjian and

Leprevost 1998) and no-slip (Khinast *et al* 2003, Janssen and Hoogendoorn 1978, Mokrani *et al* 1997, Acharya *et al* 2001, Lemenand and Peerhossaini 2002) boundaries; our choice of reactor geometry simulates a no-slip reactive boundary. Analysis of rates of transfer have been performed in the entrance region (small axial distance) and in the asymptotic region (large axial distance), and results have been quoted for various quantities such as the flux, transfer coefficient, efficiency, or effective diffusivity. We present correlations for the Sherwood number, Sh, a nondimensionalized mass transfer coefficient (see Section III for definition). We analyze both the entrance and asymptotic regions. The most useful studies for comparison to our results are those involving heat transfer in coiled tubes (Janssen and Hoogendoorn 1978, Mokrani *et al* 1997, Acharya *et al* 2001) and mass transfer in static mixers. (Khinast *et al* 2003) Janssen *et al*, and Acharya *et al*, found results similar to our own for scaling at small axial distance, but different scaling at large distances. (Janssen and Hoogendoorn 1978, Acharya *et al* 2001) Mokrani *et al*, cite an increase in the rates of transfer due to chaotic flow relative to nonchaotic flow, but do not investigate the origin of this effect. (Mokrani *et al* 1997) These studies will be further discussed with respect to our own results in Section IV.B. A clear understanding of the mechanism of mass transfer in 3D laminar flows has yet to be presented; we probe that mechanism in the work presented here.

The remainder of this paper is organized as follows: in Section II, we outline the geometry of our system and describe the model of the flow and the simulation of convection-diffusion-reaction within this flow. In Section III, we supply theoretical background on mass transfer and outline the Lévêque solution as it relates to our analysis, identifying correlations for quantities relevant to mass transfer. In Section IV.A, we present results from our simulations for mass transfer in various flows. In Section IV.B, we interpret the results in terms of the Lévêque analysis and the

correlations presented in Section III, and discuss our results for the rates of mass transfer due to transverse flows in relation to results in the literature. At the end of Section IV.B, we summarize the features of flows that are important for increasing transfer to boundaries and explain how such flows can affect the design of efficient microreactors.

II. Model and Simulation Details

We performed simulations of convection-diffusion-reaction by tracking the advection of passive tracers in a flow field down the length of a microchannel. This flow field is the solution of the equations of motion for a physical situation that approximates the flow in the actual staggered herringbone structure (see Figure 2.1). Domain perturbation analysis suggests that a simple transverse slip velocity along a smooth wall can be used to replace the mean effect of the obliquely oriented grooves. (Stroock *et al* 2002b) Taking this suggestion literally, our model flow corresponds to that of a three-dimensional lid-driven cavity with axial pressure-driven flow. A complete description of this model is given elsewhere. (Stroock and McGraw 2004) Figure 2.1(a) shows the physical structure of an experimental device. Figure 2.1(b) shows the lid-driven cavity approximation of the actual structure. Figure 2.1(c) shows the streamlines of the cross-sectional flow produced in the lid-driven cavity approximation. The parameters that control the character of the model flow are the degree of asymmetry of the pattern of slip on the bottom boundary, r, the length of a half cycle, $L_{1/2}$, the aspect ratio of the channel cross section, $\omega = W / H$, and the magnitude of the slip velocity, u_{trans}. The slip velocity can be related to the structure of the grooves in the actual SHM, as described elsewhere. (Stroock *et al* 2002b) We take the axial velocity to be the Poiseuille flow in a duct:

$$u_z(x,y) = 1 - y^2 + 4\sum_{n=1}^{\infty} \frac{(-1)^n}{\gamma_n^3 \cosh(\gamma_n \omega)} \cosh(\gamma_n x)\cos(\gamma_n y) \qquad (2.1)$$

where $\gamma_n = (2n-1)/2$. While physical grooves would perturb the axial flow in addition to creating a transverse flow, we neglect this higher order perturbation and preserve the simple Poiseuille flow.

The effective transverse slip along the floor causes the flow to recirculate in the cross section, producing two counter rotating eddies or vortices for herringbone-shaped grooves, as in Figure 2.1(c). The relative size of the eddies is determined by the degree of asymmetry, *r*. At the end of each half cycle, the flow is inverted in the cross-stream direction (along *x*), such that the larger and smaller eddies switch sides. This periodic switching leads to an interesting aspect of the flow; as can be seen in Figure 2.1(c) the streamlines of the flow in the cross section in one half-cycle cross those of the other half-cycle; this change in the structure of the flow causes the trajectories of particles that were following similar paths to diverge from one another. In the continuum sense, a region of the cross section that had been a part of one vortex is suddenly part of the other vortex. The presence of these eddies and the crossing of the streamlines as the flow alternates provide the stretching and folding, respectively, which are required for Lagrangian chaos. (Ottino 1989) For symmetrical flows (*e.g.*, $r = 1$ or $r = 1/2$), the form of the transverse flow does not vary with the axial position, and the flows are 3D, but nonchaotic.

We used the solution for the two-dimensional flow in a lid-driven cavity as presented in detail in Appendix A of Stroock and McGraw 2004. Briefly, in the Stokes regime, the momentum balance can be expressed as the biharmonic equation for the stream function in the cross section. We used a double Fourier series in *x* and *y* to approximate the solution to this equation and satisfy the slip and no-slip boundary conditions. In our simulation, we took this solution for the transverse flow and we

used (1) for the axial flow. We used 10 Fourier terms in the calculation of the axial flow and 20 Fourier terms total (10 in the *x* direction and 10 in the *y* direction) in the calculation of the transverse flow. We chose to evaluate and tabulate the velocity field at a large number of grid points in the cross section. We then interpolated from this table at a given (*x*, *y*) to find the velocity during the particle tracking. We used a lookup table of 1024×512 grid points and a third order interpolation scheme in each direction for each of the velocity components. (Press *et al* 2002)

In cases that involved varying the transverse flow along *z*, we switched the velocity instantaneously at the end of each half-cycle. This approximate treatment of the transition with a discontinuity is reasonable for flows at low *Re* for which the transition region will be short. We have shown previously that this model produces results that are consistent with experiment in studies of mixing in the bulk. (Stroock and McGraw 2004)

We seeded particles into the flow at $z = 0$ with the probability of a given initial position (*x*, *y*) at $z = 0$ taken to be proportional to the axial velocity at that point. This seeding strategy approximates the flux of the solute through the plane at $z = 0$ for a solution of uniform initial concentration. We imposed these initial conditions by the rejection method. (Press *et al* 2002) We updated the position of the particle by integration of the velocity field using a fifth order Runge-Kutta method. This method is more accurate than the standard fourth order Runge-Kutta method, and it also furnishes an estimate of the numerical error associated with the operation. Using this estimate of the error, an adaptive step size algorithm allowed the particle to take large steps through regions where the gradients of velocity were small, and required smaller steps through regions where the gradients were large. (Press *et al* 2002) This integration method improved both the efficiency through the simpler regions of the

flow and the accuracy through the more complicated regions of the flow relative to nonadaptive methods.

A diffusive step was implemented during each convective time step. We took this diffusive step as a separable random walk in x, y, and z with the step size chosen as a Gaussian random number with a mean of zero and a standard deviation of the form $\Delta x = \sqrt{2D\Delta t}$, where D is the diffusivity of the particle and Δt is the time step used in the corresponding convective step. This results in a three-dimensional, isotropic, diffusive displacement, which is appropriate for modeling diffusion over finite time steps. (McQuarrie 1976) The time step was constrained such that at $Pe = 10^2$, 85% of the diffusive steps were less than 1% of the channel height, and 99.5% were less than 2% of the channel height. At higher values of Pe, similar time steps produce smaller diffusive displacements, and therefore the above values are an upper bound on the distributions of diffusive displacements for all of the cases studied here. If at any time the particle left the channel, it reflected specularly across the wall that it crossed back into the flow. We noted the x, z position of the first crossing of a reactive wall for each particle and considered this to be the position at which it reacted. This strategy allowed for calculation of reactive flux. We also noted the position (x, y) in the cross section as each particle crossed regularly spaced axial positions; we used this information to calculate concentration profiles as a function of axial distance. We evaluated the axial convective flux by binning the particles in evenly spaced bins in the cross section at each axial position of interest. We then determined the concentration in each bin by dividing by the average axial velocity in that bin. The total number of particles was approximately 200 000 in simulations of uniaxial flow and the chaotic flow shown in Figures 2.1(b) and 2.1(c) ($r = 1/3$, $L_{1/2} = 10H$), and approximately 50000 in all other simulations; the smaller number of

particles proved sufficient to ensure convergence of the calculated profile of concentration and flux.

We tested the overall accuracy of the interpolation and integration schemes by tracking particles in a single vortex flow (r=1) with a periodic switch in the overall sign of the slip velocity at the floor. In this flow, the cross-sectional position of a particle at the end of each full cycle should be invariant. The drift introduced by velocity interpolation and finite step size integration was roughly linear in time and very small. Over the maximum axial length considered (2000 H), this drift was four orders of magnitude smaller than the displacement that would arise due to physical diffusion at Pe=10^6. For smaller Pe, the effect of physical diffusion is greater, such that the relative importance of the drift is smaller. We concluded that the accuracy of the interpolation and integration method was sufficient for all Pe considered in this work.

As a measure of the Lagrangian character of the flows considered, we created Poincaré sections for several initial conditions by recording the position in the cross section at the end of each cycle (z=0, 2 $L_{1/2}$, 4 $L_{1/2}$, . . ., where $L_{1/2}$ is the half-cycle length as in Figure 2.1), with a diffusivity of zero (Pe=∞). Figure 2.2 presents these Poincaré sections and shows the distinctions between the various flows considered. Figure 2.2(a) demonstrates the chaotic advection associated with a staggered herringbone design (r=1/3; $L_{1/2}$=10H) that we know gives good mixing in the bulk of the flow. (Stroock *et al* 2002a, Stroock and McGraw 2004) Two of the initial conditions belonged to a chaotic invariant set that spans much of the cross section. The third initial condition remained confined to a nonchaotic island in the upper right corner. Figures 2.2(b) and 2.2(c) show the periodic orbits associated with nonchaotic flows that do not change in the axial direction due to their symmetry under reflection across the y axis (r=1/2 and r=1). Figure 2.2(d) presents the Poincaré map of a flow

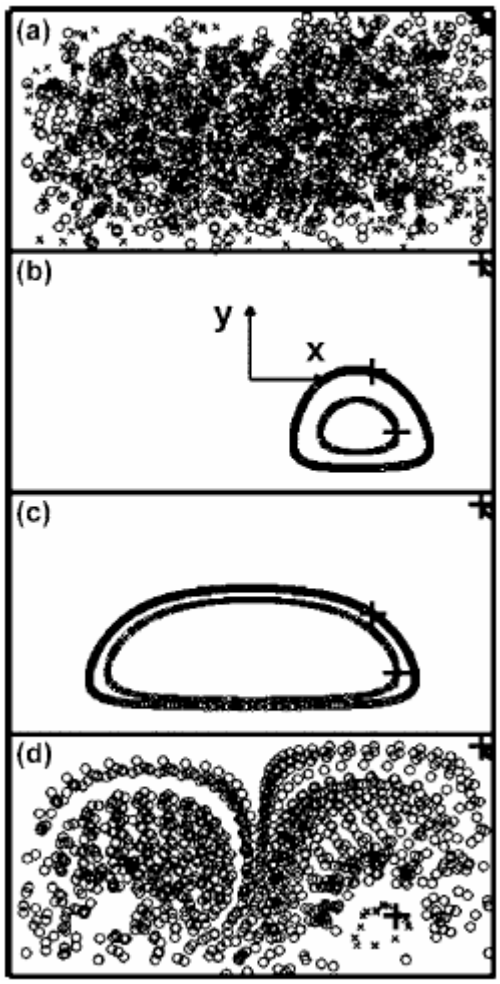

Figure 2.2. Poincaré sections for several flow geometries: (a) r= 1/3 , $L_{1/2}$=10H; (b) r= 1/2 ; (c) r=1; (d) r= 1/3 , $L_{1/2}$=2.5H. For all cases, the ratio of transverse velocity to axial velocity u_{trans} /U=0.2. Three initial conditions (x, y) =(1,0) (circles), (1.2,−0.5) (crosses), and (1.9, 0.9) (points, trapped in upper right corner) are tracked through a length equivalent to 20000 channel heights, where (x, y)=(0,0) is the center of the cross section. Large crosses mark the three initial positions, most easily seen in frames (b) and (c).

with the same asymmetry as in Figure 2.2(a) (r=1/3) but with a cycle length that was one quarter of the cycle length in Figure 2.2(a), $L_{1/2}$=2.5H.[2] This situation led to a less chaotic flow: while the invariant set for the first initial condition spanned a large fraction of the cross section, the second initial condition was quasiperiodic near the core of the right vortex. The third initial condition was still confined in the island in the upper right corner. We note that these Poincaré maps indicate dramatic differences in the Lagrangian character of these flows *in the bulk*. We will see in Section IV that the differences in rates of mass transfer to boundaries in these different flows are more subtle than the effects in the bulk.

III. Theory

III.A. Mass transfer background

We represent the rate of mass transfer to boundaries with the local Sherwood number, $Sh(z)$, a dimensionless measure of the local mass transfer coefficient averaged over the width of the channel (along x). In various contexts, Sh is an indicator of efficiency of reagent use, current density, or sensor response time.[3] The local Sherwood number is defined as

$$Sh(z)=\frac{k(z)H}{D} \tag{2.2}$$

[2] In the case of $L_{1/2}$=2.5H, our approximate representation of the transition from one form of transverse flow to another as instantaneous (see Figure 2.1(b)) may result in an overestimate of the transverse displacement per half-cycle. Nonetheless, this case is representative of physically realizable flows with small transverse displacements and distinct structure in their Poincaré maps (see Figure 2.2(d)).

[3] Efficiency $\varepsilon(z)$, current density, and sensor response time are related to Sh(z) as follows: $\varepsilon(z)$=amount reacted/amount introduced=1−exp(−∫Sh(z')dz'/PeH) where the limits of the integral are from z'=0 to z'=z; current density is proportional to total current, which is proportional to Pe $\varepsilon(z)$; sensor response time is inversely proportional to total current. Therefore by maximizing Sh(z), one can increase efficiency and current density and decrease sensor response time.

where $k(z)$ (m/s) is the local mass transfer coefficient averaged over the width of the channel (along x), H (m) is the height of the channel, and D (m^2/s) is the diffusivity of the reactive species. The average local coefficient of mass transfer is further defined as

$$k(z) = -\frac{J(z)}{C_b(z) - C_s(z)} \tag{2.3}$$

where $J(z)$ (mol/m^2s) is the local reactive flux averaged across the width of the reactive boundary (along x), $C_b(z)$ (mol/m^3) is the average bulk concentration, and $C_s(z)$ (mol/m^3) is the average concentration at the surface. For a system with fast kinetics, the concentration at the reactive surface, $C_s(z) \rightarrow 0$. We take the average bulk concentration as the cup-mixing concentration $C_{cup}(z)$ (mol/m^3): (Bird *et al* 2002)

$$\begin{aligned} C_{cup}(z) &= \frac{\int\int C(x,y,z)u_z(x,y)dxdy}{\int\int u_z(x,y)dxdy} \\ &= \frac{\int\int C(x,y,z)u_z(x,y)dxdy}{UA} \end{aligned} \tag{2.4}$$

where $u_z(x, y)$ (m/s) is the axial velocity as a function of position (x, y) in the cross section, U (m/s) is the average axial velocity, A (m^2) is the cross-sectional area, and the integrals are taken over the cross section of the channel. It can be shown by conservation of mass that the reactive flux $J(z)$ is

$$J(z) = UH\frac{dC_{cup}}{dz} \tag{2.5}$$

Combining (2.2), (2.3), and (2.5) gives the following form for *Sh*:

$$Sh(z) = -\frac{PeH}{C_{\text{cup}}(z)}\frac{dC_{\text{cup}}}{dz} = -\frac{d\ln C_{\text{cup}}}{d\dfrac{z}{PeH}} \tag{2.6}$$

The Sherwood number can therefore be viewed as a relative rate of change in C_{cup} with respect to the nondimensional axial distance traveled along the reactive boundary. This dimensionless distance is the inverse of the Grætz number, $Gz=PeH/z$.

As we will see in Section IV even in the presence of complex transverse flows, the mass transfer phenomenon we consider here shares important characteristics with the classic Grætz problem for heat transfer to the boundary of a uniaxial pipe flow (Bird *et al* 2002). We recall here the key aspects of that result: a concentration boundary layer appears at the leading edge of the reactive surface and grows in the direction normal to the reactive surface (along y, Figure 2.1) with increasing axial distance from the leading edge. This growth is due to the depletion of solute from the region adjacent to the reactive surface, and continues until this concentration boundary layer fills the height of the channel. Beyond this point, the concentration distribution decays in a self-similar manner. This transition to self-similarity defines the end of the entrance region, and, from this point on, $Sh(z)$ becomes constant; we refer to this region of constant Sh as the asymptotic or plateau region. In uniaxial flows, the plateau value, Sh_{plat}, is geometry-dependent and Pe-independent and has been calculated for flow in a round pipe ($Sh_{\text{plat}}=3.657$) and between two reactive plates ($Sh_{\text{plat}}=7.541$); (Bird *et al* 2002) geometries with less symmetry (*e.g.*, a single reactive wall in a rectangular duct) are more difficult to analyze analytically. It will suffice to say that the end of the entrance region, $z=z_{\text{plat}}$, occurs when the boundary layer is roughly the size of the channel, and Sh is of order 1. In these cases, the length of the entrance region scales as, $z_{\text{plat}}\sim PeH$, or, in other words, it corresponds to a constant value of the Grætz number, $Gz_{\text{plat}}=Pe\ H/z_{\text{plat}}$.

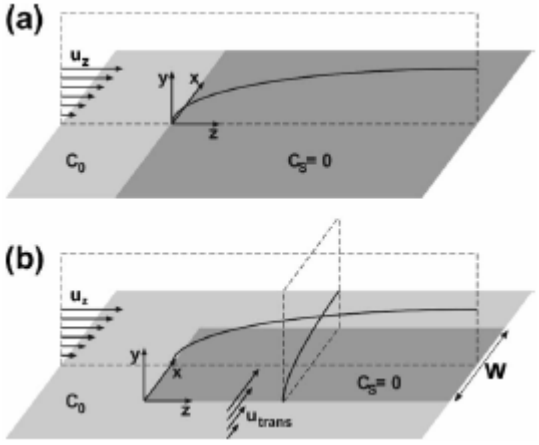

Figure 2.3. Developing boundary layers over a reactive plate. (a) Development of a boundary layer in a uniaxial flow. (b) implified model of the simultaneous growth of axial and transverse concentration boundary layers over an isolated reactive boundary. The transverse boundary layer can truncate the growth of the axial boundary layer.

III.B. Mass transfer from a simple shear flow

To build a basis with which to model mass transfer in three-dimensional flows, we consider the transfer of mass to the surface of an infinite plate in a fully developed shear flow as shown in Figure 2.3(a); this is the classic Lévêque problem. The plate is analogous to the reactive wall of a duct in the vicinity of the wall where the Poiseuille flow can be approximated by a simple shear flow and the shear rate at the wall is related to the average bulk velocity and the height of the duct. The plate lies in the plane y=0 and is reactive for $z > 0$. Assuming that the flow is a simple shear flow and that streamwise diffusion is negligible compared to convection ($Pe \gg 1$), the steady-state convective diffusion equation to be solved is

$$\mathbf{u}\cdot\nabla C = D\nabla^2 C \rightarrow u_z(y)\frac{\partial C}{\partial z} = D\frac{\partial^2 C}{\partial y^2},$$
$$u_z(y) = \dot{\gamma} y \qquad (2.7)$$

with boundary conditions

$$
\begin{aligned}
&C(y, z \le 0) = C_0, \\
&C(y = 0, z > 0) = 0, \\
&C(y \to \infty, z) = C_0
\end{aligned}
\tag{2.8}
$$

where $\mathbf{u} = u_z(y)\hat{z}$ (m/s) is the velocity field, $\dot{\gamma} = \partial u_z / \partial y\big|_{y=0}$ (s^{-1}) is the shear rate at the plate surface, and C_0 (mol/m^3) is the concentration far from the surface or, equivalently, the inlet concentration. The zero concentration boundary condition at the wall accounts for the reaction process for very fast reaction kinetics. A similarity solution gives the concentration profile:

$$
\begin{aligned}
C(\eta) &= \frac{C_0}{\Gamma\left(\frac{4}{3}\right)} \int_0^{\eta} e^{-\lambda^3} d\lambda, \\
\eta &= \left(\frac{\dot{\gamma}}{9Dz}\right)^{1/3} y
\end{aligned}
\tag{2.9}
$$

From this solution, the diffusive flux to the surface can be calculated:

$$
J(z) = -D \left.\frac{\partial C}{\partial y}\right|_{y=0} = \frac{DC_0}{\Gamma\left(\frac{4}{3}\right)} \left(\frac{\dot{\gamma}}{9D}\right)^{1/3} z^{-1/3}
\tag{2.10}
$$

which gives the following form for $Sh(z)$:

$$
Sh(z) = \frac{1}{\Gamma\left(\frac{4}{3}\right)} \left(\frac{H^2 \dot{\gamma}}{9D}\right)^{1/3} \left(\frac{z}{H}\right)^{-1/3}
\tag{2.11}
$$

The assumption of a simple shear flow is not as constraining as it may seem. In the vicinity of a no-slip surface, flows can be approximated as a simple shear. For pressuredriven flow between parallel, smooth plates, the shear rate at the wall is

$$\dot{\gamma} = \left.\frac{\partial u_z}{\partial y}\right|_{y=0} = \frac{6U}{H} \tag{2.12}$$

where U is the average axial velocity, and H is the plate separation. The shear rate at the wall for a general pressure-driven flow in a rectangular duct depends on the geometry of the duct. It is convenient to express the Sherwood number in terms of the ratio of shear rate at the reactive boundary to average axial velocity U and the Péclet number Pe:

$$Sh(z) = \frac{9^{-1/3}}{\Gamma\left(\frac{4}{3}\right)}\left(\frac{H\dot{\gamma}}{U}\right)^{1/3}\left(\frac{z}{PeH}\right)^{-1/3}, \tag{2.13}$$

where the dimensionless ratio $H\dot{\gamma}\ /U$ depends on the specific geometry of the channel and can be found by differentiating the axial velocity with respect to y at the reactive wall. As a first approximation for the shear rate in a rectangular duct, we take the value, $\dot{\gamma}$ =6U/H for flow between parallel plates from (2.12) and use (2.13) to predict the following correlation for $Sh(z)$ in a uniaxial duct flow:

$$Sh(z) = B_0\left(\frac{z}{PeH}\right)^{-1/3}, \tag{2.14}$$

where B_0 is a geometry dependent constant that is $O(1)$ for the flows considered here.

III.C. Mass transfer from a 3D duct flow and modified Grætz behavior

In this subsection, we extend the application of the Lévêque analysis to the transverse velocity components (x and y in Figure 2.1) of a 3D flow through a duct. This approximate treatment was motivated by our observation of developing

concentration boundary layers in the cross section of our simulated reactors, as presented in Section IV.A. Chang and Sen mentioned the concept of transverse boundary layers, (Chang and Sen 1994) and Xu *et al* have observed these structures experimentally in a heat transfer study. (Xu *et al* 2005) As we illustrate in the proceeding sections, this approach explains the key features of the observed phenomena and allows us to derive correlations for useful quantities.

We took the simple perspective depicted in Figure 2.3(b) in order to model mass transfer from a 3D duct flow: we consider entirely distinct axial and transverse flows encountering the reactive surface. Conceptually, each of these flows will develop a concentration boundary layer via the Lévêque-type process as described in Section III.B. A key feature of the transverse boundary layer is that its development is terminated once the fluid has traversed the width of the reactive surface, rather than growing indefinitely. If sufficiently strong, this transverse flow controls the development of the concentration distribution by convecting undepleted fluid to the edge of the reactive surface and thus arresting the growth of the axial boundary layer. By application of the standard Lévêque analysis for this transverse flow, it is possible to use (2.13) in the cross-stream direction (along x) rather than the axial direction (along z). The growth of the transverse boundary layer is arrested after a distance of order of the width, W, of the surface. Integrating (2.13) with x as the independent variable from x=0 to x=W for an average axial flow speed, U, and a transverse flow speed, u_{trans}, the Sherwood number develops as stated in (2.14) for $z<z_{plat}$, and in the following manner thereafter:

$$Sh_{\text{plat}} = \frac{(3/4)^{1/3}}{\Gamma\left(\frac{4}{3}\right)}\left(\frac{H}{W}\right)^{1/3}\left(\frac{H^2\dot{\gamma}_{\text{trans}}}{D}\right)^{1/3} = 0.81\left(\frac{H}{W}\right)^{1/3}\left(\frac{H\dot{\gamma}_{\text{trans}}}{u_{\text{trans}}}\right)^{1/3}\left(\frac{u_{\text{trans}}}{U}\right)^{1/3} Pe^{1/3}, \tag{2.15}$$

where the transverse shear rate, $\dot{\gamma}_{\text{trans}}$, is defined by the transverse flow. We expect the entrance length, z_{plat}, to scale inversely with the velocity ratio, (u_{trans}/U) due to the following simple argument: in the time that it takes for the transverse flow to traverse the width of the reactive surface, $t \sim W/u_{\text{trans}}$ the axial flow has covered a distance

$$z_{\text{plat}} = Ut \sim W\left(\frac{U}{u_{\text{trans}}}\right) \tag{2.16}$$

As in the previous subsection, we would like to adapt these predictions ((2.15) and (2.16)) for a reactive plate to the case of mass transfer from a 3D flow within a rectangular duct to a reactive wall. The prediction of the entrance length in (2.16) is unchanged. To evaluate the expression in (15), the dimensionless ratio $H\dot{\gamma}_{\text{trans}}/u_{\text{trans}}$ can be found by differentiating the transverse velocity with respect to y at the reactive wall. We estimate the transverse shear rate at the reactive boundary as $\dot{\gamma}_{\text{trans}} = u_{\text{trans}}/H$. Plugging this estimate into (2.15), we arrive at the following prediction for the asymptotic value of the Sherwood number in 3D flows in ducts with a single reactive boundary:

$$Sh_{\text{plat}} = B_1\left(\frac{u_{\text{trans}}}{U}\right)^{1/3} Pe^{1/3} = B_1 Pe_{\text{trans}}^{1/3}, \tag{2.17}$$

where $\text{Pe}_{\text{trans}} = u_{\text{trans}}H/D$ is the transverse Péclet number, and B_1 is a geometry dependent constant that is $O(1)$ for the flows considered here for which $W = 2H$. (2.14),

(2.16), and (2.17) describe a modified version of the behavior observed in the solution to the Grætz problem: the evolution of *Sh* exhibits an entrance region in which *Sh* decreases as $z^{-1/3}$ and an asymptotic region in which *Sh* takes on a constant value. Yet, the predicted modified Grætz behavior has two important distinctions from the classic result:

(1) For a three-dimensional channel flow with a fixed ratio between the axial and transverse velocities (as in the case considered here), the entrance length, $z_{plat} \sim W(U/u_{trans})$ depends only on the ratio of the axial and transverse velocity components and not on the magnitude of U. Therefore z_{plat} is a constant with respect to Pe; this behavior is distinct from the Grætz result for which $z_{plat} \sim PeH$.

(2) The plateau value, Sh_{plat}, in (2.15) and (2.17) increases with Pe; this behavior is again distinct from the Grætz result for which $Sh_{plat} = O(1)$.

The boundary layer picture presented here is simple, but, as we show in Section IV.B, it captures many of the details of transfer to reactive boundaries in the presence of transverse flows. The assumption that the fluid impinging on the leading edge of the reactive surface is undepleted with respect to the bulk is not necessarily true for all transverse flows at all values of *Pe*. With a proper choice of flow, this assumption can be satisfied. Indeed, this assumption provides the key connection between mixing in the bulk and mass transfer to boundaries: the ability of a flow to homogenize the concentration boundary layer created by the transverse flow will determine the success or failure of that flow at maintaining a high constant value of *Sh*, and therefore also high rates of mass transfer. Thus, a transverse flow that provides efficient mixing in the bulk (*e.g.*, a chaotic flow) should lead to larger, sustained rates of transfer than an equivalent (*e.g.*, in magnitude) flow that does not mix well. This prediction is substantiated by our simulation results.

IV. Results and Discussion

IV.A. Qualitative results

We will discuss the results of our simulations qualitatively in this subsection and quantitatively in the next. Figure 2.4 demonstrates the growth of the concentration boundary layer for several flow geometries at $Pe=10^4$. The left column for each series is a gray scale plot of the concentration in the cross section, while the right column is a plot of the concentration averaged along the x direction as a function of the y coordinate.[4] The growth of the concentration boundary layer in the absence of a transverse flow is apparent and consistent with expectations. The boundary layer grows more quickly near the side walls due to the slower axial velocity and longer residence times in these regions. In the second half of the channel ($1000 \le z / H \le 2000$), the boundary layer fills the channel and the concentration distribution evolves in a self-similar manner.

With a transverse flow that produces one large vortex ($r=1$), the boundary layer at the ceiling evolves in two stages toward an asymptotic form: for short axial distances ($z / H \le 80$), the depleted region remains thin due to the delivery of fresh solution to the "leading edge" of the ceiling (*i.e.*, the top left corner) by the transverse flow; later, as the depleted solution encircles the entire cross section, the "feed stream" of the ceiling becomes depleted and the boundary layer grows to fill half the height of the channel. The recirculation of depleted solution back to the reactive boundary

[4] The noise in these plots is due to the finite size of the population of tracers that we employed. We did not run more particles to eliminate this noise because these concentration distributions are only meant to convey qualitative information. The number of tracers was sufficient to ensure convergence of the locally averaged values of concentration used in evaluating mass transfer coefficients.

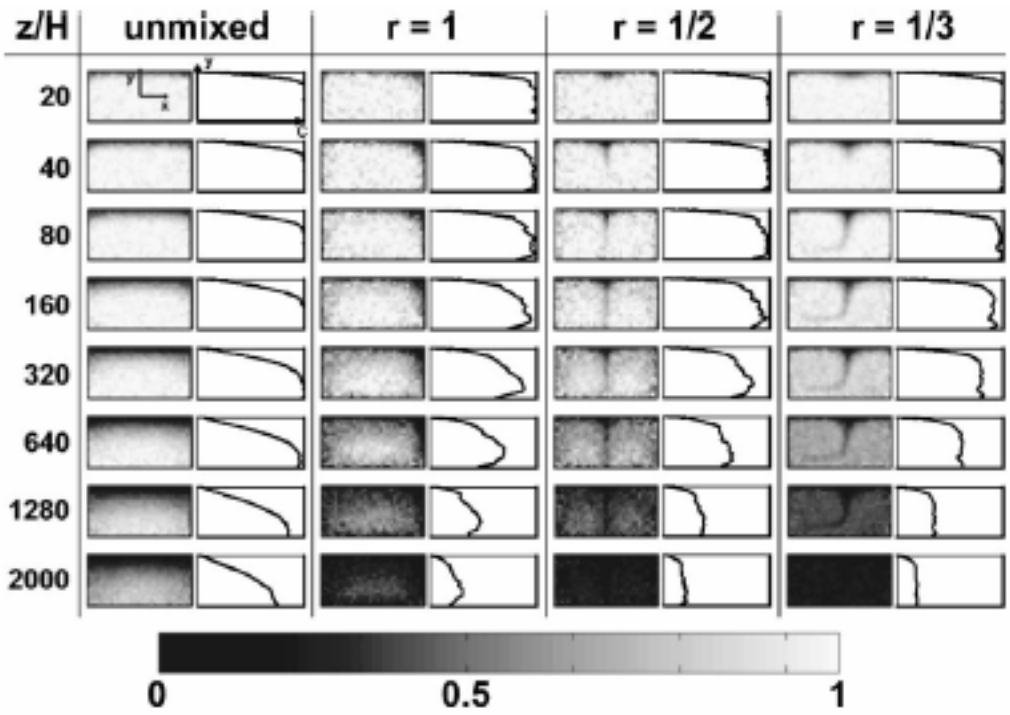

Figure 2.4. Boundary layer development as a function of axial distance. The left frame for each column is the concentration profile in the cross section with concentration represented by gray scale values shown in the color bar at the bottom. The right frame is the concentration averaged along the x direction as a function of y. In all cases, Pe=10^4 and the ratio of transverse velocity to axial velocity u_{trans} /U=0.2. The leftmost column is a uniaxial flow. The middle two columns are nonchaotic, 3D flows as in Figures 2.2(b) and 2.2(c). The rightmost column is a chaotic flow with r= 1/3 and $L_{1/2}$=10H as in Figure 2.2(a).

violates the assumption of homogenized concentration in our Lévêque treatment of the transverse boundary layer (Section III.C); thus, we do not expect these flows to exhibit the modified Grætz behavior. Despite the eventual growth of the boundary layer to a thickness controlled by the geometry (*i.e.*, ~$H/2$), its initial, thin structure leads to a significantly larger drop in the average concentration than in a purely axial flow.

The results for flow with two constant vortices ($r = 1/2$) are similar to the single vortex case, but the boundary layer is entrained into the downwelling through the center of the channel rather than circling the walls. The complete recirculation of the depleted solvent back to the reactive boundary is again observed, but the effect is less pronounced than in the single vortex case. Due to this difference, the flow with $r = 1/2$ is slightly more efficient than the flow with $r=1$ at decreasing average concentration.

Finally, the flow with $r = 1/3$ has two asymmetric vortices that alternate sides of the channel periodically along the axial direction. The boundary layer that grows into the downwelling of this flow shifts back and forth with changes in the transverse flow; this movement is not apparent in the plots presented due to the fact that they were all taken at the end of cycles of the SHM at which point the concentration distributions have the same shape. Here the boundary layer transitions directly to a thin asymptotic structure. This behavior closely resembles the prediction of the Lévêque analysis presented in Section III.C and was in fact our motivation for pursuing the concept of competing boundary layers. In this case, the depleted solution is injected into the large chaotic invariant set (see Figure 2.2(a)) and homogenized such that solution with the average concentration is continuously delivered to the leading edge of the reactive boundary. Despite this difference, the overall efficiency of this chaotic flow at transport toward the boundary is similar to that of the flow with $r = 1/2$. This result suggests that while chaotic particle trajectories are vital to generating

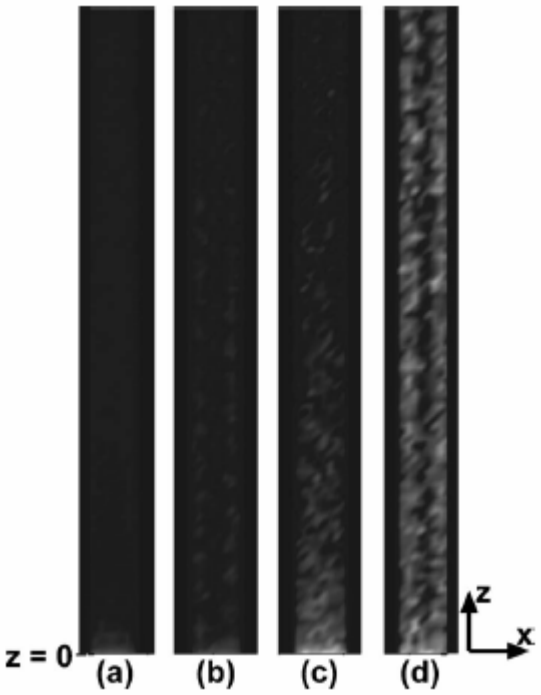

Figure 2.5. Effect of transverse flow and *Pe* on flux profile along the ceiling of the channel. (a) $Pe=10^4$, no transverse flow. (b) $Pe=10^4$, with transverse flow. (c) $Pe=10^5$, no transverse flow. (d) $Pe=10^5$, with transverse flow. In (b) and (d): $r=1/3$, $L_{1/2}=10H$, ratio of transverse velocity to axial velocity $u_{trans}/U=0.2$. Note: the plots present a total channel length, $L_{tot}=200H$. The width of the channel has been magnified by a factor of 10 relative to the length for clarity.

efficient mixing in the bulk, their effect on transfer to boundaries is more subtle. We will examine this question more thoroughly in Section IV.B.

The qualitative effect of the transverse flow can also be seen in the profile of flux along the reactive surface.[5] Figure 2.5 shows the flux at the surface with and without transverse flow. The flux in the unstirred case drops quickly with axial distance. In the stirred case, the average flux is maintained at a higher, visible level for the entire length of the device. The pattern along the center of the flux profiles in the stirred cases is due to the migration of the downwelling between half-cycles.

IV.B. Quantitative results

IV.B.1. Modified Grætz result with transverse flow

We now turn our attention to a quantitative evaluation of interfacial mass transfer in the presence of transverse flows. In the standard solution to the Grætz-Nusselt problem, $Sh(z)$ is found to decrease as $z^{-1/3}$ in the entrance region, beyond which it takes on a constant value. Figure 2.6(a) shows $Sh(z)$ as a function of z/H for the cases of pure uniaxial flow and chaotically stirred flow ($r = 1/3$, $L_{1/2}=10H$). For all values of $Pe(10^2–10^5)$, both types of flow exhibit $z^{-1/3}$ scaling of Sh at the entry of the duct. The Sherwood number in the stirred cases diverges from the unstirred cases at $z/H\sim20$, at which point it plateaus; we refer to this early transition to a constant asymptotic Sh as the modified Grætz behavior. This modified behavior is the benefit of transverse flows: $Sh(z)$ reaches its plateau earlier and at a higher value than without stirring. The plateau also appears at the same value of z/H for each value of Pe, as predicted in (2.16) from our boundary layer picture (cf. Section III.C). Figure 2.6(b)

[5] The noise in these plots is due to the finite size of the population of tracers that we employed. We did not run more particles to eliminate this noise because these concentration distributions are only meant to convey qualitative information. The number of tracers was sufficient to ensure convergence of the locally averaged values of concentration used in evaluating mass transfer coefficients.

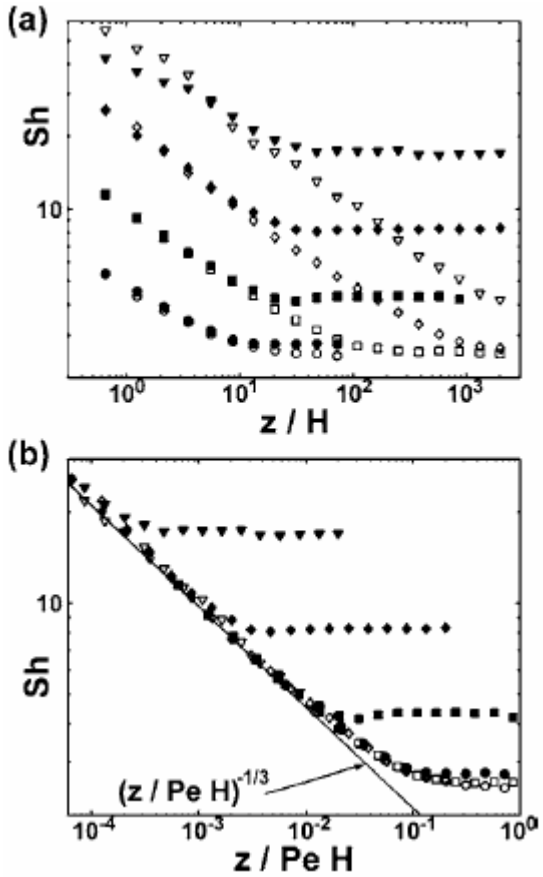

Figure 2.6. Grætz and modified Grætz behavior. (a) Local Sherwood number $Sh(z)$ as a function of axial distance. (b) $Sh(z)$ as a function of axial distance scaled by Pe. Symbol shape indicates the value of Pe: circle—10^2, square—10^3, diamond—10^4, triangle—10^5. Open symbols are unstirred, filled symbols are chaotically stirred, r= 1/3 , $L_{1/2}$=10H, and u_{trans} /U=0.2. The straight line is the evolution of $Sh(z)$ as predicted in (2.14).

further shows that the unstirred cases exhibit a universal collapse when z is scaled by $Pe\ H$, as expected from the standard Grætz solution.

In Figure 2.7, the evolution of Sh in several flow geometries is compared to that for the strongly chaotic SHM flow (r =1/3, $L_{1/2}$=10H). As seen in Figure 2.7(a), the mass transfer from the nonchaotic double vortex flow (r= 1/2) is similar to that from the chaotic flow in that Sh displays an entrance region of constant length followed by a (nearly) constant asymptotic value. We note though that Sh is slightly higher near the beginning of the plateau region and then decreases down the length of the channel rather than maintaining a constant value. The mass transfer from the single vortex flow (r=1) in Figure 2.7(b) is again similar to that from the strongly chaotic flow, but Sh drops significantly at large z /H and high Pe. This fall in the value of Sh is due to the depletion layer encircling the bulk and contaminating the feed stream as seen in Figure 2.4 and discussed in Sections III.C and IV.A. Figure 2.7(c) presents the mass transfer from a more weakly chaotic flow (r=1/3, $L_{1/2}$=2.5H; see Figure 2.2(d)); this flow clearly exhibits the modified Grætz behavior seen in the strongly chaotic flow despite the fact that the Poincaré maps of the two flows are substantially different (see Figure 2.2).[6]

From the results in Figure 2.7, it is apparent that the crucial ingredient for increasing transfer to boundaries is the presence of a strong transverse flow. Of secondary importance (at least in the regime explored here) is the complete homogenization of the transverse boundary layer before it returns to the reactive surface. The failure to meet this second condition appears in nonchaotic flows at large axial distance and high Pe.

[6] In the case of $L_{1/2}$=2.5H, our approximate representation of the transition from one form of transverse flow to another as instantaneous (see Figure 2.1(b)) may result in an overestimate of the transverse displacement per half-cycle. Nonetheless, this case is representative of physically realizable flows with small transverse displacements and distinct structure in their Poincaré maps (see Figure 2.2(d)).

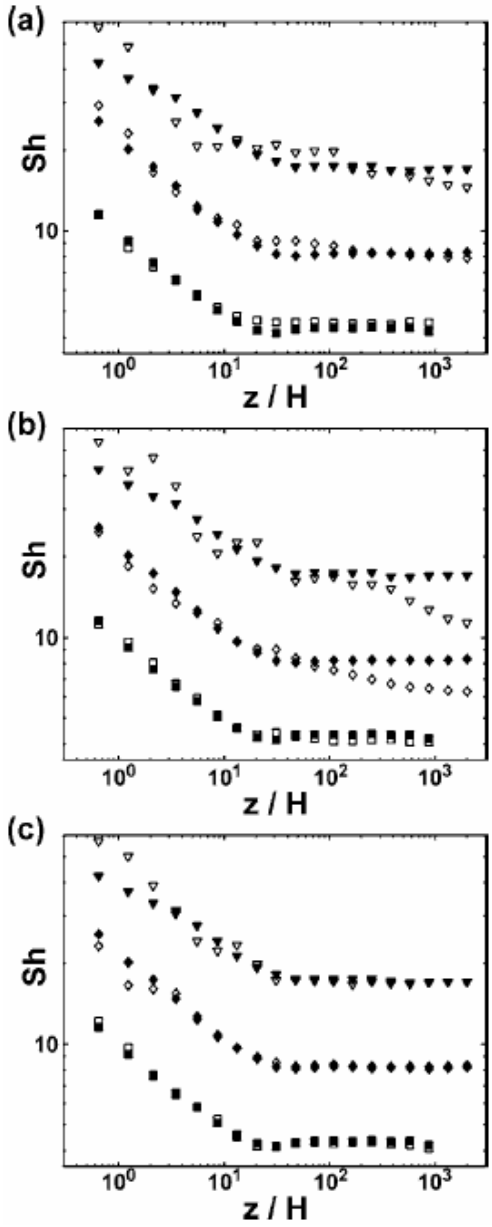

Figure 2.7. Comparison of $Sh(z)$ for different flows. (a) Nonchaotic two vortex flow (r= 1/2, as in Figure 2.2(b)—open), chaotic two vortex flow (r=1/3, as in Figure 2(a)—filled). (b) Nonchaotic single vortex flow (r=1, as in Figure 2.2(c)— open), chaotic two vortex flow (r= 1/3, as in Figure 2.2(a)—filled). The nonchaotic flows are constant with respect to axial distance, while the chaotic flow shifts with a half cycle length $L_{1/2}$=10H. (c) Chaotic flows with r= 1/3 showing the effect of a shorter half cycle. $L_{1/2}$=2.5H (as in Figure 2.2(d)—open), $L_{1/2}$=10H (as in Figure 2.2(a)—filled). Symbol shape indicates the value of Pe: square—10^3, diamond—10^4, triangle—10^5. All flows have u_{trans} /U=0.2.

IV.B.2. Test of predicted scaling and correlations

In Figure 2.8, we test the results of the Lévêque arguments presented in Section III.C for the plateau values of the Sherwood number and the entrance length for the case of a strongly chaotic flow (r=1/3, L1/2=10H). Figure 2.8(a) shows the scaling of Sh_{plat} versus $Pe_{\text{trans}}=Pe(u_{\text{trans}}/U)$ taken from results such as those in Figure 2.6 for various values of Pe and (u_{trans}/U). This scaling relation from simulation is in good agreement with our theoretical prediction (2.17). At the lowest value of Pe considered here (Pe=100, Pe_{trans}=20), Sh_{plat} deviates from the expected scaling because the unstirred case, for which Sh_{plat}=2.55, gives a lower bound on the value of Sh_{plat}. Figure 2.8(b) presents the variation of the entrance length, z_{plat}, with (u_{trans}/U) as measured approximately from results such as those in Figure 2.6. The observed scaling [$z_{\text{plat}}\sim(u_{\text{trans}}/U)^{-1}$] is as predicted in (2.16), with a prefactor somewhat larger than unity. We note again that Figure 2.6 showed that, in unstirred cases, the entrance length is proportional to $Pe\,H$ while in stirred cases the entrance length is independent of Pe, as predicted by the standard and modified Grætz (Section III.C) results. The following overall correlation for $Sh(z)$ is validated by Figure 2.8:

$$\begin{aligned} Sh(z) &= B_0\left(\frac{PeH}{z}\right)^{1/3} \qquad z < z_{\text{plat}}, \\ Sh(z) &= B_1\left(Pe\frac{u_{\text{trans}}}{u_z}\right)^{1/3} \qquad z > z_{\text{plat}} \\ &= B_1 Pe_{\text{trans}}^{1/3} \end{aligned} \tag{2.18}$$

with both B_0 and B_1 being $O(1)$. These results substantiate the simple boundary layer picture presented in Section III for this chaotic flow.

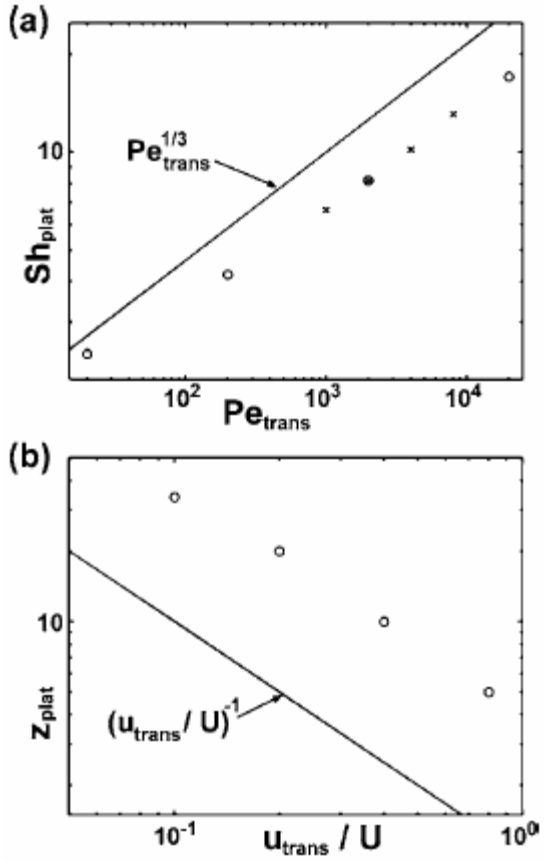

Figure 2.8. Test of theoretical correlations against simulation. (a) Sh_{plat} as a function of $Pe_{trans}=Pe(u_{trans}/U)$ in the presence of chaotic transverse flow: r= 1/3 , $L_{1/2}$=10H. Circles represent simulations with u_{trans}/U=0.2 at various values of Pe; crosses represent simulations with Pe=10^4 at various values of u_{trans}/U. The solid line shows the scaling predicted in (2.17). (b) Entrance length, z_{plat} as a function of the ratio of floor slip velocity to average axial velocity in the presence of chaotic transverse flow: r= 1/3 , $L_{1/2}$=10H, Pe=10^4. These values of z_{plat} were estimated from the elbows in plots of $Sh(z)$ such as those in Figure 2.6. The solid line shows the scaling predicted in (2.16).

IV.B.3. The role of Lagrangian chaos in mass transfer to no-slip boundaries

The similarity of the evolution of Sh shown in Figure 2.7(a) for chaotic (r=1/3) and nonchaotic (r= 1/2) flows leads to the following question: What is the role of chaotic advection in mediating mass transfer to boundaries? The flows experienced by a particle near the reactive surface are quite similar in the two cases, with similar shear rates and initial structures of the depletion layers. The distinction appears in the path that the depleted fluid follows after it leaves the reactive boundary. In nonchaotic cases, the depleted fluid is stretched and reconcentrated by diffusive exchange with the bulk, but eventually returns to the reactive surface due to the unchanging transverse flow. This inevitable depletion of the feed stream of the reactive boundary results in a breakdown of the modified Grætz behavior as it allows the concentration profile to continue to evolve. This continued growth of the boundary layer precludes the establishment of a true plateau region until the boundary layer reaches the core of the vortices, and therefore fills the entire channel.

This behavior is contrasted by that in the chaotic flow (r=1/3) that is able to keep the depleted fluid from returning to the reactive surface for all Pe explored in this study ($10^2 \le Pe \le 10^5$, and Pe=10^6, data not shown). Figure 2.9 shows the difference in $Sh(z)$ for the flow with r=1/3 and the flow with r=1/2 where the ceiling and both sidewalls are taken to be reactive. The presence of more reactive surface area accentuates the difference between chaotic and nonchaotic flows, because it increases the challenge of mixing the depleted fluid before it returns to the reactive surface. We have also considered other flows (r=5/12, r=1/3 with various cycle lengths, ducts with square cross section); all of these flows show the modified Grætz behavior in the presence of chaos and continuously growing boundary layers in the absence of chaos.

The role of chaotic advection in defining the modified Grætz behavior can therefore be stated as the ability to ensure the delivery of undepleted fluid to the

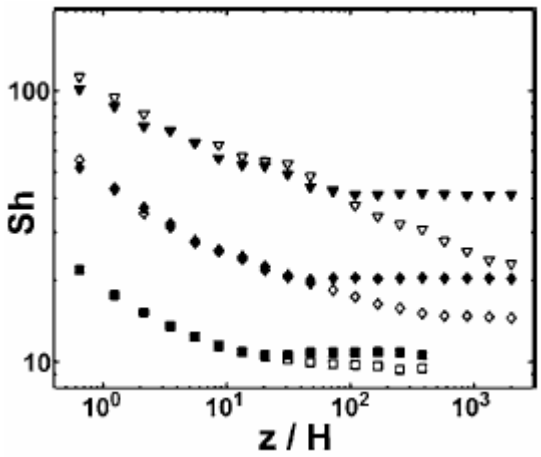

Figure 2.9. Comparison of *Sh* for chaotic (r=1/3—filled) and nonchaotic (r= 1/2—open) flows in the case of three reactive walls (*e.g.*, ceiling and sidewalls). Symbol shape indicates the value of *Pe*: square—10^3, diamond—10^4, triangle—10^5. All flows have u_{trans}/U=0.2.

reactive surface independent of *Pe* and axial distance. In this sense, chaotic advection appears to be both necessary and sufficient for the existence of the modified Grætz behavior. It is necessary in the sense that nonchaotic flows fail to ensure this behavior, and sufficient in the sense that we have been unable to find a regime in which chaotic flows do not produce such behavior. We are currently developing more rigorous support of these conclusions.

IV.B.4. Comparison to previous results

Our results share several similarities with those of other studies of heat and mass transfer in laminar flows. For the Dean flow in a helical tube, Janssen *et al*, found Sh in the entrance region to scale with $Pe^{0.33}$ with additional dependence on *Re*; the *Re* dependence is likely due to the *Re* dependence of the transverse Dean flow. (Janssen and Hoogendoorn 1978) They found however that the plateau value of *Sh* scales with $Pe^{1/6}$, while they noted that they expected scaling of $Pe^{1/3}$. Acharya *et al*, found similar results for the enhancement to heat transfer in the same system.

(Acharya *et al* 2001) They also extended the study to chaotic Dean flows by alternating the axis of the helical coil, and found an additional chaotic enhancement relative to nonchaotic flow that showed weak scaling in the Prandtl number *Pr*. Mokrani *et al*, cited an enhancement of 13%–27% for heat transfer in chaotic over nonchaotic coiled tubes, although their results were presented in terms of enhancement to efficiency, and as specific values rather than in the form of a correlation; it is difficult to generalize their results and compare them to our own. (Mokrani *et al* 1997) Khinast *et al*, claim an enhancement in *Sh* that scales linearly with *Re* for mass transfer in a static mixer, although theoretical justification of this scaling is not presented. (Khinast *et al* 2003) A system that has been studied in more depth is that of heat or mass transfer to the surface of particles in packed beds. Our results bear a similarity to established correlations for packed beds, for which the local Sherwood number scales as $Pe^{1/3}$. (Bird *et al* 2002) The velocity ratio (u_{trans}/U) for a packed bed is typically fixed, thus it does not appear explicitly in the correlations as it does in our (2.17). Our boundary layer treatment appears to provide a valid explanation of transfer from 3D laminar flows and may lead to a deeper understanding of transfer to boundaries in other laminar reactors.

IV.B.5. Design considerations

To provide insight into the use of this information for design purposes, we consider here the design of a microreactor. For given cross-sectional dimensions (H,W), transverse flow (u_{trans}/U), and diffusivity of reactants, the design of a reactor requires the choice of the total length of the channel, L_{tot}, and the flow speed (or *Pe*). The parameters that we use to define the performance of the system are the overall efficiency, ε, and the total current delivered to the surface, $\dot{N}$ (mol/s). The efficiency

is defined as the fractional number of particles that have reacted before the outlet of the channel:

$$\varepsilon = \frac{\dot{N}_{\text{in}} - \dot{N}_{\text{out}}}{\dot{N}_{\text{in}}} = \frac{C_{\text{cup}}(0) - C_{\text{cup}}(L_{\text{tot}})}{C_{\text{cup}}(0)} = 1 - \frac{C_{\text{cup}}(L_{\text{tot}})}{C_{\text{cup}}(0)} \tag{2.19}$$

where $\dot{N}_{\text{in}}$ (mol/s) and $\dot{N}_{\text{out}}$ (mol/s) are the molar flow rate of reactant in and out of the device, respectively, and L_{tot} (m) is the total length of the device. The total current is then

$$\begin{aligned} \dot{N} &= \left(C_{\text{cup}}(0) - C_{\text{cup}}(L_{\text{tot}})\right) Q = C_{\text{cup}}(0)\varepsilon HWU \\ &= C_{\text{cup}}(0)\varepsilon DWPe \end{aligned} \tag{2.20}$$

where Q (m^3/s) is the volumetric flow rate of solution, D (m^2/s) is the diffusivity of the solute, and H (m) and W (m) are the height and width of the channel, respectively. (2.20) indicates that for a given width of channel and concentration and diffusivity of the reactive solute, specification of ε and $\dot{N}$ uniquely specifies the Pe at which the system must operate. The expression for efficiency in (2.19) can then be used to specify the length of device for a given form of $C_{\text{cup}}(L_{\text{tot}})$. Although $C_{\text{cup}}(L_{\text{tot}})$ is generally a complicated function, we can find a simple approximate expression for the common scenario of high efficiency. For high efficiencies (ε >0.5), the required length is long compared to the length of the entrance region (L_{tot}>4z_{plat}). Integrating

$$\begin{aligned} \frac{C_{\text{cup}}(L_{\text{tot}})}{C_{\text{cup}}(0)} &= \frac{C_{\text{cup}}(z_{\text{plat}})}{C_{\text{cup}}(0)} \frac{C_{\text{cup}}(L_{\text{tot}})}{C_{\text{cup}}(z_{\text{plat}})} \\ &= \exp\left(-\frac{3}{2}\left(\frac{z_{\text{plat}}}{PeH} \right)^{2/3} \right) \exp\left(-\frac{Sh_{\text{plat}}}{Pe} \frac{L_{\text{tot}} - z_{\text{plat}}}{H} \right) \\ &\sim \exp\left(-\frac{Sh_{\text{plat}}}{Pe} \frac{L_{\text{tot}}}{H} \right) \end{aligned} \tag{2.21}$$

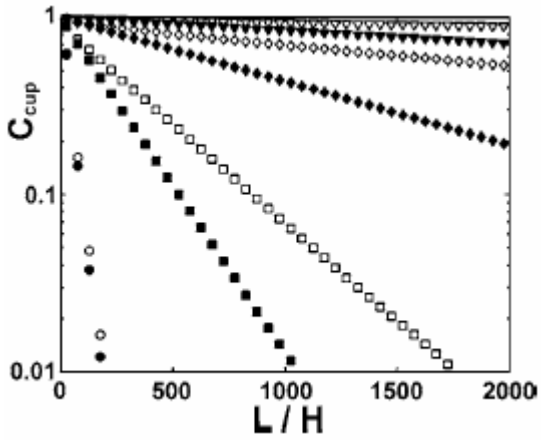

Figure 2.10. Cup mixing concentration as a function of total device length, L_{tot}. Symbol shape defines *Pe*: circle—10^2, square—10^3, diamond—10^4, triangle—10^5. Open symbols are unstirred, filled symbols are with chaotic transverse flow: r= 1/3 , $L_{1/2}$=10H, u_{trans} /U=0.2.

This last expression implies the approximation, $Sh(z) \sim Sh_{plat}$ throughout the length of the reactor. Although $Sh(z)$ is strictly larger than Sh_{plat} in the entrance region, this approximation is true to within several percent for all flows (uniaxial and 3D) considered in this work. As a further illustration of the appropriateness of the approximate expression for $C_{cup}(L_{tot})$ in (2.21), the semilog plots in Figure 2.10 show that the evolution of $C_{cup}(L_{tot})$ from simulations are nearly linear with slope Sh_{plat} / Pe. Therefore, using (2.21) and (2.19), we express the efficiency as

$$\varepsilon = 1 - \frac{C_{cup}\left(L_{tot}\right)}{C_{cup}\left(0\right)} = 1 - \exp\left(-\frac{Sh_{plat}}{Pe}\frac{L_{tot}}{H} \right) \tag{2.22}$$

(2.22) gives an expression for the length of the device in terms of the specified efficiency and *Pe*, as determined above:

$$\frac{L_{tot}}{H} \sim -\frac{\ln\left(1-\varepsilon\right) Pe}{Sh_{plat}} \tag{2.23}$$

In the case of the SHM flow (r=1/3, $L_{1/2}$=10H, u_{trans} /U=0.2) for which (2.18) provides a correlation for Sh_{plat}, we can rewrite (2.23) as

$$\frac{L_{\text{tot}}}{H} \sim -\frac{\ln(1-\varepsilon)\,Pe^{2/3}}{B_1\left(\frac{u_{\text{trans}}}{U}\right)^{1/3}} \tag{2.24}$$

Thus, in summary, one can use ε and $\dot{N}$ in (2.20) to determine the required Pe, and ε and Pe in (2.23) to determine L_{tot}. We note that for a given efficiency, the ratio of the length of device required for pure axial flow to the length required in the presence of the SHM chaotic flow is

$$\frac{L_{\text{tot}}^{\text{unstirred}}}{L_{\text{tot}}^{\text{stirred}}} \sim \frac{Sh_{\text{plat}}^{\text{stirred}}}{Sh_{\text{plat}}^{\text{unstirred}}} \sim \frac{B_1\left(\frac{u_{\text{trans}}}{U}\right)^{1/3} Pe^{1/3}}{2.55} \tag{2.25}$$

where $Sh_{\text{plat}}^{\text{unstirred}} \approx 2.55$ is approximated from the plot in Figure 2.6(b). If we take B_1~0.75 (inferred from Figure 2.8(a)), the unstirred device must be nearly twice the length of the stirred device at Pe=10^3 and more than eight times the length of the stirred device at Pe=10^5 for a flow with u_{trans} /U=0.2. The scaling predicted in (2.25) holds for any duct flow (with $L_{\text{tot}} \gg z_{\text{plat}}$) that provides the modified Grætz behavior. As a further illustration of increased transfer due to transverse flow, Figure 2.11 shows the efficiency and total current from the simulation results for a device of length 2000 H, where H is the height of the channel. At Pe=10^5, the efficiency and total current are ~3 fold higher with the SHM flow than without it. Figure 2.11 also illustrates that the difference between chaotic and nonchaotic flows only becomes appreciable at high Pe.

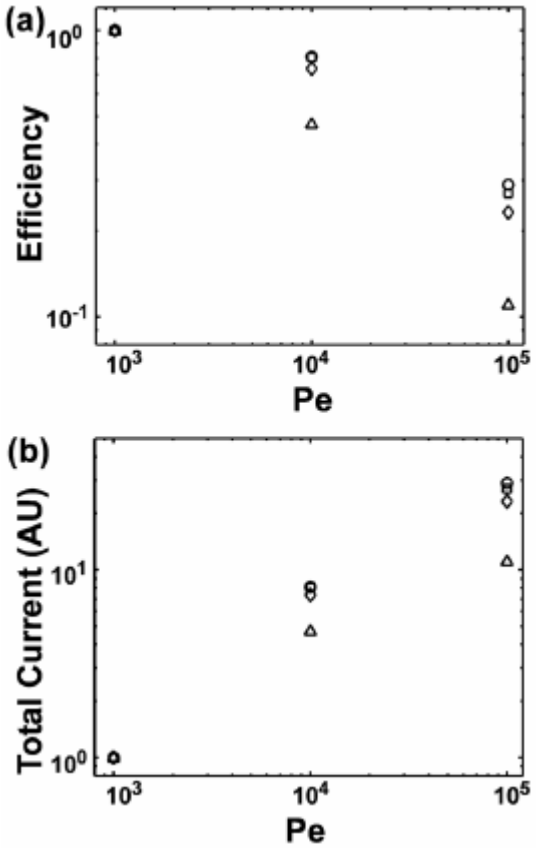

Figure 2.11. Efficiency and total current from simulation results for a device of length L_{tot}=2000H. Triangles represent uniaxial flow, diamonds represent stirred flows with r=1, squares represent r=1/2, and circles represent r =1/3 with $L_{1/2}$=10H and u_{trans} /U=0.2. Efficiency and total current are defined in (2.19) and (2.20), respectively.

V. Conclusions

In conclusion, our simulations indicate that 3D laminar flows of all types lead to increased rates of mass transfer to reactive boundaries in microchannels relative to uniaxial flows. We developed a treatment for the evolution of the concentration distribution from Lévêque-type arguments, and we validated predictions from this simple treatment with simulation results. By comparing several flows, we identified the characteristics of a flow that are important for increasing mass transfer to boundaries: (1) a high transverse shear rate at the reactive boundary; this property is of primary importance to increase the average rates of transfer relative to those from

uniaxial flows. (2) The ability to homogenize the concentration boundary layer before it returns to the reactive boundary; this characteristic leads to a modified Grætz behavior. This behavior is attractive due to the simplicity of the analysis it allows, as illustrated in Section IV.B.5. The existence of this second property appears to distinguish chaotic 3D flows from nonchaotic ones: chaotic advection appears to be both necessary and sufficient to ensure the complete homogenization of the depleted solution before returning it to the reactive surface.

We note that the position of the reactive boundary that we have considered is not optimal with respect to benefiting from the transverse flows generated by a grooved boundary. Nonetheless, this geometry is experimentally convenient, as a microchannel that contains the appropriate groove structure can simply be sealed to a reactive surface. Furthermore, rates of transfer are substantially increased in this geometry at high *Pe*. We expect more significant increases in transfer rates for reactions on the grooved surface itself, as the transverse flows are strongest in this region. Simulation of such systems will require a full computational fluid dynamics description of the flow in the vicinity of the grooves, and we have left this study for later investigation. We are pursuing experimental validation of these results and further theoretical clarification of the role of chaotic advection in defining the modified Grætz behavior.

REFERENCES

Acharya N, Sen M and Chang H C 2001 Analysis of heat transfer enhancement in coiled-tube heat exchangers *Int. J. Heat Mass Transfer* **44** 17

Bird R B, Stewart W E and Lightfoot E N 2002 *Transport Phenomena* (Danvers: Wiley)

Chang H C and Sen M 1994 Application of chaotic advection to heat transfer *Chaos, Solitons Fractals* **4** 6

Choban E R, Markoski L J, Wieckowski A and Kenis P J A 2004 Microfluidic fuel cell based on laminar flow *J. Power Sources* **128** 1

Cohen J L, Westly D A, Pechenik A and Abruna H D 2005 Fabrication and preliminary testing of a planar membraneless microchannel fuel cell *J. Power Sources* **139** 1

Ferrigno R, Stroock A D, Clark T D, Mayer M and Whitesides G M 2002 Membraneless vanadium redox fuel cell using laminar flow *J. Am. Chem. Soc.* **124** 44

Ganesan V, Bryden M D and Brenner H 1997 Chaotic heat transfer enhancement in rotating eccentric annular-flow systems *Phys. Fluids* **9** 5

Ghosh S, Chang H C and Sen M 1992 Heat-transfer enhancement due to slender recirculation and chaotic transport between counter-rotating eccentric cylinders *J. Fluid Mech*. **238** 119

Jana S C and Ottino J M 1992 Chaos-enhanced transport in cellular flows *Philos*. *Trans. R. Soc. London, Ser. A* **338** 1651

Janssen L A M and Hoogendoorn C J 1978 Laminar convective heattransfer in helical coiled tubes *Int. J. Heat Mass Transfer* **21** 9

Khinast J G, Bauer A, Bolz D and Panarello A 2003 Mass-transfer enhancement by static mixers in a wall-coated catalytic reactor *Chem. Eng. Sci*. **58** 3

Lemenand T and Peerhossaini H 2002 A thermal model for prediction of the Nusselt number in a pipe with chaotic flow *Appl. Therm. Eng*. **22** 15

Leprevost J C, Lefevre A, Brancher J P and Saatdjian E 1997 Chaotic mixing and heat transfer in a periodic 2D flow *C. R. Acad. Sci., Ser. IIb: Mec., Phys., Chim., Astron*. **325** 9

McQuarrie D A 1976 *Statistical Mechanics* (New York: Harper)

Mokrani A, Castelain C and Peerhossaini H 1997 The effects of chaotic advection on heat transfer *Int. J. Heat Mass Transfer* **40** 13

Myszka D G, Morton T A, Doyle M L and Chaiken I M 1997 Kinetic analysis of a protein antigen-antibody interaction limited by mass transport on an optical biosensor *Biophys. Chem*. **64** 1

Nishimura T and Kunitsugu K 1997 Fluid mixing and mass transfer in twodimensional cavities with time-periodic lid velocity *Int. J. Heat Fluid Flow* **18** 5

Ottino J M 1989 *The Kinematics of Mixing: Stretching, Chaos, and Transport* (Cambridge: Cambridge University Press)

Press W H, Teukolsky S A, Vetterling W T and Flannery B P 2002 *Numerical Recipes in C: the Art of Scientific Computing* (New York: Cambridge University Press)

Saatdjian E, Midoux N, Chassaing M I G, Leprevost J C and Andre J C 1996 Chaotic mixing and heat transfer between confocal ellipses: Experimental and numerical results *Phys. Fluids* **8** 3

Saatdjian E and Leprevost J C 1998 Chaotic heat transfer in a periodic two-dimensional flow *Phys. Fluids* **10** 8

Sikavitsas V, Nitsche J M and Mountziaris T J 2002 Transport and kinetic processes underlying biomolecular interactions in the BIACORE optical biosensor *Biotechnol*. *Prog*. **18** 4

Stroock A D, Dertinger S K W, Ajdari A, Mezic I, Stone H A and Whitesides G M 2002a Chaotic mixer for microchannels *Science* **295** 5555

Stroock A D, Dertinger S K, Whitesides G M and Ajdari A 2002b Patterning flows using grooved surfaces *Anal. Chem*. **74** 20

Stroock A D and McGraw G J 2004 Investigation of the staggered herringbone mixer with a simple analytical model *Philos. Trans. R. Soc. London, Ser. A* **362** 1818

Xu J L, Gan Y H, Zhang D C and Li X H 2005 Microscale heat transfer enhancement using thermal boundary layer redeveloping concept *Int. J. Heat Mass Transfer* **48** 9

Yarmush M L, Patankar D B and Yarmush D M 1996 An analysis of transport resistances in the operation of BIAcore_TM_: Implications for kinetic studies of biospecific interactions *Mol*. *Immunol*. **33** 15

CHAPTER 3

INTERFACIAL MASS TRANSPORT IN STEADY THREE-DIMENSIONAL FLOWS IN MICROCHANNELS[7]

I. Introduction

Interfacial transport is essential to the success of many processes that operate under laminar flow conditions. Heat and mass transfer to solid–liquid interfaces and across liquid–liquid interfaces are fundamental to heat exchanger design (Acharya *et al* 1992, 2001, Mokrani *et al* 1997, Peerhossaini *et al* 1993), electrochemical systems for analysis and energy production (Cohen *et al* 2005, Ferrigno *et al* 2002, Shrivastava *et al* 2008), separations with membranes (Shrivastava *et al* 2008) and without membranes (Aref and Jones 1989, Brody and Yager 1997), fabrication at fluid–fluid interfaces (Kenis *et al* 1999, 2000), and sensors involving interfacial reactions (Foley *et al* 2008, Golden *et al* 2007, Ismagilov *et al* 2000, Kamholz *et al* 1999, Squires *et al* 2008, Teles and Fonseca 2008, Vijayendran *et al* 2003). Many of these systems rely on the suppression of turbulence as a means of controlling fluid flow, whereas others are relegated to laminar flow by other constraints. These systems necessarily operate at low Reynolds number, $Re = UH / \nu < 100$, but can nonetheless also operate at high Péclet number, $Pe = UH / D > 100$, where U is the average velocity of the fluid, H is the characteristic dimension of the system, ν is the viscosity of the fluid, and D is the diffusivity of the solute in question (or the thermal diffusivity of the fluid). While low *Re* leads to the laminar conditions that are either desired or otherwise required in these systems, high *Pe* generally leads to low efficiency (*e.g.* fractional conversion of reactant) in heat and mass transfer due to slow diffusive transport relative to the

[7] *New Journal of Physics* **11** (2009) 075028, © IOP Publishing Ltd and Deutsche Physikalische Gesellschaft

overall convective transport of the fluid. As Péclet numbers tend to be higher for mass transfer than for heat transfer in liquid flows, this work focuses on mass transfer processes; the results are nonetheless relevant to heat transfer as well.

The goal of this work is to understand how the character of a given laminar flow impacts rates of interfacial mass transfer, and to illuminate the design of flows that allow for high rates of interfacial transfer. Many laminar flows are uniaxial in character, although three-dimensional flow can be induced through inertial effects at moderate *Re* (as in Dean's flows), by patterning of the bounding surfaces of the flow (Stroock *et al* 2000), or by driving the surfaces bounding the flow (as in a lid-driven cavity (LDC)). Parameters that influence the rate of transfer include: shear rates in the flow and particularly at the interface at which the transfer process is occurring; strength of the transverse components of a three-dimensional flow relative to the axial component; boundary conditions on the velocity at the interface in question; and the presence or absence of modulation or variation of the transverse flow along the axial dimension of the system. Metrics for evaluating the connection between the character of a flow and its interfacial transfer characteristics include: the mass transfer coefficient for transfer to the interface in question; the efficiency with which the flow homogenizes concentration differences in the bulk; and the structure and size of separate chaotic and non-chaotic sets that arise due to the flow.

We take as our system the class of steady flows in microfluidic channels of rectangular cross section (Figure 3.1). These flows are sufficiently simple so as to be generalizable to the greater field of laminar flows, but also allow for significant complexity through the application of velocity boundary conditions along the perimeter of the channel. By applying nonzero conditions to the tangential components of velocity along regions of the bounding surfaces, recirculation in the cross section can be induced, giving the flow a three-dimensional character. This is the

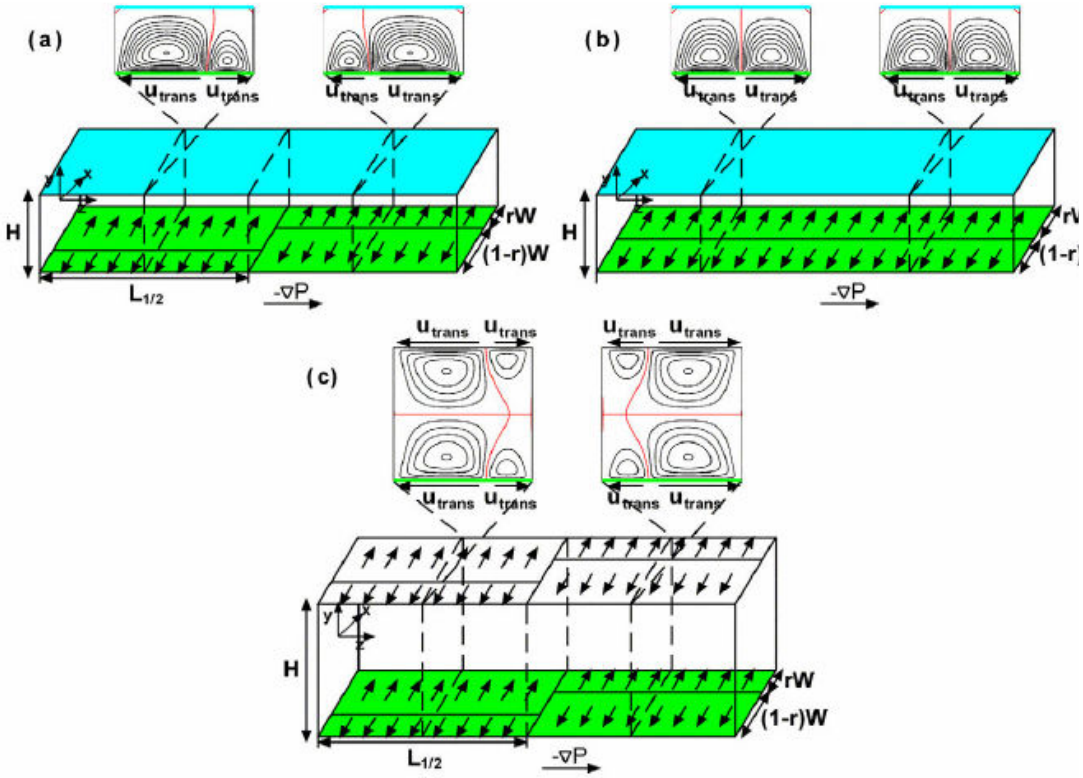

Figure 3.1. Schematic diagrams of sections of microchannels of interest. The sections shown correspond to one cycle of mixing. Arrows on floor and ceiling indicate moving boundaries. Contour lines in cross sections represent constant values of the stream function, ψ (*i.e.* streamlines) of the transverse flows that are driven by the moving boundaries: red streamlines have ψ=0 and connect the stagnation points in the flow; adjacent streamlines differ by $\Delta\psi = 0.03$. Characteristic parameters of the mixer are: channel height, H, and width, W, degree of asymmetry in moving boundary, r, half-cycle length, $L_{1/2}$ and transverse velocity at the driving boundary, u_{trans}. (a) Chaotic transverse flow ($r = 1/3$) driven from the floor only; the reactive interfaces considered in this flow include the blue (stationary) interface and the green (moving) interface. In this flow, the degree of asymmetry is switched from $r = 1/3$ to $r = 2/3$ at the end of each odd half-cycle, and switched back to $r = 1/3$ at the end of each even half-cycle. (b) Non-chaotic transverse flow ($r = 1/2$) driven from the floor only; the reactive interfaces considered in this flow include the blue (stationary) interface and the green (moving) interface. In this flow, the transverse flow is not switched as a function of axial distance. (c) Chaotic transverse flow ($r = 1/3$) driven from the ceiling and floor in a mirror-symmetric manner; due to the symmetry of the driving velocities, the flow is symmetric about the centre plane at $y = 0$, and simultaneous transport to the bottom green (moving) interface and across the horizontal centreline is considered.

so-called LDC system, which can be applied in two or three dimensions. Three examples of three-dimensional LDC flows with mean axial velocity are shown in Figure 3.1. The axial component of velocity is driven from left to right by a global difference in pressure, whereas the transverse components of the velocity are driven by slipping boundaries at the floor in Figures 3.1(a) and (b), and at the floor and ceiling in Figure 3.1(c). In Figures 3.1(a) and (c), the transverse velocity field is modulated periodically along the length of the channel (with period $2L_{1/2}$, where $L_{1/2}$ is the half-cycle length). This modulation of an asymmetric flow in space or time gives rise to chaotic trajectories in the flow, enhancing mixing (Aref 1984). Such LDC systems and the chaotic properties of the flows that they produce have been studied extensively (Aidun *et al* 1991, Chien *et al* 1986, Leong and Ottino 1989). The chaotic nature of the flows can be tuned through variation of the parameters in Figure 3.1: the degree of asymmetry, r, the half-cycle length, $L_{1/2}$, and the transverse velocity at the moving boundary, u_{trans}. The flow in Figure 3.1(b) is three-dimensional, but without modulation of the flow in space or time; it is necessarily nonchaotic (Ottino 1989). We note that the red streamlines shown in the cross sections of the flows in Figure 3.1 are the bounding lines of the vortices produced by these flows, connecting stagnation points of the transverse flow. While there is no convective transport across these streamlines, the modulation of the flows in Figures 3.1(a) and (c) cause a periodic exchange of fluid between the left and right vortices. The red vertical streamline in Figure 3.1(b) and the horizontal centerline in Figure 3.1(c) are interfaces between vortices that are never modulated and therefore there is never convective transport across these streamlines; they are purely diffusive interfaces.

The LDC geometries used in this work generate bulk flows that are similar to the flows generated by the staggered herringbone mixer (SHM), a laminar, chaotic micromixer (Stroock *et al* 2002a). Patterning the surface of a microchannel with

obliquely oriented grooves can impart a transverse component to the velocity near the grooved surface (Stroock *et al* 2002b). The net effect of these grooves on the flow in the bulk, to leading order, is equivalent to the effect of a slipping surface, as in the LDC. In this respect, we expect results for mass transfer to interfaces far from the driving surfaces in the LDC flows (such as the blue surface in Figures 3.1(a) and (b) and the horizontal centreline in Figure 3.1(c)) to reflect the effect of the transverse flows generated by SHM-like devices, as illustrated previously (Stroock and McGraw 2004). We do not expect results for mass transfer to the moving boundaries in Figure 3.1 to accurately reflect the effect on mass transfer to the grooved surface in SHM-like devices. The SHM grooves are composed of a collection of stationary surfaces whereas the moving boundary in the LDC is a single moving surface. While results for mass transfer to the moving interface cannot be directly related to those in the SHM, they are still instructive as a different type of interface for mass transfer and they may still shed light on some of the behaviours seen near the SHM grooves. Results for mass transfer across the diffusive interface at the horizontal centreline in Figure 3.1(c), being far from the surfaces driving the transverse flow, should be indicative of the effects on mass transfer across any such interface in a symmetrically driven flow, whether it be driven by moving boundaries, SHM-like grooves, or any other convective process, such as an adaptation of the T-sensor system for separations (Brody and Yager 1997) or analysis (Kamholz *et al* 1999).

The problem of mass transport to the interfaces bounding the steady, pressure-driven flow in a rectangular duct bears a significant resemblance to the classic Grætz problem for heat transfer to the interfaces bounding the laminar, fully developed flow in a round pipe or between infinite flat pipes (Grætz 1885). By the Chilton–Colburn analogy between heat transfer and mass transfer at high *Pe*, we can map the Grætz result for heat transfer between a fluid with uniform inlet temperature and the solid

bounding interface at some other uniform surface temperature onto the problem of mass transfer between a fluid with uniform inlet solute concentration and the solid bounding interface at some other uniform surface concentration (Bird *et al* 1960). We will therefore consider the classic Grætz problem for the flow between infinite flat plates using the language of mass transfer to consider an instantaneous chemical reaction at the stationary interface resulting in zero concentration at the interface.

As the fluid at uniform inlet concentration encounters the reactive interface, there is a flux of solute to the interface from the nearby fluid due to the difference in concentration between the fluid and the interface. The fluid adjacent to the interface becomes increasingly depleted of solute, and a concentration boundary layer forms and grows in the direction perpendicular to the interface with increasing axial distance. The flux to the reactive interface decreases as the growing boundary layer causes a decrease in the gradient of concentration at the interface. A mass transfer coefficient relating the flux at the interface to the concentration driving force is defined by:

$$J(z) = k(z)\left(C_{\text{bulk}}(z) - C_{\text{surface}}(z)\right) \tag{3.1}$$

where $k(z)$ is the mass transfer coefficient, $J(z)$ is the flux of solute to the interface, C_{surface} is the surface concentration at the reactive interface (taken to be zero), and $C_{\text{bulk}}(z)$ is the bulk average concentration, using the cup-mixing definition as a velocity weighted average concentration:

$$C_{\text{cup}}(z) = \frac{\int\int C(x,y,z)u_z(x,y)dxdy}{\int\int u_z(x,y)dxdy} = \frac{\int\int C(x,y,z)u_z(x,y)dxdy}{UA} \tag{3.2}$$

The mass transfer coefficient can be non-dimensionalized for comparison across systems of different size scales and solute diffusivity, and can be written by conservation of mass of solute:

$$Sh(z) = \frac{k(z)H}{D} = -\frac{PeH}{C_{\text{bulk}}}\frac{dC_{\text{bulk}}}{dz} = -\frac{d\ln C_{\text{bulk}}}{dZ} \tag{3.3}$$

where $Sh(z)$ is called the Sherwood number for mass transfer, H is the separation between the plates and $Z = z/PeH$ is the scaled axial distance. For short axial distances, the flux to the reactive interface decreases due to a decrease in the Sherwood number, while the concentration driving force stays nearly constant. This region is called the entrance region. As the thickness of the concentration boundary layer approaches the separation between the plates, however, the concentration profile develops an asymptotic shape and the Sherwood number becomes constant while the average concentration decreases with axial distance (see Figure 3.2). This region is called the asymptotic region and is characterized by an asymptotic value of the Sherwood number, Sh^{∞}, and the axial distance at which the transition occurs is called the entrance length, L_{ent}. For uniaxial flow between infinite flat plates, L_{ent}/PeH and Sh^{∞} are universal constants. For uniaxial flow in a rectangular duct, L_{ent}/PeH and Sh^{∞} have some geometry dependence, but are independent of Pe for a given geometry.

In the presence of a three-dimensional flow, the mass transfer problem considered above takes on new characteristics that can lead to larger values of the Sherwood number and higher flux of solute to the reactive interface. With flows like those created in the geometries shown in Figure 3.1, the depleted fluid near the reactive interface can be swept away from the interface and into the bulk. If the bulk is also sufficiently well mixed, the depleted fluid will be homogenized with the bulk

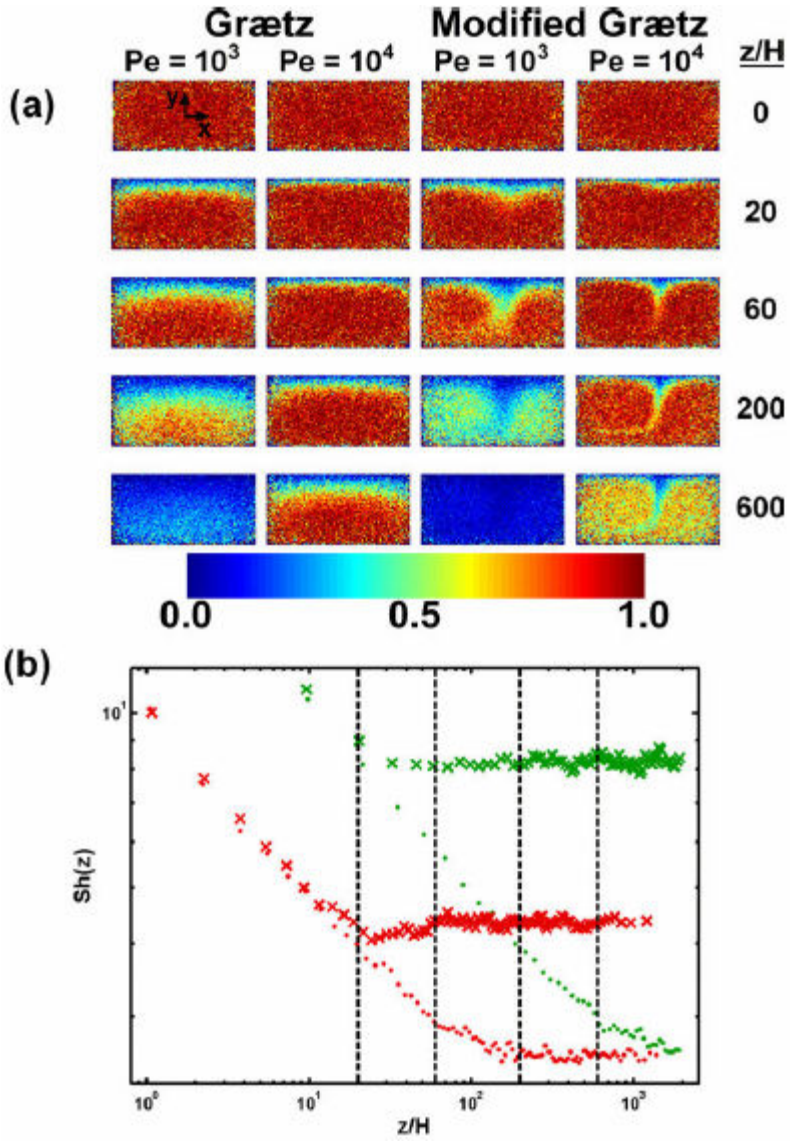

Figure 3.2. Comparison of Grætz and modified Grætz behaviours. Reaction at the blue interface in the flow shown in Figure 3.1(a) with and without transverse flow. (a) Cross-sectional concentration profile ($C(x,y)$) at several axial positions and at two values of *Pe.* The first and second columns (Grætz) represent uniaxial Poiseuille flow; the third and fourth columns (modified Grætz) represent chaotically stirred flow as in Figure 3.1(a) with $r = 1/3$, $u_{trans} = U/5$ and $L_{1/2} = 10H$. Colourbar below plot shows concentration colour scale. (b) Local Sherwood number for the cases shown in (a): dots correspond to the uniaxial flow, crosses correspond to the chaotically stirred flow; red symbols have $Pe = 10^3$, green symbols have $Pe = 10^4$. Dashed lines correspond to the axial positions of the snapshots in (a).

before it returns to the surface. In this way, solute is consistently brought near to the reactive interface by convection rather than by diffusion across a thick boundary layer. The transverse flow stops the growth of the boundary layer due to the movement of depleted fluid away from the reactive interface: once the fluid has been swept across the width of the reactive interface, it detaches and is incorporated into the bulk stream (see Figure 3.2). The entrance region in such a flow is similar to that in a uniaxial flow, but the asymptotic state is reached after a shorter scaled entrance length, L_{ent}/PeH, and at a higher asymptotic value of the Sherwood number, Sh^{∞}, which are both functions of Pe. We call this effect the modified Grætz behaviour because it shares the hallmarks of the classic Grætz solution, but it introduces dependence on Pe into L_{ent}/PeH and Sh^{∞}; these characteristics allow for significant increases in total reactive flux to the interface and efficiency of usage of the solution of reactants.

In our previous work, we demonstrated the existence of the modified Grætz behaviour in the context of transport to the stationary interface far from the surface that drives the flow, as in Figure 3.2 (Kirtland *et al* 2006). The present work has two main purposes: to extend the investigation of the modified Grætz behaviour to include internal diffusive interfaces and moving reactive interfaces; and to develop a more complete understanding of the origin and generality of the modified Grætz behaviour. The first goal (extension to new interfaces) includes the development of theoretical predictions for the effect of transverse flows on mass transfer to or across the interfaces in question, and then the validation of those predictions from numerical simulations. The second goal (understanding the origins and generality of the modified Grætz behaviour) involves the assessment of the dominant length scales in a given flow, and the determination of whether the processes that drive mixing in the bulk are sufficiently fast to keep the processes that drive depletion of the boundary layer from reinforcing and decreasing the efficiency of the system.

In order to place this work in the greater context of heat and mass transfer in laminar flow, we now consider the existing work in the field. Theoretical developments are discussed first, and experimental and numerical results follow. As discussed above, the classic problem of heat transfer from a fluid undergoing fully developed laminar flow to the surface of a round pipe was solved by Grætz in 1885. Further insight was added by Lévêque in 1928 in the form of a similarity solution for the temperature field in a shear flow, which is a good approximation of the flow near the pipe surface, and therefore is meaningful for thin boundary layers, *i.e.* in the entrance region. These ideas were mapped onto the problem of transfer across a fluid–fluid interface at the centreline of the flow in a rectangular duct by Ismagilov *et al* (2000), demonstrating that the rate of mass transfer across the interface, and therefore the rate of homogeneous reaction of initially segregated reactants, scales with the square root of *Pe* in the plug-like flow in the centre of the channel, but scales with the cube root of *Pe* near the stationary duct walls. Chang and Sen (1994) called attention to the types of resistances to transfer from flows to solid surfaces and across fluid–fluid interfaces, identifying boundary layers, recirculation regions and stagnation streamlines, and also noted that chaotic mixing leads to lower resistances than non-chaotic mixing. As the introduction of chaotic trajectories requires modulation, and, therefore, a frequency of modulation, many groups have investigated the optimal frequency for increasing rates of transfer in a given system (Bryden and Brenner 1996, Ghosh *et al* 1992, Horner *et al* 2002). Although many have noted significant increases in rates of transfer with the introduction of chaotic trajectories (Bryden and Brenner 1999, Ganesan *et al* 1997, Lefevre *et al* 2003), others (ourselves included) have cautioned against equating increases in mixing efficiency due to chaotic flows with increased rates of transfer (Ganesan *et al* 1997, Ghosh *et al* 1998, Kirtland *et al* 2006). Experimentally, many investigators have harnessed the controllability of laminar flow

to their advantage in systems depending on interfacial heat and mass transfer: liquid–liquid extraction (Brody and Yager 1997); homogeneous reaction of initially separate reactant streams (Ismagilov *et al* 2000, Kamholz *et al* 1999); microfabrication at fluid–fluid interfaces (Kenis *et al* 1999, 2000) and laminar flow-based fuel cells (Cohen *et al* 2005, Ferrigno *et al* 2002). All of these systems, however, suffer some loss of efficiency due to depleted regions near the interfaces at which transfer occurs.

Experimental efforts to understand the influence of chaos on interfacial transfer are many and varied in their conclusions. Researchers working with Dean's flows in coiled tubes have cited enhanced heat transfer due to chaos (Peerhossaini *et al* 1993), although the increases in rates of transfer are relatively small in magnitude (13–27%, Mokrani *et al* 1997) and in scaling with the Prandtl number, $Pr = \nu/\alpha$, where ν is kinematic viscosity and α is thermal diffusivity ($Pr^{0.09}$, Acharya *et al* 2001). For transport to the surface of confocal ellipses, a 100% increase over conduction is observed by Saatdjian *et al* (1996). For mass transfer to the surfaces of a sinusoidal wavy-walled channel, chaos leads to higher rates of transfer, and the effects are associated with the flow separation and oscillation induced by the wall geometry (Nishimura 1995, Nishimura and Kojima 1995, Nishimura *et al* 1993). Finally, Shrivastava *et al* (2008) were able to predict to within 4–12% the enhancements seen in experiments with ultrafiltration membrane spacers using a simple model, even though this model assumes instantaneous mixing of the fluid. While it is difficult to incorporate the many experimental, numerical and theoretical results available in the literature into a single conclusion, a theme emerges: chaos can lead to significant increases in transfer to moving interfaces and internal, fluid–fluid interfaces (Bryden and Brenner 1999, Ganesan *et al* 1997, Lefevre *et al* 2003), while for transfer to solid, stationary interfaces, chaos leads to little or no increase in rates relative to analogous,

nonchaotic flows (Acharya *et al* 2001, Ghosh *et al* 1998, Kirtland *et al* 2006, Mokrani *et al* 1997, Peerhossaini *et al* 1993).

In order to develop a better understanding for the mechanism behind the increases in rates of transfer that are seen in the presence of transverse flow, we use simulation code designed to track particles in a three-dimensional flow field to simulate the convection–diffusion–reaction process at stationary and moving solid interfaces, and also to simulate the convection–diffusion process at an internal, fluid–fluid interface. We look for signs of the modified Grætz behaviour described above in the results for mass transfer to these interfaces, and, perhaps more importantly, we look for situations in which the modified Grætz behaviour breaks down at large axial distance and at high *Pe*. In relating the success or failure of the modified Grætz behaviour to the character of the flow, we propose a more complete picture of the mechanism behind the modified Grætz behaviour and behind the maintenance of high rates of mass transfer, in general.

The paper is structured as follows: in Section II, we present a definition of the standard Grætz and modified Grætz behaviours described above and review the results from our previous work (Kirtland *et al* 2006). We then proceed to develop theoretical results for the extension of the modified Grætz behaviour to moving reactive interfaces and internal diffusive interfaces, as well as a theory for the conditions on the existence of the modified Grætz behaviour in terms of characteristic length scales in the flow. Section III describes the numerical methods used to test theoretical predictions. In Section IV, we present and discuss results for interfacial mass transfer in the flows in Figure 3.1, as well as results for characteristic length scales in the flow, and an extension of the modified Grætz framework to a broader class of flows. Finally, we present conclusions and discuss the applicability of our analysis to the field of interfacial transfer phenomena more generally.

II. Theory

In this section, we present the theoretical framework in which we will interpret our results in Section IV. Starting with the governing equation for the convection–diffusion process, we derive forms for the local value of the Sherwood number for transport to the blue and green interfaces in Figure 3.1 and for transport across the plane of symmetry in Figure 3.1(c). We also develop correlations for the asymptotic value of the Sherwood number that are valid beyond the entrance length, once the concentration profile has converged to its asymptotic shape. Finally, we develop an argument for the criteria for the existence of modified Grætz behaviour at arbitrarily large axial distance and arbitrarily large *Pe*.

II.A. Mass transfer to stationary interfaces in LDC flows

As discussed in Section I, the groundwork for the understanding of transport to stationary solid interfaces in fully developed uniaxial flow was laid by Grætz (1885). The convection–diffusion equation is the governing equation for the process (axes defined in Figure 3.1):

$$\vec{u}\cdot\vec{\nabla}C = D\nabla^2 C \rightarrow u_z \frac{\partial C}{\partial z} = D\frac{\partial^2 C}{\partial y^2}, \tag{3.4}$$

where $\vec{u}$ is the velocity, C is the concentration, and u_z is the axial component of the velocity. Symmetry is assumed in the x-direction and streamwise diffusion is assumed to be negligible compared with spanwise diffusion. A solution of the governing equation by separation of variables is possible for the case of uniform inlet concentration and uniform concentration at the interface, resulting in an exponential function of z and a power series solution in y. The full solution includes a sum over eigenmodes, but at large axial distance, only the mode with the smallest eigenvalue

persists. This mode determines the shape of the asymptotic state mentioned in Section I, and the asymptotic value of the Sherwood number. For a thin boundary layer near the interface, as is the case in the entrance region, transfer occurs in a shear flow with zero velocity at the interface. In 1928, Lévêque solved the problem of transfer from a fluid undergoing shear flow to the stationary surface bounding the flow by use of a similarity variable, making it simple to calculate the Sherwood number in the entrance region as a function of axial distance:

$$\begin{aligned} Sh(z < L_{\text{ent}}) &= B_0 \left(\frac{z}{PeH} \right)^{-1/3}, \quad B_0 \sim O(1), \\ Sh(z > L_{\text{ent}}) &= Sh^{\infty} \sim O(1), \end{aligned} \tag{3.5}$$

where Sh^{∞} and L_{ent}/PeH are geometry dependent but independent of Pe, with $Sh^{\infty} \approx 2.55$, $L_{\text{ent}}/PeH \approx 0.06$ and $B_0 \approx 1$ for the uniaxial flows considered in this work.

In systems with transverse as well as axial components of velocity, there exists the possibility of convecting the depleted fluid near the reactive interface into the bulk, such that the boundary layer does not become successively thicker with increasing axial distance. In order for this modified Grætz behaviour to hold, the transverse flow must be strong enough relative to the axial flow to sweep fluid away from the reactive interface over an axial distance that is short compared to the entrance length for the standard Grætz behaviour, otherwise, the effect of the transverse flow will be obscured by the rapid growth of the standard boundary layer. In order for this behaviour to continue to hold for large axial distances, the transverse flow must also homogenize the depleted fluid with the bulk fluid before it returns to the reactive interface. If these conditions are satisfied, the asymptotic state of the concentration distribution takes on a different form determined by the transverse flow. The Sherwood number in the entrance region is identical to that in the uniaxial case, but the entrance length is

shorter and independent of *Pe*: $L_{ent} \sim W\dot{\gamma}_{axial} / \dot{\gamma}_{trans}$ for width of interface, *W*, and axial and transverse shear rates at the interface, $\dot{\gamma}_{axial}$ and $\dot{\gamma}_{trans}$. The asymptotic state involves a concentration profile that is selfsimilar (periodically self-similar for modulated flows) with a mean concentration that continues to decay as in the uniaxial asymptotic region, but the asymptotic value of the Sherwood number for transfer to the stationary surface, Sh^{∞}_{stat}, becomes *Pe*-dependent:

$$Sh^{\infty}_{stat} = \frac{(3/4)^{1/3}}{\Gamma(4/3)}\left(\frac{H}{W}\right)^{1/3}\left(\frac{\dot{\gamma}_{trans}H}{u_{trans}}\right)^{1/3} Pe^{1/3}_{trans}, \qquad (3.6)$$

where $Pe_{trans} = Pe\ u_{trans}/U$. This result is the essence of the modified Grætz behaviour as presented in our previous work (Kirtland *et al* 2006). We proceed now to extend the modified Grætz result to other interfaces in the flows considered in this work.

II.B. Mass transfer to non-stationary interfaces in LDC flows

II.B.1. Transport to diffusive internal interface.

In order to extend the above development to moving interfaces, we start with the simple example of diffusion across the horizontal interface between two streams of different initial concentration in a uniaxial plug flow in the *z*-direction. We can approach this interface in much the same way that we approached the simple shear flow as a model of the flow near a generalized solid stationary interface (Kirtland *et al* 2006). For transfer across the *x*–*z* plane (analogous to the horizontal centreline in Figure 3.1(c) in a uniaxial plug flow), the problem is symmetric in *x*. The transverse components of the velocity are zero, and we assume that at large *Pe* we can neglect streamwise diffusion. The convection-diffusion equation is solved by similarity solution to give:

$$\vec{u}\cdot\vec{\nabla}C = D\nabla^2 C \rightarrow u_z \frac{\partial C}{\partial z} = D\frac{\partial^2 C}{\partial y^2}$$
$$\hat{C} = \frac{2C - C_0}{C_0} \rightarrow u_z \frac{\partial \hat{C}}{\partial z} = D\frac{\partial^2 \hat{C}}{\partial y^2},$$
$$\eta = \left(\frac{u_z}{4Dz}\right)^{1/2} y \rightarrow C(\eta) = \frac{C_0}{2}\left(1 + \mathrm{erf}(\eta)\right), \tag{3.7}$$

where u_z is the axial velocity, D the diffusivity and C_0 the initial difference in concentration across the centreline. The form for the local Sherwood number $Sh(z)$ is

$$Sh(z) = \frac{1}{2\sqrt{\pi}}\left(\frac{z}{Pe_{\mathrm{plug}} H}\right)^{-1/2}, \tag{3.8}$$

where $Pe_{\mathrm{plug}} = u_z H/D$. The local mass transfer coefficient decreases with increasing axial distance due to a thickening boundary layer at the interface, which results in a decreased gradient of concentration driving the transfer process.

By the same logic, we can consider transport to the diffusive internal interface ($y = 0$) in the flow in Figure 3.1(c). It should be noted, however, that (8) is the result for a true plug flow, and the extension of this result to the diffusive interface in Figure 3.1(c) is only approximate due to the mixed scaling found in the vicinity of the sidewalls, as demonstrated by Ismagilov *et al* (2000). There is a plane of symmetry at the horizontal centreline of the channel due to the mirror symmetry of the driving velocities at the ceiling and floor of the channel. The velocity normal to this plane must be zero, and the derivative of the velocity tangent to the plane must be zero. Zero velocity normal to the plane results in an interface across which solute only diffuses; there is no convective transport across this centre plane. The interface acts like the membrane in a coflowing membrane separator (Brody and Yager 1997), and such

interfaces act like a 'virtual membrane' in the context of fluid-based fuel cells (Cohen *et al* 2005, Ferrigno *et al* 2002).

The vanishing derivative of the tangential velocity gives us effectively a plug flow in both the axial and transverse directions near the centreline. We can consider the growth of a boundary layer in the axial and transverse directions. The governing equation is again the convection–diffusion equation, but now there are two convective terms:

$$\vec{u}\cdot\vec{\nabla}C = D\nabla^2 C \rightarrow u_{\text{centre}}\frac{\partial C}{\partial x} + u_{\text{axial}}\frac{\partial C}{\partial z} = D\frac{\partial^2 C}{\partial y^2}, \tag{3.9}$$

where u_{centre} is the transverse velocity at the centreline due to the driving velocity at the floor and ceiling, u_{trans}, and u_{axial} is the axial velocity at the centreline, which is roughly twice the average axial velocity U. Non-dimensionalizing (9)

$$\begin{aligned} &\hat{C} = \frac{2C - C_0}{C_0}, \quad X = \frac{x}{W}, \quad Y = \frac{y}{H}, \quad Z = \frac{z}{L}, \\ &\frac{u_{\text{centre}}}{U}\frac{H}{W}\frac{\partial \hat{C}}{\partial X} + \frac{2U}{U}\frac{H}{L_{\text{ent}}}\frac{\partial \hat{C}}{\partial Z} = \frac{D}{UH}\frac{\partial^2 \hat{C}}{\partial Y^2} = \frac{1}{Pe}\frac{\partial^2 \hat{C}}{\partial Y^2}, \end{aligned} \tag{3.10}$$

where C_0 is the initial concentration difference across the interface, W is the channel width, H is the channel height, L is the characteristic axial length over which the boundary layer develops due to the axial flow ($L = L_{\text{ent}}$) and $Pe = UH/D$. Transverse convection will dominate development of the boundary layer if the axial convective term is small compared with the transverse convective term. This situation occurs if $L_{\text{ent}} / W \gg 2U / u_{\text{centre}}$. From past results (Kirtland *et al* 2006), we expect the axial distance required to develop a boundary layer through a height h in the channel by diffusion in a uniaxial flow to be roughly $L_{\text{ent}} = 0.06Peh$, and in this case, h is the half-

height of the channel: $h = H/2$. Therefore we expect the transverse convection term to dominate for,

$$\frac{L_{\text{ent}}}{PeH} \sim 0.03 \gg \frac{2UW}{u_{\text{centre}} PeH} = \frac{2W}{Pe_{\text{centre}} H} \rightarrow Pe_{\text{centre}} \gg \frac{200W}{3H}, \tag{3.11}$$

where $Pe_{\text{centre}} = Pe\, u_{\text{centre}}/U$. In this limit, we can neglect the axial convection term in (9), such that the governing equation becomes

$$u_{\text{centre}} \frac{\partial C}{\partial x} = D \frac{\partial^2 C}{\partial y^2}. \tag{3.12}$$

As for (3.7) above, there is a similarity solution for (3.12)

$$\eta = \left(\frac{u_{\text{centre}}}{4Dx} \right)^{1/2} y \rightarrow C(\eta) = \frac{C_0}{2} \left(1 + \text{erf}(\eta)\right). \tag{3.13}$$

The form of $Sh(x)$ developing across the channel is now

$$Sh_{\text{centre}}(x) = \frac{1}{2\sqrt{\pi}} \left(\frac{x}{Pe_{\text{centre}} H} \right)^{-1/2}. \tag{3.14}$$

Physically, the concentration profile and the corresponding $Sh_{\text{centre}}(x)$ continue to develop across the channel until the fluid is swept off the internal interface and back into the bulk. This departure from the interface arrests the growth of the depleted region and leads to the plateau value of the Sherwood number, in a manner consistent with the modified Grætz behaviour (Figure 3.2). This plateau value is equal to the average of $Sh_{\text{centre}}(x)$ over the width of the channel. As can be seen in the streamlines in Figure 3.1(c), the effect of the smaller vortex at the centerline is minimal; the larger vortex accounts for most of the centreline velocity. Averaging $Sh_{\text{centre}}(x)$ over the

width of the channel, we have the following correlation for the asymptotic value of the Sherwood number at this symmetry plane:

$$Sh^{\infty}_{\text{centre}} = \frac{1}{W}\int_0^W Sh_{\text{centre}}(x)dx = \frac{1}{\sqrt{\pi}}\left(\frac{H}{W}\right)^{1/2} Pe^{1/2}_{\text{centre}}. \qquad (3.15)$$

This asymptotic value of the Sherwood number holds once the boundary layer near the internal interface has assumed its asymptotic shape, after the end of the entrance region, with length $L_{\text{ent}} \sim W2U/u_{\text{centre}}$. Within the entrance region, $Sh_{\text{centre}}(z)$ takes on the same values as the local Sherwood number in a plug flow as in (3.8) with $Pe_{\text{plug}} = u_z H/D = 2UH/D = 2Pe$.

II.B.2. Transport to a moving interface.

We now consider transport to the moving interfaces in the flows in Figures 3.1(a)–(c). The moving boundary that drives the transverse flow is unusual in that it is a mixed slip, stationary surface. In the axial direction it is stationary and presents roughly a simple shear flow near the surface, but in the transverse direction, it moves with uniform velocity. This motion creates a transverse shear flow in its vicinity: a shear flow with nonzero velocity at the wall and a negative shear rate with respect to distance from the wall. This flow can be approximated as $u_x(y) \approx u_{\text{trans}} - \dot{\gamma}_{\text{trans}} y'$ near the wall, where, y' is the distance from the wall. This shear flow term significantly complicates the solution of the governing equation, as we now have a sum of plug-like and shear-like components. If we consider the flow very near the moving boundary, say within a distance $y' \ll u_{\text{trans}} / \dot{\gamma}_{\text{trans}}$, we can assume that the plug-like component dominates and we can drop the shear-like term. We will consider the validity of this assumption by finding the approximate maximum thickness of the depleted region as compared with this condition on y'.

Proceeding with the plug flow solution from above, we take the form for $Sh(x)$ from (14), replacing Pe_{centre} with $Pe_{\text{trans}} = Pe\, u_{\text{trans}}/U$ and noting that this interface has only half the resistance to transfer compared with the centreline case above: in the centreline case, solute must cross twice the boundary layer thickness from the bulk on one side of the interface to the bulk on the other side of the interface, and therefore the form of $Sh(x)$ is twice as large at the moving reactive interface as it is at the diffusive internal interface:

$$Sh_{\text{trans}}(x) = \frac{1}{\sqrt{\pi}}\left(\frac{x}{Pe_{\text{trans}}H}\right)^{-1/2}. \tag{3.16}$$

In this case, we average across the half-width, because the smaller vortex is strong enough to contribute to the development of the depletion layer (Figure 3.1(a)). We find

$$Sh^{\infty}_{\text{trans}} = \frac{2}{W}\int_0^{W/2} Sh(x)dx = \frac{2\sqrt{2}}{\sqrt{\pi}}\left(\frac{H}{W}\right)^{1/2} Pe^{1/2}_{\text{trans}}. \tag{3.17}$$

Again we arrive at a prediction for the prefactor of $Sh^{\infty}_{\text{trans}}$ and for its scaling with Pe and u_{trans}.

In order to consider the validity of our assumption above about being sufficiently near the wall, we consider the approximate thickness of the depleted region, $\delta(x)$. For a reasonable estimate of this thickness, we take:

$$k(x) \sim \frac{D}{\delta(x)} \rightarrow \frac{\delta(W/2)}{H} \sim \frac{D}{k(W/2)H} = \frac{1}{Sh_{\text{trans}}(W/2)} = \left(\frac{\pi}{2}\right)^{1/2}\left(\frac{W}{H}\right)^{1/2} Pe^{-1/2}_{\text{trans}}. \tag{3.18}$$

In the flows considered in this study and depicted in Figure 3.1, the shear rate at the moving wall is approximately $5u_{\text{trans}}/H$. To ensure that the boundary layer does not grow thick enough to sample a region where the shear term is greater than one-tenth the size of the plug flow term, we need the following:

$$\frac{\delta(W/2)}{H} = \left(\frac{\pi}{2}\right)^{1/2}\left(\frac{W}{H}\right)^{1/2} Pe_{\text{trans}}^{-1/2} < \frac{1}{10H}\frac{u_{\text{trans}}}{\dot{\gamma}_{\text{trans}}} = \frac{1}{50},$$
$$Pe_{\text{trans}} > 50^2 \frac{\pi}{2}\frac{W}{H} \sim 4000. \tag{3.19}$$

For Pe_{trans} larger than about 4000, the region of the flow sampled by the boundary layer sees a nearly uniform plug flow with a deviation of less than 10%, and we will expect our simple plug flow arguments to hold for $Pe_{\text{trans}} > 4000$ and that (17) should provide a reasonable estimate of $Sh_{\text{trans}}^{\infty}$.

II.B.3. Summary of modified Grætz correlations.

We summarize the correlations presented here and elsewhere (Kirtland *et al* 2006) for the asymptotic Sherwood number due to the modified Grætz behaviour. The asymptotic values in Table 3.1 are expected to hold at axial distances beyond the entrance length. Within the entrance region, all interfaces that are stationary with respect to z have the same form for $Sh(z)$:

$$Sh(z) \sim \left(\frac{z}{PeH}\right)^{-1/3} \tag{3.20}$$

and interfaces that are plug-like in z have a similar form for $Sh(z)$:

$$Sh(z) \sim \left(\frac{z}{PeH}\right)^{-1/2}. \tag{3.21}$$

This allows for an estimate of the approximate entrance length by setting the Sherwood number at the transition from the entrance region equal to the value in the asymptotic region:

$$Sh(L_{\text{ent}}) \sim \left(\frac{L_{\text{ent}}}{PeH} \right)^{-m} = Sh^{\infty} \rightarrow \frac{L_{\text{ent}}}{H} \sim \left(Sh^{\infty} \right)^{-1/m} Pe. \tag{3.22}$$

Table 3.1. Predicted correlations for average Sherwood number, Sh^{∞}, at reactive and diffusive interfaces.

Reactive interface	Geometry (figure)	Form of Sh^{∞}	Flow and geometry parameters	Predicted correlation
Stationary	1(a,b)	$\frac{(3/4)^{1/3}}{\Gamma(4/3)} \left(\frac{H}{W} \right)^{1/3} \left(\frac{\dot{\gamma}_{\text{trans}} H}{u_{\text{trans}}} \right)^{1/3} Pe_{\text{trans}}^{1/3}$	$W/H = 2$ $\dot{\gamma}_{\text{trans}} \sim 0.4 u_{\text{trans}}/H$	$0.60 Pe_{\text{trans}}^{1/3}$
Moving	1(a,b)	$\frac{2\sqrt{2}}{\sqrt{\pi}} \left(\frac{H}{W} \right)^{1/2} Pe_{\text{trans}}^{1/2}$	W/H = 2	$1.13 Pe_{\text{trans}}^{1/2}$
Moving	1(c)	$\frac{2\sqrt{2}}{\sqrt{\pi}} \left(\frac{H}{W} \right)^{1/2} Pe_{\text{trans}}^{1/2}$	W/H = 1	$1.60 Pe_{\text{trans}}^{1/2}$
Centreline	1(c)	$\frac{1}{\sqrt{\pi}} \left(\frac{H}{W} \right)^{1/2} \left(\frac{u_{\text{centre}}}{u_{\text{trans}}} \right)^{1/2} Pe_{\text{trans}}^{1/2}$	$W/H = 1$ $u_{\text{trans}} \sim 6 u_{\text{centre}}$	$0.23 Pe_{\text{trans}}^{1/2}$

II.C. Requirements for the modified Grætz behaviour

With the predictions derived in the previous section for flows that have the potential to display the modified Grætz behaviour, we now consider the following questions: for a flow that demonstrates the hallmarks of the modified Grætz behaviour (departure of $Sh(Z)$ from uniaxial result at small to intermediate axial distance) what is required for the modified Grætz behaviour to hold for arbitrary axial length? For a flow that demonstrates modified Grætz behaviour at some Pe, what is required for the modified Grætz behaviour to be valid for arbitrarily large Pe?

To address these questions, we compare characteristic length scales in the flow. We start with the assumption that the flow in question has the ability to sweep the depleted fluid near the reactive interface into the bulk. If this fluid is immediately brought back to the leading edge of the reactive interface, the depletion will be reinforced and the thickness of the boundary layer will continue to grow, as in the uniaxial case. If, however, the depleted fluid remains in the bulk long enough before returning to the reactive interface that it homogenizes with the bulk, there will be no memory of the original depletion; the fluid impinging on the reactive interface will be at the local, cup-averaged concentration of the bulk. We therefore define two characteristic axial length scales: the mixing length, $L_{mix}(Pe)$, and the return length, $L_{return}(Pe)$. At a given Pe, if the flow displays modified Grætz behaviour at small to intermediate axial lengths and L_{mix} is shorter than L_{return} at that Pe, the depleted fluid will always be reconcentrated before it returns to the reactive interface and the modified Grætz behaviour will hold for arbitrarily large axial distances. If the modified Grætz behaviour holds for arbitrary axial length at some Pe and L_{mix} scales more slowly than L_{return} with Pe, then the modified Grætz behaviour will hold for arbitrarily large Pe. We now define the mixing length and return length more fully and consider how they are expected to depend on Pe.

II.C.1. Mixing length: definition and scaling.

For a diffusive scalar with a non-uniform inlet distribution, diffusion will tend to decrease the heterogeneity of concentration through flux of solute along the concentration gradients in the cross section, making the fluid more homogeneous or mixed. As a measure of the degree of mixing, we take the velocity-weighted variance of concentration in the cross section:

$$\sigma^2(z) = \frac{1}{C_{\text{cup}}\left(C_{\max} - C_{\text{cup}}\right)} \frac{1}{UA} \sum_{i=1}^{N} \left(C_i(z) - C_{\text{cup}}\right)^2 u_i A_i, \tag{3.23}$$

where the cross section has been discretized into N bins, $C_i(z)$ is the concentration in bin i, u_i is the average velocity in bin i, A_i is the area of bin i, U is the average velocity for the whole cross section, C_{cup} is the velocity-weighted average concentration for the whole cross section (as in (2)), $C_{\max}$ is the maximum inlet concentration, and A is the cross-sectional area. This measure goes from an initial value of 1 at the inlet to 0 at infinite length (complete mixing). We employ a velocity-weighted measure of mixing as opposed to the usual uniformly weighted variance because, if the fluid at a particular axial distance were sampled for some period of time, the deviations from the average concentration would contribute to the overall variance of concentration in proportion to the local axial velocity. For much the same reason, we chose the 'cup-mixing' average concentration in (2).

In order to identify the scaling of the mixing length with Pe, we plot the variance from numerical simulation versus scaled axial distance, $z/f(Pe)$, for various forms of the scaling function, $f(Pe)$; we take the $f(Pe)$ that provides the best, qualitative collapse of $\sigma^2(z/f(Pe))$ for multiple values of Pe to represent Pe-scaling of L_{mix}. For a uniaxial flow, mixing occurs purely by diffusion and the mixing length is expected to scale linearly with Pe. For an efficiently mixed flow such as the chaotic flow in Figure 3.1(a), the mixing length is expected to scale as either $\ln(Pe)$ (Ranz 1979, Villermaux and Duplat 2003, Villermaux *et al* 2008) or as a weak power law in Pe (Simonnet and Groisman 2005). The non-chaotic three-dimensional flow in Figure 3.1(b) is expected to show scaling with Pe that falls somewhere between these two extremes.

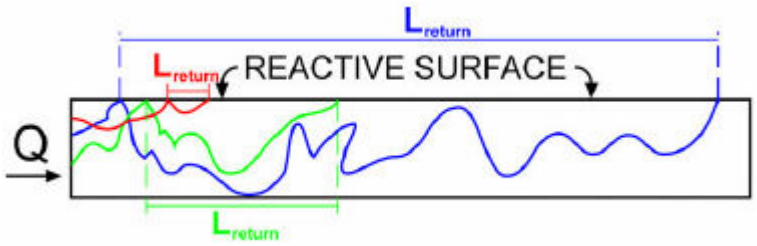

Figure 3.3. Schematic representation of the return length, L_{return}, the distance traveled between the initial and subsequent collisions with the reactive interface.

II.C.2. Return length: definition and scaling.

In determining the dependence of the return length L_{return} on Pe, we consider the trajectory of a particle of solute that has reacted at the reactive interface. We call this particle a depleton, as it represents a hole in the concentration distribution left by the depletion of fluid near the interface. The trajectory of this depleton will eventually return to the reactive interface, at which point the absence of an actual reactive particle is felt as a decrease in the available flux at the interface. The return length for a depleton is therefore defined as the axial distance between consecutive collisions with the reactive interface (see Figure 3.3). Due to the diffusive displacements of particles of solute in the flow and the non-uniformity of the three-dimensional flows considered, there is not a single, well-defined return length, but rather a distribution, as illustrated by the sample trajectories in Figure 3.3. There are some depleton trajectories that have a very short return length: these trajectories are associated with the initial depletion of the fluid as it passes near the reactive interface, *i.e.* the growth of the boundary layer, and they never actually enter the bulk. Longer return lengths correspond to depletons that have been swept into the bulk by the transverse flow, and subsequently returned to the region near the reactive interface by the transverse flow. These longer return lengths represent the part of the distribution that is relevant to the question at hand, as they correspond to the trajectories that have a chance of being mixed with the bulk before they return.

We expect L_{return} to show the same scaling with *Pe* as the axial length associated with decreasing the bulk concentration, because the transfer process that takes the depleton into the bulk and returns it to the reactive interface is the same convective process that brings unreacted solute particles from the bulk to the reactive interface. The expected scaling for a decrease in the average concentration by a factor of *e* is derived from the dependence of the concentration on axial distance and on the average Sherwood number for transport to the interface:

$$
\begin{aligned}
C(L) &= C_0 \exp\left(-\frac{\overline{Sh} L}{PeH} \right), \\
L_{1/e} &= -\frac{PeH}{\overline{Sh}_{1/e}} \ln\left(\frac{C_0 / e}{C_0} \right) = \frac{PeH}{\overline{Sh}_{1/e}}, \\
\overline{Sh}_{1/e} &= \frac{1}{L_{1/e}} \int_0^{L_{1/e}} Sh(z) dz,
\end{aligned}
\tag{3.24}
$$

where $L_{1/e}$ is the length required to decrease the concentration by a factor of *e* and $Sh_{1/e}$ is the Sherwood number averaged axially from the inlet up to length $L_{1/e}$, which, in the case of a short entrance region, can be taken as the asymptotic value of *Sh(z)*, Sh^{∞}, for transport to the interface. If $Sh^{\infty} \sim Pe^{1/3}$ as in the case of transport to a stationary interface, the return length should scale like $L_{return} \sim Pe^{2/3}$. If $Sh^{\infty} \sim Pe^{1/2}$, as in the case of transport to a moving or diffusive internal interface, the return length should scale like $L_{return} \sim Pe^{1/2}$.

III. Model and simulation details

Simulations of mass transport to interfaces were carried out by advecting diffusive tracer particles in an analytical flow field that is the approximate solution for the pressure-driven Stokes flow in a three-dimensional LDC. The basis of these

simulations is identical to that which was presented in our previous work (Kirtland *et al* 2006). The velocity field is decoupled into axial and transverse components, where the axial component is the familiar Poiseuille solution for axial flow in a duct:

$$u_z(x,y) = 1 - y^2 + 4\sum_{n=1}^{\infty} \frac{(-1)^n}{\gamma_n^3 \cosh(\gamma_n \omega)} \cosh(\gamma_n x)\cos(\gamma_n y) \tag{3.25}$$

where $\gamma_n = (2n-1)\pi/2$, and the transverse components are calculated by solving the biharmonic equation for the streamfunction in the cross section:

$$\nabla^4 \psi = 0, \quad \frac{\partial \psi}{\partial y} = u_x, \quad \frac{\partial \psi}{\partial x} = -u_y. \tag{3.26}$$

The specifics of the velocity calculations are laid out in detail elsewhere (Stroock and McGraw 2004).

For the measurements of concentration and interfacial flux, particles were seeded into the flow at the inlet and advected through a distance equivalent to 100 cycles of the modulated lid driven cavity flow shown in Figure 3.1. The initial positions were chosen to simulate the flux profile impinging on the inlet for a uniform inlet concentration in fully developed Poiseuille flow. For any given time step, the simulation integrated the velocity by use of a fifth-order Runge Kutta scheme with an adaptive time step. The velocities used in the Runge Kutta step were interpolated from a fine (512×512 or finer) grid of velocities calculated beforehand from the double Fourier expansion due to Stroock and McGraw (2004). A diffusive step was also employed by adding pseudorandom displacements in x, y and z chosen from Gaussian distributions with width $(2D\Delta t)^{1/2}$, where D is the diffusivity of the particle and Δt is the current time step.

The locations of collisions with the walls were recorded, as well as the positions in the cross section as particles reached specific axial distances (usually the end of each cycle of the mixer or an equivalent distance in uniaxial or unmodulated flows). To simulate instantaneous kinetics, each collision was taken to represent the irreversible destruction of that tracer. This information allowed for the calculation of average concentration as a function of axial distance, $C_{cup}(z)$, which was proportional to the number of unreacted particles remaining at a given axial distance, and from that data we calculated the local Sherwood number as a function of axial distance as in (3).

We also calculated concentration profiles in the cross sections as a function of axial distance by binning the unreacted tracers in the cross section to find axial convective flux; concentration within each bin was then found by dividing this flux by the average axial velocity in the bin, calculated from (3.25). The cross-sectional positions were also used for the mixing length calculations. A modification was made to the code to record multiple collisions at a given wall: a distribution of return length was generated by recording the first 100000 collisions of a tracer with each wall and analysing the distribution of distances between collisions; after each collision, we considered the particle to be a 'depleton' generated by that reaction event.

IV. Results and discussion

IV.A. Transport to stationary reactive interface

In this section, we present profiles of the concentration in the cross section of the channel and plots of the local Sherwood number, $Sh(Z)$. We also present the concentration profiles as animations to demonstrate more effectively the evolution of the boundary layer structure. In Figure 3.4 and movie 1, we show the evolution of the boundary layer for reaction at the blue (stationary) interface in the chaotically stirred flow shown in Figure 3.1(a), with ten frames during each of the first ten cycles. The

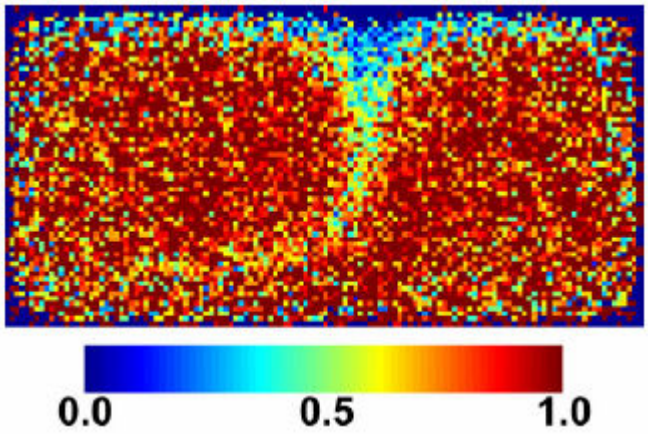

Figure 3.4. Cross-sectional concentration profile showing the structure of the depleted region at the end of the fifth cycle of the chaotically stirred flow with reaction at the blue (stationary) interface in Figure 3.1(a) with $r = 1/3$, $u_{trans} = U/5$, $L_{1/2} = 10H$, and $Pe = 10^4$. See (link to movie1.avi) for an animation of the evolution of the structure of the depleted region. Colourbar below plot shows concentration colour scale.

movie highlights the oscillating motion of the flow and how it sweeps the depleted fluid away from the reactive interface. The structure of the concentration boundary layer is well developed by the end of the first cycle, once the boundary layer has grown from the top left and right corners to the middle of the top interface. The transverse flow then sweeps the depleted fluid down into an oscillating tail and mixes it into the bulk.

The frames of all of the following animations (movies 2–4) correspond to the end of consecutive cycles in the modulated flows and corresponding axial distances in the unmodulated flows. In these movies, the concentration profiles in the modulated flows appear to be constant, despite the existence of variations throughout each cycle, as seen in movie 1. This effect is due to the fact that the profiles evolve in a periodic manner with the same period as the variations in the flow: $C(x, y, z + 2nL_{1/2}) = C(x, y, z) f(n)$ where $C(x, y, z)$ captures the periodic profile and $f(n)$ captures the asymptotic decrease in the average concentration.

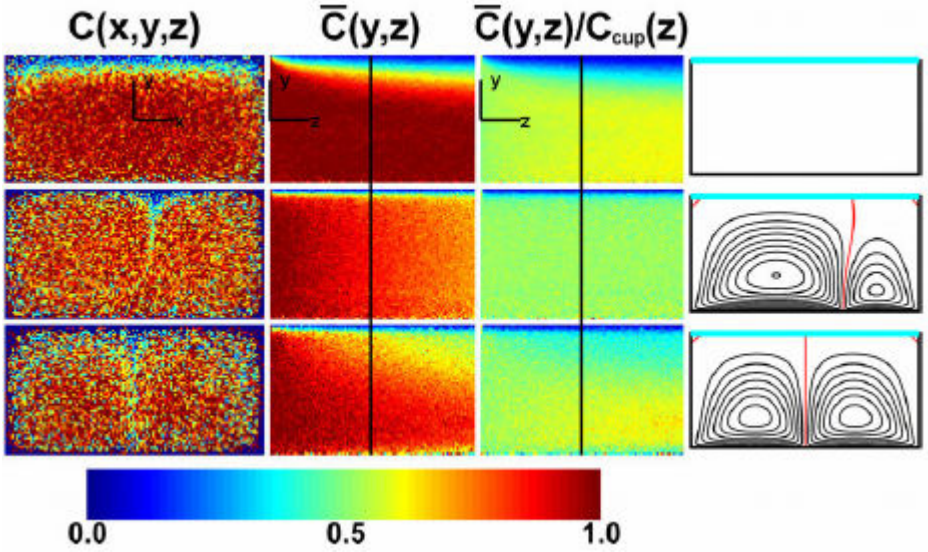

Figure 3.5. Concentration profiles as solute reacts at the blue (stationary) interface of the flows in figures 3.1(a) and (b) at $Pe = 10^5$. The flows are (from top to bottom): uniaxial; chaotically stirred with $r = 1/3$, $u_{trans} = U/5$, and $L_{1/2} = 10H$; non-chaotically stirred with $r = 1/2$ and $u_{trans} = U/5$. The first column presents the concentration, $C(x, y, z)$, in the cross section at a distance z downstream that is equivalent to fifty cycles of the mixer ($z = 100L_{1/2} = 1000H$). The second column shows the width-averaged concentration in the cross section, $C.(y, z)$, as a function of axial distance, and the black line marks the position along the length of the channel corresponding to the cross-sectional profile in the first column. The third column is equivalent to the second column normalized by the average concentration at the corresponding axial positions, $C_{cup}(z)$. The fourth column shows the streamlines of the transverse flows with the reactive interface shown in blue. See (link to movie2.avi) for an animation of the evolution of the concentration distributions. Colourbar below plot shows concentration colour scale.

As illustrated in Figure 3.5 and movie 2, more of the solute has reacted at the stationary interface at a given axial distance in the three-dimensional flows (second and third rows) than in the uniaxial flow (first row). The difference between the average concentration in the chaotic and non-chaotic flows is small relative to the difference due to the presence of a transverse flow. Figure 3.5 also shows that the transverse flows lead to an asymptotic shape of the boundary layer after a short axial distance (approximately 1 cycle = 1 frame in the movie), while the boundary layer in the uniaxial flow continues to grow throughout the length of the channel (100 frames). This is particularly clear in the third column of Figure 3.5, where we have normalized the width-averaged concentration by the bulk average concentration: with the exception of the left-most pixel (representing the initial condition) the shape of the width-averaged concentration profile is constant through the entire length of the device for the cases with transverse flow. The short entrance lengths ($L_{ent} \leq 2L_{1/2}$) in the three-dimensional flows is also consistent with our previous observations (Kirtland, 2006). Finally, we note that while the depleted region in the non-chaotic flow reconnects with the reactive boundary after circling the vortices, there is no sign of reconnection of the depleted region in the chaotic flow. The depleted fluid that is swept down through the bulk is twisted into the large vortex as the flow is modulated at the end of each half-cycle (see movie 1 at $Pe = 10^4$ to observe this process more clearly). This depleted region disappears into the bulk rather than returning directly to the reactive interface.

Figure 3.6 presents the local Sherwood number, $Sh(Z)$, as a function of scaled axial distance calculated from data such as that in Figure 3.5 and movie 2. In the case of uniaxial flow (black symbols in Figure 3.6), $Sh(Z)$ falls on a single curve for all Pe, from 10^2 to 10^6. This curve for $Sh(Z)$ at all Pe has an entrance region that shows the expected scaling of $Z^{-1/3}$, an entrance length of $L_{ent}/PeH \sim 0.06$, and an asymptotic

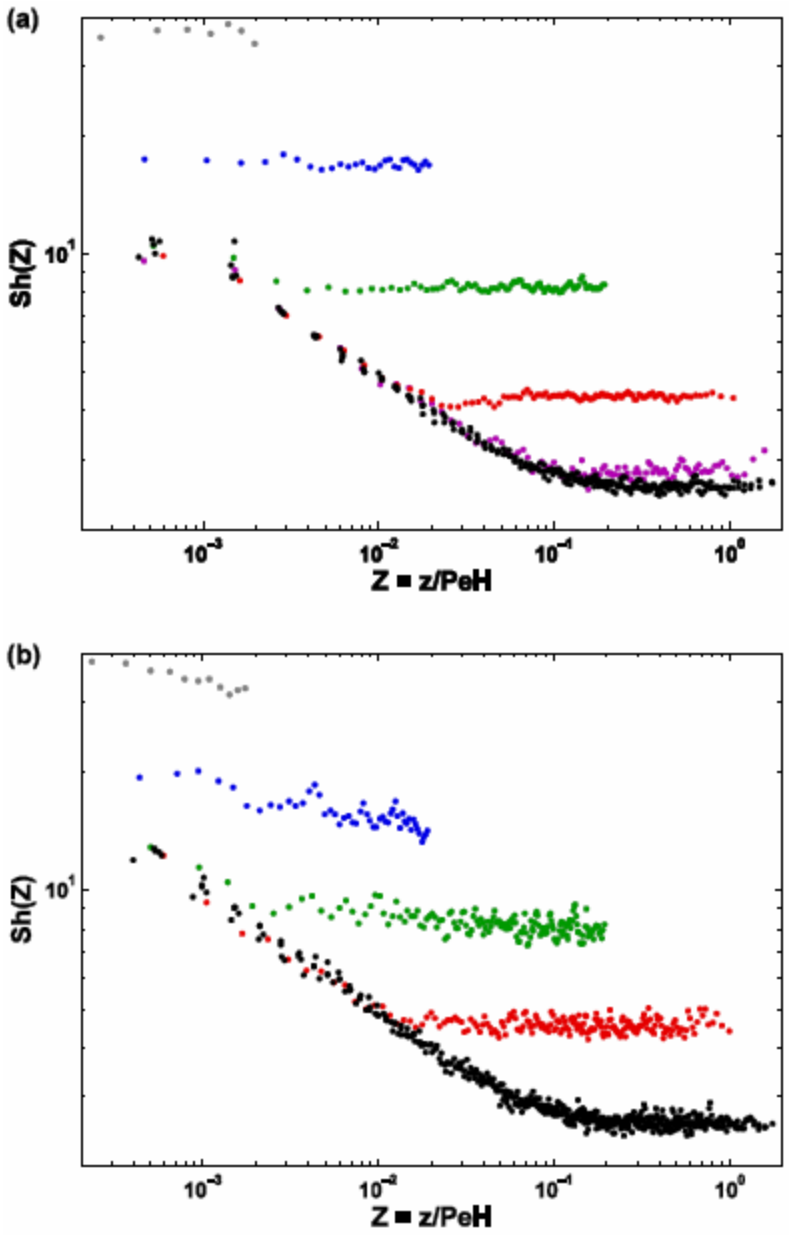

Figure 3.6. Local Sherwood number, $Sh(Z)$, as a function of scaled axial distance, $Z=z/PeH$, for transport to the blue (stationary) interface in the flow shown in Figures 3.1(a) and (b). Colours signify Pe (10^2 (purple), 10^3 (red), 10^4 (green), 10^5 (blue), 10^6 (grey)) at constant $u_{trans} = U/5$, and the black dots signify the collection of all Pe for $u_{trans} = 0$ (uniaxial Poiseuille flow). (a) Flow as in Figure 3.1(a) with r=1/3, $u_{trans} = U/5$ and $L_{1/2} = 10H$. (b) Flow as in Figure 3.1(b) with r = 1/2, and $u_{trans} = U/5$.

value of Sh^{∞}~2.55, as in Kirtland *et al* (2006). In the case of a chaotic transverse flow (coloured symbols in Figure 3.6(a)), $Sh(Z)$ has a shape similar to that of the uniaxial case, with an entrance region where $Sh(Z)$ decays and an asymptotic region where $Sh(Z)$ becomes constant. For $Pe<10^5$, the entrance region is visible and falls on the same curve as the uniaxial case, and we expect that the entrance region of the cases with $Pe > 10^5$ lie on this curve as well. We also note distinct behaviour in the presence of transverse flow: firstly, the concentration distribution reaches its asymptotic state at shorter scaled axial distances, L_{ent}/PeH as Pe increases; this short entrance length leads to a nearly constant value of $Sh(Z > L_{ent}/PeH) = Sh^{\infty}_{stat}$ through most of the length of the channel. Secondly, the value of Sh^{∞}_{stat} is Pe-dependent and can be much larger than in the uniaxial flow. The transverse flow maintains this higher rate of transfer by sweeping the depleted solution off of the reactive interface and thus maintaining a thinner depleted boundary layer, with a thickness that decreases with increasing Pe. The evenly spaced plateaus on this logarithmic plot imply a power law scaling of Sh^{∞}_{stat} with Pe, as will be confirmed in Figure 3.11.

Figure 3.6(b) presents $Sh(Z)$ for the non-chaotic flow in the third row of Figure 3.5 and movie 2. We see much the same effect due to transverse flow as was seen in Figure 3.6(a): an entrance region that collapses to the uniaxial case (visible for $Pe<10^5$) out to a scaled distance that is shorter than in the uniaxial case, followed by a Pe-dependent value of $Sh(Z)$ beyond the entrance length L_{ent}/PeH. For $Pe<10^5$, $Sh(Z)$ reaches a well-defined plateau over two orders of magnitude in axial distance, with similar values to those seen for the chaotic flow (Figure 3.6(a)). At higher Pe, $Sh(Z)$ does not plateau; rather, it continues to decrease with increasing axial distance. This decrease in $Sh(Z)$ with increasing axial distance is due to the reinforcement of the boundary layer as depleted fluid returns to the reactive interface without being mixed with the bulk, as seen in the later frames of movie 2. For $Pe<10^5$, the depleted fluid is

sufficiently reconcentrated as it circles the vortex that returns it to the surface, but for $Pe > 10^5$, mixing from the cores of the vortices to the depleted fluid surrounding the cores is too slow to reconcentrate the fluid sufficiently. While a specific value of Sh^{∞}_{stat} cannot be defined in these cases due to the continuing decrease of $Sh(Z)$, it is instructive to note that $Sh(Z)$ is similar in magnitude for the chaotic and non-chaotic flows. From a globally averaged Sherwood number or from a total integrated flux over the entire reactive interface, it is very difficult to distinguish the transport process in Figure 3.6(a) from that in Figure 3.6(b). The non-chaotic flow fails to exhibit modified Grætz behaviour for $Pe > 10^5$, but this failure is subtle in the sense that in many cases it would not even be measurable from an external, global measurement.

IV.B. Transport to moving, reactive boundary

In Figure 3.7, the evolution of the concentration profile is depicted as in Figure 3.5, but in this case solute reacts at the moving interface at the floor of the channel. The uniaxial flow presents the same behaviour that we saw in Figure 3.5 because the uniaxial case is vertically symmetric, such that transfer to the top, stationary interface (as in Figure 3.5) is equivalent to transfer to the bottom, stationary interface (as in Figure 3.7). The chaotic flow keeps the boundary layer extremely thin (on the order of one pixel) and the rate of transport to the moving interface is so high that essentially all solute has reacted within the first half of the device. This high rate of transfer is due to both the magnitude and the plug-like character of the velocity at the interface. The non-chaotic flow looks quite similar initially, but as the depleted fluid encircles the vortices and returns to the reactive interface, the depletion is reinforced and the boundary layer continues to grow thicker with axial distance. A region of high concentration persists at the core of each vortex; these regions are not convectively connected to the depleted fluid outside of the core and thus cannot be efficiently

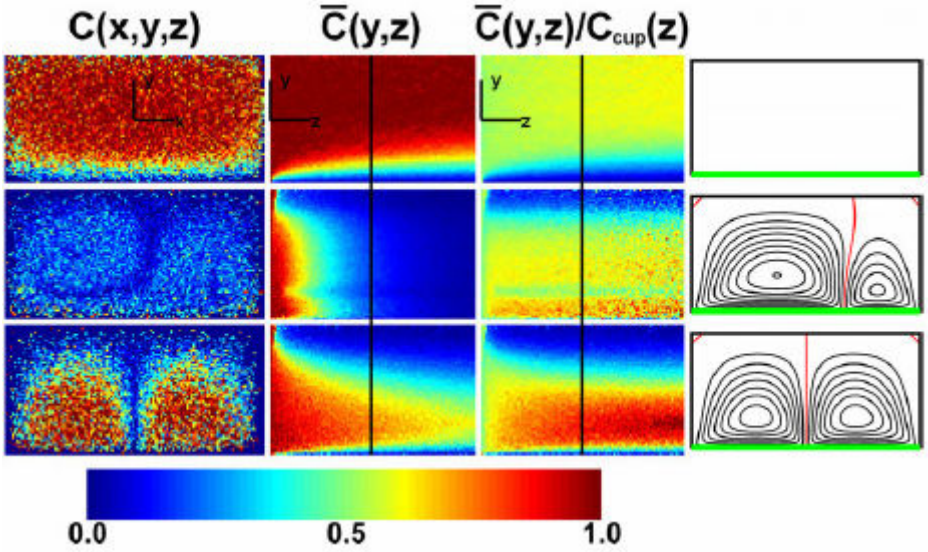

Figure 3.7. Concentration profiles as solute reacts at the green (moving) interface of the flows in Figures 3.1(a) and (b) at $Pe = 10^5$. The flows are (from top to bottom): uniaxial; chaotically stirred with $r = 1/3$, $u_{trans} = U/5$, and $L_{1/2} = 10H$; non-chaotically stirred with $r = 1/2$ and $u_{trans} = U/5$. The first column presents the concentration, $C(x, y, z)$, in the cross section at a distance z downstream that is equivalent to fifty cycles of the mixer ($z = 100L_{1/2} = 1000H$). The second column shows the width-averaged concentration in the cross section, $C(y, z)$, as a function of axial distance, and the black line marks the position along the length of the channel corresponding to the cross-sectional profile in the first column. The third column is equivalent to the second column normalized by the average concentration at the corresponding axial positions, $C_{cup}(z)$. The fourth column shows the streamlines of the transverse flows with the reactive interface shown in green. See (link to movie3.avi) for an animation of the evolution of the concentration distributions. Colourbar below plot shows concentration colour scale.

mixed with the depleted fluid. Both the chaotic and non-chaotic flows send the newly depleted fluid to the region near the far wall, producing what is effectively an inverted boundary layer: the transverse flow moves the depleted solution away from the reactive interface to form a depleted zone near the far, non-reactive boundary; this zone is similar in shape to the usual boundary layer formed when solute reacts at the stationary interface. This inversion has the effect of keeping the concentrated fluid near the bottom reactive interface, thereby increasing transfer to the surface. The chaotic flow distinguishes itself by twisting the oscillating tail of depleted solution seen in Figure 3.4 (of similar shape in Figures 3.5 and 3.7) into the bulk rather than allowing it to reconnect to the surface as it does in the non-chaotic flow. The concentration profile in the chaotic flow again reaches an asymptotic shape within the first several cycles, as is evident in the normalized side view. In the non-chaotic flow, the boundary layer near the reactive interface and the inverted boundary layer near the ceiling both continue to grow thicker through the length of the device. The asymptotic state in the non-chaotic flow is reached only once the boundary layer near the reactive interface has grown thick enough to reach the core of the vortices, similar to the standard Grætz behaviour in the uniaxial case.

Figure 3.8 presents $Sh(Z)$ as a function of scaled axial distance for transport to the moving interface as shown in Figure 3.7 and movie 3. The behaviour observed in Figure 3.8(a) in the presence of chaotic transverse flow shares several important features with the results of Figure 3.6(a) for transport to the stationary interface. The entrance region again lies on the curve for uniaxial flow, although, due to significantly higher rates of transfer at the moving interface, this collapse onto the uniaxial curve is only visible for $Pe = 10^2$. Again we expect $Sh(Z)$ in the entrance region to fall on the uniaxial curve for all Pe. Plots at very short axial length show agreement with this supposition, although the data are very noisy at such small distances, and one must

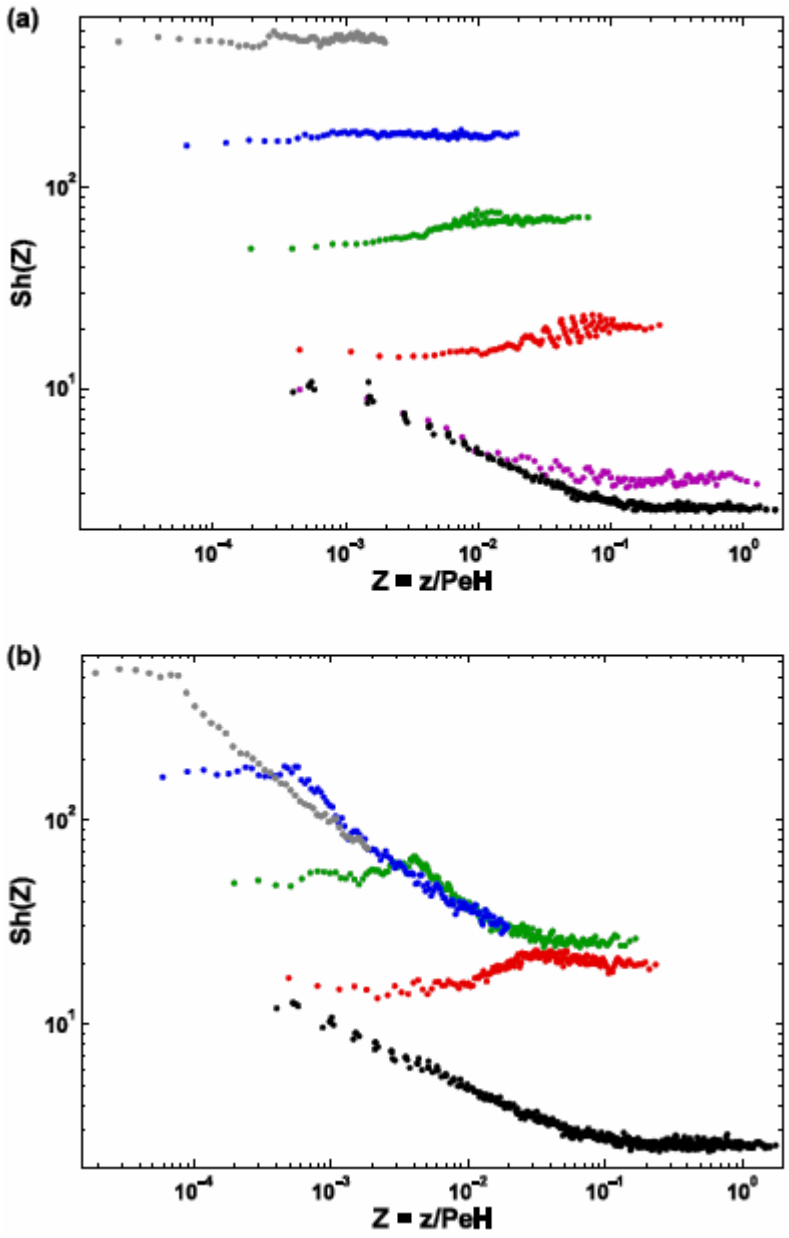

Figure 3.8. Local Sherwood number, $Sh(Z)$, as a function of scaled axial distance, $Z = z/PeH$, for transport to the green (moving) interface in the flow shown in Figures 1(a) and (b). Colours signify Pe (10^2 (purple), 10^3 (red), 10^4 (green), 10^5 (blue), 10^6 (grey)) at constant $u_{trans} = U/5$, and the black dots signify the collection of all Pe for $u_{trans} = 0$ (uniaxial Poiseuille flow). (a) Flow as in Figure 3.1(a) with r=1/3, $u_{trans} = U/5$, and $L_{1/2} = 10H$. (b) Flow as in Figure 3.1(b) with $r = 1/2$, and $u_{trans} = U/5$.

infer by the overlap of the scattered data that they exhibit the same behaviour. Assuming this behaviour, the scaled entrance length can be inferred from the graphs, and is again a function of *Pe*, which decreases with increasing *Pe*. The asymptotic value of the Sherwood number, Sh^{∞}_{trans}, again increases with increasing *Pe*. As compared with Figure 3.6(a), however, the inferred L_{ent}/PeH decreases and Sh^{∞}_{trans} increases significantly more quickly with increasing *Pe* than in the case of transport to the stationary interface. This stronger dependence on *Pe* leads to very large values for Sh^{∞}_{trans} at high *Pe*, nearly 20 times larger than Sh^{∞}_{stat} and over 200 times larger than the asymptotic value in the absence of transverse flow.

We note several peculiarities in the curves in Figure 3.8(a). All of the curves show some local variations in $Sh(Z)$ that deserve comment.We attribute the non-periodic variations early in the entrance region and around the asymptotic value to the finite number of reaction events in these regions: the smoothness of the evaluation of $Sh(Z)$ as in (3) is limited by the total number of particles and by the number of points at which $Sh(Z)$ is evaluated. We also note coherent oscillations (*e.g.* $Pe = 10^3$ and 10^4 in Figure 3.8(a)) and a significant rise in the average value of $Sh(Z)$ for transport to the moving interface above the initial plateau (again for $Pe = 10^3$ and 10^4 in Figure 3.8(a)). The spatial frequency of the oscillations equals the length of a halfcycle and arises due to an oscillation in the concentration of fluid that is swept down toward the reactive interface. The rise in $Sh(Z)$ at large axial distance is attributable to the inverted boundary layer that forms in the case of a moving reactive interface, as discussed above in reference to Figure 3.7: the persistent region of low concentration that forms opposite the reactive boundary significantly affects the average bulk concentration, C_{cup}, used in calculating $Sh(Z)$ as in (3). Yet, it is the difference between the concentration just outside the boundary layer and the concentration at the reactive interface itself that drives transfer; as the inverted boundary layer develops,

this concentration becomes larger than C_{cup} and leads to the rise in $Sh(Z)$ to a second plateau. The value of $Sh(Z)$ on the earlier plateau, before this rise in $Sh(Z)$, is the value that will be tested in Figure 3.11 against the theory presented in Section II.B.2, because the theoretical development lacks this detailed accounting for the actual shape of the concentration profile. This effect provides interesting insight for the design of flows for rapid transfer to a reactive interface: if a flow sends depleted fluid to a region far from the reactive interface, thereby maintaining a higher concentration just outside the boundary layer near the reactive interface relative to the bulk average concentration, transfer will be faster than in a flow with a similar surface process that immediately mixes its depleted fluid into the bulk (as in the case of the stationary boundary in Figures 3.5 and 3.6). Indeed, the ideal flow would deplete the fluid near the reactive interface quickly and completely and then send that depleted fluid as far from the surface as possible, such that it only returns to the reactive interface once the entire bulk has passed near the surface and been depleted to a similar extent.

For the case of transport to the moving interface, there are again similarities and differences between the chaotic (Figure 3.8(a)) and non-chaotic flows (Figure 3.8(b)). For the first few equivalent cycle lengths ($z<60H$), the curves in Figure 3.8(b) are nearly identical to those in Figure 3.8(a): $Sh(Z)$ appears to reach the same asymptotic values in the non-chaotic flow as it did in the chaotic flow. But, for $z > 60H$, all curves collapse onto a new Pe-independent curve for $Sh(Z)$ in the non-chaotic flow, which decays with increasing axial distance to an asymptotic value that is an order of magnitude larger than the uniaxial case. As in Figure 3.6(b) for transport to the stationary interface, this decrease is due to the reinforcement of the boundary layer after depleted fluid has circled the vortices and returned to the reactive interface. Because the transfer to the moving interface is so much more efficient than that to the stationary interface, the depleted fluid that returns to the interface is significantly more

depleted and results in a larger reinforcement. It is important to note, however, that the final plateau in $Sh(Z)$ for the non-chaotic flow is still significantly larger than that for uniaxial flow. This increase is due to two factors: firstly, the flow near the moving interface is much more conducive to transport than the stationary boundary in the uniaxial case. Secondly, the final thickness of the boundary layer only extends to the cores of the vortices, rather than through the full depth of the channel; this distance is still independent of Pe, however, so we expect that all Pe will eventually collapse to this final plateau value. This collapse to a Pe-independent $Sh(Z)$ again demonstrates a failure of the modified Grætz behaviour in the non-chaotic flow, as noted in reference to Figure 3.6(b). The overall Sherwood number for transport to the moving interface averaged over the entire device will be much smaller than in the chaotic case, due to the fact that $Sh(Z)$ decreases by an order of magnitude or more due to the reinforced depletion seen in Figure 3.7.

The strong oscillations in $Sh(Z)$ for the chaotic flow in Figure 3.8(a) are absent for the nonchaotic flow in Figure 3.8(b); this observation supports the idea that the oscillations are connected to the modulation of the chaotic flow. We again observe the rise in $Sh(Z)$ for $Pe = 10^3$ at large axial distance, with a nearly identical shape to that in Figure 3.8(a).We again attribute this increase to the formation of an inverted boundary layer (as seen in Figure 3.7 and movie 2). This increase in $Sh(Z)$ only appears at $Pe = 10^3$ because for $Pe > 10^4$, the asymptotic value of $Sh(Z)$ approaches the Pe-independent curve for the non-chaotic flow, which has a lower asymptotic value than the corresponding value of $Sh_{\text{trans}}^{\infty}$ for the chaotic flow.

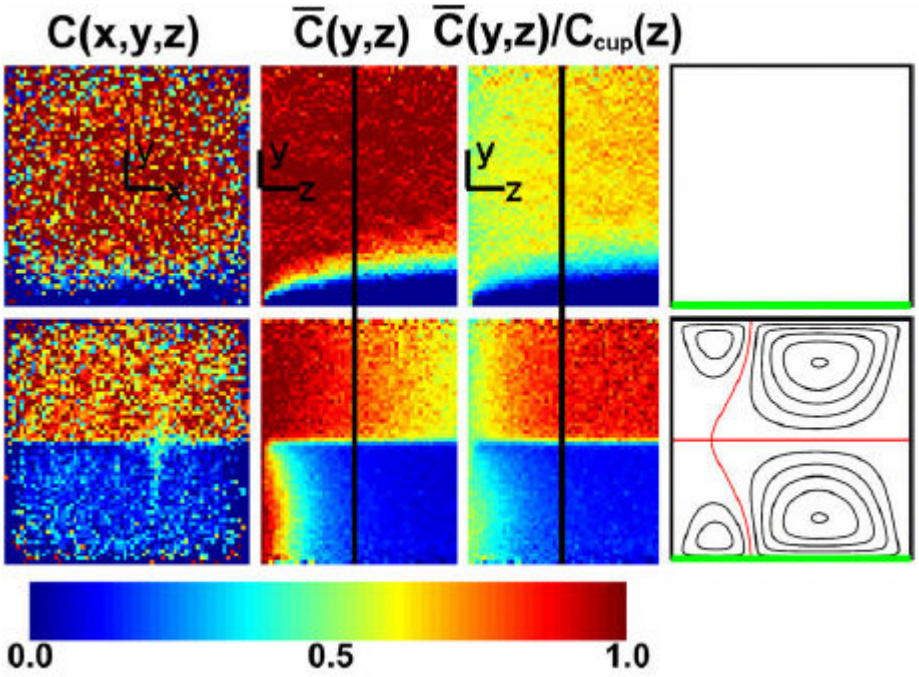

Figure 3.9. Concentration profiles as solute reacts at the green (moving) interface of the flow in Figure 3.1(c) at $Pe = 10^5$. The flows are (from top to bottom): uniaxial; chaotically stirred with $r = 1/3$, $u_{trans} = U/5$ and $L_{1/2} = 10H$. The first column presents the concentration, $C(x, y, z)$, in the cross section at a distance z downstream that is equivalent to twenty-five cycles of the mixer ($z = 50L_{1/2}=500H$). The second column shows the width-averaged concentration in the cross section, $C(y, z)$, as a function of axial distance, and the black line marks the position along the length of the channel corresponding to the cross-sectional profile in the first column. The third column is equivalent to the second column normalized by the average concentration at the corresponding axial positions, $C_{cup}(z)$. The fourth column shows the streamlines of the transverse flow with the reactive interface shown in green. See (link to movie4.avi) for an animation of the evolution of the concentration distributions. Colourbar below plot shows concentration colour scale.

IV.C. Transport to moving interfaces with simultaneous transport across diffusive internal interfaces

Figure 3.9 shows the evolution of the concentration profile in a vertically symmetric flow, driven by a slipping boundary at the ceiling and floor as in Figure 3.1(c). The uniaxial case looks similar to the analogous cases in Figures 3.5 and 3.7. The entire device remains in the entrance region; the boundary layer continues to grow for the entire length of the channel. In the chaotic flow, the depletion of solute proceeds in two steps: firstly, transfer of solute to the bottom reactive interface rapidly depletes the lower half of the channel, and the concentration drops to a small, nearly constant value; secondly, once a significant gradient exists between the top and bottom halves, transfer from top to bottom slowly depletes the top half. We note that the normalized side view demonstrates the convergence of the concentration profile in the chaotically stirred flow within the first ten cycles of the device, after which the concentration profile is self-similar and continues to decay in magnitude with increasing axial distance.

Figure 3.10 shows the dependence of the local Sherwood number on scaled axial distance for transport to the moving interface in the chaotic flow shown in Figure 3.9 and movie 4. As discussed above, transfer of solute to the bottom interface proceeds in two steps: firstly, the bottom half of the channel empties due to a rapid transfer process to the moving interface. This process defines the first plateau (at short axial distance) for each value of *Pe* in Figure 3.10 This plateau corresponds to the asymptotic value of $Sh(Z)$ predicted in Table 3.1 for transport to the moving interface in a duct of square cross section. This step is similar to the transfer to the moving boundary in the channel of lower aspect ratio (Figure 3.1(a)), and, as such, the early behaviour of $Sh(Z)$ shares some important features with Figure 3.8(b), with slightly higher plateau values due to the difference in geometry. Secondly, after an axial

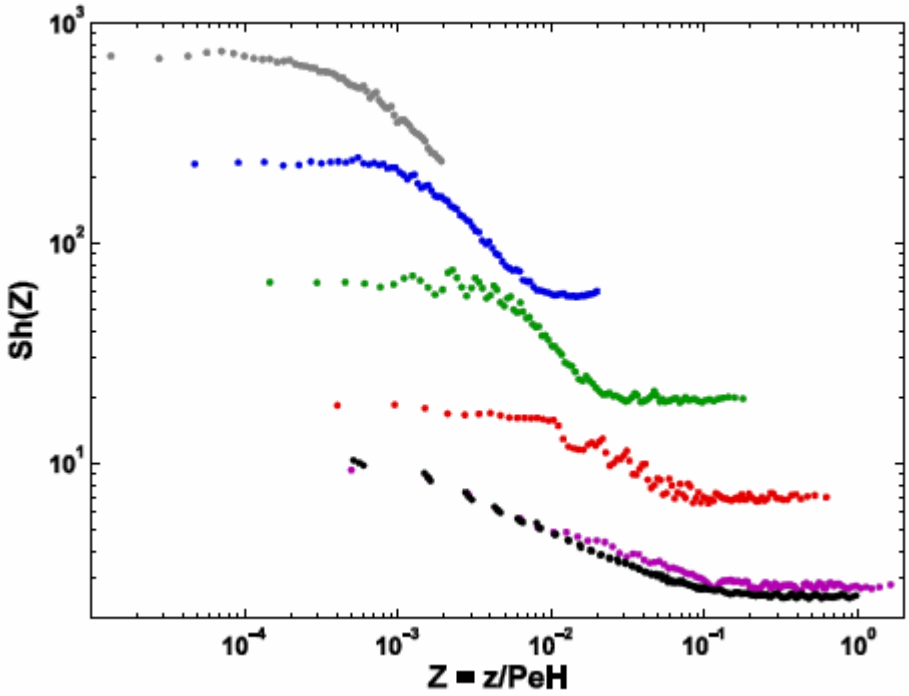

Figure 3.10. Local Sherwood number, $Sh(Z)$, as a function of scaled axial distance, $Z = z/PeH$, for transport to the green (moving) interface in the flow shown in Figure 3.1(c) with $r = 1/3$, $u_{trans} = U/5$ and $L_{1/2} = 10H$. Colours signify Pe (10^2 (purple), 10^3 (red), 10^4 (green), 10^5 (blue), 10^6 (grey)) at constant $u_{trans} = U/5$, and the black dots signify the collection of all Pe for $u_{trans} = 0$ (uniaxial Poiseuille flow).

distance, $z \cong 40H$, the top half of the channel empties slowly, as solute passes through both the diffusive internal interface defined by the plane of symmetry and the fluid-solid interface at the bottom, moving boundary. After this transition, $Sh(Z)$ drops to a second, lower plateau; the two transfer steps in series—at the symmetry plane and at the fluid-solid boundary—define this asymptotic value.

The behaviour of $Sh(Z)$ for transport to the reactive interface in a uniaxial flow with square cross section, shown in black in Figure 3.10, demonstrates collapse for all Pe and an asymptotic value that is the same as that in the rectangular cross section with aspect ratio of $W/H = 2$. The data for $Sh(Z)$ for transport to the moving interface at $Pe = 10^2$ show an entrance region that falls on this curve as well, and so we conjecture that all values of Pe demonstrate the same entrance region behaviour at sufficiently short axial distances. The oscillations seen in Figure 3.8(a) also appear in Figure 3.10 for the chaotically stirred flow at $Pe = 10^3$ and 10^4. The appearance of these oscillations makes sense as this flow is modulated, as explained for Figure 3.8 above. The rise in $Sh(Z)$ that is seen in the presence of both transverse flows in Figures 3.8(a) and (b) is absent here. As the depleted fluid is swept slowly near the centreline, transport across the centreline reconcentrates this fluid, leading to a more uniform concentration in the lower half of the channel than that which is present in the flow driven by only the bottom boundary; the inverted boundary layer does not form.

IV.D. Asymptotic values of Sherwood number and comparison to predicted correlations

Before moving on to compare the results for Sh^{∞} from Figures 3.6, 3.8 and 3.10 with the predictions in Table 3.1, we must consider how the final asymptotic value in Figure 3.10 is related to the Sherwood number at the centreline, $Sh^{\infty}_{\text{centre}}$. The process that defines the final asymptotic value of $Sh(Z)$ is a combination of $Sh^{\infty}_{\text{centre}}$ and

$Sh^{\infty}_{\text{trans}}$ from Table 3.1. The usual way to combine such processes is to apply the analogy of resistances in series, where the resistance to each transport process is the inverse of the Sherwood number for that process (Bird *et al* 1960). We note, however, that $Sh^{\infty}_{\text{trans}}$ is defined in terms of the difference in concentration across the centreline while $Sh^{\infty}_{\text{trans}}$ is defined in terms of the difference between the concentration in the lower half of the channel and the concentration at the reactive interface. The overall effective Sherwood number, $Sh^{\infty}_{\text{overall}}$, is defined in terms of the overall average concentration in the entire cross section. By equating the expressions for flux at the reactive interface due to transport out of the lower half by $Sh^{\infty}_{\text{trans}}$, due to transport out of the entire bulk by $Sh^{\infty}_{\text{overall}}$, and due to transport from the upper half to the reactive interface across the equivalent resistance imposed by $Sh^{\infty}_{\text{centre}}$ and $Sh^{\infty}_{\text{trans}}$, we have

$$Sh^{\infty}_{\text{trans}} C_{\text{lower}} = Sh^{\infty}_{\text{overall}} C_{\text{total}} = Sh^{\infty}_{\text{overall}} \frac{\left(C_{\text{upper}} + C_{\text{lower}}\right)}{2} = \frac{Sh^{\infty}_{\text{centre}} Sh^{\infty}_{\text{trans}}}{Sh^{\infty}_{\text{centre}} + Sh^{\infty}_{\text{trans}}} \left(C_{\text{upper}} - C_{\text{lower}}\right). \tag{3.27}$$

After some algebraic manipulation and inserting the predictions from Table 3.1 for $Sh^{\infty}_{\text{centre}}$ and $Sh^{\infty}_{\text{trans}}$, we find that

$$Sh^{\infty}_{\text{overall}} = \frac{2Sh^{\infty}_{\text{centre}} Sh^{\infty}_{\text{trans}}}{2Sh^{\infty}_{\text{centre}} + Sh^{\infty}_{\text{trans}}} \sim 0.38 Pe^{1/2} \tag{3.28}$$

and this $Sh^{\infty}_{\text{overall}}$ is the value that is measured by the second set of plateaus in Figure 3.10.

Figure 3.11 presents the asymptotic values of the Sherwood numbers, Sh^{∞} extracted from the data in Figures 3.6, 3.8 and 3.10. This summary allows us to demonstrate the relative magnitudes of Sh^{∞} for the various cases, and to evaluate the

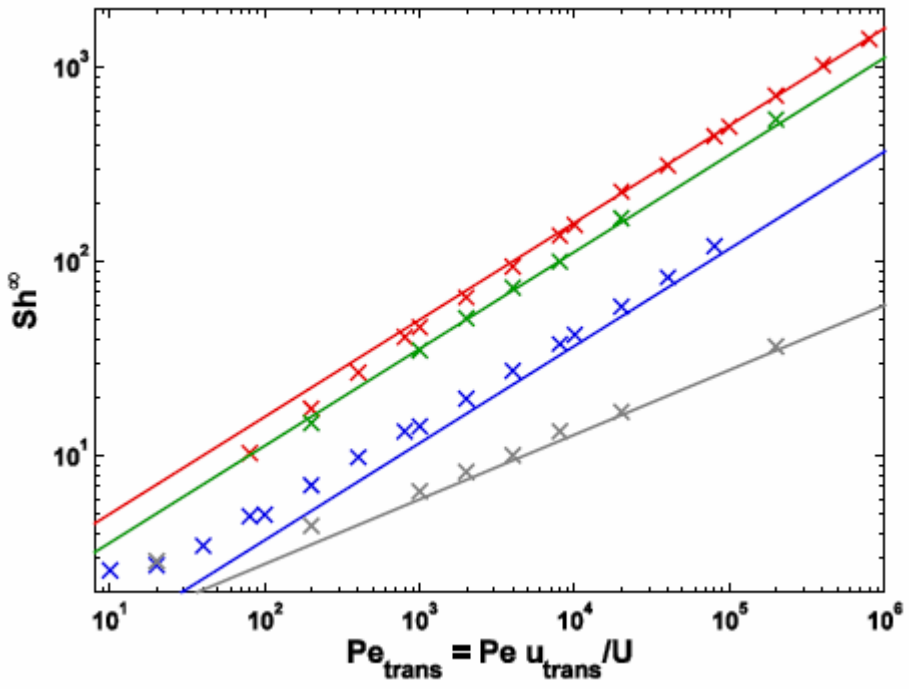

Figure 3.11. Combined results for the asymptotic value of the Sherwood number, Sh^{∞}, for various flows, and predicted correlations from Table 1. Colours: red— first plateau for transport to the green (moving) interface as in Figure 3.1(c), $Sh^{\infty}_{\text{trans}} \sim 1.6\, Pe^{1/2}_{\text{trans}}$; green—transport to the green (moving) interface as in Figure 3.1(a), $Sh^{\infty}_{\text{trans}} \sim 1.13\, Pe^{1/2}_{\text{trans}}$; blue—second plateau for transport to the green (moving) interface as in Figure 3.1(c), $Sh^{\infty}_{\text{overall}} \sim 0.38\, Pe^{1/2}_{\text{trans}}$; grey—transport to the blue (stationary) interface as in Figure 3.1(a), $Sh^{\infty}_{\text{stat}} \sim 0.6\, Pe^{1/3}_{\text{trans}}$.

success of the predicted correlations in Table 3.1. All of the data show good agreement in scaling with the predicted correlations at high Pe_{trans}. The data for Sh^{∞}_{trans} for transport to the moving interface in the flows in Figures 3.1(a) and (c) also show excellent agreement in their prefactors (within 2%). The data for Sh^{∞}_{trans} in the flow in Figure 3.1(c) begin to fall off of the predicted correlation for $Pe_{trans}<10^4$, which was also predicted due to the influence of the shear-like component of the velocity at the moving boundary as the boundary layer grows thick enough to sample the shear flow (see Section II.B.2). The data for Sh^{∞}_{stat} and $Sh^{\infty}_{overall}$ exceed the predicted correlations by about 8 and 12%, respectively at high Pe_{trans}. For $Pe_{trans}<10^3$ both Sh^{∞}_{stat} and $Sh^{\infty}_{overall}$ exceed their respective correlations by increasing amounts with decreasing Pe_{trans}. The plateau in the uniaxial case (Sh^{∞}~2.55) is a lower bound on the possible values of $Sh(Z)$ for all flows in these geometries and therefore Sh^{∞}_{stat} and $Sh^{\infty}_{overall}$ cannot decrease beyond Sh^{∞}~2.55 as Pe_{trans} decreases.

IV.E. Mixing length, return length, and the modified Grætz behaviour

We now present results for the mixing length and return length in the flows in Figures 3.1(a) and (b) and discuss the implications of these results on the ability of flows to sustain high rates of mass transfer associated with the modified Grætz behaviour.

In Figure 3.12, we test the scaling of the mixing length with Pe by scaling the axial distance of the curves of the axial velocity-weighted variance of concentration as defined in (23) for flows with an initial concentration difference between two streams of equal area in the cross section. The inlet concentration condition in each case consists of a stream of uniform high concentration occupying the upper half of the channel and a stream of zero concentration occupying the lower half of the channel; this initial distribution is representative of the distributions that are generated by

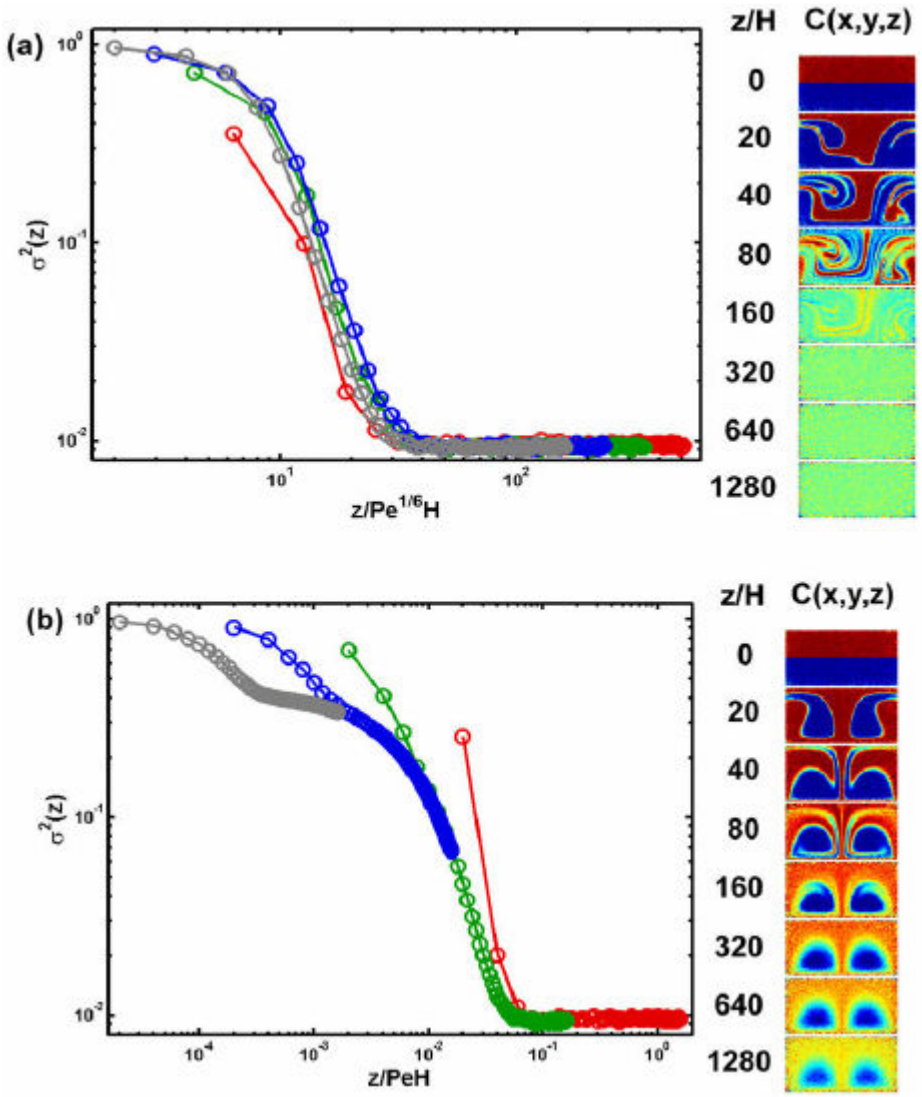

Figure 3.12. Decay of velocity weighted variance (3.23) with scaled axial distance for determination of scaling of mixing length with *Pe*: (a) chaotically stirred flow as in Figure 3.1(a) with $r = 1/3$, $u_{trans} = U/5$; $L_{1/2} = 10H$ with axial distance scaled by $Pe^{1/6}$; (b) non-chaotically stirred flow as in Figure 3.1(b) with $r = 1/2$, $u_{trans} = U/5$ with axial distance scaled by *Pe*. Colours signify *Pe* (10^3 (red), 10^4 (green), 10^5 (blue), 10^6 (grey)). Representative concentration profiles as a function of axial distance at $Pe = 10^5$ are shown to the right.

reaction at the top or bottom interface. By scaling the axial distance by power laws in *Pe* with scaling exponents between 0 and 1, as well as by ln(*Pe*), we have found reasonable estimates of the dependence of mixing length on *Pe*. Figure 3.12(a) shows the result of scaling the axial distance in the chaotically stirred flow in Figure 3.1(a) by $Pe^{1/6}$. This scaling provides notably better collapse than ln(*Pe*), that was expected due to Ranz (1979) and Villermaux *et al* (2008). Scaling by ln(*Pe*) causes the curves for various *Pe* to have similar shapes, *i.e.* similar curvatures and slopes, but the curves do not coincide or collapse to any significant extent. We conclude that this weak power law is a better representation of the scaling of the mixing length based on this velocity-weighted measure of mixing. The concentration profiles to the right in Figure 3.12(a) show the mixing process at $Pe = 10^5$.

For the non-chaotic flow in Figure 3.1(b), the mixing curves in Figure 3.12(b) demonstrate that mixing occurs by a process involving two steps that occur in series and present distinct scaling with respect to *Pe*. These two distinct processes can be seen qualitatively in the concentration profiles to the right of Figure 3.12(b), where the transition between the two regimes occurs in the vicinity of $z/H = 160$. The early process mixes the cores of the vortices and the exteriors of the vortices separately without significant mixing between these two regions. This process is analogous to the mixing of the depleted fluid from the boundary layer throughout the exterior of the vortices in the nonchaotic flow; this portion of the curves collapses when plotted against $z/Pe^{1/3}$ (characteristic of transfer across a shear flow). The second process is responsible for mixing the fluid in the cores of the vortices with the fluid outside of these cores. This second process is much slower than the initial process, with a mixing length that scales linearly with *Pe*, as demonstrated in Figure 3.12(b). It is this second process on which we depend for mixing of the high concentration fluid in the cores of the vortices with the depleted fluid that has been swept off of the reactive interface;

therefore the scaling of the relevant mixing process for transport to reactive interfaces in the non-chaotic flow is linear in *Pe*.

To determine the scaling of return length with *Pe* for a given flow, we injected a tracer particle into the flow and recorded the axial positions of its first 100000 collisions with each reactive interface. Return length is defined as the axial distance traversed between subsequent collisions (Figure 3.3). The distributions of return lengths were calculated and plotted, as shown in Figures 3.13(a) and (b). The distribution of return lengths for returning to the stationary interface in the chaotic and non-chaotic flows are continuous, relatively smooth and both have the same general features, as seen at $Pe = 10^4$ in Figure 3.13(a): an initial decay of short distance return lengths (this segment of the histogram contains most of the calculated trajectories), a minimum at intermediate return length, and a wide peak of long return lengths. The initial decays are nearly identical for both cases; the minima occur at similar return length, and the peak of long return lengths are of essentially the same shape. The initial decay corresponds to the growth of the boundary layer, wherein a particle collides with the reactive interface many times while remaining near the interface. This behaviour is seen in trajectories of particles that have clusters of short return lengths; they appear to skip across the interface like a rock skipping across the surface of a lake. When the particle is pulled away from the reactive interface into the bulk of the flow, there is a decrease in the probability of encountering the interface until the flow brings the particle back around to the interface again. This decrease in the probability of collision corresponds to the minimum in the distribution of return lengths. Finally, the wide peak after this minimum corresponds to the distribution of return lengths that involve a trip into the bulk prior to returning. We are interested in the ability of the flow to mix fluid that has been removed from the reactive interface before it returns from the bulk to the interface, and accordingly we only use the return

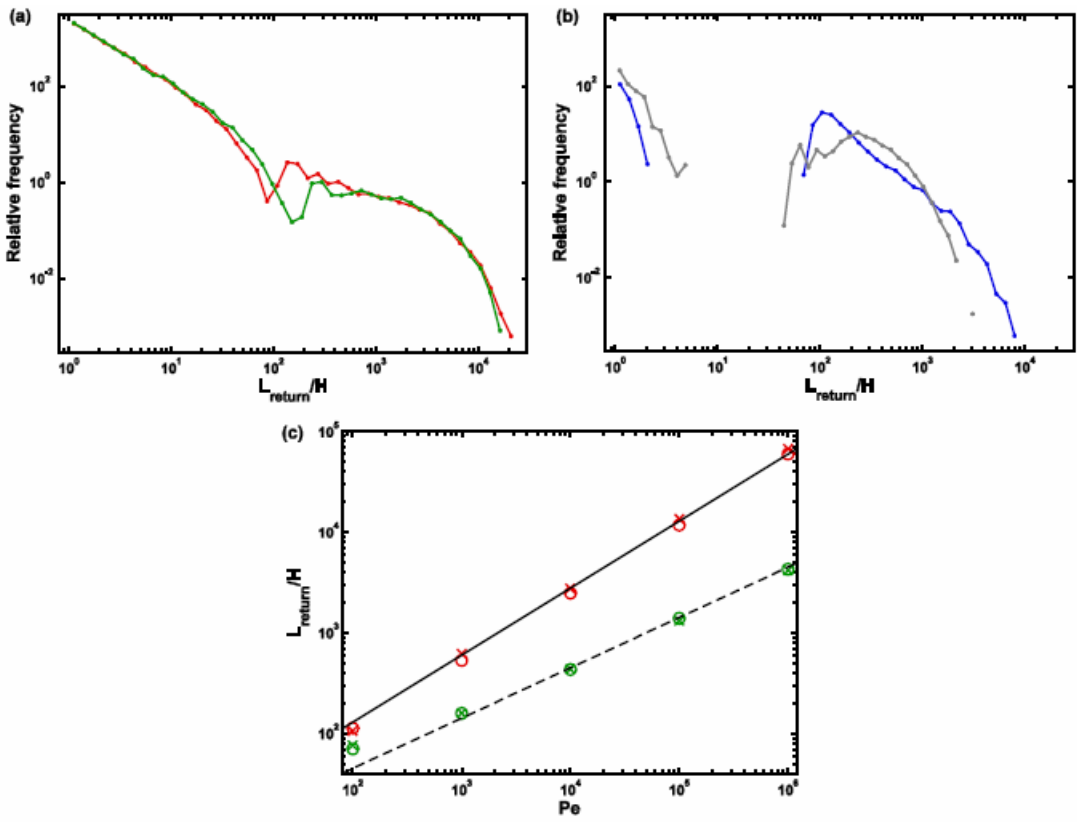

Figure 3.13. Dependence of return length on *Pe*. (a) Distribution of return lengths as defined in Figure 3.3 for particles returning to the blue (stationary) reactive interface in the flow shown in Figures 3.1(a) and (b) with $Pe = 10^4$: (red curve) r=1/2, $u_{trans} = U/5$; (green curve) $r = 1/3$, $u_{trans} = U/5$, $L_{1/2} = 10H$. (b) Distribution of return lengths as defined in Figure 3.3 for particles returning to the green (moving) reactive interface in the flow shown in Figures 3.1(a) and (b) with $Pe = 10^4$: (blue curve) $r = 1/2$, $u_{trans} = U/5$; (grey curve) $r = 1/3$, $u_{trans} = U/5$, $L_{1/2} = 10H$. (c) Dependence of characteristic return length on *Pe* for return to the reactive interface: (crosses) $r = 1/3$, $u_{trans} = U/5$, $L_{1/2} = 10H$; (circles) $r = 1/2$, $u_{trans} = U/5$. Colours: (red symbols) return to the blue (stationary) interface; (green symbols) return to the green (moving) interface; solid line = $6Pe^{2/3}$; dashed line = $4.5Pe^{1/2}$.

lengths beyond the minimum in the distribution to calculate the characteristic return lengths that are plotted in Figure 3.13(c).

Figure 3.13(b) shows the distribution of return lengths for a particle returning to the green, (moving) reactive interface in Figures 3.1(a) and (b). Again the distributions for particles in the chaotic and non-chaotic flows are quite similar to each other, although the features of the distributions are somewhat different from those in Figure 3.13(a). The distributions have an initial decay that corresponds to the growth of the boundary layer as in Figure 3.13(a). This portion of the distribution contains far fewer of the return lengths than the initial decay for return to the stationary surface. The time spent traversing the interface is much smaller, leaving less time during which to collide with the surface before being swept into the bulk. The minima in the distributions of return lengths, in this case, become gaps; no trajectories in our sample had return lengths larger than the initial decay but smaller than the final peak. While it is possible to spend multiple cycles near the stationary interface without being swept definitively into the bulk, the transverse flow always sweeps particles near the moving interface away within one half-cycle of the mixer due to the magnitude of velocities and the length of the half cycle. The distributions again show a wide peak at large return length, and we use this portion of the distribution for calculation of the characteristic lengths plotted in Figure 3.13(c) as stated above.

The characteristic return lengths plotted in Figure 3.13(c) demonstrate scaling of $Pe^{2/3}$ for return to the stationary interface and $Pe^{1/2}$ for return to the moving interface. These results validate the simple arguments in Section II.C.2 and in (24) based on the behaviour of the average concentration at long axial distance and its relation to the Sherwood number for transport to the reactive interface. The chaotic character of the flow has essentially no effect on the characteristic return length.

We can now consider the ability of the flows considered here to maintain high rates of mass transfer in the framework of the modified Grætz behaviour out to arbitrary axial lengths and values of *Pe*. The chaotic flow in Figure 3.1(a) presents modified Grætz behaviour in the ranges of *Pe* and of axial distances considered in this work for transfer to both stationary and moving interfaces (Figures 3.6(a) and 3.8(a)). Based on the discussion in Section II.C, this observation implies that, at each *Pe* considered, the mixing length is shorter than the return length, such that the depleted fluid is mixed with the bulk before returning to the reactive interface. Thus, for all *Pe* considered in this work, we predict that the chaotic flow will behave according to the modified Grætz behaviour out to arbitrarily large axial distances. Having shown that the return length scales more strongly than the mixing length with increasing *Pe* for both reactive interfaces (stationary and moving—Figure 3.13(c)), we also induce that the modified Grætz behaviour will hold out to arbitrarily large *Pe*. The non-chaotic flow in Figure 3.1(b) demonstrates modified Grætz behaviour for transport to the stationary surface for $Pe<10^5$ over at least two orders of magnitude in axial distance (Figure 3.6(b)); this observation leads us to conclude that for low to intermediate Pe, the non-chaotic flow is able to transport solute out of the cores of its vortices fast enough to keep up with transport to the stationary interface, and will therefore show modified Grætz behaviour out to arbitrarily large axial distance. Yet, for transport to the stationary interface at large *Pe* (Figure 3.6(b)) and for transport to the moving interface at all *Pe* considered (Figure 3.8(b)), the modified Grætz behaviour breaks down at sufficiently large axial distance. Having shown that the relevant mixing length scales more strongly than the return length with increasing *Pe* for both reactive interfaces, we induce that the modified Grætz behaviour will not hold for the non-chaotic flow for any *Pe* larger than those considered in this work.

IV.F. Further generalization of the modified Grætz behaviour

The transport processes involving the convectively disconnected sets in the chaotic flow of Figure 3.1(c) and Figures 3.9 and 3.10 are a special case of a more general property of the modified Grætz behaviour. In the case of a symmetric flow as in Figure 3.1(c), the internal interface presents a well-defined, purely diffusive boundary to transport between the two disconnected sets. Generally speaking, the presence of any poorly mixed islands in the bulk or on the wall can have similar effects on the overall transport process. If each set is well-mixed individually, all sets should show modified Grætz behaviour and a cascade of concentration as seen in Figures 3.9 and 3.10. Any sets that are not well mixed individually and any interfaces that lead to a continuously broadening boundary layer for transport across the interface will show standard Grætz behaviour with an asymptotic value, Sh^{∞}, that is determined primarily by the absolute size of the set or the maximum thickness of the boundary layer, as in the behaviour of the non-chaotic flow at large axial distance (see Figures 3.5–3.8). The relative size of the sets and the properties of the velocity conditions near the interfaces between sets will determine how strongly each set affects the overall Sherwood number.

As an example of the generality of this behaviour Figure 3.14 shows $Sh(Z)$ and representative concentration profiles for a flow similar to the flow in Figure 3.1(a), but with a width equal to the height, $W = H$, rather than $W = 2H$ in Figure 3.1(a). We see in the concentration profiles that a large fraction of the cross section is well mixed, but there is also a large region near the top wall that is poorly mixed with the rest of the bulk. As solute reacts out of the system through the green (moving) interface, the average concentration in the well-mixed set decreases quickly while the poorly mixed set remains at roughly the inlet concentration. As in Figure 3.10, this process corresponds to the initial plateaus seen in $Sh(Z)$ in Figure 3.14. At large axial

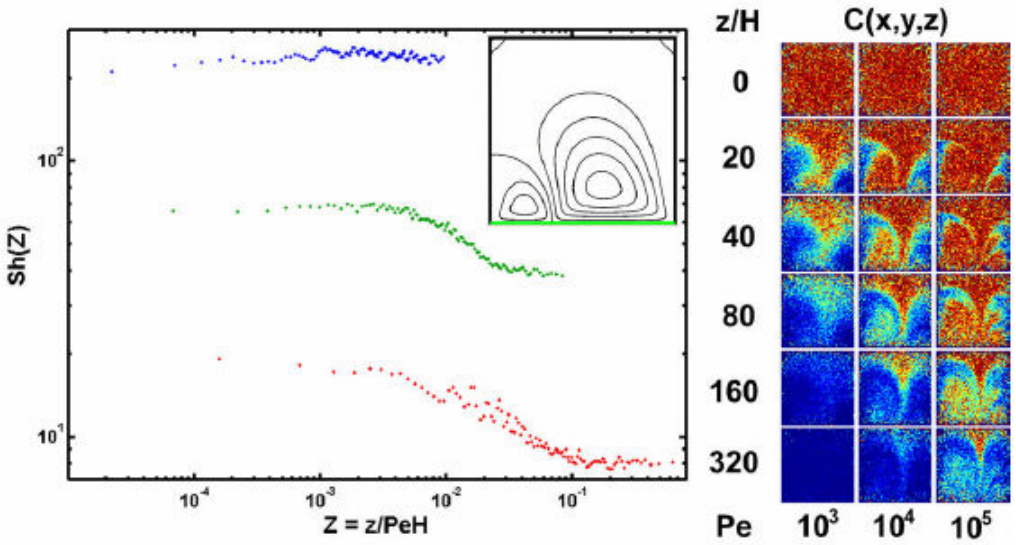

Figure 3.14. Local Sherwood number, $Sh(Z)$, as a function of scaled axial distance, $Z = z/PeH$, for transport to the green (moving) interface in the flow shown in Figure 3.1(a) with $r = 1/3$, $u_{trans} = U/5$, and $L_{1/2} = 10H$, but with $W = H$. Colours signify Pe (10^2 (purple), 10^3 (red), 10^4 (green), 10^5 (blue), 10^6 (grey)) at constant $u_{trans} = U/5$, and the black dots signify the collection of all Pe for $u_{trans} = 0$ (uniaxial Poiseuille flow). Inset: streamlines of the transverse flow, with reactive interface in green. Right: concentration profiles at several axial distances for each Pe in the plot of $Sh(Z)$.

distances, transport from the poorly mixed set near the top wall across the well-mixed set to the bottom (moving) interface defines the final asymptotic value of $Sh(Z)$. It is interesting to note that the spacing between the initial and final plateau values of $Sh(Z)$ in Figure 3.10 was independent of Pe, implying a constant multiplicative factor between $Sh^{\infty}_{\text{overall}}$ and $Sh^{\infty}_{\text{trans}}$ and the same scaling with Pe for $Sh^{\infty}_{\text{centre}}$ and $Sh^{\infty}_{\text{trans}}$, as predicted in Table 3.1 and shown in Figure 3.11. In Figure 3.14, the spacing between the plateau values at $Pe = 10^3$ appears to be larger than that at $Pe = 10^4$, and the second plateau is not even seen at $Pe = 10^5$ (although it may exist at larger axial distance), implying a scaling for $Sh^{\infty}_{\text{overall}}$ (second plateau) that is different from (in fact higher than) the scaling for $Sh^{\infty}_{\text{trans}}$ (first plateau). A higher scaling for $Sh^{\infty}_{\text{overall}}$ also implies a higher scaling for the Sherwood number for transfer between the two disconnected sets. This increased scaling makes sense, as there is some convective transfer across the interface between the sets in Figure 3.14 at the end of each half-cycle, while there is only diffusive transfer across the well-defined interface at the centreline in Figures 3.9 and 3.10.

V. Conclusions

In this work, we have extended the concept of the modified Grætz behaviour to the problems of mass transfer to moving interfaces and internal diffusive interfaces. Our predicted correlations (see Table 3.1) for the scaling and prefactor of the asymptotic value of the Sherwood number for mass transfer to stationary, moving, and diffusive interfaces accurately represent the observed results from numerical simulations (see Figure 3.11). Concentration profiles in the case of transport to moving interfaces revealed an interesting property of the LDC flows with which we work: as the depleted fluid is swept off of the moving reactive interface, in some cases it forms an inverted boundary layer far from the reactive interface. This inverted

boundary layer sequesters depleted fluid to a large region near the stationary boundary opposite the moving, reactive interface; this segregation maintains high concentration near the reactive interface and allows for higher rates of mass transfer than would be achieved were the concentration in the bulk uniform. Although non-chaotic, 3D flows initially show higher $Sh(Z)$ relative to uniaxial flow, they eventually lead to an asymptotic value, Sh^{∞}, that is independent of Pe, as in the standard Grætz case.

We have also presented the criterion for the existence of modified Grætz behaviour: for a flow at a given Pe, the flow must mix depleted fluid with the bulk before it returns to the reactive interface; the characteristic length for return of a depleted fluid element (a 'depleton') to the interface must be longer than the length required to homogenize it into the bulk. We argued further that the persistence of modified Grætz with increasing axial length and Pe should depend on the Pe-scaling of the return and mixing lengths: if the return length grows more rapidly than the mixing length, then, if modified Grætz is observed at finite Pe and length, it should persist for all higher values of these parameters. By simulation, we found weak scaling of the mixing length ($\sim Pe^{1/6}$) relative to return length ($\sim Pe^{2/3}$ for return to the stationary interface and $\sim Pe^{1/2}$ for return to the moving interface) in the chaotically stirred flow. We thus conclude that modified Grætz should persist in this flow; this conclusion is borne out by our direct calculation of Sh from simulations out to $Pe=10^6$. In contrast, for the non-chaotic flow, strong scaling of the mixing length ($\sim Pe$) should lead to the breakdown of modified Grætz at high Pe; this prediction is consistent with our observation that non-chaotic flow fails to sustain the modified Grætz behaviour beyond intermediate Pe.

Finally, we note that there is not a direct analogy between the results for transfer to moving interfaces in the LDC flows and for transfer to the stationary grooved surfaces that drive similar flows in the SHM. As such, we cannot expect to

see the same increase in Sh^{∞} in the SHM that we report here for Sh^{∞} at the moving interface. We are currently pursuing further investigations of transport to grooved boundaries.

Acknowledgments

We thank Hector Abruña, Donald Koch and Pavithra Sundararajan for helpful conversations. This work was funded by the National Science Foundation (CTS-0529042), and the Department of Energy (DE-FG02-05ER46250). This research was conducted using the resources of the Cornell University Center for Advanced Computing, which receives funding from Cornell University, New York State, the National Science Foundation, and other leading public agencies, foundations and corporations.

REFERENCES

Acharya N, Sen M and Chang H C 1992 Heat transfer enhancement in coiled tubes by chaotic mixing *Int. J. Heat Mass Transfer* **35** 2475–89

Acharya N, Sen M and Chang H C 2001 Analysis of heat transfer enhancement in coiled-tube heat exchangers *Int. J. Heat Mass Transfer* **44** 3189–99

Aidun C K, Triantafillopoulos N G and Benson J D 1991 Global stability of a lid-driven cavity with throughflow: flow visualization studies *Phys. Fluids* A **3** 2081–91

Aref H 1984 Stirring by chaotic advection *J. Fluid Mech.* **143** 1–21

Aref H and Jones S W 1989 Enhanced separation of diffusing particles by chaotic advection *Phys. Fluids* A **1** 470–4

Bird R B, Stewart W E and Lightfoot E N 1960 *Transport Phenomena* (New York: Wiley)

Brody J P and Yager P 1997 Diffusion-based extraction in a microfabricated device *Sensors Actuators* A **58** 13–8

Bryden M D and Brenner H 1996 Effect of laminar chaos on reaction and dispersion in eccentric annular flow *J. Fluid Mech.* **325** 219–37

Bryden M D and Brenner H 1999 Mass-transfer enhancement via chaotic laminar flow within a droplet *J. Fluid Mech.* **379** 319–31

Chang H C and Sen M 1994 Application of chaotic advection to heat transfer *Chaos Solitons Fractals* **4** 955–75

Chien W L, Rising H and Ottino J M 1986 Laminar mixing and chaotic mixing in several cavity flows *J. Fluid Mech.* **170** 355–77

Cohen J L, Westly D A, Pechenik A and Abruna H D 2005 Fabrication and preliminary testing of a planar membraneless microchannel fuel cell *J. Power Sources* **139** 96–105

Ferrigno R, Stroock A D, Clark T D, Mayer M and Whitesides G M 2002 Membraneless vanadium redox fuel cell using laminar flow *J. Am. Chem. Soc.* **124** 12930–1

Foley J O, Mashadi-Hossein A, Fu E, Finlayson B A and Yager P 2008 Experimental and model investigation of the time-dependent 2-dimensional distribution of binding in a herringbone microchannel *Lab Chip* **8** 557–64

Ganesan V, Bryden M D and Brenner H 1997 Chaotic heat transfer enhancement in rotating eccentric annular-flow systems *Phys. Fluids* **5** 1296–306

Ghosh S, Chang H C and Sen M 1992 Heat transfer enhancement due to slender recirculation and chaotic transport between counter-rotating eccentric cylinders *J. Fluid Mech.* **238** 119–54

Ghosh S, Leonard A and Wiggins S 1998 Diffusion of a passive scalar from a no-slip boundary into a twodimensional chaotic advection field *J. Fluid Mech.* **372** 119–63

Golden J P, Floyd-Smith T M, Mott D R and Ligler F S 2007 Target delivery in a microfluidic immunosensor *Biosens. Bioelectron.* **22** 2763–7

Grætz L 1885 *Ann. Phys. Chem.* **25** 337–57 Q1

Horner M, Metcalfe G, Wiggins S and Ottino J M 2002 Transport enhancement mechanisms in open cavities *J. Fluid Mech.* **452** 199–229

Ismagilov R F, Stroock A D, Kenis P J A, Whitesides G and Stone H A 2000 Experimental and theoretical scaling laws for transverse diffusive broadening in two-phase laminar flows in microchannels *Appl. Phys. Lett.* **76** 2376–8

Kamholz A E, Weigl B H, Finlayson B A and Yager P 1999 Quantitative analysis of molecular interaction in a microfluidic channel: the T-sensor *Anal. Chem.* **71** 5340–7

Kenis P J A, Ismagilov R F and Whitesides G M 1999 Microfabrication inside capillaries using multiphase laminar flow patterning *Science* **285** 83–5

Kenis P J A, Ismagilov R F, Takayama S, Whitesides G M, Li S L and White H S 2000 Fabrication inside microchannels using fluid flow *Acc. Chem. Res.* **33** 841–7

Kirtland J D, McGraw G J and Stroock A D 2006 Mass transfer to reactive boundaries from steady threedimensional flows in microchannels *Phys. Fluids* **18** 073602

Lefevre A, Mota J P B, Rodrigo A J S and Saatdjian E 2003 Chaotic advection and heat transfer enhancement in Stokes flows *Int. J. Heat Fluid Flow* **24** 310–21

Leong C W and Ottino J M 1989 Experiments on mixing due to chaotic advection in a cavity *J. Fluid Mech.* **209** 463

Lévêque A M 1928 Les lois de la transmission de chaleur par convection *Annal. Mines* **13** 283–99

Mokrani A, Castelain C and Peerhossaini H 1997 The effects of chaotic advection on heat transfer *Int. J. Heat Mass Transfer* **40** 3089–104

Nishimura T, Murakami S and Kawamura Y 1993 Mass transfer in a symmetrical sinusoidal wavy-walled channel for oscillatory flow *Chem. Eng. Sci.* **48** 1793–800

Nishimura T 1995 Oscillatory flow and mass transfer within asymmetric and symmetrical channels with sinusoidal wavy walls *Heat Mass Transfer* **30** 269–78

Nishimura T and Kojima N 1995 Mass transfer in a symmetrical sinusoidal wavy-walled channel for pulsatile flow *Int. J. Heat Mass Transfer* **38** 1719–31

Ottino J M 1989 *The Kinematics of Mixing: Stretching, Chaos and Transport* (Cambridge: Cambridge University Press)

Peerhossaini H, Castelain C and Leguer Y 1993 Heat exchanger design based on chaotic advection *Exp. Therm. Fluid Sci.* **7** 333–44

Ranz W E 1979 Applications of a stretch model to mixing, diffusion, and reaction in laminar and turbulent flows *AIChE J.* **25** 41–7

Saatdjian E, Midoux N, Chassaing M I G, Leprevost J C and Andre J C 1996 Chaotic mixing and heat transfer between confocal ellipses: experimental and numerical results *Phys. Fluids* **8** 677–91

Shrivastava A, Kumar S and Cussler E L 2008 Predicting the effect of membrane spacers on mass transfer *J. Memb. Sci.* **323** 247–56

Simonnet C and Groisman A 2005 Chaotic mixing in a steady flow in a microchannel *Phys. Rev. Lett.* **94** 134501 Squires T M, Messinger R J and Manalis S R 2008 Making it stick: convection, reaction and diffusion in surfacebased biosensors *Nat. Biotechnol.* **26** 417–26

Squires T M, Messinger R J and Manalis S R 2008 Making it stick: convection, reaction and diffusion in surfacebased biosensors *Nat. Biotechnol.* **26** 417–26

Stroock A D, Weck M, Chiu D T, Huck W T S, Kenis P J A, Ismagilov R F and Whitesides G 2000 Patterning electro-osmotic flow with patterned surface charge *Phys. Rev. Lett.* **84** 3314–7

Stroock A D, Dertinger S K W, Ajdari A, Mezic I, Stone H A and Whitesides G M 2002a Chaotic mixer for microchannels *Science* **295** 647–51

Stroock A D, Dertinger S KW, Whitesides G M and Ajdari A 2002b Patterning flows using grooved surfaces *Anal. Chem.* **74** 20

Stroock A D and McGraw G J 2004 Investigation of the staggered herringbone mixer with a simple analytical model *Philos. Trans. R. Soc.* A **362** 971–86

Teles F R R and Fonseca L P 2008 Trends in DNA biosensors *Talanta* **77** 606–23

Vijayendran R A, Motsegood K M, Beebe D J and Leckband D E 2003 Evaluation of a three-dimensional micromixer in a surface-based biosensor *Langmuir* **19** 1824–8

Villermaux E and Duplat J 2003 Mixing as an aggregation process *Phys. Rev. Lett.* **91** 184501

Villermaux E, Stroock A D and Stone H A 2008 Bridging kinematics and concentration content in a chaotic micromixer *Phys. Rev.* E **77** 015301

CHAPTER 4

EXPERIMENTAL MEASUREMENTS OF INTERFACIAL MASS TRANSFER IN MICROFLUIDIC SYSTEMS

I. Introduction

Interfacial mass transfer is of significant technological relevance in many analytical, industrial and commercial applications. The delivery of solute to solid, stationary, reactive or diffusive boundaries is crucial in electrochemical systems (Ferrigno *et al* 2002, Cohen *et al* 2005, Shrivastava *et al* 2008), sensors involving reaction at a solid surface (Kamholz *et al* 1999, Ismagilov *et al* 2000, Vijayendran *et al* 2003, Golden *et al* 2007, Foley *et al* 2008, Squires *et al* 2008, Teles and Fonseca 2008), membrane separations (Shrivastava *et al* 2008), and heat exchanger design (Acharya *et al* 1992, Peerhossaini *et al* 1993, Mokrani *et al* 1997, Acharya *et al* 2001), through the Chilton-Colburn analogy between heat and mass transfer. Many of these systems operate with uniaxial flow in the laminar flow regime, where turbulent instabilities are entirely suppressed by viscous effects, and mixing in the cross section occurs slowly by diffusion only. The Reynolds number in these systems, which gives the strength of inertial effects relative to viscous effects, is generally small: $Re = UH/\nu < 100$, where U is the average fluid velocity, H is the characteristic size scale in the cross section, and v is the kinematic viscosity of the fluid. Turbulence generally does not occur for $Re < 2000$; the flow in these systems is therefore entirely laminar. Microfluidic systems tend to operate in this regime due to their small cross sectional size and the inability to achieve high flow rates at pressure drops that are not destructive to the device.

For transfer processes in these systems, we also define the Péclet number, which can be thought of as the ratio of diffusive to convective time scales in the flow: $Pe = UH / D > 100$, where D is the molecular diffusivity of the solute in question. Due to the fact that the Schmidt number, the ratio of fluid viscosity to solute diffusivity, is large ($Sc = \nu / D > 1000$) for most solvent/solute combinations, *Pe* is often quite large in these systems even if *Re* is small. This combination of low *Re* and high *Pe* leads to the growth of thick depleted regions near reactive or diffusive interfaces which in turn leads to low rates of mass transfer to these interfaces due to a small driving force for transfer. Efficiency of solute usage and total flux of solute to the surface are decreased due to these depleted regions. While operating at a lower flow rate increases efficiency, total flux is decreased at lower flow rates, demonstrating the inevitable compromise between the two. Mixing in the cross section can diminish these effects by keeping the depleted regions thin and maintaining a high driving force for transfer to the surface, increasing the efficiency and total flux to the surface simultaneously.

In this work, we present a study of mass transfer between solid, stationary surfaces and laminar flows in microchannels. We consider three classes of flow: uniaxial, three-dimensional non-chaotic, and three-dimensional chaotic. We seek to experimentally test predictions made in our previous works (Kirtland *et al* 2006, Kirtland *et al* 2009) as to the effects of three-dimensional flow on rates of mass transfer, and also to inform the design of microfluidic systems that favor mass transfer for analytical electrochemical systems, fuel cells, and other contexts such as binding assays. The three-dimensional flows that we consider are generated by variations on the passive micromixer called the staggered herringbone mixer (SHM) (Stroock *et al* 2002a, 2002b). This mixer generates transverse flow by patterns of oblique grooves along one or more of the channel walls; these structures entrain some of the passing

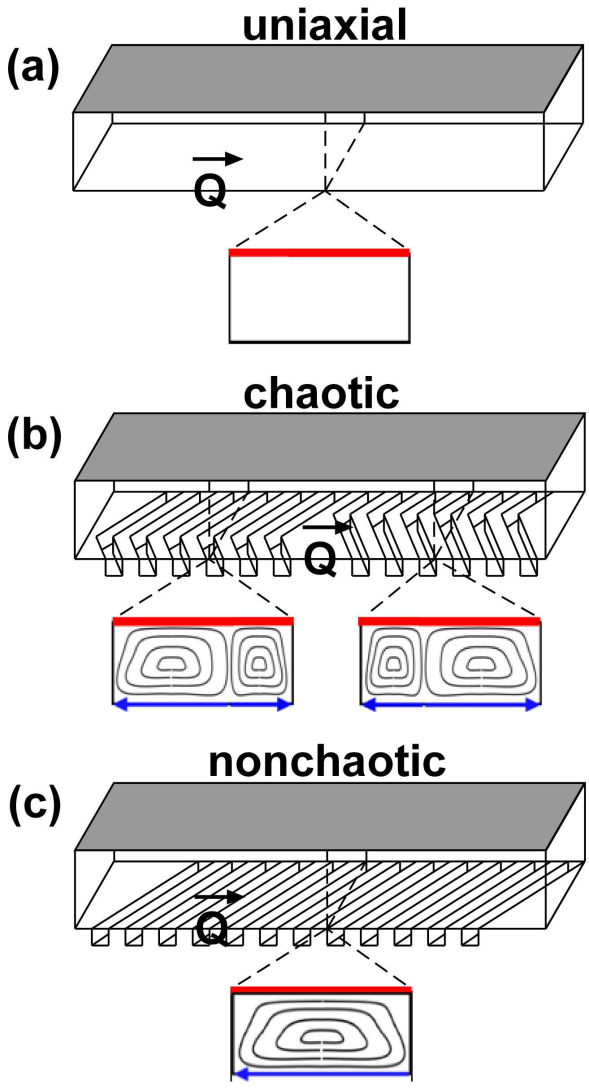

Figure 4.1. Flow geometries. (a) Uniaxial flow. (b) Chaotic three-dimensional flow generated by staggered herringbone grooves. (c) Non-chaotic three-dimensional flow generated by diagonal grooves.

fluid and impart a transverse component of velocity (see Figure 4.1). This transverse velocity causes a recirculation in the bulk, allowing for more efficient mixing relative to the uniaxial case. The geometry of the grooves allows for the tuning of 1) the transverse shear rate relative to the axial shear rate, 2) the presence or absence of chaotic fluid trajectories, and 3) the size of chaotic sets in the bulk.

We consider two geometries of grooves: a staggered herringbone structure as in Figure 4.1(b) and a diagonal structure as in Figure 4.1(c). The SHM structure creates counter-rotating vortices in the flow, and the interface between these vortices is modulated along the axial dimension of the channel. This geometry with modulation of boundary conditions gives rise to chaotic fluid trajectories and also to efficient mixing in the bulk (Aref 1984). The diagonal structure creates a single vortex in the flow, with no modulation of the transverse flow along the axial dimension, and therefore no chaotic trajectories. While the strength of the transverse flow in this case is roughly equal to that in the SHM case, the absence of chaos makes the system less capable of efficiently mixing the bulk.

We consider transfer to flat surfaces in uniaxial flows as well as flat and grooved surfaces in three-dimensional flows. The measurements take place in an electrochemical potential cell using a fast, reversible redox couple as the reactive solute. In our system, the electrodes are opposing walls of the microchannel. Thus in a system where one of the walls is grooved so as to induce transverse flow (as in Figure 4.1(b) and 4.1(c)), we can measure transfer to the flat wall opposite the surface that drives the transverse flow as well as transfer to the driving surface itself (see Figure 4.2(b)). We call this geometry the “generator-collector” because it facilitates recycling of the reactive solute between its two oxidation states. This process leads to amplification of the signal at the working electrode, as a single molecule can

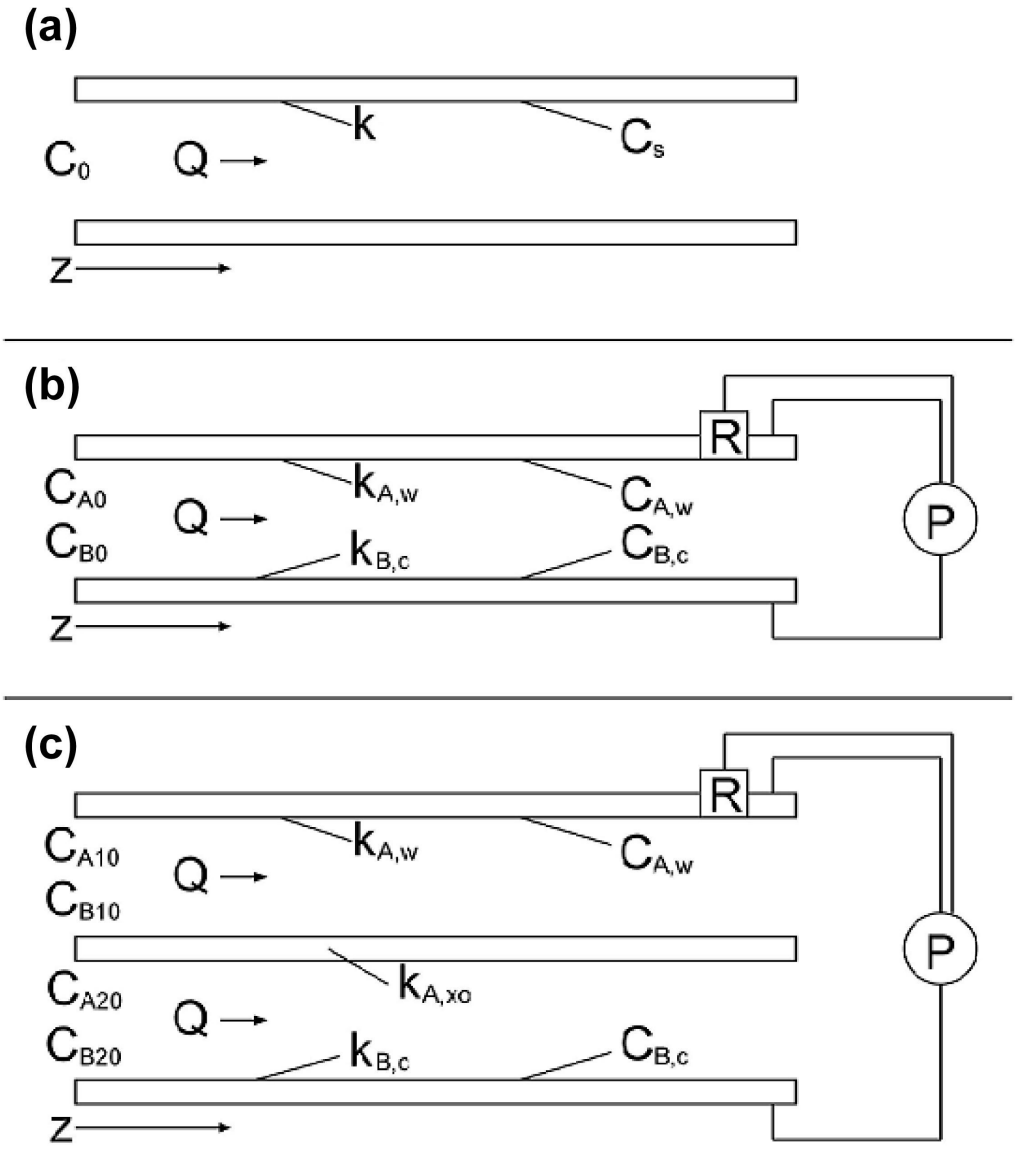

Figure 4.2. Surface reaction geometries. (a) Irreversible reaction. (b) Generator-collector. (c) Double cell. P represents the potentiostat that sets the electrode potential and measures the current passed by the working electrode. R represents the reference electrode used to measure the solution potential.

contribute to the current measured at the working electrode by reacting several times at various positions along the length of the reactor. In addition to the measurements in the generator-collector geometry, we have also measured transfer in the geometry of a microfluidic fuel cell. This geometry, which we call the "double-cell", is composed of two microchannels flowing in parallel, separated by a diffusive membrane. The outermost walls, opposite the membrane, are the electrodes, and can be either flat or grooved. This geometry allows for the measurement of overall reactive flux, which necessarily involves a transfer process not only from the stream flowing near the electrode to the electrode surface, but also a crossover transfer process between the two streams. This geometry is particularly important because crossover between the fuel and oxidant streams is a major problem in the design of microfluidic fuel cells. It is crucial that we understand how the flow in the two streams affects the rate of crossover as well as the rate of transfer to the reactive surface.

The remainder of this paper is structured as follows: Section II presents theoretical arguments for the expected relationship between the efficiency of solute usage and the length averaged Sherwood number for mass transfer to the working electrode in an electrochemical potential cell for a single reactive interface with an irreversible surface reaction, two reactive interfaces with coupled reversible reactions bounding a single fluid stream, and two reactive interfaces with coupled reversible reactions bounding two fluid streams separated by a diffusively permeable membrane; Section III describes the experimental setup, including fabrication, characterization, and operation of the microfluidic devices; Section IV presents the electrochemical measurements in the various geometries and operating conditions; and Section V summarizes the conclusions of this work and suggests future directions for the project.

II. Theory

In order to quantify the extent to which a flow decreases resistance to mass transfer, the standard quantity to consider is the mass transfer coefficient, as it represents the conductance of the mass transfer process. The mass transfer coefficient $k(z)$ is defined as:

$$k(z) = -\frac{J(z)}{C_b(z) - C_s(z)} \tag{4.1}$$

where $J(z)$ is the flux of solute to the surface, $C_b(z)$ is the average concentration in the bulk, and $C_s(z)$ is the concentration at the reactive surface. This mass transfer coefficient is an indication of how well a particular flow can translate a difference in concentration into reactive flux. The flux itself is defined as:

$$J(z) = -D\left.\frac{\partial C}{\partial y}\right|_{y=0} \tag{4.2}$$

where D is the diffusivity of the solute and $\left.\partial C / \partial y\right|_{y=0}$ is the gradient of concentration at the reactive surface. Finally, we define the Sherwood number $Sh(z)$, a non-dimensionalized mass transfer coefficient that is generalizable across systems of different size and with different solute diffusivities:

$$Sh(z) = \frac{k(z)H}{D} \tag{4.3}$$

where H is the height of the channel. The Sherwood number can be related to the efficiency of solute usage $\varepsilon = i_w / i_{theoretical}$, where i_w is the current at the working electrode and $i_{theoretical}$ is the current expected if all reactive solute particles introduced into the system react exactly once. Note that in the case of a reversible reaction, a particle of solute can be recycled through reaction at the counter electrode, making it available to contribute to the total current at the working electrode multiple times, and

therefore the efficiency as calculated can exceed unity in the presence of recycling. The efficiency depends on the Sherwood number for the various surface reaction and diffusion processes occurring at the electrodes and the membrane, respectively. In our previous work, we have presented predictions for the local Sherwood number for transfer from uniaxial and three-dimensional flows, like those considered here, to a solid stationary interface (Kirtland *et al* 2009), and in this work we test these predictions by calculation of the efficiency and the length averaged Sherwood number from measurements of the electrochemical current.

Early work on the theory of transfer to solid, stationary interfaces in laminar uniaxial flow (on which much of our predictions are built) was accomplished in large part by Grætz (1885) and Lévêque (1928). More recently, Ismagilov *et al* (2000) developed scaling laws for the growth of the boundary layer in shear-like and plug-like flows. There have also been a variety of theoretical studies on the effect of chaos on rates of interfacial mass transfer: on sources of resistance to mass transfer, including boundary layers, recirculation regions, and stagnation streamlines (Chang and Sen 1994); on optimal frequencies for modulation of the flow (Bryden and Brenner 1996, Ghosh *et al* 1992, Horner *et al* 2002); studies that find significant increases in rates of mass transfer due to chaos (Bryden and Brenner 1999, Ganesan *et al* 1997, Lefevre *et al* 2003); and studies that show that chaos has little or no effect in some cases (Ganesan *et al* 1997, Ghosh *et al* 1998, Kirtland *et al* 2006). Experimental studies in a variety of systems have been likewise mixed, including: transfer to the surface of coiled tubes experiencing Dean's flows (Peerhossaini *et al* 1993, Mokrani *et al* 1997, Acharya *et al* 2001); transfer to the surface of confocal rotating ellipses (Saatdjian *et al* 1996); transfer to the surface of a wavy-walled channel (Nishimura 1995, Nishimura and Kojima 1995, Nishimura *et al* 1993); and ultrafiltration systems

(Shrivastava *et al* 2008). In summary, chaos tends to produce significant increases in rates of transfer to fluid-fluid diffusive interfaces and to moving, solid interfaces (Bryden and Brenner 1999, Ganesan *et al* 1997, Lefevre *et al* 2003), but chaos results in little or no increase in rates of transfer to solid, stationary interfaces (Acharya *et al* 2001, Ghosh *et al* 1998, Kirtland *et al* 2006, Mokrani *et al* 1997, Peerhossaini *et al* 1993). Our most recent findings agree on both counts (Kirtland *et al* 2009). It should be noted that the reactive interfaces in this work are composed of multiple solid, stationary surfaces. Therefore the chaotic flow as in Figure 4.1(b) may not display a significant difference in rates of transfer from the non-chaotic flow as in Figure 4.1(c).

Grætz (1885) and Lévêque (1928) have laid out arguments for how the thickness of the boundary layer (the region of depleted fluid near the reactive interface) should grow in uniaxial flow, and our previous work has extended those arguments to flows with transverse velocity components (Kirtland *et al* 2006, Kirtland *et al* 2009). In the standard Grætz problem, the Sherwood number initially decreases (and the boundary layer thickness initially grows) with increasing axial distance according to

$$Sh(z) = \begin{cases} \dfrac{9^{-1/3}}{\Gamma(4/3)}\left(\dfrac{H\dot{\gamma}_{\text{axial}}}{U}\right)^{1/3}\left(\dfrac{z}{PeH}\right)^{-1/3} = A_0\left(\dfrac{z}{PeH}\right)^{-1/3} & z < z_{\text{plat}} \\ Sh^{\infty} = 2 & z > z_{\text{plat}} \end{cases} \qquad (4.4)$$

where $\dot{\gamma}_{\text{axial}} \sim 6U/H$ is the axial shear rate and z_{plat} is the axial distance at which the boundary layer approaches the size of the channel, at which point $Sh(z)$ reaches an asymptotic value $Sh^{\infty} = 2$. In the presence of a transverse flow with the ability to remove the depleted fluid from the reactive interface and mix it with the bulk fluid before returning it to the surface, the boundary layer grows in a similar manner initially, but reaches its asymptotic thickness at a shorter axial distance, resulting in an

asymptotic value of the Sherwood number that is larger than the uniaxial case, and depends on *Pe* according to the following relation (adapted from Kirtland *et al* 2006):

$$Sh_{stat}^{\infty} = \frac{(2/3)^{1/3}}{\Gamma(4/3)}\left(\frac{\dot{\gamma}_{\text{trans}}}{\dot{\gamma}_{\text{axial}}}\right)^{1/3}\left(\frac{H}{W}\right)^{1/3} Pe^{1/3} = B_0 Pe^{1/3} \tag{4.5}$$

where $\dot{\gamma}_{\text{trans}}$ is the shear rate of the transverse flow at the surface. We will see in Section III.B that the ratio of the transverse shear rate to the axial shear rate is approximately 1/8 near the flat surface opposite the grooves and approximately 1 at the grooved surface itself. Therefore, for the flow near the grooves $B_0 \sim 1.47$, and for the flow near the flat surface $B_0 \sim 0.734$. We call this deviation from the standard Grætz case due to three-dimensional flow the modified Grætz behavior (Kirtland *et al* 2006, Kirtland *et al* 2009).

These arguments for the local Sherwood number form the basis for the equations governing the evolution of concentration with axial distance presented in the following sections. The length averaged Sherwood number, however, is a more accessible measure of the rate of mass transfer of an experimental system, because it is easier to measure the total current than to measure the local flux, local bulk concentration, or local mass transfer coefficient. Due to the high transverse shear rates in the three-dimensional flows considered in this work (see Figure 4.1(b) and (c)), we expect the asymptotic state to be reached at sufficiently short axial distances that the length averaged and asymptotic Sherwood numbers have nearly the same value. In the case of the uniaxial flow, however, the local Sherwood number continues to be a function of axial distance at high *Pe*, while the length averaged value looks similar to the asymptotic value in the mixed case. The expected forms for the average Sherwood number in the geometries considered in this work are therefore:

$$Sh_{\text{ave}} = \frac{1}{L}\int_0^L Sh(z)dz = \begin{cases} 0.179Pe^{1/3}, & \text{flat electrode in uniaxial flow} \\ 0.734Pe^{1/3}, & \text{flat electrode in 3D flow} \\ 1.47Pe^{1/3}, & \text{grooved electrode in 3D flow} \end{cases} \quad (4.6)$$

II.A. Single reactive interface with irreversible surface reaction

In order to establish a direct comparison to results presented previously for transfer to a stationary reactive interface in uniaxial and three-dimensional duct flows (Kirtland *et al* 2006, Kirtland *et al* 2009), the simplest possible system with heterogeneous reaction is considered. Consider a stream of fluid flowing through a rectangular duct of height H, width W, and length L with volumetric flow rate Q (see Figure 4.2(a)). This stream contains a solute A, initially at concentration C_0, which reacts irreversibly along the ceiling of the duct according to the electrochemical reaction:

$$\text{A} \rightarrow \text{B} + ne^- \quad (4.7)$$

where n is the number of electrons transferred per particle of A that reacts at the interface. We assume that there is a constant concentration C_s of A at the surface. For very fast reaction kinetics, this surface concentration will approach zero. Defining the mass transfer coefficient $k(z)$ as the ratio of the reactive flux at the surface $J(z)$ to the concentration driving force $C(z)$-C_s:

$$J(z) = k(z)\left(C(z) - C_s\right) \quad (4.8)$$

the equation that describes the evolution of the average concentration with respect to axial distance z is:

$$Q\frac{dC}{dz} = -Wk(z)\left(C(z) - C_s\right) \quad (4.9)$$

where Q is the volumetric flow rate, W is the width of the channel, and C_s is the concentration at the reactive interface. The average concentration $C(z)$ is the cup-mixing concentration, a velocity-weighted average concentration:

$$C_{\text{cup}}(z) = \frac{1}{UHW} \iint_{X,Y} C(x,y,z) u_z(x,y,z)\, dxdy \tag{4.10}$$

where $C(x,y,z)$ is the local concentration, $u_z(x,y,z)$ is the axial velocity, and U is the average axial velocity. Unless otherwise specified, all concentrations will be assumed to be cup-mixing concentrations.

In order to generalize across systems of different size scale and solute diffusivity, we non-dimensionalize the system by transforming the variables in the following manner:

$$\begin{aligned} Pe &= \frac{UH}{D} = \frac{Q}{WD}, Z = \frac{z}{PeH} \\ Sh(Z) &= \frac{k(Z)H}{D}, \hat{C}(Z) = \frac{C(Z) - C_s}{C_o - C_s} \end{aligned} \tag{4.11}$$

where Pe is the Péclet number; Z is a non-dimensionalized axial distance; the Sherwood number Sh is a non-dimensionalized mass transfer coefficient; and $\hat{C}(z)$ is a non-dimensionalized bulk average concentration. This results in the following form for the governing equation (4.9):

$$\frac{d\hat{C}}{dZ} = -Sh(Z)\hat{C}(Z) \rightarrow \frac{d \ln \hat{C}}{dZ} = -Sh(Z) \tag{4.12}$$

Integrating (4.12), we find the concentration as a function of scaled axial distance Z:

$$\hat{C}(Z) = \exp\left(-\int_0^Z Sh(Z')dZ' \right) \tag{4.13}$$

The Sherwood number averaged over the length of the duct is a useful quantity as we consider the effect of various surface geometries:

$$Sh_{\text{ave}} = \frac{1}{L}\int_0^L Sh(z)\,dz = \frac{PeH}{L}\int_0^{\frac{L}{PeH}} Sh(Z)\,dZ \tag{4.14}$$

The total current, i [A] at the reactive surface can be found by integrating the reactive flux (4.8) over the entire reactive surface and multiplying by the number of electrons transferred per molecule of solute reacted and the number of coulombs of charge per mol of electrons:

$$\begin{aligned} i &= nFW\int_0^L k(z)\left(C(z) - C_{\text{s}}\right)dz \\ &= nF\left(C_0 - C_{\text{s}}\right)Q\int_0^{\frac{L}{PeH}} Sh(Z)\exp\left(-\int_0^Z Sh(Z')\,dZ' \right)dZ \\ &= nF\left(C_0 - C_{\text{s}}\right)Q\left(1 - \exp\left(-\frac{Sh_{\text{ave}}L}{PeH} \right)\right) \end{aligned} \tag{4.15}$$

remembering that for fast reaction kinetics, the surface concentration goes to zero. In (4.15), n is the number of electrons transferred per ion of A reacted, F is Faraday's constant [96485 C/mol], and Q [m^3/s] is the volumetric flow rate. The efficiency of solute usage can be calculated by dividing the current (4.15) by the theoretical current produced if all of the initial concentration were to react:

$$\varepsilon = \frac{i}{nFC_0Q} = 1 - \exp\left(-\frac{Sh_{\text{ave}}L}{PeH} \right) \tag{4.16}$$

Since the efficiency is a macroscopic quantity easily calculated from experimental data, it is useful to re-write (4.16) to find the average Sherwood number in terms of the efficiency:

$$Sh_{\text{ave}} = -\frac{PeH}{L}\ln(1-\varepsilon) \tag{4.17}$$

Expressions (4.16) and (4.17) allow for the extraction of the average Sherwood number from the measured current, flow rate, and initial concentration. This approach provides a measure of the ability of a flow to deliver reactant to a reactive interface given geometric parameters (L, H), operating conditions (Pe, Q, C_0), and the total measured current. The non-dimensional nature of Sh_{ave} also allows for the comparison of resistance to transfer across systems of various geometries and flow conditions.

II.B. Two reactive interfaces with coupled reversible reactions – the generator-collector

In order to extend the concepts of efficiency and average Sherwood number to systems that involve the forward and reverse steps of a reversible reaction at opposite surfaces bounding the flow, consider a stream with two reactive solutes A and B that react at the ceiling (hereafter known as the working electrode) and floor (hereafter known as the counter electrode) of the duct, respectively, according to the following reactions (see Figure 4.2(b)):

$$\begin{aligned} &working: \mathrm{A} \rightarrow \mathrm{B} + ne^- \\ &counter: \mathrm{B} + ne^- \rightarrow \mathrm{A} \end{aligned} \tag{4.18}$$

where n is the number of electrons transferred per particle of A or B that reacts at the interface. The electrons generated at the working electrode drive a current through an

external circuit to the counter electrode, supplying the electrons required to complete the reaction. Defining distinct mass transfer coefficients $k_{A,w}$ [m/s] and $k_{B,c}$ [m/s] and constant surface concentrations $C_{A,w}$ and $C_{B,c}$ for the working and counter electrodes respectively, the system of equations that describes this electrochemical system is the following:

$$\begin{aligned} Q\frac{dC_A}{dz} &= W\left(-k_{A,w}(z)\left(C_A(z)-C_{A,w}\right)+k_{B,c}(z)\left(C_B(z)-C_{B,c}\right)\right) \\ Q\frac{dC_B}{dz} &= W\left(-k_{B,c}(z)\left(C_B(z)-C_{B,c}\right)+k_{A,w}(z)\left(C_A(z)-C_{A,w}\right)\right) \end{aligned} \tag{4.19}$$

Again we non-dimensionalize the system for the sake of generality:

$$\begin{aligned} &Pe=\frac{Q}{WD_A}, Z=\frac{z}{PeH}, Sh_w(z)=\frac{k_{A,w}(z)H}{D_A}, Sh_c(z)=\frac{k_{B,c}(z)H}{D_B} \\ &\alpha=\frac{D_B}{D_A}, \hat{C}_A(z)=\frac{C_A(z)-C_{A,w}}{C_{A0}-C_{A,w}}, \hat{C}_B(z)=\frac{C_B(z)-C_{B,c}}{C_{A0}-C_{A,w}} \end{aligned} \tag{4.20}$$

where we have introduced a parameter α, which is the ratio of the diffusivities of the two solutes A and B. The non-dimensionalized system is now:

$$\begin{aligned} \frac{d\hat{C}_A}{dZ} &= -Sh_w(Z)\hat{C}_A(Z)+\alpha Sh_c(Z)\hat{C}_B(Z) \\ \frac{d\hat{C}_B}{dZ} &= -\alpha Sh_c(Z)\hat{C}_B(Z)+Sh_w(Z)\hat{C}_A(Z) \end{aligned} \tag{4.21}$$

The sum of the concentrations of the two species is constant because the reaction of one ion of A creates one ion of B and vice versa. This result can also be seen by adding the two equations in (4.19) or (4.21), showing that the derivative of the sum of concentrations of A and B is zero. It can also be shown, through numerical integration of the governing equation with reasonable forms for $Sh_w(Z)$ and $Sh_c(Z)$ (as

in Kirtland *et al* 2009), that the individual concentrations of A and B are approximately constant along the length of the channel, to within 2% of C_{A0} and C_{B0} for $Pe > 100$. The concentrations are nearly constant even in the case of different scaling of the Sherwood number with Pe at the two electrodes because at a given axial distance, the difference between the number of particles of A leaving the flow (through reaction of A at the working electrode) and the number of particles of A entering the flow (through reaction of B at the counter electrode) is small compared to the total number of particles of A present in the flow at that axial distance. This assumption could be violated if there were, for instance, stepwise changes in the values of Sh_w and Sh_c , but the only cases considered in this work involve smooth, continuous variation of $Sh(z)$. Constant concentration allows for a significant simplification to the problem at hand:

$$\hat{C}_A(Z) = \hat{C}_{A0}, \hat{C}_B(Z) = \hat{C}_{B0} \tag{4.22}$$

Given the approximations in (4.22), it is straightforward to calculate the total current at the working electrode:

$$\begin{aligned} i_w &= nFW\int_0^L k_{A,w}(z)\left(C_A(z) - C_{A,w}\right)dz \\ &= nF\left(C_{A0} - C_{A,w}\right)Q\int_0^{\frac{L}{PeH}} Sh_w(Z)\,dZ \\ &= nF\left(C_{A0} - C_{A,w}\right)Q\frac{Sh_{w,ave}L}{PeH} \end{aligned} \tag{4.23}$$

and the efficiency:

$$\varepsilon = \frac{i_{\mathrm{w}}}{nFC_{\mathrm{A0}}Q} = \frac{Sh_{\mathrm{w,ave}}L}{PeH} \tag{4.24}$$

for fast kinetics and vanishing surface concentration. Again, we can write the average Sherwood number in terms of easily observed and calculated quantities:

$$Sh_{\mathrm{w,ave}} = \frac{PeH}{L}\varepsilon \tag{4.25}$$

We note that while in the irreversible case above (Section II.A) the efficiency cannot be greater than unity, in the generator-collector, recycling allows for multiple reactions of a given particle of solute and thus efficiencies that can exceed unity.

II.C. Coupled streams separated by diffusive membrane – the double cell

We now consider two streams flowing through a rectangular duct, separated by a membrane (see Figure 4.2(c)). This scenario models the behavior in the reversible reaction analog of the fuel cell geometry, referred to here as the double cell, with recycling of reactants and products between the two electrodes and crossover of species through a diffusively permeable membrane. Stream 1 is bounded by the working electrode and membrane on opposing surfaces, and stream 2 is bounded by the counter electrode and membrane on opposing surfaces. The membrane is taken to be diffusively permeable, but not convectively permeable. This system geometry introduces new mass transfer coefficients for the crossover of solutes A and B, $k_{\mathrm{A,xo}}$ and $k_{\mathrm{B,xo}}$ between the streams and requires the use of four bulk average concentrations.

$$
\begin{aligned}
Q\frac{dC_{\mathrm{A},1}}{dz} &= W\left(-k_{\mathrm{A,w}}(z)\left(C_{\mathrm{A},1}(z)-C_{\mathrm{A,w}}\right)-k_{\mathrm{A,xo}}(z)\left(C_{\mathrm{A},1}(z)-C_{\mathrm{A},2}(z)\right)\right)\\
Q\frac{dC_{\mathrm{A},2}}{dz} &= W\left(k_{\mathrm{B,c}}(z)\left(C_{\mathrm{B},2}(z)-C_{\mathrm{B,c}}\right)-k_{\mathrm{A,xo}}(z)\left(C_{\mathrm{A},2}(z)-C_{\mathrm{A},1}(z)\right)\right)\\
Q\frac{dC_{\mathrm{B},1}}{dz} &= W\left(k_{\mathrm{A,w}}(z)\left(C_{\mathrm{A},1}(z)-C_{\mathrm{A,w}}\right)-k_{\mathrm{B,xo}}(z)\left(C_{\mathrm{B},1}(z)-C_{\mathrm{B},2}(z)\right)\right)\\
Q\frac{dC_{\mathrm{B},2}}{dz} &= W\left(-k_{\mathrm{B,c}}(z)\left(C_{\mathrm{B},2}(z)-C_{\mathrm{B,c}}\right)-k_{\mathrm{B,xo}}(z)\left(C_{\mathrm{B},2}(z)-C_{\mathrm{B},1}(z)\right)\right)
\end{aligned}
\tag{4.26}
$$

We note that again the sum of all concentrations is constant, because adding equations (4.26) gives the derivative of the sum of the concentrations equal to zero. To understand this condition, we consider the reactive process occurring at the counter electrode that increases the concentration of solute A in stream 2. The flux of solute B toward the counter electrode must be equal and opposite to the flux of solute A away from the counter electrode:

$$
k_{\mathrm{B,c}}(z)\left(C_{\mathrm{B},2}(z)-C_{\mathrm{B,c}}\right)=k_{\mathrm{A,c}}(z)\left(C_{\mathrm{A,c}}-C_{\mathrm{A},2}(z)\right) \tag{4.27}
$$

which allows us to rewrite the second equation in (4.26) and consider only the concentrations of species A:

$$
\begin{aligned}
Q\frac{dC_{\mathrm{A},1}}{dz} &= W\left(-k_{\mathrm{A,w}}(z)\left(C_{\mathrm{A},1}(z)-C_{\mathrm{A,w}}\right)-k_{\mathrm{A,xo}}(z)\left(C_{\mathrm{A},1}(z)-C_{\mathrm{A},2}(z)\right)\right)\\
Q\frac{dC_{\mathrm{A},2}}{dz} &= W\left(k_{\mathrm{A,c}}(z)\left(C_{\mathrm{A,c}}-C_{\mathrm{A},2}(z)\right)-k_{\mathrm{A,xo}}(z)\left(C_{\mathrm{A},2}(z)-C_{\mathrm{A},1}(z)\right)\right)
\end{aligned}
\tag{4.28}
$$

Non-dimensionalizing:

$$Pe = \frac{Q}{WD_{\mathrm{A}}}, Z = \frac{z}{PeH}, \alpha = \frac{D_{\mathrm{B}}}{D_{\mathrm{A}}}$$
$$Sh_{\mathrm{w}}(Z) = \frac{k_{\mathrm{A,w}}(z)H}{D_{\mathrm{A}}}, Sh_{\mathrm{c}}(Z) = \frac{k_{\mathrm{A,c}}(z)H}{D_{\mathrm{A}}}, Sh_{\mathrm{xo}}(Z) = \frac{k_{\mathrm{A,xo}}(z)H}{D_{\mathrm{A}}} \qquad (4.29)$$
$$\hat{C}_{\mathrm{A},1}(Z) = \frac{C_{\mathrm{A},1}(Z) - C_{\mathrm{A,w}}}{C_{\mathrm{A10}} + C_{\mathrm{A20}}}, \hat{C}_{\mathrm{A},2}(Z) = \frac{C_{\mathrm{A},2}(Z) - C_{\mathrm{A,c}}}{C_{\mathrm{A10}} + C_{\mathrm{A20}}}$$

At this point we make use of the fact that the only two stream systems considered in this work have $Sh_{\mathrm{c}}(Z) = Sh_{\mathrm{w}}(Z)$, with either both electrodes flat or both electrodes with the same groove structure, and therefore the governing equation becomes:

$$\frac{d\hat{C}_{\mathrm{A},1}}{dZ} = -Sh_{\mathrm{w}}(Z)\hat{C}_{\mathrm{A},1}(Z) - Sh_{\mathrm{xo}}(Z)\left(\hat{C}_{\mathrm{A},1}(Z) - \hat{C}_{\mathrm{A},2}(Z) + \frac{C_{\mathrm{A,w}}}{C_{\mathrm{A10}} + C_{\mathrm{A20}}} - \frac{C_{\mathrm{A,c}}}{C_{\mathrm{A10}} + C_{\mathrm{A20}}}\right) \qquad (4.30)$$
$$\frac{d\hat{C}_{\mathrm{A},2}}{dZ} = Sh_{\mathrm{w}}(Z)\hat{C}_{\mathrm{A},2}(Z) - Sh_{\mathrm{xo}}(Z)\left(\hat{C}_{\mathrm{A},2}(Z) - \hat{C}_{\mathrm{A},1}(Z) + \frac{C_{\mathrm{A,c}}}{C_{\mathrm{A10}} + C_{\mathrm{A20}}} - \frac{C_{\mathrm{A,w}}}{C_{\mathrm{A10}} + C_{\mathrm{A20}}}\right)$$

It can further be shown that the sum $C_{\mathrm{A},1}(Z)+C_{\mathrm{A},2}(Z)$ can be written in terms of only the initial concentrations (C_{A10}, C_{A20}, C_{B10}, C_{B20}) and the surface concentrations ($C_{\mathrm{A,w}}$, $C_{\mathrm{A,c}}$, $C_{\mathrm{B,w}}$, $C_{\mathrm{B,c}}$). All of these concentrations are individually constant, and therefore the sum $C_{\mathrm{A},1}(Z)+C_{\mathrm{A},2}(Z)$ must also be constant, which implies, from (4.30), that $\hat{C}_{\mathrm{A},1}(Z) = -\hat{C}_{\mathrm{A},2}(Z)$. The form of the governing equation for the concentration of species A in stream 1 is therefore:

$$\frac{d\hat{C}_{\mathrm{A},1}}{dZ} = -Sh_{\mathrm{w}}(Z)\hat{C}_{\mathrm{A},1} - 2Sh_{\mathrm{xo}}(Z)\hat{C}_{\mathrm{A},1} - Sh_{\mathrm{xo}}(Z)\frac{C_{\mathrm{A,w}} - C_{\mathrm{A,c}}}{C_{\mathrm{A10}} + C_{\mathrm{A20}}} \qquad (4.31)$$
$$\frac{dC_{\mathrm{A},1}}{dZ} = -\left(Sh_{\mathrm{w}}(Z) + 2Sh_{\mathrm{xo}}(Z)\right)\left(C_{\mathrm{A},1}(Z) - C_{\mathrm{A,w}}\right) + Sh_{\mathrm{xo}}(Z)\left(C_{\mathrm{A10}} + C_{\mathrm{A20}} - C_{\mathrm{A,w}}\right)$$

In the electrochemical system, at least one of the surface concentrations can be driven to zero by an appropriate choice of electrode potential, and so by setting the potential at the working electrode far in excess of the formal potential for the reaction in question, we have $C_{\mathrm{A,w}} \sim 0$:

$$\frac{dC_{A,1}}{dZ} = -\left(Sh_w(Z) + 2Sh_{xo}(Z)\right)C_{A,1}(Z) + Sh_{xo}(Z)\left(C_{A10} + C_{A20}\right) \tag{4.32}$$

(4.32) can be solved by integrating factor to yield:

$$C_{A,1}(Z) = \frac{C_{A10} + C_{A20}}{Sh_w + 2Sh_{xo}} Sh_{xo} + \frac{C_{A10}Sh_w + \left(C_{A10} + C_{A20}\right)Sh_{xo}}{Sh_w + 2Sh_{xo}} \exp\left(-\left(Sh_w + 2Sh_{xo}\right)Z\right) \tag{4.33}$$

for the case of well mixed flows with constant Sh_w and Sh_{xo} equal to their respective asymptotic values throughout the length of the channel, and:

$$C_{A,1}(Z) = \frac{C_{A10} + C_{A20}}{A_w + 2A_{xo}} A_{xo} + \frac{C_{A10}A_w + \left(C_{A10} + C_{A20}\right)A_{xo}}{A_w + 2A_{xo}} \exp\left(-\frac{3}{2}\left(A_w + 2A_{xo}\right)Z^{2/3}\right) \tag{4.34}$$

for the case of uniaxial flow at high *Pe* with Sherwood numbers of the form $Sh_w = A_w Z^{1/3}$, $Sh_{xo} = A_{xo} Z^{1/3}$. Finally, we can calculate the current at the working electrode and the efficiency:

$$\begin{aligned} i_w &= nFW\int_0^L k_{A,w}(z)C_{A,1}(z)\,dz \\ \varepsilon &= \frac{i_w}{nF\left(C_{A10} + C_{A20}\right)Q} = \frac{\int_0^{L/PeH} Sh_w(Z)C_{A,1}(Z)\,dZ}{C_{A10} + C_{A20}} \end{aligned} \tag{4.35}$$

Defining the concentration fraction $f = C_{A10}/(C_{A10} + C_{A20})$, the efficiency takes the following forms:

$$\varepsilon = \frac{Sh_w Sh_{xo}}{Sh_w + 2Sh_{xo}} \frac{L}{PeH} + \frac{fSh_w^2 + (2f-1)Sh_w Sh_{xo}}{\left(Sh_w + 2Sh_{xo}\right)^2}\left[1 - \exp\left(-\left(Sh_w + 2Sh_{xo}\right)\frac{L}{PeH}\right)\right] \tag{4.36}$$

for the well mixed case, and:

$$\varepsilon = \frac{3}{2}\frac{A_{\mathrm{w}}A_{\mathrm{xo}}}{A_{\mathrm{w}}+2A_{\mathrm{xo}}}\left(\frac{L}{PeH}\right)^{\frac{2}{3}} + \frac{fA_{\mathrm{w}}{}^{2}+(2f-1)A_{\mathrm{w}}A_{\mathrm{xo}}}{\left(A_{\mathrm{w}}+2A_{\mathrm{xo}}\right)^{2}}\left[1-\exp\left(-\frac{3}{2}\left(A_{\mathrm{w}}+2A_{\mathrm{xo}}\right)\left(\frac{L}{PeH}\right)^{\frac{2}{3}}\right)\right] \quad (4.37)$$

for the uniaxial case. The method for deriving expressions (4.36) and (4.37) for the Sherwood numbers (*i.e.*, Sh_{w} and Sh_{xo}) is somewhat different from those in the irreversible reaction and generator-collector cases, in that observed values of the efficiency do not directly imply a form for the Sherwood numbers. Instead, one must assume the functional forms and adjust the parameters of these functions (the prefactors and/or the scaling exponents in the correlations (4.4) and (4.5)) to fit measured efficiencies.

III. Experimental

III.A. Fabrication

The grooves that drive the transverse flow in our system were fabricated by patterned glass etching in hydrofluoric acid. Borosilicate glass wafers (Borofloat, 100 mm diameter, 1.7 mm thickness, purchased from Mark Optics) were rinsed in deionized water, cleaned in buffered HF (6:1) for 1.5 minutes, and cleaned in a Hamatech automated hot piranha wafer processor. A hard mask of amorphous silicon (a-Si) was deposited in a plasma-enhanced chemical vapor deposition system (IPE 1000 PECVD) at 200C, to a total thickness of ~500 nm. The a-Si deposition is prone to forming particulates that can compromise the integrity of the film, so the deposition was carried out in three steps with a full clean (manual and plasma clean) of the system between steps. The completed film was annealed at 400C for 2.5 hours and cooled to 80C before removal from the hot plate.

A photomask was patterned with the regions to be etched for defining the mixing grooves with a GCA Mann Pattern Generator. Because of the isotropic nature

of the hydrofluoric acid etch and the undercut associated with the etch, narrow windows in the a-Si mask produce nearly half-cylindrical grooves with quarter-spherical ends. It is therefore important to understand the morphology of grooves that will be generated from a given etch window pattern when designing the photomask. Photoresist (Shipley 1818, 2.2 μm) was spun over the a-Si layer and patterned using the photomask and an EVG 620 contact aligner and developed in a Hamatech HMR900 automated wafer processor. The pattern was transferred to the a-Si film by SF_6 / O_2 reactive ion etch (RIE) in an Oxford 80 reactive ion etcher. The wafer was then submerged in concentrated HF (49%) for 7.5 minutes to etch the glass through the pattern in the a-Si mask to a depth of 50 μm. The photoresist was stripped in acetone and the a-Si mask was stripped with the SF_6 / O_2 etch in the Oxford 80 RIE.

Before metallization, the deionized water / buffered HF / piranha clean was repeated, followed by dehydration on a hot plate at 175C for 5 minutes. An adhesion layer (10 nm Ti) and seed layer (50 nm Au) were deposited on the wafers by electron beam evaporation in a CVC SC4500 evaporation system (with evaporation pressure ~$2x10^{-6}$ Torr and evaporation rate ~0.05 nm per second). A thick layer (~4 um) of electroplated Au was deposited to increase conductance and stability of the film. The wafers were coated with a protective layer of photoresist and diced to their final dimensions (1 cm by 7.5 cm) in a KS7100 wafer saw. Through holes were sandblasted for use as inlets and outlets, and the photoresist was stripped in acetone.

Poly-dimethyl-siloxane (PDMS) gaskets were used to define the placement of the microfluidic channel between the electrodes. A photomask with the design for the gaskets was patterned with the GCA Mann Pattern Generator. Master patterns for the PDMS gaskets were prepared by spinning SU-8 (thickness ~110μm) on a silicon wafer and patterning with an EVG 620 contact aligner. The unexposed SU-8 was

developed away to leave a pattern of ridges on the silicon wafer. The surface of the master was functionalized with (tridecafluoro-1,1,2,2-tetrahydrooctyl) trichlorosilane (Gelest). PDMS was prepared using the Sylgard 184 kit from Dow Corning, with a ratio of 10:1 PDMS base to curing agent. The mixed PDMS was poured over the master and all visible bubbles and dust were removed from the PDMS. A transparency was rolled onto the surface, with care taken not to generate bubbles at the PDMS-transparency interface. A rigid glass plate (~2mm thick) was placed on the transparency and a large weight (~2kg) was placed on the glass plate such that the transparency was in contact with the top of the SU-8 pattern. In order to avoid problems due to thermal expansion, the PDMS was allowed to cure overnight at room temperature, then was placed in an oven at 65C for several hours to make the gasket firmer and easier to handle.

III.B. Characterization

The groove structures were characterized by scanning electron microscope (see Figure 4.3(a)) and profilometer and found to be well-defined half-cylindrical and quarter-spherical in shape and uniform with width 100μm and depth 50μm, with variation of several microns. There were defects where pinholes in the a-Si allowed HF to etch undesired regions of the wafer, but in most cases these defects were very small and/or far from the structures of interest. The final thickness of the PDMS gaskets was found to be 110um with variation of 5-10μm. The PDMS tends to compress to about 90% of its thickness when clamped in the acrylic jig, resulting in an actual channel depth of ~100um.

In order to predict the prefactors in (4.5), the ratio of transverse shear rate to axial shear rate near the flat and grooved surfaces was characterized by flow

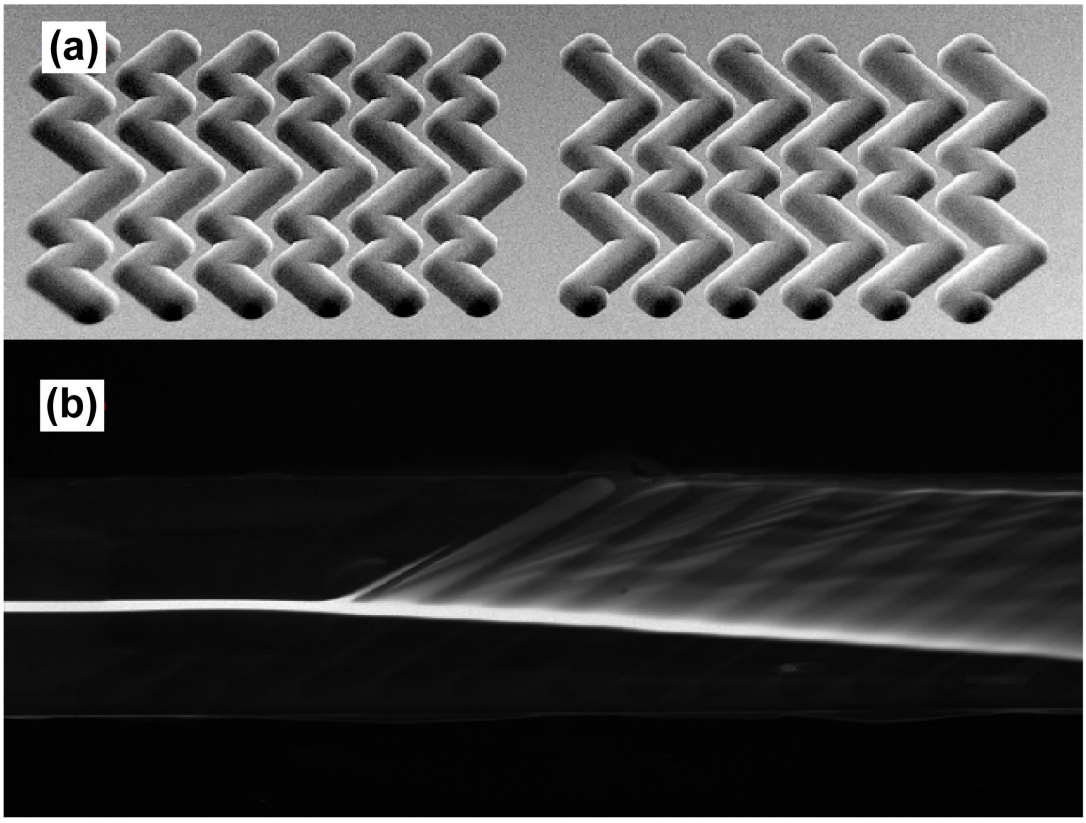

Figure 4.3. Characterization of experimental SEM structures. (a) SEM image of SHM grooves in glass. Groove depth is 50 μm, pattern width is 1 mm, and cycle length is 2.5 mm. (b) Stereoscope image from above of vertical sheet of fluorescent solution being twisted in the transverse flow generated by the grooves. Deflection angle relative to the axial flow direction is ~7.5° near the flat ceiling and ~45° near the grooved floor.

visualization, with images taken from above (see Figure 4.3(b)). The system was assembled with one grooved electrode and one gasket, using the acrylic jig as the opposite bounding surface. Three inlet streams were introduced, an inner stream with a high concentration of fluorescently labeled Dextran of high molecular weight in water and two outer streams of pure water with much higher flow rate. The fluorescent stream forms a sheet in the center of the channel, extending from ceiling to floor. When this stream encounters the grooved surface, it is twisted in the cross section. This twisting is seen as a deflection of the fluorescent stream at the ceiling and floor, in opposite directions (see Figure 4.3(b)). The angle of the deflection with respect to the axial direction gives a measure of the strength of the transverse flow relative to the axial flow. The flow near the ceiling causes a deflection of nearly 7.5 degrees, which corresponds to a ratio of transverse shear rate to axial shear rate of ~1/8 at the ceiling. It is significantly harder to measure the ratio of shear rates near the grooved surface, but the deflection angle is nearly 45 degrees, implying that the transverse flow is nearly as strong as the axial flow, *i.e.* a ratio of shear rates of ~1. There are visible structures downstream in the flow at angles of 25 to 35 degrees, but these structures are more likely indicative of spiraling flow near the top of the groove than the flow near the solid surface. An electrode with long, diagonal grooves that run the full width of the channel (as in Figure 4.1(c)) was used in this characterization step in order to improve the accuracy of the measurement by developing a longer angle to measure. The result for the flow near the flat ceiling should be approximately the same in the chaotically stirred case, but the flow near the grooved surface is likely somewhat weaker in the chaotically stirred case due to the many rounded edges of the grooves that contribute less to the local transverse flow.

III.C. Electrochemical flow cells

The microfluidic system of electrodes and PDMS gasket was clamped in an acrylic jig with inlets and outlets aligned with the holes sandblasted through the electrodes. A standard Ag/AgCl reference electrode (BASi, MR-5275) was fitted into a small reservoir in the jig with a fluid connection to the microchannel for monitoring the solution potential. The working and counter electrodes were connected to a Gamry PCI4 potentiostat card driven by Gamry VFP600 Virtual Front Panel software. Before each run, the working electrode potential was cycled in the range 0 to 1.5V while flowing 0.1M sulfuric acid through the cell in order to clean the electrodes and ensure that the electrodes produced the characteristic cyclic voltammogram (CV) associated with a clean gold surface. Solutions containing ferrocyanide and ferricyanide ions were then introduced into the systems, and CVs were again taken to ensure that only the electrochemical species of interest were active in the voltage range considered. These CVs also furnished an estimate of the formal potential of the ferrocyanide-ferricyanide system in the particular solution in use. Current vs. flow rate data was then taken by holding the working electrode at a potential 200mV in excess of the formal potential, in order to ensure that the working electrode was operating under mass transfer limited conditions. The flow rate was held constant for sufficient time for the current to reach a steady value before moving to a new flow rate.

III.D. Operating conditions

Solutions were prepared using deionized water, sodium sulphate as supporting electrolyte (0.4M, Acros), sodium ferrocyanide as reactant for the reaction at the working electrode (1mM, Sigma-Aldrich), potassium ferricyanide as reactant for the reaction at the counter electrode (2-10mM, Fisher Scientific), and glycerol as an

additive to vary the solution viscosity (0-60wt%, Fisher Scientific). Solution viscosity was measured using Cannon-Fenske viscometers (Cannon Instrument, Models 9721-A59 and 9721-A65).

Experiments were run using flow rates in the range of 1μL/min to 5.75mL/min, delivered by a Harvard Apparatus PHD2000 syringe pump. At a given viscosity, flow rate was varied over three orders of magnitude, and maximum flow rate for a given viscosity was chosen such that the system did not leak and the maximum pressure drop was roughly the same across all viscosities. Solution parameters are given in Table 4.1.

Table 4.1. Solution parameters for electrochemical experiments.
(0.4M Na_2SO_4, 1mM $Na_4Fe(CN)_6$, 2-10mM $K_3Fe(CN)_6$

wt% glycerol	ν (cm^2/s)	η (mPa s)	D_A ($10^{-6}cm^2/s$)	$Sc = \nu/D_A$
0	0.0110	1.14	6.6	1680
40	0.0385	4.36	1.72	22400
60	0.114	13.5	0.56	206000

IV. Results and Discussion

IV.A. Irreversible reaction

Although many attempts were made, a suitable irreversible electrochemical reaction was not found in order to directly test the predictions from our numerical work (Kirtland *et al* 2006, Kirtland *et al* 2009). Most reactions that are chemically irreversible are not sufficiently kinetically fast so as to maintain mass transfer limited

conditions. Attempts were made to find operating conditions that would allow only the oxidation or reduction reaction of a given redox couple to take place, but even when there is another counter reaction that is favored over the reverse reaction of the redox species, there is no way to be sure that the reverse reaction is not occurring at all. In this case, there could be some amount of recycling taking place, and only the total current (arising from all electrochemical reactions taking place) can be measured. Attempts were also made to alter the geometry of the system, such that the counter electrode was placed entirely downstream of the working electrode. At moderate to high *Pe*, this would exclude any recycling current. Unfortunately, due to the small cross section of the channel and the low conductivity of the solutions, this also led to an electrical resistance that was too large to maintain adequate control of the potentials of the working and counter electrodes. An attempt was also made to find a pair of electrochemical half reactions such that the products of one reaction would not be the reactants of the other, but it was not possible to find such a pair that would lead to absolutely no recycling current. Although the conditions of our previous work could not be realized exactly, the theoretical framework developed above for the generator-collector and the double cell system makes it possible to test the predictions for the Sherwood numbers in our previous work without replicating the conditions presented in those works.

IV.B. Generator-collector

Figure 4.4 presents measurements of the length averaged Sherwood number as a function of *Pe* in the generator-collector geometry (Figure 4.2(b)). For flat electrodes (triangles in Figure 4.4), the cube root scaling of Sh_{ave} with *Pe* predicted in (4.6) was confirmed at high *Pe*. The calculated prefactor of 0.116 is smaller than the expected

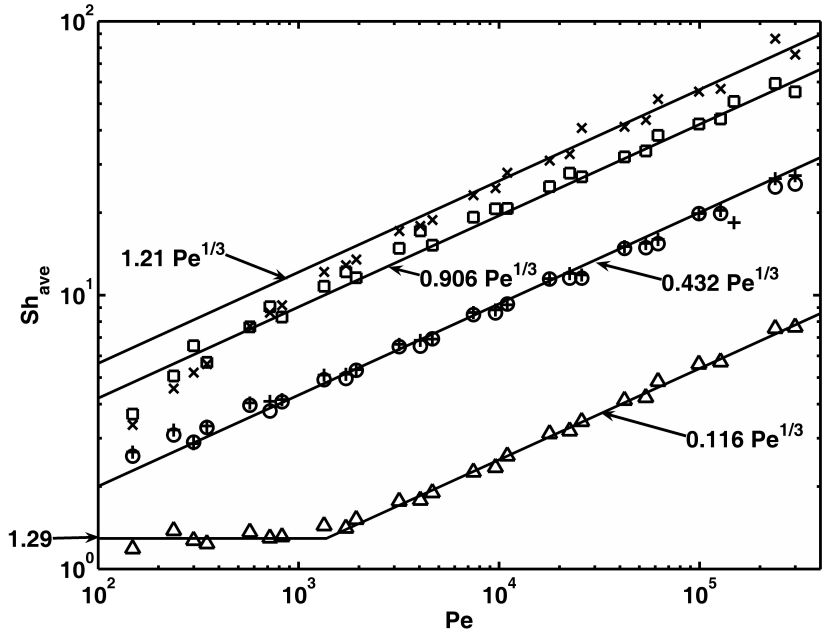

Figure 4.4. Sh_{ave} vs. *Pe* for several generator-collector systems. Symbols are as follows: triangles – flat working electrode (WE), flat counter electrode (CE); + - flat WE, grooved CE, with chaotic flow; circles – flat WE, grooved CE, with non-chaotic flow; squares – grooved WE, flat CE, with chaotic flow; x – grooved WE, flat CE, with non-chaotic flow. Fits to grooved WE data taken above *Pe* = 10000; fits to flat WE, grooved CE data taken using entire range of *Pe*; fits to flat WE, flat CE data taken above *Pe* = 3000 and below *Pe*= 1000. Potential held at 200mV beyond the formal potential of the ferrocyanide-ferricyanide redox couple. All experiments are with ferricyanide in 10:1 excess over ferrocyanide such that the only reaction at the CE is the reduction of ferricyanide.

value of 0.179 in (4.6) by 35%, and the asymptotic value of 1.29, which dominates at low *Pe*, is also smaller than the expected value of 2, as in (4.4), again by about 35%. For all cases with three-dimensional flow (+, x, ○, □), the scaling of *Sh* is again cube root in *Pe* at high *Pe*, as predicted by (4.6). For transfer to a flat working electrode with grooved counter electrode (+ and ○), the prefactor, 0.432, is lower than the expected value of 0.734, by 41%. It is interesting to note that the curves for the chaotically stirred case (+) and the non-chaotically stirred case (○) coincide, which agrees with the results in our previous work. We found that the difference between the Sherwood number in the presence and absence of chaos is subtle near stationary surfaces, and that the effect of a poorly mixed 3D flow (one lacking Lagrangian chaos) is only noticeable as a slight decrease in the local Sherwood number at large axial distance (Kirtland *et al* 2009). The length averaged Sherwood number is not likely to demonstrate this difference for a device of moderate length, which explains the fact that the chaotic (+) and non-chaotic (○) cases coincide.

For transfer to the grooved surface, assuming a ratio of axial to transverse shear rate of about 1 from the visual characterization of the flow (see Section III.B), the prefactors calculated for the chaotic (□) and non-chaotic (x) case, 0.906 and 1.21 respectively, are again smaller than the expected value of 1.47 (by 38% in the chaotic flow and 18% in the non-chaotic flow). In this case the non-chaotic result exceeds the chaotic result. This observation is surprising given our previous work on the modified Grætz behavior (Kirtland *et al* 2006, Kirtland *et al* 2009). As mentioned above, the difference between the effects due to chaotic and non-chaotic flow is subtle, but chaotic flow should not result in a lower flux. The well mixed flow should be able to maintain a thinner boundary layer near the reactive surface by mixing depleted fluid into the bulk before it returns to the reactive surface. In the generator-collector system,

however, the counter electrode reconcentrates fluid as it passes near the electrode surface, decreasing the effects of reinforced depletion. An explanation for the fact that the Sherwood number in the non-chaotic flow exceeds that in the chaotic flow is that the shear rate near the grooved surface may be stronger for the long, diagonal grooves than for the herringbone structures. The many spherical caps at the intersection of the legs of the SHM pattern (see Figure 4.3(a)) will contribute less to the transverse flow, and therefore to the average shear rate, than regions without these caps. The non-chaotic case only has caps at the very edges of the channel. The average shear rate in the chaotic flow will therefore be smaller compared to the average shear rate in the non-chaotic case, leading to a smaller prefactor for the chaotic case. That this effect is not seen for transfer near the flat surface opposite the grooves implies that transfer at the far surface is less sensitive to the specifics of the local flow at the grooved surface, which is in agreement with our previous result that transfer to flat, stationary surfaces is less sensitive to the chaotic character of the flow.

With all cases other than the non-chaotic grooved surface showing errors of 35-41% below the expected values, it seems likely that there is a systematic error in the system. Expanding the expression for the average Sherwood number (4.25):

$$Sh_{\text{ave}} = \frac{PeH}{L}\varepsilon = \frac{QH}{WDL}\frac{i_{\text{w}}}{nFC_{\text{A0}}Q} = \frac{i_{\text{w}}}{nFL}\left(\frac{H}{WDC_{\text{A0}}}\right) \tag{4.38}$$

the quantity in parentheses contains parameters that may have significant uncertainties. Due to the compression or shifting of the PDMS gasket, H and W may differ from their expected values by 10% or more, but unless the compression or shifting is inherent to the setup of the gasket or jig, the effect should introduce random error rather than systematic error. The value of D depends on measurements of the

viscosity, which may also have errors on the order of 10%, but independent measurements of the viscosities of the three solutions used for each experiment should also introduce random error, rather than systematic error. It is possible that an error in the concentration of the stock solution of ferrocyanide from which the working solutions were diluted could have produced a systematic shift in the initial concentrations across the entire set of experiments, as the same working solution was used in all of the generator-collector experiments. This error in concentration seems likely to be the reason for the consistent error in the prefactors, and further study of the source of this error is warranted.

It should be noted that for transfer to the grooved surface in the non-chaotically stirred flow and, to a lesser extent, the chaotically stirred flow, the average Sherwood number falls off of the $Pe^{1/3}$ line with decreasing Pe, implying faster scaling with Pe at low Pe. This effect may be due to the boundary layer growing thick enough that it extends outside of the grooves. The transverse flow acts approximately like a slipping surface, and this effective slip may be what the concentration profile sees once the boundary layer is sufficiently thick (Stroock *et al* 2002b). A slipping surface should show square root scaling in Pe, rather than cube root scaling, which would cause the curve to look steeper at low Pe.

IV.C. Double cell: recycling and crossover

Figure 4.5 presents measurements of the efficiency as a function of Pe in the double cell geometry (Figure 4.2(c)). Due to the dependence of the efficiency on the Sherwood number for the various transfer processes in the double cell geometry, (4.36) and (4.37) cannot be solved directly for Sh_{ave}. We therefore present the efficiency as a function of Pe for the uniaxial and chaotically stirred cases in the

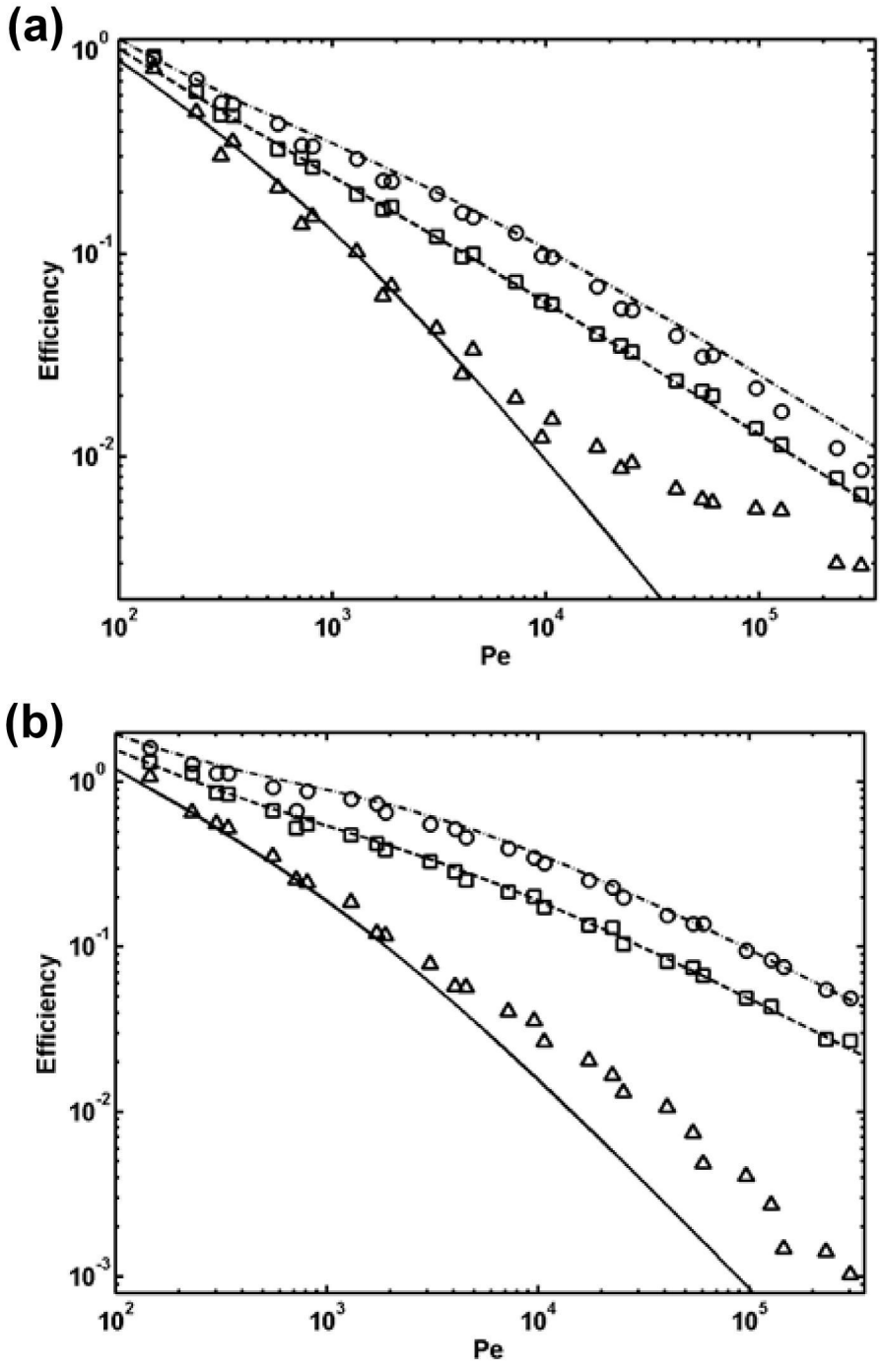

Figure 4.5. Efficiency vs. *Pe* for double cell systems. (a) Both electrodes flat. (b) Both electrodes grooved with $r = 1/3$. Symbols are as follows: triangles – $f = 0$; squares – $f = ½$; circles – $f = 1$. Curves are fits to equation (29) and (30) with $Sh_w = 0.558Z^{1/3}$ and $Sh_{xo} = 0.857Z^{1/3}$ in (a) and $Sh_w = 0.541Pe^{1/3}$ and $Sh_{xo} = 0.183Pe^{1/3}$ in (b).

double cell. We fit this data to the expressions (4.36) and (4.37) using a nonlinear least-squares Marquardt-Levenberg fit in the software package Gnuplot, varying the prefactors that appear in (4.36) [B_w and B_{xo} in Sh_w and Sh_{xo}, as in (4.5)] and (4.37) [A_w and A_{xo} as in (4.4)] but maintaining the predicted scaling for Pe in all cases. The curves for ferrocyanide injected near the working electrode ($f = 1$) and on both sides of the membrane ($f = ½$) are represented well by the fits for both uniaxial and chaotically stirred flow. The case of complete crossover (with ferrocyanide introduced only near the counter electrode, $f = 0$) is well represented at low Pe, but tends to exceed the fit curve at high Pe. The reason for this behavior in the crossover case is likely due to convective crossover through the membrane due to local differences in pressure that are accentuated at high flow rate. Pressure differences across the membrane are larger when both streams are at higher pressure, resulting in larger volumes of fluid convected through the pores in the membrane. The amount of crossover is small enough that its effect is negligible in the presence of the large efficiencies in the $f = 1$ and $f = ½$ cases, but at low efficiencies with $f = 0$, it becomes relevant.

The expected scaling of $(z/PeH)^{-1/3}$ for uniaxial flow and $Pe^{1/3}$ for chaotically stirred flow are demonstrated by the goodness of the fits. The anomalous scaling that is present at low Pe in the generator-collector case is not clearly seen at low Pe in the double cell. It should be noted, however, that the effect is only noticeable in the chaotically stirred generator-collector case for $Pe < 300$. The prefactors in the uniaxial case, $A_w = 0.558$ and $A_{xo} = 0.857$, are smaller than the expected value of $A_0 = 0.98$ in (4.4) for transfer in uniaxial flow. The prefactors in the chaotically stirred flow, $B_w = 0.541$ and $B_{xo} = 0.183$, are smaller than the expected values for transfer to the grooved surface (*i.e.* the electrode) and the flat surface (*i.e.* the membrane) respectively, but they are also smaller than the observed values in Figure 4.4 by more than a factor of 2.

The deviation of our prefactors from the theoretically predicted values and the inconsistency of results for the same prefactor in different geometries calls for a closer look at the values of the geometric and operating parameters of the system. A rigid material, like silicon, to replace the PDMS, might also ensure that the geometric parameters are measured correctly.

V. Conclusions

We have demonstrated the modified Grætz behavior experimentally through electrochemical measurements. We have generalized our study to add two system geometries to the irreversible reaction case in our previous work: the generator-collector, where solute can be recycled between the working and counter electrodes resulting in a feedback that amplifies the signal; and the double cell, where the working and counter electrodes are in separate streams separated by a diffusively permeable membrane. Our predictions of the scaling of the average Sherwood number with the Péclet number, $Pe^{1/3}$, due to the Grætz and modified Grætz behavior in uniaxial, chaotically stirred, and non-chaotically stirred flows are confirmed by the experimental measurements. The theoretically predicted prefactors exceed the experimentally determined values in all cases, which calls for more investigation into sources of systematic error in the calculation of efficiency and length-averged Sherwood number. An increase in the length-averaged Sherwood number of up to an order of magnitude over the uniaxial case was observed, which is technologically important in such fields as bioanalytical chemistry, where analysis time could be reduced by an order of magnitude, and microfluidic power generation for consumer electronics, where fuel efficiency and total power output could be increased by an order of magnitude. Future directions include further investigation of the stronger

scaling of *Sh* with *Pe* in stirred generator-collector systems at low *Pe* and of the prefactors in all cases studied here, the suspected convective crossover in the double cell at high flow rate, and running the SHM system as a surface-based immunoassay as a means of probing the irreversible reaction geometry that was elusive in our electrochemical study.

REFERENCES

Acharya N, Sen M and Chang H C 1992 Heat transfer enhancement in coiled tubes by chaotic mixing *Int. J. Heat Mass Transfer* **35** 2475–89

Acharya N, Sen M and Chang H C 2001 Analysis of heat transfer enhancement in coiled-tube heat exchangers *Int. J. Heat Mass Transfer* **44** 3189–99

Aref H 1984 Stirring by chaotic advection *J. Fluid Mech.* **143** 1–21

Bryden M D and Brenner H 1996 Effect of laminar chaos on reaction and dispersion in eccentric annular flow *J. Fluid Mech.* **325** 219–37

Bryden M D and Brenner H 1999 Mass-transfer enhancement via chaotic laminar flow within a droplet *J. Fluid Mech.* **379** 319–31

Chang H C and Sen M 1994 Application of chaotic advection to heat transfer *Chaos Solitons Fractals* **4** 955–75

Cohen J L, Westly D A, Pechenik A and Abruna H D 2005 Fabrication and preliminary testing of a planar membraneless microchannel fuel cell *J. Power Sources* **139** 96–105

Ferrigno R, Stroock A D, Clark T D, Mayer M and Whitesides G M 2002 Membraneless vanadium redox fuel cell using laminar flow *J. Am. Chem. Soc.* **124** 12930–1

Foley J O, Mashadi-Hossein A, Fu E, Finlayson B A and Yager P 2008 Experimental and model investigation of the time-dependent 2-dimensional distribution of binding in a herringbone microchannel *Lab Chip* **8** 557–64

Ganesan V, Bryden M D and Brenner H 1997 Chaotic heat transfer enhancement in rotating eccentric annular-flow systems *Phys. Fluids* **5** 1296–306

Ghosh S, Chang H C and Sen M 1992 Heat transfer enhancement due to slender recirculation and chaotic transport between counter-rotating eccentric cylinders *J. Fluid Mech.* **238** 119–54

Ghosh S, Leonard A and Wiggins S 1998 Diffusion of a passive scalar from a no-slip boundary into a twodimensional chaotic advection field *J. Fluid Mech.* **372** 119–63

Golden J P, Floyd-Smith T M, Mott D R and Ligler F S 2007 Target delivery in a microfluidic immunosensor *Biosens. Bioelectron.* **22** 2763–7

Grætz L 1885 *Ann. Phys. Chem.* **25** 337–57

Horner M, Metcalfe G, Wiggins S and Ottino J M 2002 Transport enhancement mechanisms in open cavities *J. Fluid Mech.* **452** 199–229

Ismagilov R F, Stroock A D, Kenis P J A, Whitesides G and Stone H A 2000 Experimental and theoretical scaling laws for transverse diffusive broadening in two- phase laminar flows in microchannels *Appl. Phys. Lett.* **76** 2376–8

Kamholz A E, Weigl B H, Finlayson B A and Yager P 1999 Quantitative analysis of molecular interaction in a microfluidic channel: the T-sensor *Anal. Chem.* **71** 5340–7

Kirtland J D, McGraw G J and Stroock A D 2006 Mass transfer to reactive boundaries from steady threedimensional flows in microchannels *Phys. Fluids* **18** 073602

Kirtland J D, Siegel C R and Stroock A D 2009 Interfacial mass transport in steady three-dimensional flows in microchannels *New J. Phys.* **11** 075028

Lefevre A, Mota J P B, Rodrigo A J S and Saatdjian E 2003 Chaotic advection and heat transfer enhancement in Stokes flows *Int. J. Heat Fluid Flow* **24** 310–21

Lévêque A M 1928 Les lois de la transmission de chaleur par convection *Annal. Mines* **13** 283–99

Mokrani A, Castelain C and Peerhossaini H 1997 The effects of chaotic advection on heat transfer *Int. J. Heat Mass Transfer* **40** 3089–104

Nishimura T, Murakami S and Kawamura Y 1993 Mass transfer in a symmetrical sinusoidal wavy-walled channel for oscillatory flow *Chem. Eng. Sci.* **48** 1793–800

Nishimura T 1995 Oscillatory flow and mass transfer within asymmetric and symmetrical channels with sinusoidal wavy walls *Heat Mass Transfer* **30** 269–78

Nishimura T and Kojima N 1995 Mass transfer in a symmetrical sinusoidal wavy-walled channel for pulsatile flow *Int. J. Heat Mass Transfer* **38** 1719–31

Peerhossaini H, Castelain C and Leguer Y 1993 Heat exchanger design based on chaotic advection *Exp. Therm. Fluid Sci.* **7** 333–44

Saatdjian E, Midoux N, Chassaing M I G, Leprevost J C and Andre J C 1996 Chaotic mixing and heat transfer between confocal ellipses: experimental and numerical results *Phys. Fluids* **8** 677–91

Shrivastava A, Kumar S and Cussler E L 2008 Predicting the effect of membrane spacers on mass transfer *J. Memb. Sci.* **323** 247–56

Squires T M, Messinger R J and Manalis S R 2008 Making it stick: convection, reaction and diffusion in surfacebased biosensors *Nat. Biotechnol.* **26** 417–26

Stroock A D, Dertinger S K W, Ajdari A, Mezic I, Stone H A and Whitesides G M 2002a Chaotic mixer for microchannels *Science* **295** 647–51

Stroock A D, Dertinger S KW, Whitesides G M and Ajdari A 2002b Patterning flows using grooved surfaces *Anal. Chem.* **74** 20

Teles F R R and Fonseca L P 2008 Trends in DNA biosensors *Talanta* **77** 606–23

Vijayendran R A, Motsegood K M, Beebe D J and Leckband D E 2003 Evaluation of a three-dimensional micromixer in a surface-based biosensor *Langmuir* **19** 1824–8

CHAPTER 5

CONCLUSION

In this dissertation, we have motivated and expounded a new perspective on the problem of interfacial mass transfer in steady, laminar flows. The modified Grætz behavior explains, both mathematically and mechanistically, how three-dimensional flows can increase mass transfer to interfaces over the case of similar uniaxial flows. The classic Grætz result for transfer to a stationary solid surface bounding a uniaxial flow predicts the presence of an entrance region (where the Sherwood number for mass transfer *Sh* decreases rapidly as the thickness of the concentration boundary layer increases with increasing axial distance) and an asymptotic region (where the boundary layer fills the system and *Sh* assumes an asymptotic value that is geometry dependent, but does not depend on the Péclet number *Pe* or the axial distance). In contrast, the modified Grætz behavior predicts that in the presence of a certain class of three-dimensional laminar flows, the depleted fluid in the boundary layer can be swept away from the reactive surface and into the bulk, halting the growth of the boundary layer, in which case *Sh* takes on an asymptotic value that is larger than that in the uniaxial case and that increases with increasing *Pe*. The modified Grætz behavior also elucidates the role of Lagrangian chaos in maintaining high rates of interfacial transfer in the laminar flow regime: the only way to guarantee that the boundary layer will not continue to grow is to ensure that fluid leaving the reactive interface is mixed with the bulk before it returns to the interface. In laminar flows, chaos is essential to mixing the fluid efficiently enough to outpace the return of depleted fluid to the surface.

We have accomplished these advances through three main approaches: development of a numerical code to track reactive solute particles in a simulated flow; development of a theoretical framework with the ability to predict the characteristics

of transfer processes, especially the local Sherwood number for mass transfer *Sh* to interfaces; and development of experimental systems to test predictions for *Sh*. Results from our numerical code were the original source of inspiration for the articulation of the modified Grætz behavior. Reactive flux and concentration profiles built from trajectories of solute particles first made clear the connection between the Eulerian concentration field and its associated boundary layer, the Lagrangian trajectories of individual solute particles experiencing the convection-diffusion process, and the local rate of mass transfer to the reactive interface (i.e. the density of collisions of solute with the wall). The success of the theoretical framework in distilling the overall convection-diffusion process into a mass transfer coefficient (*i.e*. *Sh*) made it possible to extend our understanding to include transfer to solid, moving interfaces and diffusive, fluid-fluid interfaces in the flow, and also facilitated our understanding of the necessary considerations for a full theoretical development of the experimental systems that we have studied. The numerical and experimental results verified our theoretical predictions for the scaling of *Sh* with *Pe* and axial distance; the numerical estimates of the prefactors in the correlations for *Sh* supported our theoretical predictions, although the experimental estimates were consistently lower than the predicted values. The numerical code also allowed us to study the relationship between the mixing length (the axial length scale associated with mixing the fluid) and the return length (the axial length scale associated with the return of depleted fluid to the reactive interface), leading to our conclusions on the role of Lagrangian chaos in interfacial mass transfer.

Future directions for the development of the modified Grætz behavior include: implementation of an experimental system analogous to our numerical system, requiring an irreversible (but kinetically fast) surface reaction, such as a surface binding immunoassay, to further test our theoretical predictions; investigation of

possible sources of error in the experimental prefactors due to systematic errors in measurements of geometric parameters, viscosity, and concentration and development of a more rigid gasket; exploration of the anomalous scaling exhibited by the generator-collector system at low *Pe* and determination as to its possible origin in an effective slipping boundary condition (see Figure 4.4); analysis of the validity of the modified Grætz behavior in cases involving transfer between partially disconnected sets with some convective crossover (see Figures 3.14 and 4.5); and consideration of a general solution to a periodic Sturm-Liouville problem for the modified Grætz case in a periodic flow, analogous to the Sturm-Liouville problem that characterizes the classic Grætz problem, but with an asymptotic state that is periodically self-similar (*i.e.* $C(x,y,z) = C(x,y,z_0)\, f(\mathrm{n})$, where $z = z_0 + n\, L$, and L is the period of the velocity modulation) rather than uniformly self-similar (*i.e.* $C(x,y,z) = C(x,y)\, f(\mathrm{z})$).

APPENDIX

shm06a.c: code for particle tracking in a simulated flow field

```
// LIBRARIES
#include <stdio.h>   // standard input/output
#include <stddef.h> // standard definitions
#include <stdlib.h>  // standard library
#include <sys/time.h>        // timing functions
#include <math.h>   // mathematical functions

// MACROS
#define MAXINT 2147483647
#define NR_END 1  // Definitions for Numerical
#define FREE_ARG char*  // Recipes (NR) routines

// FUNCTION PROTOTYPES ( functions are defined and commented after
main() )
void nrerror(char error_text[]);
double *dvector(long nl, long nh);
double **dmatrix(long nrl, long nrh, long ncl, long nch);
int **imatrix(long nrl, long nrh, long ncl, long nch);
double ***d3tensor(long nrl, long nrh, long ncl, long nch, long ndl, long ndh);
int ***i3tensor(long nrl, long nrh, long ncl, long nch, long ndl, long ndh);
double ran3(long *idum);
double gasdev(long *idum);
void free_dvector(double *v, long nl, long nh);
void free_dmatrix(double **m, long nrl, long nrh, long ncl, long nch);
void free_imatrix(int **m, long nrl, long nrh, long ncl, long nch);
void free_d3tensor(double ***t, long nrl, long nrh, long ncl, long nch,
                long ndl, long ndh);
void free_i3tensor(int ***t, long nrl, long nrh, long ncl, long nch,
                long ndl, long ndh);
void check(char point[80]);
void interp_setup(double **ux, double **uy, double **uz, int Nx, int Ny, int Ni,
                double w, double *dxinv, double *dyinv, double Lcyc,
                  double *Lcycinv2);
inline void interp1D(double x, double *xa, double *ua, int Ni, double *u,
           double *dxinv, double **P);
inline void interp2D(double *x, double *xa, double *ya, double **ua, int Ni,
           double *u, double *dxinv, double *dyinv, double **P, double *ytmp);
inline void interp(double *x, double *xa, double *ya, double **ux, double **uy,
           double **uz, double **uxi, double **uyi, double **uzi, int Ni,
           double *u, double *dxinv, double *dyinv, double **P, double *ytmp,
           double w, int Nx, int Ny, double Lcycinv2, int plugflag,
```

```
            double uzave);

// MAIN PROGRAM
int main(int argc, char *argv[])
{
  // DECLARATION OF VARIABLES
  int i, j, k, l, m, n, ll, mm, nn, Zflag=0, tflag=0, flags[4], dummyint, status=0,
statflag = 1;
  double x[4], k1[4], k2[4], k3[4], k4[4], k5[4], k6[4], u[4], sigma;
  double pos[4], xold[4], err[4], dt, dtnew, f, *ytmp, **P;
  int Ncyc, plugflag, Nsteps, Ni, poincare, Nframe, Nt, Nskip, statframe;
  double w, Lcyc, Uslip, Uz, D, dtmax, maxerr;
  double Lframe, tframe, Lcycinv2;
  int Nx, Ny;
  double **ux, **uy, **uz, **uxi, **uyi, **uzi, *xa, *ya;
  double uzave=0, dx, dy, *dxinv, *dyinv;
  int Npart, initflag;
  double **initpos;
  long idumx, idumy, idumz;
  int ***Lf, ***Rf, ***Bf, ***Tf, ***Zf, ***tf;
  double ***Lx, ***Rx, ***Bx, ***Tx, ***Zx, ***tx;
  FILE *infile, *outfile, *Lfile, *Rfile, *Bfile, *Tfile, *remfile, *snapfile;
  char velname[80], initname[80], Zname[80],
tname[80],dummystr[80],remname[80];
  char Lname[80], Rname[80], Bname[80], Tname[80], trajname[80],
trajnameM[80];
  struct timeval start, finish;
  double calctime=0, Nsec;
  int Nrxn, nL, nR, nB, nT;
  // CONSTANTS FOR 5TH ORDER RUNGE-KUTTA INTEGRATION
  double b21=.2, b31=.075, b32=.225, b41=.3, b42=-.9, b43=1.2;
  double b51=-11./54., b52=2.5, b53=-70./27., b54=35./27., b61=1631./55296.;
  double b62=175./512, b63=575./13824., b64=44275./110592.,
b65=253./4096.;
  double c1=37./378., c2=0., c3=250./621., c4=125./594, c5=0.,
c6=512./1771.;
  double dc1=c1-2825./27648., dc2=c2-0., dc3=c3-18575./48384.;
  double dc4=c4-13525./55296., dc5=c5-277./14336., dc6=c6-.25;
  check("Variables declared");

  // READ IN PARAMETERS
  infile = fopen(argv[1], "r");
  //infile = fopen("params", "r"); // for profiling
  fscanf(infile, "%s %lf %s %lf %s %d %s %lf",
```

```
    &dummystr, &w, &dummystr, &Lcyc, &dummystr, &Ncyc, &dummystr,
&Uslip);
  fscanf(infile, "%s %lf %s %lf %s %d %s %lf",
    &dummystr, &Uz, &dummystr, &D, &dummystr, &plugflag, &dummystr,
&dtmax);
  fscanf(infile, "%s %d %s %lf %s %d",
    &dummystr, &Nsteps, &dummystr, &maxerr, &dummystr, &Ni);
  fscanf(infile, "%s %s %s %d %s %d",
    &dummystr, &velname, &dummystr, &Npart, &dummystr, &initflag);
  fscanf(infile, "%s %s %s %d %s %d",
    &dummystr, &initname, &dummystr, &poincare, &dummystr, &Nframe);
  fscanf(infile, "%s %s %s %d %s %s %s %s",
    &dummystr, &Zname, &dummystr, &Nt, &dummystr, &tname, &dummystr,
&Lname);
  fscanf(infile, "%s %s %s %s %s %s",
    &dummystr, &Rname, &dummystr, &Bname, &dummystr, &Tname);
  fscanf(infile, "%s %d %s %s %s %d",
    &dummystr, &Nskip, &dummystr, &trajname, &dummystr, &statframe);
  fscanf(infile, "%s %s %s %d",
    &dummystr, &remname, &dummystr, &Nrxn);
  fclose(infile);
  remfile = fopen(remname, "w");
  fprintf(remfile,
"w\t=%g\nLcyc\t=%g\nNcyc\t=%d\nUslip\t=%g\nUzmax\t=%g\n",
                w, Lcyc, Ncyc, Uslip, Uz);
  fprintf(remfile,
"D\t=%g\nplug\t=%d\ndtmax\t=%g\nNsteps\t=%d\nmaxerr\t=%g\n",
                D, plugflag, dtmax, Nsteps, maxerr);
  fprintf(remfile, "Ni\t=%d\nvel\t=%s\nNpart\t=%d\ninitflag\t=%d\ninit\t=%s\n",
                Ni, velname, Npart, initflag, initname);
  fprintf(remfile,
"poincare\t=%d\nNframe\t=%d\nZ\t=%s\nNt\t=%d\nt\t=%s\nL\t=%s",
                poincare, Nframe, Zname, Nt, tname, Lname);
  fprintf(remfile,
"\nR\t=%s\nB\t=%s\nT\t=%s\nNskip\t=%d\ntraj\t=%s\nstat\t=%d\nNrxn\t=%d\n
",
                Rname, Bname, Tname, Nskip, trajname, statframe, Nrxn);
  fflush(remfile);
  check("Parameters read");

  // CALCULATE SOME USEFUL CONSTANTS
  sigma = sqrt(2. * D * dtmax);
  Lframe = Lcyc * Ncyc / Nframe;

  // GENERATE SEEDS FOR (PSEUDO)RANDOM NUMBER GENERATOR
```

```
gettimeofday(&start, NULL); // reads clock time
idumx = start.tv_sec + start.tv_usec;
idumy = (int)(MAXINT*ran3(&idumx));
idumz = (int)(MAXINT*ran3(&idumy));
idumx = (int)(MAXINT*ran3(&idumz));

// READ IN VELOCITIES
infile = fopen(velname, "r");
fscanf(infile, "%d %d", &Nx, &Ny); // number of grid points in x and y
for(i = 3; i <= Nx; i++) fscanf(infile, "%d", &dummyint); // for uniform width
xa = dvector(1, Nx);
for(i = 1; i <= Nx; i++) xa[i] = -w + 2. * w * (i - 1) / (Nx - 1);
ya = dvector(1, Ny);
for(j = 1; j <= Ny; j++) ya[j] = -1. + 2. * (j - 1) / (Ny - 1);
ux = dmatrix(1, Nx, 1, Ny); // allocate memory for velocity matrices
uy = dmatrix(1, Nx, 1, Ny);
uz = dmatrix(1, Nx, 1, Ny);
for(j = 1; j <= Ny; j++)
  for(i = 1; i <= Nx; i++) {
    fscanf(infile, "%lf", &ux[i][j]);
    ux[i][j] *= Uslip*Uz;
  }
for(j = 1; j <= Ny; j++)
  for(i = 1; i <= Nx; i++) {
    fscanf(infile, "%lf", &uy[i][j]);
    uy[i][j] *= Uslip*Uz;
  }
for(j = 1; j <= Ny; j++)
  for(i = 1; i <= Nx; i++) {
    fscanf(infile, "%lf", &uz[i][j]);
    uz[i][j] *= Uz;
    uzave += uz[i][j]; // sums axial velocity for division below
  }
fclose(infile);
uzave /= Nx * Ny; // simple average of axial velocity at all grid points
tframe = Lcyc * Ncyc / uzave / Nt; // length of each time frame
fprintf(remfile, "uz_ave = %g\nuz_corner = %g\nuz_center = %g\n",
        uzave, uz[1][1], uz[(Nx+1)/2][(Ny+1)/2]);
fflush(remfile);
check("Velocities read");

// MEMORY ALLOCATION
Lx = d3tensor(1, Nrxn, 1, Npart, 0, 3);
Rx = d3tensor(1, Nrxn, 1, Npart, 0, 3);
Bx = d3tensor(1, Nrxn, 1, Npart, 0, 3);
```

```
  Tx = d3tensor(1, Nrxn, 1, Npart, 0, 3);
  Lf = i3tensor(1, Nrxn, 1, Npart, 0, 3);
  Rf = i3tensor(1, Nrxn, 1, Npart, 0, 3);
  Bf = i3tensor(1, Nrxn, 1, Npart, 0, 3);
  Tf = i3tensor(1, Nrxn, 1, Npart, 0, 3);
  Zx = d3tensor(0, Nframe, 1, Npart, 0, 3);
  Zf = i3tensor(0, Nframe, 1, Npart, 0, 4);
  tx = d3tensor(0, Nt, 1, Npart, 0, 3);
  tf = i3tensor(0, Nt, 1, Npart, 0, 4);
  uxi = dmatrix(1, Ni, 1, Ni);
  uyi = dmatrix(1, Ni, 1, Ni);
  uzi = dmatrix(1, Ni, 1, Ni);
  dxinv = dvector(1, Ni);
  dyinv = dvector(1, Ni);
  ytmp = dvector(1, Ni);
  P = dmatrix(1, Ni, 1, Ni);
  initpos = dmatrix(1, Npart, 0, 3);
  check("Memory allocated");
  interp_setup(ux, uy, uz, Nx, Ny, Ni, w, dxinv, dyinv, Lcyc, &Lcycinv2);
  fprintf(remfile, "2/Lcyc = %g\n1/2dx = %g\n1/3dy = %g\n", Lcycinv2, dxinv[2],
dyinv[3]);
  fflush(remfile);
  // INITIALIZE POSITIONS
  if(!initflag) { // initial positions from file
    infile = fopen(initname, "r");
    for(m = 1; m <= Npart; m++)
      for(n = 0; n <= 3; n++)
        fscanf(infile, "%lf", &initpos[m][n]);
    fclose(infile);
  }
  else { // (pseudo)randomly generated initial positions
    outfile = fopen(initname, "w");
    for(m = 1; m <= Npart; m++) {
      initpos[m][3] = 1.;
      u[3] = 0.;
      while(initpos[m][3] > u[3]) { // velocity weighted by rejection method
        initpos[m][1] = 2. * w * ran3(&idumx) - w;
        initpos[m][2] = 2. * ran3(&idumy) - 1.;
        initpos[m][3] = Lcyc /4.;
        interp(initpos[m], xa, ya, ux, uy, uz, uxi, uyi, uzi, Ni, u, dxinv,
                dyinv, P, ytmp, w, Nx, Ny, Lcycinv2, plugflag, uzave);
        initpos[m][3] = ran3(&idumz);
      }
      initpos[m][0] = 0.;
      initpos[m][3] = 0.;
```

```
    if(poincare) fprintf(outfile, "%23.15e%23.15e%23.15e%23.15e\n",
            initpos[m][0], initpos[m][1], initpos[m][2], initpos[m][3]);
    else fprintf(outfile, "%13.5e%13.5e%13.5e%13.5e\n",
            initpos[m][0], initpos[m][1], initpos[m][2], initpos[m][3]);
  }
  fclose(outfile);
}
check("Initial positions ready");

// ACTUAL CALCULATION
gettimeofday(&start, NULL);
calctime = start.tv_sec;
calctime = calctime - 86400*floor(calctime/86400);
fprintf(remfile, "Current time: %d:", (int) floor(calctime/3600));
calctime = calctime - 3600*floor(calctime/3600);
fprintf(remfile, "%d:", (int)floor(calctime/60));
calctime = calctime - 60*floor(calctime/60);
fprintf(remfile, "%d\n", (int)calctime);
fprintf(remfile, "Starting simulation:\n");
fprintf(remfile, "# of particles: %d\n# of cycles: %d\n", Npart, Ncyc);
fflush(remfile);
dtnew = dtmax;

// LOOP OVER PARTICLES
for(m = 1; m <= Npart; m++) {
  dt = dtmax;
  for(n = 0; n <= 3; n++) {
    flags[n] = 0;
    for(l = 1; l <= Nrxn; l++) {
      Lf[l][m][n] = 0;
      Rf[l][m][n] = 0;
      Bf[l][m][n] = 0;
      Tf[l][m][n] = 0;
      Lx[l][m][n] = -1.;
      Rx[l][m][n] = -1.;
      Bx[l][m][n] = -1.;
      Tx[l][m][n] = -1.;
    }
    for(l = 0; l <= Nframe; l++) {
        Zf[l][m][n] = 0;
        Zx[l][m][n] = -1.;
    }
    for(l = 0; l <= Nt; l++) {
        tf[l][m][n] = 0;
        tx[l][m][n] = -1.;
```

```
      }
      pos[n] = initpos[m][n];
    }
    Zflag = 0;
    tflag = 0;
    if(Nskip > 0 && poincare) { // start trajectory output
      sprintf(trajnameM, "%s_%d", trajname, m);
      outfile = fopen(trajnameM,"w");
      for(n = 0; n <= 3; n++) fprintf(outfile, "%23.15e", pos[n]);
      fprintf(outfile, "\n");
    }
    k = 0;
//    while(k <= Nsteps && (flags[0]+flags[1]+flags[2]+flags[3]) < 4*Nrxn) {
    while(k <= Nsteps && pos[3] < Ncyc*Lcyc) {
//    while(k <= Nsteps && ((flags[0]+flags[1]+flags[2]+flags[3]) < 4*Nrxn || Zflag
< Nframe)) {
      for(n=1;n<=3;n++) {
          x[n] = pos[n];
          xold[n] = pos[n];
          k1[n] = 0.;
          k2[n] = 0.;
          k3[n] = 0.;
          k4[n] = 0.;
          k5[n] = 0.;
          k6[n] = 0.;
      }
      // 5th order Runge Kutta integration - adaptive step size
      err[0] = -1.;
      while(err[0] < 0. && k <= Nsteps) {
        interp(x, xa, ya, ux, uy, uz, uxi, uyi, uzi, Ni, u, dxinv, dyinv, P,
              ytmp, w, Nx, Ny, Lcycinv2, plugflag, uzave);
          for(n=1;n<=3;n++) {
            k1[n] = dt*u[n];
            x[n] = xold[n] + b21*k1[n];
          }
        interp(x, xa, ya, ux, uy, uz, uxi, uyi, uzi, Ni, u, dxinv, dyinv, P,
              ytmp, w, Nx, Ny, Lcycinv2, plugflag, uzave);
          for(n=1;n<=3;n++) {
            k2[n] = dt*u[n];
            x[n] = xold[n] + b31*k1[n] + b32*k2[n];
          }
        interp(x, xa, ya, ux, uy, uz, uxi, uyi, uzi, Ni, u, dxinv, dyinv, P,
              ytmp, w, Nx, Ny, Lcycinv2, plugflag, uzave);
          for(n=1;n<=3;n++) {
            k3[n] = dt*u[n];
```

```
      x[n] = xold[n] + b41*k1[n] + b42*k2[n] + b43*k3[n];
    }
  interp(x, xa, ya, ux, uy, uz, uxi, uyi, uzi, Ni, u, dxinv, dyinv, P,
       ytmp, w, Nx, Ny, Lcycinv2, plugflag, uzave);
    for(n=1;n<=3;n++) {
      k4[n] = dt*u[n];
      x[n] = xold[n] + b51*k1[n] + b52*k2[n] + b53*k3[n] + b54*k4[n];
    }
  interp(x, xa, ya, ux, uy, uz, uxi, uyi, uzi, Ni, u, dxinv, dyinv, P,
       ytmp, w, Nx, Ny, Lcycinv2, plugflag, uzave);
    for(n=1;n<=3;n++) {
      k5[n] = dt*u[n];
      x[n] = xold[n] + b61*k1[n] + b62*k2[n] + b63*k3[n] + b64*k4[n]
             + b65*k5[n];
    }
  interp(x, xa, ya, ux, uy, uz, uxi, uyi, uzi, Ni, u, dxinv, dyinv, P,
       ytmp, w, Nx, Ny, Lcycinv2, plugflag, uzave);
    err[0] = 0.;
    for(n=1;n<=3;n++) {
      k6[n] = dt*u[n];
      err[n] = fabs(dc1*k1[n] + dc2*k2[n] + dc3*k3[n] + dc4*k4[n]
                    + dc5*k5[n] + dc6*k6[n]);
      if(err[n] > err[0]) err[0] = err[n];
    }
    if(err[0] <= maxerr) {
      for(n=1;n<=3;n++) pos[n] += c1*k1[n] + c2*k2[n] + c3*k3[n] + c4*k4[n]
              + c5*k5[n] + c6*k6[n];
      sigma = sqrt(2.*D*dt);
      if(err[0] > 0.) dtnew = .9*dt*pow(maxerr/err[0],.2);
      else dtnew = dtmax;
      if(dtnew > dtmax) dtnew = dtmax;
    }
    else {
      dt = .9*dt*pow(maxerr/err[0],.25);
      err[0] = -1.;
      k++;
    }
}
if(sigma > 0.) { // diffuse particle
    pos[1] = pos[1] + sigma*gasdev(&idumx);
    pos[2] = pos[2] + sigma*gasdev(&idumy);
    pos[3] = pos[3] + sigma*gasdev(&idumz);
}
if(flags[0] < Nrxn)
    if(pos[1] < -w) {
```

```
          f = (-w - xold[1])/(pos[1] - xold[1]);
        Lx[flags[0]+1][m][0] = pos[0] + f*dt;
        Lx[flags[0]+1][m][1] = xold[1] + f*(pos[1] - xold[1]);
        Lx[flags[0]+1][m][2] = xold[2] + f*(pos[2] - xold[2]);
        Lx[flags[0]+1][m][3] = xold[3] + f*(pos[3] - xold[3]);
        while(fabs(Lx[flags[0]+1][m][2]) > 1.)
          Lx[flags[0]+1][m][2] = 2.*Lx[flags[0]+1][m][2]/fabs(Lx[flags[0]+1][m][2]) -
Lx[flags[0]+1][m][2];
          for(n = 0; n <= 3; n++)
          Lf[flags[0]+1][m][n] = flags[n];
        flags[0] += 1;
        }
    if(flags[1] < Nrxn)
        if(pos[1] > w) {
          f = (w - xold[1])/(pos[1] - xold[1]);
        Rx[flags[1]+1][m][0] = pos[0] + f*dt;
        Rx[flags[1]+1][m][1] = xold[1] + f*(pos[1] - xold[1]);
        Rx[flags[1]+1][m][2] = xold[2] + f*(pos[2] - xold[2]);
        Rx[flags[1]+1][m][3] = xold[3] + f*(pos[3] - xold[3]);
        while(fabs(Rx[flags[1]+1][m][2]) > 1.)
          Rx[flags[1]+1][m][2] = 2.*Rx[flags[1]+1][m][2]/fabs(Rx[flags[1]+1][m][2])
- Rx[flags[1]+1][m][2];
          for(n = 0; n <= 3; n++)
          Rf[flags[1]+1][m][n] = flags[n];
        flags[1] += 1;
        }
    if(flags[2] < Nrxn)
        if(pos[2] < -1.) {
          f = (-1. - xold[2])/(pos[2] - xold[2]);
        Bx[flags[2]+1][m][0] = pos[0] + f*dt;
        Bx[flags[2]+1][m][1] = xold[1] + f*(pos[1] - xold[1]);
        Bx[flags[2]+1][m][2] = xold[2] + f*(pos[2] - xold[2]);
        Bx[flags[2]+1][m][3] = xold[3] + f*(pos[3] - xold[3]);
        while(fabs(Bx[flags[2]+1][m][1]) > w)
          Bx[flags[2]+1][m][1] =
2.*w*Bx[flags[2]+1][m][1]/fabs(Bx[flags[2]+1][m][1]) - Bx[flags[2]+1][m][1];
          for(n = 0; n <= 3; n++)
          Bf[flags[2]+1][m][n] = flags[n];
        flags[2] += 1;
        }
    if(flags[3] < Nrxn)
        if(pos[2] > 1.) {
          f = (1. - xold[2])/(pos[2] - xold[2]);
        Tx[flags[3]+1][m][0] = pos[0] + f*dt;
        Tx[flags[3]+1][m][1] = xold[1] + f*(pos[1] - xold[1]);
```

```
        Tx[flags[3]+1][m][2] = xold[2] + f*(pos[2] - xold[2]);
        Tx[flags[3]+1][m][3] = xold[3] + f*(pos[3] - xold[3]);
        while(fabs(Tx[flags[3]+1][m][1]) > w)
          Tx[flags[3]+1][m][1] =
2.*w*Tx[flags[3]+1][m][1]/fabs(Tx[flags[3]+1][m][1]) - Tx[flags[3]+1][m][1];
          for(n = 0; n <= 3; n++)
          Tf[flags[3]+1][m][n] = flags[n];
        flags[3] += 1;
        }
    if(pos[0]+dt > tflag*tframe && tflag <= Nt) {
        f = (tflag*tframe - pos[0])/(pos[0]+dt - pos[0]);
        tx[tflag][m][0] = pos[0] + f*dt;
        tx[tflag][m][1] = xold[1] + f*(pos[1] - xold[1]);
        tx[tflag][m][2] = xold[2] + f*(pos[2] - xold[2]);
        tx[tflag][m][3] = xold[3] + f*(pos[3] - xold[3]);
        for(n = 0; n <= 3; n++)
          tf[tflag][m][n] = flags[n];
        tf[tflag][m][4] = k;
        tflag++;
    }
    if(pos[3] > Zflag*Lframe && Zflag <= Nframe) {
        f = (Zflag*Lframe - xold[3])/(pos[3] - xold[3]);
        Zx[Zflag][m][0] = pos[0] + f*dt;
        Zx[Zflag][m][1] = xold[1] + f*(pos[1] - xold[1]);
        Zx[Zflag][m][2] = xold[2] + f*(pos[2] - xold[2]);
        Zx[Zflag][m][3] = xold[3] + f*(pos[3] - xold[3]);
        while(fabs(Zx[Zflag][m][1]) > w)
          Zx[Zflag][m][1] = 2.*w*Zx[Zflag][m][1]/fabs(Zx[Zflag][m][1]) -
Zx[Zflag][m][1];
        while(fabs(Zx[Zflag][m][2]) > 1.)
          Zx[Zflag][m][2] = 2.*Zx[Zflag][m][2]/fabs(Zx[Zflag][m][2]) -
Zx[Zflag][m][2];
        for(n = 0; n <= 3; n++)
          Zf[Zflag][m][n] = flags[n];
        Zf[Zflag][m][4] = k;
        Zflag++;
    }
    status = (int)(100. * (Nrxn*4*(m-1) + flags[0] + flags[1] + flags[2] + flags[3])
/ (Nrxn*4*Npart));
    if(status >= statflag*statframe) {
      gettimeofday(&finish, NULL);
      calctime = finish.tv_sec;
      calctime = calctime - 86400*floor(calctime/86400);
      fprintf(remfile, "Current time: %d:", (int) floor(calctime/3600));
      calctime = calctime - 3600*floor(calctime/3600);
```

```
fprintf(remfile, "%d:", (int)floor(calctime/60));
calctime = calctime - 60*floor(calctime/60);
fprintf(remfile, "%d\t", (int)calctime);
fprintf(remfile, "%d%% complete\n", statflag*statframe);
fflush(remfile);
statflag++;
// send output in case of crash before completion
// OUTPUT //
Lfile = fopen(Lname,"w");
Rfile = fopen(Rname,"w");
Bfile = fopen(Bname,"w");
Tfile = fopen(Tname,"w");
for(mm = 1; mm <= m; mm++) {
  for(ll = 1; ll <= Nrxn; ll++) {
    for(nn = 0; nn <= 3; nn++) {
      if(!poincare) {
          fprintf(Lfile, "%13.5e", Lx[ll][mm][nn]);
        fprintf(Rfile, "%13.5e", Rx[ll][mm][nn]);
        fprintf(Bfile, "%13.5e", Bx[ll][mm][nn]);
        fprintf(Tfile, "%13.5e", Tx[ll][mm][nn]);
      }
      else {
          fprintf(Lfile, "%23.15e", Lx[ll][mm][nn]);
        fprintf(Rfile, "%23.15e", Rx[ll][mm][nn]);
        fprintf(Bfile, "%23.15e", Bx[ll][mm][nn]);
        fprintf(Tfile, "%23.15e", Tx[ll][mm][nn]);
      }
    }
    for(nn = 0; nn <= 3; nn++) {
      fprintf(Lfile, "%8d", Lf[ll][mm][nn]);
      fprintf(Rfile, "%8d", Rf[ll][mm][nn]);
      fprintf(Bfile, "%8d", Bf[ll][mm][nn]);
      fprintf(Tfile, "%8d", Tf[ll][mm][nn]);
    }
    fprintf(Lfile, "\n");
    fprintf(Rfile, "\n");
    fprintf(Bfile, "\n");
    fprintf(Tfile, "\n");
  }
}
fclose(Lfile);
fclose(Rfile);
fclose(Bfile);
fclose(Tfile);
snapfile = fopen(Zname,"w");
```

```
    if(!poincare) fprintf(snapfile, "%13d%13d%13d%13d%2d%2d%2d%2d\n",
            Npart, Nframe+1, start.tv_sec, start.tv_usec, 0, 0, 0, 0);
    else fprintf(snapfile, "%23d%23d%23d%23d%2d%2d%2d%2d\n",
            Npart, Nframe+1, start.tv_sec, start.tv_usec, 0, 0, 0, 0);
    for(mm = 1; mm <= m; mm++) {
      for(ll = 0; ll <= Nframe; ll++) {
        for(nn = 0; nn <= 3; nn++) {
            if(!poincare) fprintf(snapfile, "%13.5e", Zx[ll][mm][nn]);
            else fprintf(snapfile, "%23.15e", Zx[ll][mm][nn]);
        }
        for(nn = 0; nn <= 3; nn++)
            fprintf(snapfile, "%8d", Zf[ll][mm][nn]);
        fprintf(snapfile, "\n");
      }
    }
    fclose(snapfile);
    snapfile = fopen(tname,"w");
    if(!poincare) fprintf(snapfile, "%13d%13d%13d%13d%2d%2d%2d%2d\n",
            Npart, Nt+1, 0, 0, 0, 0, 0, 0);
    else fprintf(snapfile, "%23d%23d%23d%23d%2d%2d%2d%2d\n",
            Npart, Nt+1, 0, 0, 0, 0, 0, 0);
    for(ll = 0; ll <= Nt; ll++) {
      for(mm = 1; mm <= m; mm++) {
        for(nn = 0; nn <= 3; nn++) {
            if(!poincare) fprintf(snapfile, "%13.5e", tx[ll][mm][nn]);
            else fprintf(snapfile, "%23.15e", tx[ll][mm][nn]);
        }
        for(nn = 0; nn <= 3; nn++)
            fprintf(snapfile, "%8d", tf[ll][mm][nn]);
        fprintf(snapfile, "\n");
      }
    }
    fclose(snapfile);
  }
  // If particle leaves channel, reflect off side walls
  while(fabs(pos[1]) > w) pos[1] = 2.*w*pos[1]/fabs(pos[1]) - pos[1];
  while(fabs(pos[2]) > 1.) pos[2] = 2.*pos[2]/fabs(pos[2]) - pos[2];
  pos[0] += dt;
  dt = dtnew;
  if(Nskip > 0 && k % Nskip == 0 && poincare) {
      for(n = 0; n <= 3; n++) fprintf(outfile, "%23.15e", pos[n]);
      fprintf(outfile, "\n");
  }
  k++;
}
```

```
    if(Nskip > 0 && poincare) fclose(outfile);
  }
  gettimeofday(&finish,NULL);
  calctime = finish.tv_sec-start.tv_sec+(finish.tv_usec-start.tv_usec)/1.e6;
  fprintf(remfile,"Sim complete: %g sec / %d part / %g H = %g sec/part/H\n",
          calctime, Npart, Ncyc*Lcyc/2., calctime/Npart/(Ncyc*Lcyc/2.));
  fclose(remfile);

  // FREE MEMORY
  free_dvector(xa, 1, Nx);
  free_dvector(ya, 1, Ny);
  free_dmatrix(ux, 1, Nx, 1, Ny);
  free_dmatrix(uy, 1, Nx, 1, Ny);
  free_dmatrix(uz, 1, Nx, 1, Ny);
  free_dmatrix(uxi, 1, Ni, 1, Ni);
  free_dmatrix(uyi, 1, Ni, 1, Ni);
  free_dmatrix(uzi, 1, Ni, 1, Ni);
  free_d3tensor(Lx, 1, Nrxn, 1, Npart, 0, 3);
  free_d3tensor(Rx, 1, Nrxn, 1, Npart, 0, 3);
  free_d3tensor(Bx, 1, Nrxn, 1, Npart, 0, 3);
  free_d3tensor(Tx, 1, Nrxn, 1, Npart, 0, 3);
  free_i3tensor(Lf, 1, Nrxn, 1, Npart, 0, 3);
  free_i3tensor(Rf, 1, Nrxn, 1, Npart, 0, 3);
  free_i3tensor(Bf, 1, Nrxn, 1, Npart, 0, 3);
  free_i3tensor(Tf, 1, Nrxn, 1, Npart, 0, 3);
  free_d3tensor(Zx, 0, Nframe, 1, Npart, 0, 3);
  free_d3tensor(tx, 0, Nt, 1, Npart, 0, 3);
  free_i3tensor(Zf, 0, Nframe, 1, Npart, 0, 4);
  free_i3tensor(tf, 0, Nt, 1, Npart, 0, 4);
  free_dvector(dxinv, 1, Ni);
  free_dvector(dyinv, 1, Ni);
  free_dvector(ytmp, 1, Ni);
  free_dmatrix(P, 1, Ni, 1, Ni);
  free_dmatrix(initpos, 1, Npart, 0, 3);
  return 0;
}

void nrerror(char error_text[])
/* Numerical Recipes standard error handler */
{
        fprintf(stderr,"Numerical Recipes run-time error...\n");
        fprintf(stderr,"%s\n",error_text);
        fprintf(stderr,"...now exiting to system...\n");
        exit(1);
}
```

```
double *dvector(long nl, long nh)
/* allocate a double vector with subscript range v[nl..nh] */
{
        double *v;

        v=(double *)malloc((size_t) ((nh-nl+1+NR_END)*sizeof(double)));
        if (!v) nrerror("allocation failure in dvector()");
        return v-nl+NR_END;
}

double **dmatrix(long nrl, long nrh, long ncl, long nch)
/* allocate a double matrix with subscript range m[nrl..nrh][ncl..nch] */
{
        long i, nrow=nrh-nrl+1,ncol=nch-ncl+1;
        double **m;

        /* allocate pointers to rows */
        m=(double **) malloc((size_t)((nrow+NR_END)*sizeof(double*)));
        if (!m) nrerror("allocation failure 1 in matrix()");
        m += NR_END;
        m -= nrl;

        /* allocate rows and set pointers to them */
        m[nrl]=(double *)
malloc((size_t)((nrow*ncol+NR_END)*sizeof(double)));
        if (!m[nrl]) nrerror("allocation failure 2 in matrix()");
        m[nrl] += NR_END;
        m[nrl] -= ncl;

        for(i=nrl+1;i<=nrh;i++) m[i]=m[i-1]+ncol;

        /* return pointer to array of pointers to rows */
        return m;
}

int **imatrix(long nrl, long nrh, long ncl, long nch)
/* allocate an integer matrix with subscript range m[nrl..nrh][ncl..nch] */
{
        long i, nrow=nrh-nrl+1,ncol=nch-ncl+1;
        int **m;

        /* allocate pointers to rows */
        m=(int **) malloc((size_t)((nrow+NR_END)*sizeof(int*)));
        if (!m) nrerror("allocation failure 1 in matrix()");
```

```
	m += NR_END;
	m -= nrl;


	/* allocate rows and set pointers to them */
	m[nrl]=(int *) malloc((size_t)((nrow*ncol+NR_END)*sizeof(int)));
	if (!m[nrl]) nrerror("allocation failure 2 in matrix()");
	m[nrl] += NR_END;
	m[nrl] -= ncl;

	for(i=nrl+1;i<=nrh;i++) m[i]=m[i-1]+ncol;

	/* return pointer to array of pointers to rows */
	return m;
}

double ***d3tensor(long nrl, long nrh, long ncl, long nch, long ndl, long ndh)
/* allocate a double 3tensor with range t[nrl..nrh][ncl..nch][ndl..ndh] */
{
	long i,j,nrow=nrh-nrl+1,ncol=nch-ncl+1,ndep=ndh-ndl+1;
	double ***t;

	/* allocate pointers to pointers to rows */
	t=(double ***) malloc((size_t)((nrow+NR_END)*sizeof(double**)));
	if (!t) nrerror("allocation failure 1 in d3tensor()");
	t += NR_END;
	t -= nrl;

	/* allocate pointers to rows and set pointers to them */
	t[nrl]=(double **)
malloc((size_t)((nrow*ncol+NR_END)*sizeof(double*)));
	if (!t[nrl]) nrerror("allocation failure 2 in d3tensor()");
	t[nrl] += NR_END;
	t[nrl] -= ncl;

	/* allocate rows and set pointers to them */
	t[nrl][ncl]=(double *)
malloc((size_t)((nrow*ncol*ndep+NR_END)*sizeof(double)));
	if (!t[nrl][ncl]) nrerror("allocation failure 3 in d3tensor()");
	t[nrl][ncl] += NR_END;
	t[nrl][ncl] -= ndl;

	for(j=ncl+1;j<=nch;j++) t[nrl][j]=t[nrl][j-1]+ndep;
	for(i=nrl+1;i<=nrh;i++) {
		t[i]=t[i-1]+ncol;
```

```
		t[i][ncl]=t[i-1][ncl]+ncol*ndep;
		for(j=ncl+1;j<=nch;j++) t[i][j]=t[i][j-1]+ndep;
	}

	/* return pointer to array of pointers to rows */
	return t;
}

int ***i3tensor(long nrl, long nrh, long ncl, long nch, long ndl, long ndh)
/* allocate an integer 3tensor with range t[nrl..nrh][ncl..nch][ndl..ndh] */
{
	long i,j,nrow=nrh-nrl+1,ncol=nch-ncl+1,ndep=ndh-ndl+1;
	int ***t;

	/* allocate pointers to pointers to rows */
	t=(int ***) malloc((size_t)((nrow+NR_END)*sizeof(int**)));
	if (!t) nrerror("allocation failure 1 in i3tensor()");
	t += NR_END;
	t -= nrl;

	/* allocate pointers to rows and set pointers to them */
	t[nrl]=(int **) malloc((size_t)((nrow*ncol+NR_END)*sizeof(int*)));
	if (!t[nrl]) nrerror("allocation failure 2 in i3tensor()");
	t[nrl] += NR_END;
	t[nrl] -= ncl;

	/* allocate rows and set pointers to them */
	t[nrl][ncl]=(int *)
malloc((size_t)((nrow*ncol*ndep+NR_END)*sizeof(int)));
	if (!t[nrl][ncl]) nrerror("allocation failure 3 in i3tensor()");
	t[nrl][ncl] += NR_END;
	t[nrl][ncl] -= ndl;

	for(j=ncl+1;j<=nch;j++) t[nrl][j]=t[nrl][j-1]+ndep;
	for(i=nrl+1;i<=nrh;i++) {
		t[i]=t[i-1]+ncol;
		t[i][ncl]=t[i-1][ncl]+ncol*ndep;
		for(j=ncl+1;j<=nch;j++) t[i][j]=t[i][j-1]+ndep;
	}

	/* return pointer to array of pointers to rows */
	return t;
}

#define MBIG 1000000000
```

```
#define MSEED 161803398
#define MZ 0
#define FAC (1.0/MBIG)

double ran3(long *idum)
{
	static int inext,inextp;
	static long ma[56];
	static int iff=0;
	long mj,mk;
	int i,ii,k;

	if (*idum < 0 || iff == 0) {
		iff=1;
		mj=labs(MSEED-labs(*idum));
		mj %= MBIG;
		ma[55]=mj;
		mk=1;
		for (i=1;i<=54;i++) {
			ii=(21*i) % 55;
			ma[ii]=mk;
			mk=mj-mk;
			if (mk < MZ) mk += MBIG;
			mj=ma[ii];
		}
		for (k=1;k<=4;k++)
			for (i=1;i<=55;i++) {
				ma[i] -= ma[1+(i+30) % 55];
				if (ma[i] < MZ) ma[i] += MBIG;
			}
		inext=0;
		inextp=31;
		*idum=1;
	}
	if (++inext == 56) inext=1;
	if (++inextp == 56) inextp=1;
	mj=ma[inext]-ma[inextp];
	if (mj < MZ) mj += MBIG;
	ma[inext]=mj;
	return mj*FAC;
}
#undef MBIG
#undef MSEED
#undef MZ
#undef FAC
```

```
double gasdev(long *idum)
{
	double ran3(long *idum);
	static int iset=0;
	static double gset;
	double fac,rsq,v1,v2;

	if (*idum < 0) iset=0;
	if  (iset == 0) {
		do {
			v1=2.0*ran3(idum)-1.0;
			v2=2.0*ran3(idum)-1.0;
			rsq=v1*v1+v2*v2;
		} while (rsq >= 1.0 || rsq == 0.0);
		fac=sqrt(-2.0*log(rsq)/rsq);
		gset=v1*fac;
		iset=1;
		return v2*fac;
	} else {
		iset=0;
		return gset;
	}
}
void free_dvector(v,nl,nh)
double *v;
long nh,nl;
/* free a double vector allocated with dvector() */
{
	free((FREE_ARG) (v+nl-NR_END));
}

void free_dmatrix(m,nrl,nrh,ncl,nch)
double **m;
long nch,ncl,nrh,nrl;
/* free a double matrix allocated by dmatrix() */
{
	free((FREE_ARG) (m[nrl]+ncl-NR_END));
	free((FREE_ARG) (m+nrl-NR_END));
}

void free_imatrix(m,nrl,nrh,ncl,nch)
int **m;
long nch,ncl,nrh,nrl;
/* free an int matrix allocated by imatrix() */
```

```
{
        free((FREE_ARG) (m[nrl]+ncl-NR_END));
        free((FREE_ARG) (m+nrl-NR_END));
}

void free_d3tensor(t,nrl,nrh,ncl,nch,ndl,ndh)
double ***t;
long nch,ncl,ndh,ndl,nrh,nrl;
/* free a double d3tensor allocated by d3tensor() */
{
        free((FREE_ARG) (t[nrl][ncl]+ndl-NR_END));
        free((FREE_ARG) (t[nrl]+ncl-NR_END));
        free((FREE_ARG) (t+nrl-NR_END));
}

void free_i3tensor(t,nrl,nrh,ncl,nch,ndl,ndh)
int ***t;
long nch,ncl,ndh,ndl,nrh,nrl;
/* free an integer i3tensor allocated by i3tensor() */
{
        free((FREE_ARG) (t[nrl][ncl]+ndl-NR_END));
        free((FREE_ARG) (t[nrl]+ncl-NR_END));
        free((FREE_ARG) (t+nrl-NR_END));
}

void check(char point[80]) // displays a string, for debugging
{
  fprintf(stderr,"%s\n", point);
  fflush(stderr);
}

void interp_setup(double **ux, double **uy, double **uz, int Nx, int Ny, int Ni,
                  double w, double *dxinv, double *dyinv, double Lcyc,
                    double *Lcycinv2)
{
  int i, j;
  double dx, dy;

  dx = 2. * w / (Nx - 1.);
  dy = 2. / (Ny - 1.);
  for(i = 1; i <= Ni; i++) { dxinv[i] = 1./dx/i; dyinv[i] = 1./dy/i; }
  for(j = 1; j <= Ny; j++)
    for(i = 1; i <= Nx; i++) {
      ux[i][j] *= dxinv[1]*dyinv[1];
      uy[i][j] *= dxinv[1]*dyinv[1];
```

```
      uz[i][j] *= dxinv[1]*dyinv[1];
    }
  *Lcycinv2 = 2. / Lcyc;
}

inline void interp1D(double x, double *xa, double *ua, int Ni, double *u,
                double *dxinv, double **P)
{
  int m, n;

  for(n = Ni - 1; n; n--)
    P[1][n] = (x - xa[n]) * ua[n+1] - (x - xa[1+n]) * ua[n];
  for (m = 2; m < Ni - 1; m++)
    for (n = Ni - m; n; n--)
      P[m][n] = ((x - xa[n]) * P[m-1][n+1] - (x - xa[m+n]) * P[m-1][n])*dxinv[m];
  *u = ((x - xa[1]) * P[Ni-2][2] - (x - xa[Ni]) * P[Ni-2][1])*dxinv[Ni-1];
}

inline void interp2D(double *x, double *xa, double *ya, double **ua, int Ni,
                double *u, double *dxinv, double *dyinv, double **P, double *ytmp)
{
  int j;
  double y[2];

  for(j = Ni; j; j--)
    interp1D(x[2], ya, ua[j], Ni, &ytmp[j], dyinv, P);
  interp1D(x[1], xa, ytmp, Ni, &y[0], dxinv, P);
  *u = y[0];
}

inline void interp(double *x, double *xa, double *ya, double **ux, double **uy,
              double **uz, double **uxi, double **uyi, double **uzi, int Ni,
              double *u, double *dxinv, double *dyinv, double **P, double *ytmp,
              double w, int Nx, int Ny, double Lcycinv2, int plugflag,
              double uzave)
{
  int i, j, xlo, ylo;
  double flag = 1.;

  if((int)(ceil(x[3] * Lcycinv2)) % 2 == 0) flag = -1.;
  x[1] *= flag;
  xlo = (int)(floor((x[1] + w) * dxinv[1] + 1. - Ni / 2.));
  if(xlo < 0) xlo = 0;
  if(xlo > Nx - Ni) xlo = Nx - Ni;
  ylo = (int)(floor((x[2] + 1.) * dyinv[1] + 1. - Ni / 2.));
```

```
  if(ylo < 0) ylo = 0;
  if(ylo > Ny - Ni) ylo = Ny - Ni;
  for(j = Ni; j; j--)
    for(i = Ni; i; i--) {
      uxi[i][j] = ux[i+xlo][j+ylo];
      uyi[i][j] = uy[i+xlo][j+ylo];
      uzi[i][j] = uz[i+xlo][j+ylo];
    }
  interp2D(x, &xa[xlo], &ya[ylo], uxi, Ni, &u[1], dxinv, dyinv, P, ytmp);
  interp2D(x, &xa[xlo], &ya[ylo], uyi, Ni, &u[2], dxinv, dyinv, P, ytmp);
  if(plugflag)
    u[3] = uzave;
  else
    interp2D(x, &xa[xlo], &ya[ylo], uzi, Ni, &u[3], dxinv, dyinv, P, ytmp);
  x[1] *= flag;
  u[1] *= flag;
}
```

shmparams: example input file for use with shm06a

```
aspect_ratio  2.
cycle_length  40.
num_cycles      20
slip_vel        0.1
max_axial_vel         1.
diffusivity      0.000
plug_flow?    0
max_time_step       0.1
max_num_steps   2147483646
RK_error_param     1.e-12
order_of_interp       4
vel_file       U2_3_100
num_particles         99
rand_init?     0
init_file      inits
poincare?      1
num_Z_frames       1
Z_file         Zthread
num_t_frames         1
t_file         timethread
L_file         Lthread
R_file          Rthread
B_file         Bthread
T_file         Tthread
frames_2_skip   1
```

```
traj_file       trajthread
progress_skip          1
remark_file     outputthread
max_num_rxns    1
```

shmlib.c: library routines for simulating LDC approximation to SHM flows

```
#include <stdio.h>
#include <math.h>
#include <stddef.h>
#include <stdlib.h>
#include "ranlib.h"
#include "nrutil.h"
#include "p480.h"

#define J 4

//  For the most part vectors start with element 1, for easier bookkeeping
//
//  Unless otherwise noted the variables used are:
//  w - aspect ratio of channel, usually 2.0
//  r - degree of asymmetry, width of left vortex over total width, usually 1/3
//  N - number of Fourier coefficients in x-dir of expansion of u_xy
//  I - number of Fourier coefficients in y-dir of expansion of u_xy
//  NZ - number of Fourier coefficients in expansion of u_z
//  pi - 3.1415..., 4.0*atan(1.0)
//  cycle_length - length of full cycle in half-heights of the channel
//  u_slip - ratio of u_floor / uz_max

void check(char point[80]) // displays a string, for debugging
{
  fprintf(stderr,"%s\n", point);
  fflush(stderr);
}

double coth(double x) // hyperbolic cotangent function, not in math.h
{
  return 1./tanh(x);
}

void calc_constants(double **alpha, double **beta, double *gamma,
    double *gammac, double ***Pc, double ***Qc, double ***Rc, double ***Sc,
    double pi, double w, int N, int I, int NZ, double *uzave)
//  calculates constants that will be used in the calculation
//  input - pi, w, N, I, NZ
```

```
//  output - alpha, beta, gamma, gammac, Pc, Qc, Rc, Sc, u_z_ave
//  note - u_z_ave may not work correctly
{
  int n, i, nz, j;

  for(n=1;n<=N;n++) {
    alpha[n][1] = (2.*n-1.)*pi/2./w;
    alpha[n][3] = alpha[n][1];
    alpha[n][2] = n*pi/w;
    alpha[n][4] = alpha[n][2];
    for(j=1;j<=J;j++) {
      Pc[n][j][1] = 1./cosh(alpha[n][j]);
      Pc[n][j][2] = tanh(alpha[n][j]);
      Pc[n][j][3] = Pc[n][j][1]*(Pc[n][j][2]*alpha[n][j] - 1.);
      Rc[n][j][1] = 1./sinh(alpha[n][j]);
      Rc[n][j][2] = coth(alpha[n][j]);
      Rc[n][j][3] = Rc[n][j][1]*(Rc[n][j][2]*alpha[n][j] - 1.);
    }
  }
  for(i=1;i<=I;i++) {
    beta[i][1] = (2.*i-1.)*pi/2.;
    beta[i][4] = beta[i][1];
    beta[i][2] = i*pi;
    beta[i][3] = beta[i][2];
    for(j=1;j<=J;j++) {
      Qc[i][j][1] = 1./cosh(beta[i][j]*w);
      Qc[i][j][2] = w*tanh(beta[i][j]*w);
      Qc[i][j][3] = Qc[i][j][1]*(Qc[i][j][2]*beta[i][j] - 1.);
      Sc[i][j][1] = 1./sinh(beta[i][j]*w);
      Sc[i][j][2] = w*coth(beta[i][j]*w);
      Sc[i][j][3] = Sc[i][j][1]*(Sc[i][j][2]*beta[i][j] - 1.);
    }
  }
  uzave[0] = 2./3.;
  for(nz=1;nz<=NZ;nz++) {
    gamma[nz] = (2.*nz-1.)*pi/2.;
    gammac[nz] = 4. * pow(-1.,nz)*pow(gamma[nz],-3.)/cosh(gamma[nz]*w);
    uzave[0] +=
gammac[nz]*sin(gamma[nz])*sinh(gamma[nz]*w)*pow(gamma[nz],-2.)/w;
  }
}

void calc_abxy(double **alphax, double **alphay, double **betax, double
**betay,
    double **alpha, double **beta, double *x, int N, int I)
```

```
//  calculates alpha*x, alpha*y, beta*x, beta*y - speeds up calculation
//  input - alpha, beta, x = [x y z], N, I
//  output - alphax, alphay, betax, betay
{
  int n, i, j;

  for(j=1;j<=J;j++) {
    for(n=1;n<=N;n++) {
      alphax[n][j] = alpha[n][j]*x[1];
      alphay[n][j] = alpha[n][j]*x[2];
    }
    for(i=1;i<=I;i++) {
      betax[i][j] = beta[i][j]*x[1];
      betay[i][j] = beta[i][j]*x[2];
    }
  }
}

void calc_PQRS(double **P, double **Q, double **R, double **S,
    double ***Pc, double ***Qc, double ***Rc, double ***Sc,
    double **alphay, double **betax, double *x, int N, int I)
//  calculates functions P,Q,R,S
//  input - Pc, Qc, Rc, Sc, alphay, betax, x = [x y z], N, I
//  output - P, Q, R, S
{
  int i,j,n;

  for(n=1;n<=N;n++) {
    P[n][1] = Pc[n][1][1]*(Pc[n][1][2]*cosh(alphay[n][1])
          - x[2]*sinh(alphay[n][1]));
    P[n][4] = Pc[n][4][1]*(Pc[n][4][2]*cosh(alphay[n][4])
          - x[2]*sinh(alphay[n][4]));
    R[n][2] = Rc[n][2][1]*(Rc[n][2][2]*sinh(alphay[n][2])
          - x[2]*cosh(alphay[n][2]));
    R[n][3] = Rc[n][3][1]*(Rc[n][3][2]*sinh(alphay[n][3])
          - x[2]*cosh(alphay[n][3]));
  }
  for(i=1;i<=I;i++) {
    Q[i][1] = Qc[i][1][1]*(Qc[i][1][2]*cosh(betax[i][1])
          - x[1]*sinh(betax[i][1]));
    Q[i][3] = Qc[i][3][1]*(Qc[i][3][2]*cosh(betax[i][3])
          - x[1]*sinh(betax[i][3]));
    S[i][2] = Sc[i][2][1]*(Sc[i][2][2]*sinh(betax[i][2])
          - x[1]*cosh(betax[i][2]));
    S[i][4] = Sc[i][4][1]*(Sc[i][4][2]*sinh(betax[i][4])
```

```
        - x[1]*cosh(betax[i][4]));
  }
}

void calc_dPQRS(double **dP, double **dQ, double **dR, double **dS,
    double ***Pc, double ***Qc, double ***Rc, double ***Sc,
    double **alphay, double **betax, double *x, int N, int I)
//  calculates dP/dy, dQ/dx, dR/dy, dS/dx
//  input - Pc, Qc, Rc, Sc, alphay, betax, x = [x y z], N, I
//  output - dP, dQ, dR, dS
{
  int i, j, n;

  for(n=1;n<=N;n++) {
    dP[n][1] = Pc[n][1][3]*sinh(alphay[n][1])
      - Pc[n][1][1]*alphay[n][1]*cosh(alphay[n][1]);
    dP[n][4] = Pc[n][4][3]*sinh(alphay[n][4])
      - Pc[n][4][1]*alphay[n][4]*cosh(alphay[n][4]);
    dR[n][2] = Rc[n][2][3]*cosh(alphay[n][2])
      - Rc[n][2][1]*alphay[n][2]*sinh(alphay[n][2]);
    dR[n][3] = Rc[n][3][3]*cosh(alphay[n][3])
      - Rc[n][3][1]*alphay[n][3]*sinh(alphay[n][3]);
  }
  for(i=1;i<=I;i++) {
    dQ[i][1] = Qc[i][1][3]*sinh(betax[i][1])
      - Qc[i][1][1]*betax[i][1]*cosh(betax[i][1]);
    dQ[i][3] = Qc[i][3][3]*sinh(betax[i][3])
      - Qc[i][3][1]*betax[i][3]*cosh(betax[i][3]);
    dS[i][2] = Sc[i][2][3]*cosh(betax[i][2])
      - Sc[i][2][1]*betax[i][2]*sinh(betax[i][2]);
    dS[i][4] = Sc[i][4][3]*cosh(betax[i][4])
      - Sc[i][4][1]*betax[i][4]*sinh(betax[i][4]);
  }
}

void calc_u(double *u, double **X, double **Y, double **alpha, double **beta,
    double **P, double **Q, double **R, double **S,
    double **dP, double **dQ, double **dR, double **dS,
    double **alphax, double **betay, double *gamma, double *gammac,
    double *x, int N, int I, int NZ, double cycle_length, double u_z,
    double *uzave, int plug)
//  the actual velocity calculation
//  input - X, Y, alpha, beta, P, Q, R, S, dP, dQ, dR, dS, alphax, betay,
//    gamma, gammac, x = [x y z], N, I, NZ, cycle_length, u_z
//  output - u = [ux uy uz]
```

```
{
  int i, n, nz;
  double flag;

  u[1] = 0.;
  u[2] = 0.;
  u[3] = 0.;

//  determine which halfcycle to use, odd -> flag = 1., even -> flag = -1.
  if((int)(ceil(x[3]/(cycle_length/2.))) % 2 == 0) flag = -1.;
  else flag = 1.;

  for(n=1;n<=N;n++) { // x-dir terms in expansion of uxy
    u[1] += flag*X[n][1]*dP[n][1]*cos(alphax[n][1])
      + X[n][2]*dR[n][2]*sin(alphax[n][2])
      + flag*X[n][3]*dR[n][3]*cos(alphax[n][3])
      + X[n][4]*dP[n][4]*sin(alphax[n][4]);
    u[2] += flag*X[n][1]*P[n][1]*alpha[n][1]*sin(alphax[n][1])
      - X[n][2]*R[n][2]*alpha[n][2]*cos(alphax[n][2])
      + flag*X[n][3]*R[n][3]*alpha[n][3]*sin(alphax[n][3])
      - X[n][4]*P[n][4]*alpha[n][4]*cos(alphax[n][4]);
  }
  for(i=1;i<=I;i++) { // y-dir terms in expansion of uxy
    u[1] += -flag*Y[i][1]*Q[i][1]*beta[i][1]*sin(betay[i][1])
      + Y[i][2]*S[i][2]*beta[i][2]*cos(betay[i][2])
      + flag*Y[i][3]*Q[i][3]*beta[i][3]*cos(betay[i][3])
      - Y[i][4]*S[i][4]*beta[i][4]*sin(betay[i][4]);
    u[2] += -flag*Y[i][1]*dQ[i][1]*cos(betay[i][1])
      - Y[i][2]*dS[i][2]*sin(betay[i][2])
      - flag*Y[i][3]*dQ[i][3]*sin(betay[i][3])
      - Y[i][4]*dS[i][4]*cos(betay[i][4]);
  }
  if(plug == 1) u[3] = uzave[0];
  else {
    u[3] = 1 - x[2]*x[2]; // expansion of uz
    for(nz=1;nz<=NZ;nz++) u[3] += cosh(gamma[nz]*x[1])*cos(gamma[nz]*x[2])
      * gammac[nz];
  }
  for(n=1;n<=3;n++) u[n] *= u_z; // multiply by overall velocity prefactor
}

void calc_psi(double *psi, double **X, double **Y, double **alpha, double
**beta,
    double **P, double **Q, double **R, double **S,
    double **dP, double **dQ, double **dR, double **dS,
```

```
    double **alphax, double **betay, double *gamma, double *gammac,
    double *x, int N, int I, int NZ, double cycle_length, double u_z)
//  calculates the streamfunction - mostly useful for visualization of
//    streamlines, not used in simulation
//  input - X, Y, alpha, beta, P, Q, R, S, dP, dQ, dR, dS, alphax, betay,
//    gamma, gammac, x = [x y z], N, I, NZ, cycle_length, u_z
//  output - psi (represented as a vector, but only psi[0] is used
{
  int i, n, nz;
  double flag;

  psi[0] = 0.;

// determine halfcycle
if((int)(ceil(x[3]/(cycle_length/2.))) % 2 == 0) flag = -1.;
  else flag = 1.;

  for(n=1;n<=N;n++) { // x-dir terms
    psi[0] += flag*X[n][1]*P[n][1]*cos(alphax[n][1])
      + X[n][2]*R[n][2]*sin(alphax[n][2])
      + flag*X[n][3]*R[n][3]*cos(alphax[n][3])
      + X[n][4]*P[n][4]*sin(alphax[n][4]);
  }
  for(i=1;i<=I;i++) { // y-dir terms
    psi[0] += flag*Y[i][1]*Q[i][1]*cos(betay[i][1])
      + Y[i][2]*S[i][2]*sin(betay[i][2])
      + flag*Y[i][3]*Q[i][3]*sin(betay[i][3])
      + Y[i][4]*S[i][4]*cos(betay[i][4]);
  }
}

void calc_F(double ***FcosP, double ***FcosQ, double ***FsinR, double
***FsinS,
    double **FcosU, double **FsinU, double **alpha, double **beta,
    double w, double r, int N, int I, double u_slip)
//  calculates the sine and cosine transforms of P,Q,R,S, and u_floor
//  input - alpha, beta, w, r, N, I, u_slip
//  output - FcosP, FcosQ, FsinR, FsinS, FcosU, FsinU
{
  int i,j,n;
  double constant;

  for(j=1; j<=J; j++) {
    for(n=1; n<=N; n++) {
      for(i=1; i<=I; i++) {
```

```
            constant = -4. * alpha[n][j] * beta[i][j]
              / pow((alpha[n][j] * alpha[n][j] + beta[i][j] * beta[i][j]), 2.);
            FcosP[n][i][j] = constant * pow(-1., (double)i);
            FsinR[n][i][j] = FcosP[n][i][j];
            FcosQ[n][i][j] = constant * pow(-1., (double)n) / w;
            FsinS[n][i][j] = FcosQ[n][i][j];
        }
        // This code can produce two vortex pairs alternating small,big,small,big
        // For one vortex pair, leave this in, comment out below
        FcosU[n][j] = -u_slip*sin(alpha[n][j] * w * (2.*r - 1.)) / (alpha[n][j] * w);
        FsinU[n][j] = u_slip*(cos(alpha[n][j] * w * (2.*r - 1.)) - cos(alpha[n][j] * w))
            / (alpha[n][j] * w);
        // For two vortex pairs, leave this in, comment out above
        /*FcosU[n][j] = u_slip*(sin(alpha[n][j] * w * (1. - r))-sin(alpha[n][j]*w*r)) /
(alpha[n][j] * w);
        FsinU[n][j] = u_slip*(cos(alpha[n][j] * w * (1. - r)) - cos(alpha[n][j] * w) +
cos(alpha[n][j]*w*r) - 2.)
            / (alpha[n][j] * w); */
        // For four vortex pairs, small-big-big-small-small-big-big-small
        /* FcosU[n][j] = 0.;
        FsinU[n][j] = u_slip*(2.*cos(alpha[n][j] * w * (0.5*r - 1.)) - cos(alpha[n][j] * w)
- 2.*cos(alpha[n][j]*w*0.5) + 2.*cos(alpha[n][j]*r*w*0.5) - 1.)
            / (alpha[n][j] * w); */
        // For small-big-big-small-small-big-big-small in left 1/3 of channel
        /*FcosU[n][j] = u_slip*(sin(alpha[n][j] * w) - 2.*sin(alpha[n][j] * w *(6./6.-r/6.))
+ 2.*sin(alpha[n][j] * w *5./6.) - 2.*sin(alpha[n][j] * w *(5./6.-r/6.)) +
2.*sin(alpha[n][j] * w *4./6.) - 2.*sin(alpha[n][j] * w *(4./6.-r/6.)) +
2.*sin(alpha[n][j] * w *3./6.) - 2.*sin(alpha[n][j] * w *(3./6.-r/6.)) + sin(alpha[n][j] *
w *2./6.)) / (alpha[n][j] * w);
        FsinU[n][j] = u_slip*(cos(alpha[n][j] * w) - 2.*cos(alpha[n][j] * w *(6./6.-r/6.))
+ 2.*cos(alpha[n][j] * w *5./6.) - 2.*cos(alpha[n][j] * w *(5./6.-r/6.)) +
2.*cos(alpha[n][j] * w *4./6.) - 2.*cos(alpha[n][j] * w *(4./6.-r/6.)) +
2.*cos(alpha[n][j] * w *3./6.) - 2.*cos(alpha[n][j] * w *(3./6.-r/6.)) +
cos(alpha[n][j] * w *2./6.)) / (alpha[n][j] * w); */
    }
  }
}

void calc_coeffs(double **X, double **Y, double **alpha, double **beta,
    double **dP, double **dQ, double **dR, double **dS,
    double ***FcosP, double ***FcosQ, double ***FsinR, double ***FsinS,
    double **FcosU, double **FsinU, double w, double r, int N, int I)
//  calculates coefficients X and Y for the double Fourier expansion
//  matrix inversion modified from Numerical Recipes
//  input - alpha, beta, dP, dQ, dR, dS, FcosP, FcosQ, FsinR, FsinS,
```

```
//    FcosU, FsinU, w, r, N, I
//  output - X, Y
{
  int i,j,k,l,m,n;
  double ***M,**b;

  double **G, *u;
  int *indx;
  double tmp, sgn;

  M = d3tensor(1,N+I,1,N+I,1,J);
  b = dmatrix(1,N+I,1,J);

  for(j=1; j<=J; j++)
    for(n=1; n<=N+I; n++) {
      for(i=1; i<=N+I; i++)
          M[n][i][j] = 0.;
      b[n][j] = 0.;
    }

  for(n=1; n<=N; n++) {
    M[n][n][1] = dP[n][1];
    M[n][n][2] = dR[n][2];
    M[n][n][3] = dR[n][3];
    M[n][n][4] = dP[n][4];
    for(i=1; i<=I; i++) {
      M[n][N+i][1] = -beta[i][1] * sin(-beta[i][1]) * FcosQ[n][i][1];
      M[n][N+i][2] =  beta[i][2] * cos(-beta[i][2]) * FsinS[n][i][2];
      M[n][N+i][3] =  beta[i][3] * cos(-beta[i][3]) * FcosQ[n][i][3];
      M[n][N+i][4] = -beta[i][4] * sin(-beta[i][4]) * FsinS[n][i][4];
    }

    //    Options here include:
    //      velocity along the floor only
    //      velocity along floor and ceiling in same directions (symmetric)
    //      velocity along floor and ceiling in opposite directions (asymmetric)
    //
    //      comment out the portions you don't want

    // floor velocity only
    /* b[n][1] = FcosU[n][1];
    b[n][2] = FsinU[n][2];
    b[n][3] = FcosU[n][3];
    b[n][4] = FsinU[n][4]; */
```

```
  // vertically symmetric
  b[n][1] = 0.;
  b[n][2] = 2.*FsinU[n][2];
  b[n][3] = 2.*FcosU[n][3];
  b[n][4] = 0.;

  // vertically asymmetric
  /* b[n][1] = 2.*FcosU[n][1];
  b[n][2] = 0.;
  b[n][3] = 0.;
  b[n][4] = 2.*FsinU[n][4]; */
}

for(i=1; i<=I; i++) {
  M[N+i][N+i][1] = dQ[i][1];
  M[N+i][N+i][2] = dS[i][2];
  M[N+i][N+i][3] = dQ[i][3];
  M[N+i][N+i][4] = dS[i][4];
  for(n=1; n<=N; n++) {
    M[N+i][n][1] = -alpha[n][1] * sin(alpha[n][1] * w) * FcosP[n][i][1];
    M[N+i][n][2] =  alpha[n][2] * cos(alpha[n][2] * w) * FsinR[n][i][2];
    M[N+i][n][3] = -alpha[n][3] * sin(alpha[n][3] * w) * FsinR[n][i][3];
    M[N+i][n][4] =  alpha[n][4] * cos(alpha[n][4] * w) * FcosP[n][i][4];
  }
}

G=dmatrix(1,N+I,1,N+I);
u=dvector(1,N+I);
indx = ivector(1,N+I);

for(j=1; j<=J; j++) {
  for(n=1; n<=N+I; n++) {
    for(i=1; i<=N+I; i++)
        G[n][i] = M[n][i][j];
    u[n] = b[n][j];
  }
  ludcmpp480(G,N+I,indx,&sgn);
  lubksbp480(G,N+I,indx,u);
  for(n=1;n<=N;n++)
    X[n][j] = u[n];
  for(i=1;i<=I;i++)
    Y[i][j] = u[N+i];
}
for(n=1;n<=N;n++)
        //for(j=1;j<=J;j++)
```

```
                    fprintf(stdout,"%g %g %g
%g\n",alpha[n][1],alpha[n][1]*(X[n][1]+X[n][3]),alpha[n][2],alpha[n][2]*(X[n][2]+X
[n][4]));
  free_d3tensor(M,1,N+I,1,N+I,1,J);
  free_dmatrix(b,1,N+I,1,J);
  free_dmatrix(G,1,N+I,1,N+I);
  free_dvector(u,1,N+I);
  free_ivector(indx,1,N+I);
}

void diffuse(double *x, double diffusivity, double tstep, double pi,
    double xmax, double ymax, long *idumr, long *idumt, long *idump,
    long *idumy)
//  diffusion step, not used, not quite right and very inefficient
{
  int n;
  double sigma, r, y, xnew[4], theta, phi, rmax;

  sigma = sqrt(diffusivity*tstep);
  rmax = 2.*sqrt(xmax*xmax + ymax*ymax);

  for(n=1;n<=3;n++) xnew[n] = x[n];
  xnew[1] = 2.*xmax;
  xnew[2] = 2.*ymax;
  while(fabs(xnew[1])>xmax || fabs(xnew[2])>ymax) {
    r = rmax*ran1(idumr);
    y = ran1(idumy);
    while(exp(-r*r/2/sigma/sigma) < y) {
      r = rmax*ran1(idumr);
      y = ran1(idumy);
    }
    theta = 2*pi*ran1(idumt);
    phi = pi*ran1(idump);
    xnew[1] = x[1] + r*cos(theta)*sin(phi);
    xnew[2] = x[2] + r*sin(theta)*sin(phi);
    xnew[3] = x[3] + r*cos(phi);
  }
  for(n=1;n<=3;n++) x[n] = xnew[n];
}

void diffuse2(double *x, double diffusivity, double tstep, double pi,
    double xmax, double ymax, long *idumr, long *idumt, long *idump,
    long *idumy)
//  diffusion step, not used, not quite right but more efficient
{
```

```
  int n;
  double sigma, r, xnew[4], theta, phi, rsq, v1, v2;

  sigma = sqrt(diffusivity*tstep);

  xnew[1] = 2.*xmax;
  xnew[2] = 2.*ymax;
  xnew[3] = x[3];
  while(fabs(xnew[1])>xmax || fabs(xnew[2])>ymax) {
    fprintf(stderr,"%g %g\n",xnew[1],xnew[2]);
    check("bad");
//    r = sigma*gasdev(idumr);
    rsq = 2.;
    while(rsq >= 1. || rsq == 0.) {
      v1 = 2.*ran1(idumr)-1.;
      v2 = 2.*ran1(idumy)-1.;
      rsq = v1*v1 + v2*v2;
    }
    r = v1 * sqrt(-2.*log(rsq)/rsq) * sigma;
    theta = 2*pi*ran1(idumt);
    phi = pi*ran1(idump);
    xnew[1] = x[1] + r*cos(theta)*sin(phi);
    xnew[2] = x[2] + r*sin(theta)*sin(phi);
    xnew[3] = x[3] + r*cos(phi);
  }
  check("good");
  for(n=1;n<=3;n++) x[n] = xnew[3];
}

void calc_u_prof(double *xa, double *ya, int Nux, int Nuy, double **ux,
    double **uy, double **uz, double w, double r, double u_slip, int N, int I,
    int NZ, double u_z)
//  calculates a velocity profile at the points on the grid defined by the
//    vectors xa[1...Nux] and ya[1...Nuy]
//  useful for visualization or for calculating a lookup table for interpolation
//  input - xa, ya, Nux, Nuy, w, r, u_slip, N, I, NZ, u_z
//  output - ux, uy, uz
{
  int i, j, k, n, plug = 0;
  double x[4], u[4], **alpha, **beta, **alphax, **alphay, **betax, **betay;
  double *gamma, *gammac, **X, **Y, **P, **Q, **R, **S, **dP, **dQ, **dR,
**dS;
  double ***Pc, ***Qc, ***Rc, ***Sc, ***FcosP, ***FcosQ, ***FsinR, ***FsinS;
  double **FcosU, **FsinU, pi, u_ave, uzave[2];
```

```
  pi = 4.*atan(1.);

  alpha = dmatrix(1,N,1,J);
  beta = dmatrix(1,I,1,J);
  alphax = dmatrix(1,N,1,J);
  alphay = dmatrix(1,N,1,J);
  betax = dmatrix(1,N,1,J);
  betay = dmatrix(1,N,1,J);
  gamma = dvector(1,NZ);
  gammac = dvector(1,NZ);
  X = dmatrix(1,N,1,J);
  Y = dmatrix(1,I,1,J);
  P = dmatrix(1,N,1,J);
  Q = dmatrix(1,I,1,J);
  R = dmatrix(1,N,1,J);
  S = dmatrix(1,I,1,J);
  dP = dmatrix(1,N,1,J);
  dQ = dmatrix(1,I,1,J);
  dR = dmatrix(1,N,1,J);
  dS = dmatrix(1,I,1,J);
  Pc = d3tensor(1,N,1,J,1,3);
  Qc = d3tensor(1,I,1,J,1,3);
  Rc = d3tensor(1,N,1,J,1,3);
  Sc = d3tensor(1,I,1,J,1,3);
  FcosP = d3tensor(1,N,1,I,1,J);
  FcosQ = d3tensor(1,N,1,I,1,J);
  FsinR = d3tensor(1,N,1,I,1,J);
  FsinS = d3tensor(1,N,1,I,1,J);
  FcosU = dmatrix(1,I,1,J);
  FsinU = dmatrix(1,I,1,J);

  // calulate constants //
  calc_constants(alpha, beta, gamma, gammac, Pc, Qc, Rc, Sc, pi, w, N, I, NZ,
uzave);
  check("constants calculated");

  // calculate coeffs //
  x[1] = w;
  x[2] = -1.;
  x[3] = 0.;
  calc_abxy(alphax, alphay, betax, betay, alpha, beta, x, N, I);
  calc_dPQRS(dP, dQ, dR, dS, Pc, Qc, Rc, Sc, alphay, betax, x, N, I);
  calc_F(FcosP,FcosQ,FsinR,FsinS,FcosU,FsinU,alpha,beta,w,r,N,I,u_slip);
  calc_coeffs(X, Y, alpha, beta, dP, dQ, dR, dS, FcosP, FcosQ, FsinR, FsinS,
     FcosU, FsinU, w, r, N, I);
```

```
check("coeffs calculated");

// calculate velocity profile
for(j = 1; j <= Nuy; j++) {
  for(i = 1; i <= Nux; i++) {
    x[1] = xa[i];
    x[2] = ya[j];
    x[3] = 1.;
    calc_abxy(alphax, alphay, betax, betay, alpha, beta, x, N, I);
    calc_PQRS(P, Q, R, S, Pc, Qc, Rc, Sc, alphay, betax, x, N, I);
    calc_dPQRS(dP, dQ, dR, dS, Pc, Qc, Rc, Sc, alphay, betax, x, N, I);
    calc_u(u, X, Y, alpha, beta, P, Q, R, S, dP, dQ, dR, dS,
          alphax, betay, gamma, gammac, x, N, I, NZ, 4., u_z, uzave, plug);
    ux[i][j] = u[1];
    uy[i][j] = u[2];
    uz[i][j] = u[3];
  }
}
free_dmatrix(alpha,1,N,1,J);
free_dmatrix(beta,1,I,1,J);
free_dmatrix(alphax,1,N,1,J);
free_dmatrix(alphay,1,N,1,J);
free_dmatrix(betax,1,N,1,J);
free_dmatrix(betay,1,N,1,J);
free_dvector(gamma,1,NZ);
free_dvector(gammac,1,NZ);
free_dmatrix(X,1,N,1,J);
free_dmatrix(Y,1,I,1,J);
free_dmatrix(P,1,N,1,J);
free_dmatrix(Q,1,I,1,J);
free_dmatrix(R,1,N,1,J);
free_dmatrix(S,1,I,1,J);
free_dmatrix(dP,1,N,1,J);
free_dmatrix(dQ,1,I,1,J);
free_dmatrix(dR,1,N,1,J);
free_dmatrix(dS,1,I,1,J);
free_d3tensor(Pc,1,N,1,J,1,3);
free_d3tensor(Qc,1,I,1,J,1,3);
free_d3tensor(Rc,1,N,1,J,1,3);
free_d3tensor(Sc,1,I,1,J,1,3);
free_d3tensor(FcosP,1,N,1,I,1,J);
free_d3tensor(FcosQ,1,N,1,I,1,J);
free_d3tensor(FsinR,1,N,1,I,1,J);
free_d3tensor(FsinS,1,N,1,I,1,J);
free_dmatrix(FcosU,1,I,1,J);
```

```
  free_dmatrix(FsinU,1,I,1,J);
}

void calc_psi_prof(double *xa, double *ya, int Nux, int Nuy, double **psi,
    double w, double r, double u_slip, int N, int I, int NZ, double u_z)
//  calculates a streamfunction profile at the points on the grid defined by the
//    vectors xa[1...Nux] and ya[1...Nuy], useful for visualization
//  input - xa, ya, Nux, Nuy, w, r, u_slip, N, I, NZ, u_z
//  output - psi
{
  int i, j, k, n;
  double x[4], psitemp[4], **alpha, **beta, **alphax, **alphay, **betax, **betay;
  double *gamma, *gammac, **X, **Y, **P, **Q, **R, **S, **dP, **dQ, **dR,
**dS;
  double ***Pc, ***Qc, ***Rc, ***Sc, ***FcosP, ***FcosQ, ***FsinR, ***FsinS;
  double **FcosU, **FsinU, pi, u_ave, uzave[2];

  pi = 4.*atan(1.);

  alpha = dmatrix(1,N,1,J);
  beta = dmatrix(1,I,1,J);
  alphax = dmatrix(1,N,1,J);
  alphay = dmatrix(1,N,1,J);
  betax = dmatrix(1,N,1,J);
  betay = dmatrix(1,N,1,J);
  gamma = dvector(1,NZ);
  gammac = dvector(1,NZ);
  X = dmatrix(1,N,1,J);
  Y = dmatrix(1,I,1,J);
  P = dmatrix(1,N,1,J);
  Q = dmatrix(1,I,1,J);
  R = dmatrix(1,N,1,J);
  S = dmatrix(1,I,1,J);
  dP = dmatrix(1,N,1,J);
  dQ = dmatrix(1,I,1,J);
  dR = dmatrix(1,N,1,J);
  dS = dmatrix(1,I,1,J);
  Pc = d3tensor(1,N,1,J,1,3);
  Qc = d3tensor(1,I,1,J,1,3);
  Rc = d3tensor(1,N,1,J,1,3);
  Sc = d3tensor(1,I,1,J,1,3);
  FcosP = d3tensor(1,N,1,I,1,J);
  FcosQ = d3tensor(1,N,1,I,1,J);
  FsinR = d3tensor(1,N,1,I,1,J);
  FsinS = d3tensor(1,N,1,I,1,J);
```

```
  FcosU = dmatrix(1,I,1,J);
  FsinU = dmatrix(1,I,1,J);

  // calulate constants //
  calc_constants(alpha, beta, gamma, gammac, Pc, Qc, Rc, Sc, pi, w, N, I, NZ,
uzave);
  check("constants calculated");

  // calculate coeffs //
  x[1] = w;
  x[2] = -1.;
  x[3] = 0.;
  calc_abxy(alphax, alphay, betax, betay, alpha, beta, x, N, I);
  calc_dPQRS(dP, dQ, dR, dS, Pc, Qc, Rc, Sc, alphay, betax, x, N, I);
  calc_F(FcosP,FcosQ,FsinR,FsinS,FcosU,FsinU,alpha,beta,w,r,N,I,u_slip);
  calc_coeffs(X, Y, alpha, beta, dP, dQ, dR, dS, FcosP, FcosQ, FsinR, FsinS,
     FcosU, FsinU, w, r, N, I);
  check("coeffs calculated");

  // calculate stream function profile
  for(j = 1; j <= Nuy; j++) {
    for(i = 1; i <= Nux; i++) {
      x[1] = xa[i];
      x[2] = ya[j];
      x[3] = 1.;
      calc_abxy(alphax, alphay, betax, betay, alpha, beta, x, N, I);
      calc_PQRS(P, Q, R, S, Pc, Qc, Rc, Sc, alphay, betax, x, N, I);
      calc_dPQRS(dP, dQ, dR, dS, Pc, Qc, Rc, Sc, alphay, betax, x, N, I);
      calc_psi(psitemp, X, Y, alpha, beta, P, Q, R, S, dP, dQ, dR, dS,
            alphax, betay, gamma, gammac, x, N, I, NZ, 4., u_z);
      psi[i][j]=psitemp[0];
    }
  }
  free_dmatrix(alpha,1,N,1,J);
  free_dmatrix(beta,1,I,1,J);
  free_dmatrix(alphax,1,N,1,J);
  free_dmatrix(alphay,1,N,1,J);
  free_dmatrix(betax,1,N,1,J);
  free_dmatrix(betay,1,N,1,J);
  free_dvector(gamma,1,NZ);
  free_dvector(gammac,1,NZ);
  free_dmatrix(X,1,N,1,J);
  free_dmatrix(Y,1,I,1,J);
  free_dmatrix(P,1,N,1,J);
  free_dmatrix(Q,1,I,1,J);
```

```
  free_dmatrix(R,1,N,1,J);
  free_dmatrix(S,1,I,1,J);
  free_dmatrix(dP,1,N,1,J);
  free_dmatrix(dQ,1,I,1,J);
  free_dmatrix(dR,1,N,1,J);
  free_dmatrix(dS,1,I,1,J);
  free_d3tensor(Pc,1,N,1,J,1,3);
  free_d3tensor(Qc,1,I,1,J,1,3);
  free_d3tensor(Rc,1,N,1,J,1,3);
  free_d3tensor(Sc,1,I,1,J,1,3);
  free_d3tensor(FcosP,1,N,1,I,1,J);
  free_d3tensor(FcosQ,1,N,1,I,1,J);
  free_d3tensor(FsinR,1,N,1,I,1,J);
  free_d3tensor(FsinS,1,N,1,I,1,J);
  free_dmatrix(FcosU,1,I,1,J);
  free_dmatrix(FsinU,1,I,1,J);
}

#include <math.h>
#define NRANSI
#include "nrutil.h"

void polint(double xa[], double ya[], int n, double x, double *y, double *dy,
   double *c, double *d)
//  linear interpolation routine adapted from Numerical Recipes
{
        int i,m,ns=1;
        double den,dif,dift,ho,hp,w;

        dif=fabs(x-xa[1]);
        for (i=1;i<=n;i++) {
                if ( (dift=fabs(x-xa[i])) < dif) {
                        ns=i;
                        dif=dift;
                }
                c[i]=ya[i];
                d[i]=ya[i];
        }
        *y=ya[ns--];
        for (m=1;m<n;m++) {
                for (i=1;i<=n-m;i++) {
                        ho=xa[i]-x;
                        hp=xa[i+m]-x;
                        w=c[i+1]-d[i];
                        if ( (den=ho-hp) == 0.0) nrerror("Error in routine polint");
```

```
                        den=w/den;
                        d[i]=hp*den;
                        c[i]=ho*den;
                }
                *y += (*dy=(2*ns < (n-m) ? c[ns+1] : d[ns--]));
        }
}
#undef NRANSI

#define NRANSI
#include "nrutil.h"

void polin2(double x1a[], double x2a[], double **ya, int m, int n, double x1,
        double x2, double *y, double *dy,
        double *ymtmp, double *c, double *d)
//  bipolynomial interpolation routine adapted from Num Rec, uses polint
{
        int j;

        for (j=1;j<=m;j++) {
                polint(x2a,ya[j],n,x2,&ymtmp[j],dy,c,d);
        }
        polint(x1a,ymtmp,m,x1,y,dy,c,d);
}
#undef NRANSI

void interp(double *xa, double *ya, double **ux, double **uy, double **uz,
   int Nx, int Ny, double *x, double *u, int Nix, int Niy,
   double *xai, double *yai, double **uxi, double **uyi, double **uzi,
   double *ymtmp, double *c, double *d, double dx, double dy, double w,
double Lcyc)
//  interpolates to find the velocity at a point using polin2 above and the
//    vectors xa[1...Nx] and ya[1...Ny] and the lookup tables ux, uy, uz as
//    created above, using a 2 Nix * 2 Niy portion of the grid
//  input - xa, ya, ux, uy, uz, Nx, Ny, x = [x y z], Nix, Niy
//  output - u = [ux uy uz]
{
  int i, j, k, m, n, xlo, xhi, xhilo, ylo, yhi, yhilo;
  double yerr, flag = 1.;

  // to suspend switching, comment next line out
  if((int)(ceil(x[3]/(Lcyc/2.))) % 2 == 0) flag = -1.;
  x[1] *= flag;

  //  find the brackets of x on the grid
```

```
  xlo = (int)(floor((x[1] + w)/dx));
  //  define interpolation limits
  xhi = xlo + Nix;
  xlo = xlo - Nix + 1;
  if(xlo < 1) {
    xhi = xhi - (xlo-1);
    xlo = 1;
  }
  if(xhi > Nx) {
    xlo = xlo - (xhi-Nx);
    xhi = Nx;
  }
  xhilo = 2*Nix;
  for(n=1; n<=xhilo; n++) xai[n] = xa[xlo+n-1];
  //  find the brackets of y on the grid
  ylo = (int)(floor((x[2] + 1.)/dy));
  //  define interpolation limits
  yhi = ylo + Niy;
  ylo = ylo - Niy + 1;
  if(ylo < 1) {
    yhi = yhi - (ylo-1);
    ylo = 1;
  }
  if(yhi > Ny) {
    ylo = ylo - (yhi-Ny);
    yhi = Ny;
  }
  yhilo = 2*Niy;
  for(n=1; n<=xhilo; n++) yai[n] = ya[ylo+n-1];
  // allocate space for interpolation grid
  for(n=1; n<=yhilo; n++)
    for(m=1; m<=xhilo; m++) {
      uxi[m][n] = ux[xlo+m-1][ylo+n-1];
      uyi[m][n] = uy[xlo+m-1][ylo+n-1];
      uzi[m][n] = uz[xlo+m-1][ylo+n-1];
    }
  // do the actual interpolation
  polin2(xai, yai, uxi, xhilo, yhilo, x[1], x[2], &u[1], &yerr, ymtmp, c, d);
  polin2(xai, yai, uyi, xhilo, yhilo, x[1], x[2], &u[2], &yerr, ymtmp, c, d);
  polin2(xai, yai, uzi, xhilo, yhilo, x[1], x[2], &u[3], &yerr, ymtmp, c, d);
  x[1] *= flag;
  u[1] *= flag;
}
```

velprof.c: create velocity profile for lid-driven cavity approximation of SHM

```
#include <stdio.h>
#include <math.h>
#include <stddef.h>
#include <stdlib.h>
#include "nrutil.h"
#include "ranlib.h"
#include "p480.h"

int main(int argc, char *argv[])
{
  int i, j, k, l, m, n, nz, Zflag, **Lf, **Rf, **Bf,
**Tf, ***Zf, flags[4];
  double **Lx, **Rx, **Bx, **Tx, ***Zx, Umax, ***umat;
  FILE *paramfile, *randfile, *Ufile;
  FILE *Lfile, *Rfile, *Bfile, *Tfile, *Zfile;
  double one_sixth, pi, w, r, Lcyc, Uslip, dt, Uz, D;
  int N, I, NZ, Npart, Nsteps, Nskip, Ncyc, order, kbad,
Nx, Ny;
  double x[4], k1[4], k2[4], k3[4], k4[4], k5[4], k6[4],
u[4], sigma;
  long idumx, idumy, idumz, idum1, idum2, idum3;
  double pos[4], xold[4], xmin, xmax, ymin, ymax;
  char Zname[80];

  double t, err[4], maxerr, dtnew, dtold, f, dx, dy;
  double umin[4], umax[4], uave[4], *xa, *ya, **ux, **uy,
**uz, **psi, uzmax;

  // read in params //
  paramfile = fopen(argv[1],"r");
  fscanf(paramfile,
      "%lf %lf %lf %lf %lf %d %d %d %d %lf %lf %d %d %d
%d %lf %lf %lf %lf %lf %d %d",
      &w, &r, &Lcyc, &Uslip, &dt, &N, &I, &NZ, &Npart,
&Uz, &D, &Nsteps, &Nskip,
      &Ncyc, &order, &maxerr, &xmin, &xmax, &ymin, &ymax,
&Nx, &Ny);
  fclose(paramfile);
  check("params read");

  r = 1./r;

  xa = dvector(1,Nx);
  ya = dvector(1,Ny);
  ux = dmatrix(1,Nx,1,Ny);
```

```
  uy = dmatrix(1,Nx,1,Ny);
  uz = dmatrix(1,Nx,1,Ny);
  psi = dmatrix(1,Nx,1,Ny);
  for(i = 1; i <= Nx; i++)
    xa[i] = -w + (i-1)*2.*w/(Nx-1);
  for(j = 1; j <= Ny; j++)
    ya[j] = -1. + (j-1)*2./(Ny-1);
  calc_u_prof(xa, ya, Nx, Ny, ux, uy, uz, w, r, 1., N, I,
NZ, 1.);
  calc_psi_prof(xa, ya, Nx, Ny, psi, w, r, 1., N, I, NZ,
1.);
  uzmax = uz[1][1];
  for(j = 1; j <= Ny; j++)
    for(i = 1; i <= Nx; i++) if(uz[i][j] > uzmax) uzmax =
uz[i][j];

  Ufile = fopen(argv[2],"w");
  fprintf(Ufile, "%24d%24d", Nx, Ny);
  for(i = 3; i <= Nx; i++) fprintf(Ufile, "%24d", 0);
  fprintf(Ufile, "\n");
  for(j = 1; j <= Ny; j++) {
    for(i = 1; i <= Nx; i++)
      fprintf(Ufile, "%24.15g", ux[i][j]);
    fprintf(Ufile, "\n");
  }
  for(j = 1; j <= Ny; j++) {
    for(i = 1; i <= Nx; i++)
      fprintf(Ufile, "%24.15g", uy[i][j]);
    fprintf(Ufile, "\n");
  }
  for(j = 1; j <= Ny; j++) {
    for(i = 1; i <= Nx; i++)
      fprintf(Ufile, "%24.15g", uz[i][j]/uzmax);
    fprintf(Ufile, "\n");
  }
  for(j = 1; j <= Ny; j++) {
    for(i = 1; i <= Nx; i++)
      fprintf(Ufile, "%24.15g", psi[i][j]);
    fprintf(Ufile, "\n");
  }
  fclose(Ufile);
  //Ufile = fopen(argv[3], "w");
  //fprintf(Ufile, "%d\n%d\n", Nx, Ny);
  //for(i = 1; i <= Nx; i++) fprintf(Ufile, "%24.15g\n",
xa[i]);
```

```
  //for(j = 1; j <= Ny; j++) fprintf(Ufile, "%24.15g\n",
ya[j]);
  //fclose(Ufile);
  check("velocities written");

  free_dvector(xa,1,Nx);
  free_dvector(ya,1,Ny);
  free_dmatrix(ux,1,Nx,1,Ny);
  free_dmatrix(uy,1,Nx,1,Ny);
  free_dmatrix(uz,1,Nx,1,Ny);
  free_dmatrix(psi,1,Nx,1,Ny);

  return 0;
}
```

velparams: sample input for use with velprof

```
24.
3.
40.
0.1
0.1
12
9
1
1
1.
0.001
10000000
0
10
5
1.e-12
-2.
2.
-1.
1.
385
17
```

makefile: for compiling code using a standard C compiler

```
LIBRARIES = -lm
OBJECTS = p480.o nrutil.o ranlib.o shmlib.o
HEADERS = p480.h nrutil.h ranlib.h shmlib.h
OPTS = -O3 -funroll-loops -fomit-frame-pointer -finline-limit=1000000
```

```
shmprog: shm06a.c
	gcc $(OPTS) -o shmprog.exe shm06a.c -lm
velprof: velprof.c $(OBJECTS) $(HEADERS)
	gcc $(OPTS) -o velprof.exe velprof.c $(OBJECTS) $(LIBRARIES)
```